Stony Brook University

Measurement of the WW and WZ production cross section in the semi-leptonic final state using $\sqrt{s} = 7$ TeV pp collisions with the ATLAS detector

A Dissertation presented

by

David Puldon

to

The Graduate School

in Partial Fulfillment of the

Requirements

for the Degree of

Doctor of Philosophy

in

Physics

Stony Brook University

August 2014

Stony Brook University

The Graduate School

David Puldon

We, the dissertation committee for the above candidate for the

Doctor of Philosophy degree, hereby recommend

acceptance of this dissertation

Dmitri Tsybychev - Dissertation Advisor
Professor, Department of Physics and Astronomy

George Sterman - Chairperson of Defense
Professor, Department of Physics and Astronomy
Director, C.N. Yang Institute for Theoretical Physics

Michael Zingale
Professor, Department of Physics and Astronomy

Marc-André Pleier
Physicist, Brookhaven National Laboratory

This dissertation is accepted by the Graduate School

Charles Taber
Dean of the Graduate School

Abstract of the Dissertation

Measurement of the WW and WZ production cross section

in the semi-leptonic final state using $\sqrt{s} = 7$ TeV

pp collisions with the ATLAS detector

by

David Puldon

Doctor of Philosophy

in

Physics

Stony Brook University

2014

Presented is a measurement of the WW+WZ production cross section in proton-proton collisions at $\sqrt{s} = 7$ TeV using data produced by the Large Hadron Collider and recorded with the ATLAS detector in 2011. The measurement tests understanding of the electroweak sector of the Standard Model at high energies and is potentially sensitive to new physics models that go beyond the Standard Model. The production cross section is measured in the WW/WZ semi-leptonic decay channel where one W boson decays into a lepton (either an electron or muon) and a neutrino, and the other W or Z boson decays hadronically into two quarks. The semi-leptonic final state is challenging due to a substantial background contribution coming from W boson production in association with jets. The measurement is therefore performed in a fiducial phase space that enhances the signal-to-background ratio and provides an adequate separation between the shape templates of the backgrounds including their systematics and of those expected by the WW/WZ signal. The signal contribution is extracted from the data within this fiducial phase space by fitting the electron and muon channel contributions simultaneously using a maximum-likelihood fit to the invariant mass distributions of the two jets that form the hadronically decaying W or Z candidate.

The dataset used corresponds to an integrated luminosity of 4.7 ± 0.2 fb^{-1}. The total WW+WZ cross section is measured to be 68 ± 7 (statistical) ± 18 (systematic) pb with a Gaussian significance of 3.5 standard deviations, consistent with the Standard Model prediction of 61.1 ± 2.5 pb. In addition, limits are set on anomalous contributions to triple gauge couplings using the transverse momentum distribution of the dijet system from the hadronically decaying W or Z candidate.

To my parents,

thank you for everything.

Contents

List of Figures

List of Tables

List of Abbreviations

AFII - Atlfast-II
aTGC - Anomalous Triple Gauge Coupling
BCID - Bunch Crossing Identification
BCM - Beam Conditions Monitor
CERN - European Organization for Nuclear Research
CI - Confidence Interval
CL - Confidence Level
CR - Control Region
CS - Central Solenoid
CSC - Cathode Strip Chambers
CTP - Central Trigger Processor
EF - Event Filter
EFT - Effective Field Theory
EWK - Electroweak
FCAL - LAr Forward Calorimeter
FEs - Front-End Chips
FS - Full Simulation
FSR - Final State Radiation
GRL - Good Runs List
HEC - Hadronic Endcap Calorimeter
HF - Heavy Flavor
ID - Inner Detector
ISR - Initial State Radiation
JER - Jet Energy Resolution
JES - Jet Energy Scale
JVF - Jet Vertex Fraction
LAr - Liquid Argon
LBs - Luminosity Blocks
LCW - Local Cluster Weighting
LHC - Large Hadron Collider
LO - Leading Order
MC - Monte Carlo
MCP - Muon Combined Performance
MDT - Monitored Drift Tubes
ME - Matrix Element

MET - Missing Transverse Momentum
MJ - Multi-jet
MS - Muon Spectrometer
NLO - Next-to-Leading Order
NNLL - Next-to-Next-to-Leading Logarithmic
NNLO - Next-to-Next-to-Leading Order
OQ - Object Quality
p.d.fs - Probability Density Functions
PDFs - Parton Distribution Functions
pQCD - Perturbative Quantum Chromodynamics
PS - Parton Shower
QCD - Quantum Chromodynamics
QED - Quantum Electrodynamics
qfac - Renormalization/Factorization Multiplicative Scale for ALPGEN
r.m.s - Root Mean Square
ROBs - Readout Buffers
RODs - Readout Drivers
RoI - Region-of-Interest
RPC - Resistive-Plate Chambers
SCT - Semi-Conductor Tracker
SF - Scale Factor
SM - Standard Model
TGC - Thin-Gap Chambers
TRT - Transition Radiation Tracker
UE - Underlying Event

Acknowledgements

It is very difficult to express in words the amount of gratitude I have towards all the people that have helped me throughout my graduate school experience, but I will try to do my best. Thank you to my advisor Dmitri Tsybychev for mentoring me and fueling my professional drive to do more and do it better. I am extremely grateful for the constant pressure you put on me, it has always helped me to stay on task and focus. The analysis group: Chiara Roda, Brian Lindquist, Viviana Cavaliere, Federico Bertolucci, and Sasha Solodkov have all played key roles in this research and more importantly in helping me develop the tools and knowledge I needed to become a better particle physicists. Thank you to my fellow ATLAS graduate students and friends, namely Karen Chen, Aungshuman Zaman, Regina Caputo, John Stupak, Burton DeWilde, and Rafael Lopes de Sa, it has been a wonderful experience to learn from each other.

Thank you to the other professors, secretaries, and personnel in the Physics Department at Stony Brook University, since the very first day I visited, you have all made it a point to be very welcoming. Your accepting attitude, and calm outlook at life and physics made me want to come here right away, and now makes me sad that I am soon departing. Over the last six years, I have made countless friends here at Stony Brook and at CERN. You have all been invaluable in keeping me happy and sane. A special thanks goes to Ciprian Gal and Betul Pamuk, two of my closest friends who have always been there for me and I hope to continue to be there for them in the future wherever our paths may take us.

Thank you to my brother, your unwavering positive attitude has always been an anchor for me. I still don't know how you do it sometimes, but it's something that I have come to admire and am always pleasantly surprised by. Thanks to my mom and dad, you have given me so much love and comfort in my life that pursuing a PhD became possible. Even now when I am thousands of miles away, I always feel like I'm so close to home.

Chapter 1

Introduction

This thesis describes the measurement of the WW+WZ production cross section and limits on anomalous triple gauge couplings using data collected from the ATLAS detector during proton-proton collisions at a center-of-mass energy of 7 TeV. This chapter will provide the theoretical framework needed to understand the measurement and finish by providing an overview of the analysis. Chapter 2 describes the experimental apparatus used to perform the measurement, namely the Large Hadron Collider (LHC) particle accelerator and the ATLAS detector. Chapter 3 details how the data collected from ATLAS is reconstructed into particle-like objects that can be analyzed. The generation of Monte Carlo events used to model the data is described in Chapter 4. Chapter 5 explains the event selection used to extract the WW and WZ signal from the collected data, and Chapters 6 through 8 explain the procedure used to measure the cross section, including the evaluation of the systematic uncertainties. The final results are shown in Chapter 9.

Additionally, limits for beyond the Standard Model anomalous Triple Gauge Couplings (aTGCs) are calculated and that study is described in chapter 10 with accompanying results.

1.1 Introduction to the Standard Model

The Standard Model (SM) of particle physics is the theoretical foundation for the current understanding of all sub-atomic particles and their interactions. It describes the dynamics of particles through their interactions with the strong force described by Quantum Chromodynamics (QCD) and with the Electroweak (EWK) force, a unification of the electromagnetic and weak forces. The SM theory has proven to be a powerful predictive tool in particle physics, notably predicting the existence of the W and Z bosons as well as several other particles. Experiments in particle physics use predictions calculated from the SM as a benchmark, testing all experimental results against it, whether it be a precision measurement of a known parameter or a search for new physics that would show deviations from the SM. The following theoretical background on the SM will only give an overview of the concepts as they relate to the measurements done in this dissertation. For a more indepth explanation of the Standard Model please consider the following references [31, 32].

The SM is a gauge quantum field theory described by the combination of the symmetry groups SU(2)×U(1), which describes electroweak interactions, and SU(3) which describes the

strong interactions. The fundamental[1] particles of the theory are spin 1/2 particles known as fermions, spin 1 force carriers known as gauge bosons, and the recently discovered spin-0[2] Higgs boson [33]. The $W^{\pm}$, Z, and γ bosons mediate the electroweak interactions, while the strong force is mediated by gluons g. Gravity is excluded from the formulation of the Standard Model.

Fermions

The fermions are separated into three generations, each consisting of two leptons and two quarks. The biggest difference between the generations is that the masses of the particles within them increases with each generation, though their quantum numbers (charge, spin, etc) remain constant. Table 1.1 gives a summary of the generations and the quantum properties of the fermions. Each fermion has an associated anti-particle (e.g. electron→positron or up-quark→anti-up-quark), not listed on the table, with the same mass but opposite values for their quantum numbers. Additionally, due to how the weak force interacts with only left-handed particles, each generation of lepton and quark can be found in either a left-handed doublet state and/or a right-handed singlet state; more about this will be discussed in section 1.2.

		First Generation		Second Generation		Third Generation	
	Charge [e]		Mass [MeV]		Mass [MeV]		Mass [GeV]
Quarks	+2/3	u	1.5 to 3.3	c	1270^{+70}_{-90}	t	$172.0 \pm 0.6 \pm 1.3$
	-1/3	d	4.1 to 5.8	s	101^{+29}_{-21}	b	$4.19^{+0.18}_{-0.05}$
Leptons	-1	e	$0.510998910 \pm 0.000000013$	μ	105.658367 ± 0.000004	τ	1776.84 ± 0.17
	0	ν_e	< 2 eV	ν_μ	< 0.19	ν_τ	< 18.2 MeV

Table 1.1: Table depicting the three generations of leptons and quarks along with their associated masses and charge. The anti-particles of each fermion are not shown. The neutrino masses listed are the experimental upper bounds [24].

The leptons in each generation can be further divided into charged and neutral charged particles. For each charged lepton (electron (e), muon (μ), tau (τ)) there is an associated neutrino with zero charge and approximately zero mass[3] denoted as ν_e, ν_μ, and ν_τ. Each charged and neutral lepton pair is assigned a lepton number that is conserved in the SM. For example, the electron and electron neutrino each have an electron lepton number $L_e = 1$ and $L_\mu = L_\tau = 0$. This results in the SM only allowing the creation or destruction of lepton and anti-lepton pairs from the same generation.

The quarks each have an electric charge equal to $+2/3$ (up (u), charm (c), top (t)) or $-1/3$ (down (d), strange (s), bottom (b)) in units of the electron charge e. Unlike leptons, free quarks have never been observed in nature due to the properties of the strong force (discussed in section 1.3). Instead quarks are found in bound states restricted by the conservation of baryon number and color charge. The quark bound states, denoted as hadrons, consist of

[1]Fundamental in this instance means these particles are not made up of any additional constituents.

[2]The spin of the discovered particle has not been experimentally measured yet.

[3]In the SM theory, neutrinos have zero mass but experimentally [34] it has been seen that neutrinos oscillate between generations and therefore can not be massless.

quark–anti-quark pairs called mesons and three quark (either three quarks or three anti-quarks) bound states called baryons. Each (anti)quark has a baryon quantum number equal to (-1/3)1/3, resulting in mesons having a total baryon number equal to 0 and baryons having a baryon number equal to 1 or -1. The color charge described through QCD is unique to quarks and gluons. It is analogous to the electric charge in electromagnetism, representing the quantum property that is exchanged in the strong interactions. There are three types of color charge, denoted here as blue (b), green (g), and red (r). These colors like the other quantum numbers have their complementary anti-colors (anti-blue, anti-green, and anti-red) that are associated to the anti-quarks. Hadrons in nature are required to be color-neutral, therefore all mesons are formed from a quark with one color and an anti-quark with the same corresponding anti-color. Likewise, all baryons are formed with all three different colors or anti-colors, which is analogous to white light (colorless).

Force Carriers

Unlike the fermions, all bosons have an integer spin and mediate the interactions between the fermions themselves. The photon γ couples to particles that have an electric charge and is responsible for all electromagnetic interactions (e.g. the attraction and repulsion between electrically charged particles). The $W^{\pm}$ and Z bosons responsible for weak interactions couple to all fermions, other weak bosons, and photons through the weak isospin quantum number and are responsible for radioactive decays. The weak force is different from the EM and strong forces, due to its force carriers being massive particles compared to the massless photon or gluon. Additionally, it is the only force that is capable of changing the flavor of quarks and leptons through interactions and has been observed to violate parity and charge-parity symmetry.

The strong force is responsible for the binding of nuclei and thus the stability of all matter. The gluon boson is responsible for mediating strong interactions and couples to particles with color charge. Since a gluon can mediate the strong interaction between two differently colored particles it means that each gluon must carry at least two different types of color charge. Due to the SU(3) symmetry, the gluons are separated into a color octet which is a superposition of color states shown below [35]:

$$\begin{aligned} |1\rangle &= (r\bar{b} + b\bar{r})/\sqrt{2} & |5\rangle &= -i(r\bar{g} - g\bar{r})/\sqrt{2} \\ |2\rangle &= -i(r\bar{b} - b\bar{r})/\sqrt{2} & |6\rangle &= (b\bar{g} + g\bar{b})/\sqrt{2} \\ |3\rangle &= (r\bar{r} - b\bar{b})/\sqrt{2} & |7\rangle &= -i(b\bar{g} - g\bar{b})/\sqrt{2} \\ |4\rangle &= (r\bar{g} + g\bar{r})/\sqrt{2} & |8\rangle &= (r\bar{r} + b\bar{b} - 2g\bar{g})/\sqrt{6} \end{aligned} \tag{1.1}$$

and a color singlet

$$|9\rangle = (r\bar{r} + b\bar{b} + g\bar{g})/\sqrt{3} \tag{1.2}$$

The color singlet is experimentally ruled out, leaving a total of 8 different types of gluons.

Lastly, the Higgs boson in the SM is spin-0 boson with no electric or color charge. Interactions with its field allow massive particles in the SM to acquire their mass. More

discussion on the Higgs mechanism and how the Higg's breaks the EWK symmetry will be discussed in the next section.

Table 1.2 gives a summary of the bosons in the SM.

Boson	Mass [GeV]	Charge [e]	Force
Photon (γ)	0	0	Electromagnetic
$W^{\pm}$	80.398 ± 0.025	± 1	Weak
Z	91.1876 ± 0.0021	0	Weak
Gluon g	0	0	Strong
Higgs	$125.36 \pm 0.37 \pm 0.18$ [36]	–	–

Table 1.2: The guage bosons of the SM with their associated charges, mass, and the forces that they each mediate [24].

1.2 Formalism of the Electroweak Theory

The SM is built on the principles of local gauge invariance, the concept that the dynamics of a system described by a Lagrangian should be invariant under transformations which vary between one space-time point to another. This concept can be simply introduced in the context of Quantum Electrodynamics (QED), starting with the *free* Dirac Lagrangian for a Spin-$\frac{1}{2}$ field (ψ):

$$\mathcal{L} = \bar{\psi}(i\gamma^{\mu}\partial_{\mu} - m)\psi. \tag{1.3}$$

It is simple to see that this Lagrangian is invariant under a global gauge (or phase) transformation of the form

$$\psi \rightarrow e^{i\theta}\psi \tag{1.4}$$

where θ is any real number. Instead, under a local gauge transformation of the form

$$\psi \rightarrow e^{i\theta(x)}\psi, \tag{1.5}$$

where the phase, θ, is now a function dependent on space-time points x, the Lagrangian of equation 1.3 is no longer invariant. It picks up an extra term such that

$$\mathcal{L} \rightarrow \mathcal{L} + (\partial_{\mu}\theta)\bar{\psi}\gamma^{\mu}\psi \tag{1.6}$$

Demanding that the Lagrangian remain invariant under local gauge transformations requires the addition of a gauge field, A_{μ} that couples with ψ such that

$$\mathcal{L} = \bar{\psi}(i\gamma^{\mu}\partial_{\mu} - m)\psi + e\bar{\psi}\gamma^{\mu}A_{\mu}\psi \tag{1.7}$$

where A_{μ} transforms according to

$$A_{\mu} \rightarrow A_{\mu} + \partial_{\mu}\theta \tag{1.8}$$

Though equation 1.7 is now invariant under local gauge transformations, the Lagrangian is incomplete. The gauge field A_{μ} should also have a *free* term associated with it by its Lagrangian

$$\mathcal{L} = -\frac{1}{4}F_{\mu\nu}F^{\mu\nu} + \frac{1}{2}m_A A_{\mu}A^{\mu} \tag{1.9}$$

where $F^{\mu\nu} = \partial^\mu A^\nu - \partial^\nu A^\mu$ and m_A is the mass term associated with the vector field A_μ. Testing the complete Lagrangian described by the addition of equations 1.7 and 1.9 for local gauge invariance, results in the condition that the A_μ field must be massless ($m_A = 0$). This Lagrangian

$$\mathcal{L} = -\frac{1}{4}F_{\mu\nu}F^{\mu\nu} + \bar{\psi}(i\gamma^\mu\partial_\mu - m)\psi + e\bar{\psi}\gamma^\mu A_\mu\psi \tag{1.10}$$

represents the Lagrangian for QED[4], describing a fermion with mass m, charge e, and spin 1/2, that interacts with a massless vector field, also called a photon. The phase transformation of $e^{i\theta}$ used in this example is equivalent to the unitary 1×1 matrix group $U(1)$, therefore QED is said to be $U(1)$ gauge invariant. Just for completeness, equation 1.10 is usually written in terms of its covariant derivative $\mathcal{D}_\mu$, where $\mathcal{D}_\mu = \partial_\mu - ieA_\mu$ and the Lagrangian becomes

$$\mathcal{L} = -\frac{1}{4}F_{\mu\nu}F^{\mu\nu} + \bar{\psi}(i\gamma^\mu\mathcal{D}_\mu - m)\psi \tag{1.11}$$

Yang-Mills theory expands on the principles described above to apply in the same fashion, but with a little more subtlety (due to the non-Abelian nature of higher order matrices) to matrix groups of SU(N), where N is an integer. For example, starting from a Lagrangian consisting of the sum of two spin-$\frac{1}{2}$ fields (two free Dirac Lagrangians added together) it is possible to show that the SU(2) gauge invariance is achieved through the addition of three massless spin-0 fields. Likewise, Quantum Chromodynamics (QCD) shows a SU(3) gauge invariance and can be derived starting from the sum of three free Dirac Lagrangians (representing the three color flavors), resulting in the need for eight massless spin-0 fields(gluons).

The weak force Lagrangian is inherently more complicated due to the fact that it has been experimentally verified that the $W^\pm$ and Z bosons are massive and therefore the basic SU(2) gauge invariant model would be incorrect. In addition, the weak force has been experimentally shown to violate parity and as a result considers the *handedness*[5] (right or left) of each particle it interacts with. This is defined as the weak force only being allowed to couple to left-handed fermions or right-handed anti-fermions. The electroweak theory proposed by Glashow, Weinberg, and Salam unified the electromagnetic and weak interactions under $\mathrm{SU}(2)_L \times \mathrm{U}(1)$ gauge symmetry (where the L stands for left-handed), which through spontaneous symmetry breaking by the Higgs mechanism granted the weak bosons mass.

The EWK Lagrangian, $\mathcal{L}_{EWK}$ can be described by its four components

$$\mathcal{L}_{\text{EWK}} = \mathcal{L}_{\text{fermion}} + \mathcal{L}_{\text{gauge}} + \mathcal{L}_{\text{Higgs}} + \mathcal{L}_{\text{Yukawa}} \tag{1.12}$$

Concentrating on the first two components, the fermionic term is given by

$$\mathcal{L}_{\text{fermion}} = \bar{\psi_L} i\gamma^\mu(\partial_\mu)\psi_L + \bar{\psi_R} i\gamma^\mu(\partial_\mu)\psi_R \tag{1.13}$$

where, ψ_L now denotes a left-handed isospin doublet of a lepton-neutrino pair $\binom{\nu_L}{\ell_L}$ and ψ_R is a right-handed isospin singlet of the lepton ℓ_R. The neutrinos are massless in the SM and

[4]The QED Lagrangian shown only looks at one spin 1/2 particle. For the full QED Lagrangian, additional free and photon coupling terms for all SM fermions would have to be added to the equation.

[5]Right-handed particles have their spin aligned with their momentum and left-handed particles have their spin and momentum anti-aligned.

are shown to interact with the weak force, so are strictly only allowed to be left-handed. Following a similar method as in the QED derivation and requiring the *free* fermion term to be invariant under local gauge transformations results in the need to add four spin-0 massless gauge fields. The three fields from SU(2) are denoted as $W_\mu = W^a_\mu \sigma_a$, where σ_a are the Pauli matrices. The one field from U(1), is denoted as B_μ. The Lagrangian for the fermion and gauge components is given by

$$\mathcal{L}_{\text{fermion}} + \mathcal{L}_{\text{gauge}} = (\bar{\psi_L} i\gamma^\mu(\mathcal{D}_\mu)\psi_L + \bar{\psi_R} i\gamma^\mu(\mathcal{D}_{\mu,R})\psi_R) - \left(\frac{1}{4}B_{\mu\nu}B^{\mu\nu} - \sum_{i=1}^{3}\frac{1}{4}W^i_{\mu\nu}W^{i\mu\nu}\right) \quad (1.14)$$

where $\mathcal{D}_\mu$ and $\mathcal{D}_{\mu,R}$ are the covariant derivatives of the left and right-handed states denoted by

$$\mathcal{D}_\mu = \partial_\mu + i\frac{g}{2}\tau W_\mu + i\frac{g'}{2}Y_L B_\mu, \quad (1.15)$$

$$\mathcal{D}_{\mu,R} = \partial_\mu + i\frac{g'}{2}Y_e B_\mu. \quad (1.16)$$

Y is the U(1) hypercharge, τ is the SU(2) weak isospin related to the Pauli matrices, and g and g' are the coupling strengths. The gauge field tensors are given by

$$W^i_{\mu\nu} = \partial_\mu W^i_\nu - \partial_\nu W^i_\mu + g\epsilon^{ijk}W^j_\mu W^k_\nu, \quad (1.17)$$

$$B_{\mu\nu} = \partial_\mu B_\nu - \partial_\nu B_\mu \quad (1.18)$$

where ϵ^{ijk} is the structure constant of SU(2). At this point it is trivial to add the remaining lepton and quark[6] fermion contributions to the Lagrangian as a sum over the first term of equation 1.14 for each fermion generation and type (lepton/quark). The current Lagrangian describes the electroweak interactions between the weak bosons and fermions, but there is still no mass term associated with either set of particles.

Therefore, it is necessary to shift focus to the Higgs contribution of the EWK Lagrangian. A complex scalar SU(2) doublet, $\Phi = \binom{\Phi^+}{\Phi^0}$ can be introduced to couple to the gauge fields in the form

$$\mathcal{L}_{Higgs} = (\mathcal{D}^\mu\Phi)^\dagger(\mathcal{D}^\mu\Phi) - V(\Phi), \quad (1.19)$$

where $V(\Phi)$ denotes the scalar potential given by

$$V(\Phi) = -\mu^2\Phi^\dagger\Phi + \lambda(\Phi^\dagger\Phi)^2. \quad (1.20)$$

In the case where $\mu^2 < 0$, the resulting shape of the potential $V(\Phi)$ is that of a "Mexican Hat," where the minimum is not at V(0), but at a non-zero value

$$(\Phi^\dagger\Phi)_{min} = \frac{1}{\sqrt{2}}\begin{pmatrix}0\\ \nu\end{pmatrix}. \quad (1.21)$$

[6]The quark contribution to the Lagrangian for each generation will have an extra term compared to the lepton generations due to a second right-handed singlet state coming from the other massive quark.

where ν is the vacuum expectation value, or *vev*, and is equal to $\sqrt{\frac{\mu^2}{\lambda}}$. The electroweak local symmetry is now said to be broken due to shift of the ground state to an asymmetrical local minimum (the *vev*). As a result of the Higgs field acquiring a *vev*, the gauge bosons interacting with the Higgs field in equation 1.19 now acquire a mass. The physical gauge fields ($W^{\pm}$,Z,γ) can be rewritten into their mass eigen states as a linear combination of the W^i and B_μ fields

$$\begin{aligned} W_\mu^{\pm} &= \frac{1}{\sqrt{2}}(W_\mu^1 \mp iW_\mu^2) \\ Z^\mu &= \frac{-g'B_\mu + gW_\mu^3}{\sqrt{g^2+g'^2}} \\ A^\mu &= \frac{gB_\mu + g'W_\mu^3}{\sqrt{g^2+g'^2}} \end{aligned} \tag{1.22}$$

with masses given by

$$\begin{aligned} M_W^2 &= \frac{1}{4}g^2\nu^2 \\ M_Z^2 &= \frac{1}{4}(g^2+g'^2)\nu^2 \\ M_\gamma &= 0. \end{aligned} \tag{1.23}$$

The last term in the Lagrangian from equation 1.12 is the Yukawa term, which explains how the leptons and quarks also obtain their masses through coupling with the Higgs field. This derivation is beyond the scope of this thesis, but a nice derivation can be found in references [31, 32].

The important thing to take away from this formalism, other than the Higgs mechanism, is that the EWK bosons have self-interaction vertices. Looking at equation 1.17, the square of the field tensor denotes self-interaction vertices or gauge coupling between three (triple gauge couplings) and four (quadratic gauge couplings) EWK gauge bosons. The interactions are shown as Feynman vertices in figure 1.1. The coupling strengths of the triple gauge couplings are investigated in this analysis for anomalous contributions from beyond the SM processes, described in section 1.5.

In summary, the electroweak theory of the SM has therefore successfully described many aspects of the EWK force that have been observed in nature. Specifically, it shows how four gauge bosons couple and interact with the fermionic terms of the SM, it gives these bosons/fermions their mass through spontaneous symmetry breaking using the Higgs mechanism, and lastly explains self-interactions between the different gauge bosons.

1.3 QCD and Proton-Proton Collisions

The theory of Quantum Chromodynamics (QCD) is the theory of the strong force and therefore describes the dynamics of quarks and gluons through color interactions mediated by the gluons themselves. QCD is a non-Abelian gauge theory, similar to the EWK theory,

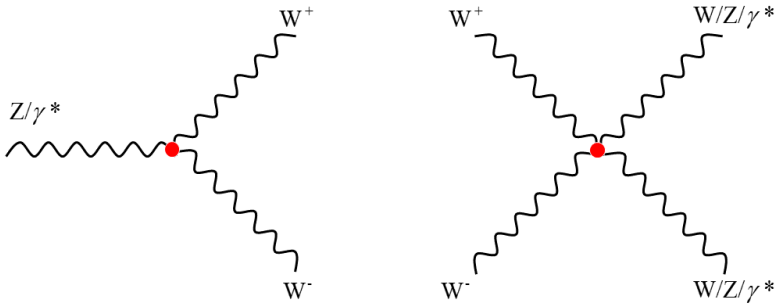

Figure 1.1: The self-interaction EWK vertices, triple gauge couplings (left) and quadratic gauge coupling (right).

based on the gauge symmetry group SU(3) [24], a component of the SU(3)×SU(2)×U(1) SM theory. It is important to point out that gluons also contain self-interaction vertices in the form of triple gauge couplings and quadratic gauge couplings, like that of the EWK bosons.

QCD has two important concepts, color confinement and asymptotic freedom. Color confinement is the reason why color charged particles can not be observed in isolated free states and instead must form into color-neutral bound states (hadrons), mesons or baryons. Unlike the electromagnetic force which decreases as $1/r^2$, where r is the distance between two charged objects, the strong force between two colored particles does not decrease with distance. Instead the coupling strength increases with distance up to a point where it becomes more energetically favorable to produce a quark and anti-quark pair that neutralizes the color charge.

This behavior can best be described through the equation[7] of the running QCD coupling strength

$$\alpha_s(\mu_R) \cong \frac{12\pi}{(33 - 2n_f)\ln(\mu_R/\Lambda)} \tag{1.24}$$

where $n_f = 6$ is the number of quark flavors, μ_R is the renormalization scale, and Λ is the QCD scale. The renormalization scale, usually taken to be equal to the momentum transfer of the interaction Q, corrects for ultraviolent divergences seen in perturbative quantum field theory. The QCD scale[8] $\Lambda \cong 217MeV$ is defined as the point where the perturbtively-defined coupling would diverge and therefore below this scale only non-perturbative QCD calculations can be done. The behavior of $\alpha_s(Q)$ shows that for high energies $Q^2 \gg \Lambda^2$ (or short distance scales) that $\alpha_s(Q) \to 0$ and therefore the colored particles act as if they are effectively free. This behavior of the strong coupling, depicted in figure 1.2, is called

[7]Using the modified minimal subtraction,$\overline{MS}$, scheme [31], higher order terms are ignored.

[8]Based on the $\overline{MS}$ scheme.

asymptotic freedom and it allows perturbative QCD (pQCD) to be calculable for small values of α_s since the quarks themselves are no longer bounded by the hadronic system. The opposite is also true, that for very low energies or large distances the QCD coupling strength grows and this leads to color confinement between colored particles.

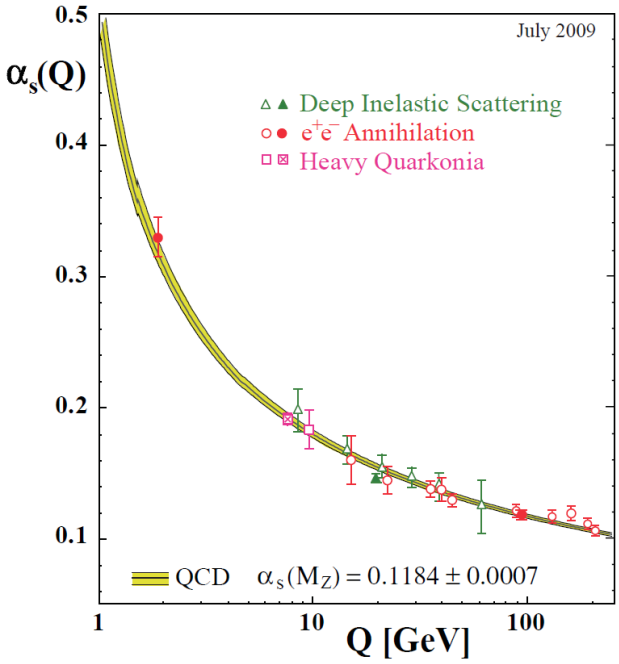

Figure 1.2: Summary of the measurements of α_s as a function of the respective energy scale Q. Figure from [1].

Proton-Proton Collisions

For the proton-proton collisions seen at hadron colliders, the principles of asymptotic freedom and color confinement play a key role in the characteristics of any high energy collision. Protons are a bound state of two up quarks and a down quark usually referred to as "valence" quarks. In addition, within the protons are gluons which communicate with the valence quarks and produce quark-anti-quark pairs, these quarks are referred to as "sea" quarks. The valence quarks, gluons, and sea quarks that compose the proton and other hadrons are referred to as "partons." As protons interact in a high energy collision the interactions are done at an energy scale much greater than that of the QCD scale Λ. Effectively due to asymptotic freedom these interactions between protons can be characterized as interactions between individual partons that reside in each proton. The parton-parton interaction is denoted as the hard scattering process.

The hard scattering process between two partons inside the proton is calculable with perturbative QCD allowing for the calculations of scattering amplitudes and cross sections. The difficulty comes when trying to combine the hard scattering process with the additional "soft" QCD interactions that continue to occur within the proton that are non-perturbative.

In effect, it becomes unmanageable to calculate the total cross section for a proton-proton process since it is a combination of the high energy (short distance) hard scattering and the low energy (long distance) soft interaction behavior.

The factorization theorem [37] solves this problem by separating the hard process from the hadronic structure of the proton using an arbitrary factorization scale μ_F[9]. The factorization scale denotes the cutoff between the hard processes ($> \mu_F$) and the soft processes ($< \mu_F$). The proton structure containing the soft processes can then be characterized by Parton Distribution Functions (PDFs) which are a function of the momentum fraction[10] x of each parton in the proton and μ_F. A PDF shows the probability of finding a parton with a momentum fraction x at a scale of μ_F and is therefore independent of the hard process. The fact that the PDF is independent of the hard process means that PDFs themselves can be considered universal, regardless of what cross section is being measured.

The inclusive cross section [3] for a hadron-hadron scattering with a 4-momentum P_1 and P_2 can then be written as

$$\sigma(P_1, P_2) = \sum_{i,j} \int dx_1 \int dx_2 f_1(x_i, \mu_F^2) f_2(x_j, \mu_F^2) \sigma_{ij}(p_1, p_2, \alpha_s(\mu_R), Q^2/\mu_F^2, Q^2/\mu_R^2). \quad (1.25)$$

In equation 1.25 the hard interaction between partons i, j is calculated from the cross section σ_{ij} using pQCD and the PDFs for partons i, j are represented by $f(x, \mu_F^2)$. The sum i, j is over all partons in each respective hadron. The PDFs are determined independently from previous experiments, particularly deep inelastic scattering experiments in which a lepton is scattered off a hadron. Since the total inclusive cross section is a convolution of the PDF and the parton-parton cross section, both must be determined to the same order (Leading Order (LO), Next-to-Leading Order (NLO), etc.) in perturbation theory. An example of a NLO PDF is shown in figure 1.3.

The hard scattering process itself can contain and/or produce additional quarks and gluons in the interaction. These isolated colored particles can not be observed in nature and therefore must hadronize to become color-neutral. The process of emitting gluons, and pulling gluons and quark-anti-quark pairs from the vacuum is called fragmentation. The fragmentation of these hard partons happens in small angles along the same direction of the initial parton resulting in a approximate collinear shower of quarks and gluons. In experimental particle physics, the resulting hadronized product of this shower is called a "jet" and represents the physical observable measured by the detector.

Additionally, gluon emissions coming from the partons involved in the hard scattering process that are above the factorization scale must be taken into account within the parton-parton cross section. Gluon emissions that later hadronize and produce final state hadrons coming from the initial partons prior to the scattering are referred to as Initial State Radiation (ISR) and emissions from the final state partons are referred to as Final State Radiation (FSR). An illustration depicting a hadron-hadron interaction with the elements discussed in this secton is shown in figure 1.4.

[9]The factorization scale and renormalization scale are usually taken to both equal the momentum transfer Q, but this is not required.

[10]The momentum fraction of parton i is $x_i = p_i/P$ where P is the total momentum of the hadron and p_i is the momentum of parton i.

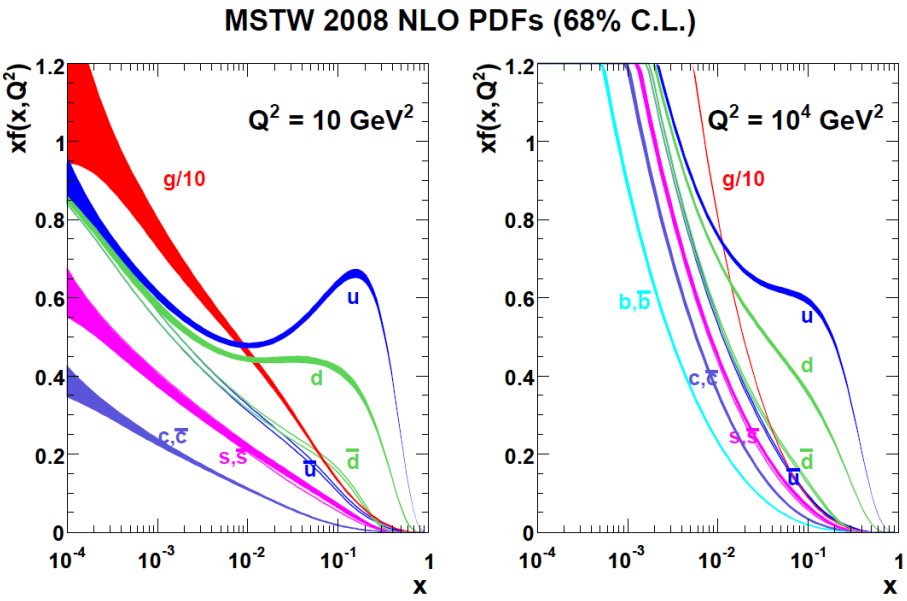

Figure 1.3: An example of a parton distribution function calculated at Next-to-Leading Order (NLO) by the MSTW group [2].

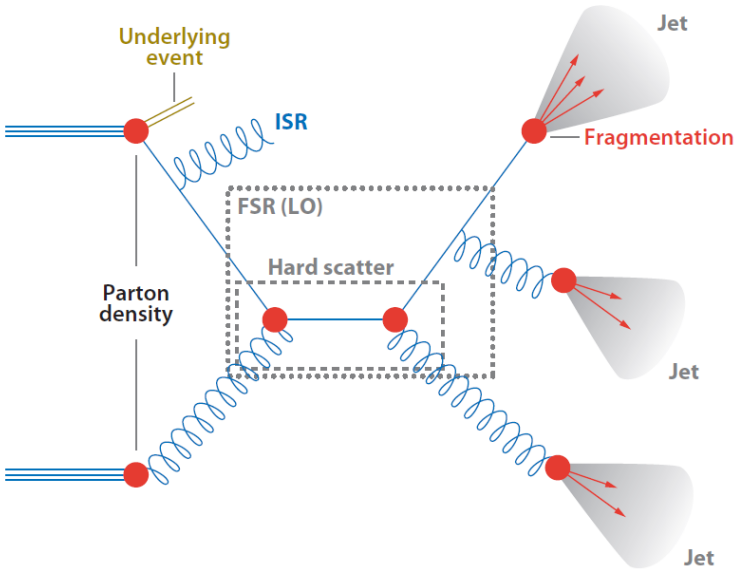

Figure 1.4: Illustration depicting a hadron-hadron interaction with many of the elements necessary in modeling a particle interaction identified. ISR(FSR) stands for Initial(Final) state radiation and LO stands for Leading Order. Figure from [3].

1.4 WW and WZ Production

The goal of this analysis is to measure the total cross section in which the hard scattering process results in a WW or WZ diboson pair being produced and decaying semi-leptonically. The Leading-Order (LO) Feynman diagrams for WW and WZ production are illustrated in figure 1.5. The t channel shows the exchange of an intermediate quark to produce the diboson system, while the s-channel shows quark-anti-quark annihilation to a W, Z, or virtual photon. The s-channel is the only LO diagram containing the triple gauge coupling vertex. The predicted SM cross section for WW and WZ calculated using MCNLO [38] with the CT10 [39] NLO PDF are calculated to be 43.7 ± 2.1 pb and 17.4 ± 1.2, respectively.

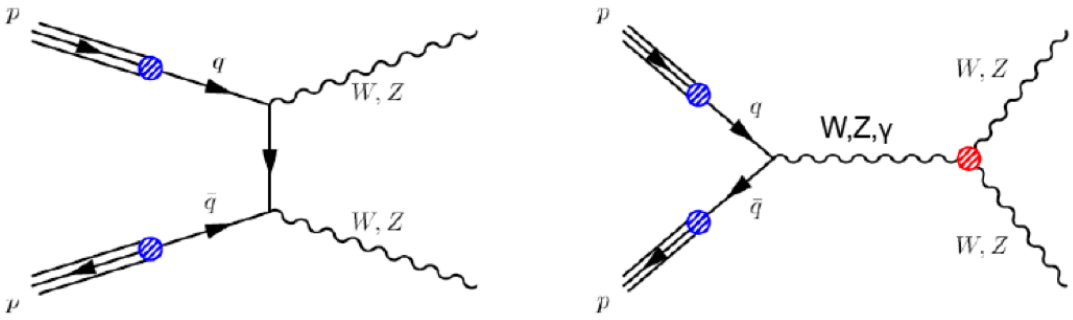

Figure 1.5: Leading order Feynman diagrams for diboson WW/WZ production at the LHC. The red dot indicates the TGC vertex for the s-channel.

The branching ratios for each W and Z decay mode are shown in table 1.3. An easy calculation of the branching ratios shows that the $WW \to \ell\nu qq$ decay will occur approximately 14.5% (per lepton flavor) of the time and a $WZ \to \ell\nu q\bar{q}$ decay will occur approximately 7.5% (per lepton flavor) of the time [24]. This can be compared to the fully leptonic decay modes, where $WW \to \ell\nu\ell\nu$ decays are 10.5% (per all lepton flavors) and $WZ \to \ell\nu\ell\ell$ are 3.3% (per all lepton flavors). Therefore, an advantage to the semi-leptonic final state is that it will have significantly more data events due to the branching ratios of the diboson pair.

$W^{\pm}$ Boson	
Decay Modes	Branching Ratio (%)
$\ell^{\pm}\nu$ (per flavor)	10.80 ± 0.09
Hadrons	67.60 ± 0.27
Z Boson	
Decay Modes	Branching Ratio (%)
$\ell^{+}\ell^{-}$ (per flavor)	3.3658 ± 0.0023
$\nu\nu$ (all flavors)	20.00 ± 0.06
Hadrons	69.91 ± 0.06

Table 1.3: The W and Z boson branching ratios [24].

1.5 Anomalous Triple Gauge Couplings

The SM has been successful in many aspects of particle physics. Even so, there are still problems or gaps in the theory that have not been explained. These include known issues like gravity, neutrino oscillations, or dark matter/energy. In addition, the SM itself has not been completely validated experimentally, particularly in higher energy regimes above the 1 TeV scale. The SM may be just a low energy component of a much higher energy theory. One way to test for new physics at a higher energy scale is through studying triple gauge couplings between vector bosons, WWZ and $WW\gamma$, which may be modified due to the addition of new physics beyond the Standard Model.

In the case of new physics being present at an energy scale well beyond what is being experimentally probed, the addition of this new physics can be integrated out and expressed as anomalous interaction vertices or anomalous Triple Gauge Couplings (aTGCs) [40]. Experimentally, the addition of non-SM physics in the form of aTGCs results in enhancements for observable variables dependent on the invariant mass of the diboson system. These variables include the total cross section, the mass of the WW or WZ system, and the kinematic distributions related to the diboson system (lepton transverse momentum or the momentum of the gauge boson itself).

The Lagrangian for triple gauge boson self-interaction can be generalized into the form [41]:

$$\begin{aligned}\mathcal{L} = i\ g_{WWV}\Big[&g_1^V(W^\dagger_{\mu\nu}W^\mu V^\nu - W^\dagger_\mu V_\nu W^{\mu\nu}) + \kappa_V W^\dagger_\mu W_\nu V^{\mu\nu} + \frac{\lambda_V}{m_W^2}W^\dagger_{\rho\mu}W^\mu_\nu V^{\nu\rho} \\ &+ ig_4^V W^\dagger_\mu W_\nu(\partial^\mu V^\nu + \partial^\nu V^\mu) - ig_5^V\epsilon^{\mu\nu\rho\sigma}(W^\dagger_\mu\partial_\rho W_\nu - \partial_\rho W^\dagger_\mu W_\nu)V_\sigma \\ &+ \tilde{\kappa}_V W^\dagger_\mu W_\nu \tilde{V}^{\mu\nu} + \frac{\tilde{\lambda}_V}{m_W^2}W^\dagger_{\lambda\mu}W^\mu_\nu\tilde{V}^{\nu\lambda}\Big].\end{aligned} \tag{1.26}$$

Neglecting all terms that are charge or parity violating results in a effective Lagrangian of

$$\mathcal{L} = i\ g_{WWV}\Big[g_1^V(W^\dagger_{\mu\nu}W^\mu V^\nu - W^\dagger_\mu V_\nu W^{\mu\nu}) + \kappa_V W^\dagger_\mu W_\nu V^{\mu\nu} + \frac{\lambda_V}{m_W^2}W^\dagger_{\rho\mu}W^\mu_\nu V^{\nu\rho}\Big], \tag{1.27}$$

where $V \in\{Z,\gamma\}$; $W_{\mu\nu} \equiv \partial_\mu W_\nu - \partial_\nu W_\mu$; $Z_{\mu\nu} \equiv \partial_\mu Z_\nu - \partial_\nu Z_\mu$, and the overall coupling constants are given by $g_{WW\gamma} = -e$ and $g_{WWZ} = -e\cot\theta_W$, where θ_W is the weak mixing angle. In the Standard Model, the remaining six coupling parameters in equation 1.27 have values of $g_1^V = 1$, $\kappa^V = 1$, and $\lambda_V = 0$. From the aTGC point of view, it is generally more convenient to express these coupling parameters as deviations from the SM:

$$\Delta g_1^V = g_1^V - 1; \qquad \Delta\kappa^V = \kappa^V - 1; \qquad \lambda_V. \tag{1.28}$$

In the case of Δg_1^γ, it is taken to be zero as a result of electromagnetic gauge invariance. Therefore, this aTGC approach results in five free parameters: Δg_1^Z, $\Delta\kappa^Z$, $\Delta\kappa^\gamma$, λ_Z, and λ_γ.

The effective Lagrangian shown above will eventually violate[11] unitarity[12] at high enough energies above the energy scale used to define the new physics. In order to conserve unitarity

[11] Unitarity is only violated due to the Lagrangian not taking into account higher order terms, which add large correction factors.

[12] The condition that the total scattering would not occur with a probability greater than unity.

a dipole form factor can be introduced to the aTGC parameters as

$$\alpha \rightarrow \frac{\alpha}{(1+\frac{\hat{s}}{\Lambda^2})}, \tag{1.29}$$

where $\alpha \in \{\Delta g_1^Z, \Delta\kappa^V, \lambda_V\}$, $\hat{s}$ is the invariant mass of the diboson pair, and Λ is the scale in which new physics appears. The addition of this form factor restores unitarity but the somewhat ambiguous choice of the Λ scale results in the potential for new physics to be missed. The dampening effect of Λ, on the aTGCs, results in less sensitivity to potential new physics around and above the scale choice (usually taken to be in the TeV range). For this analysis, the convention of not applying any form factors is used, resulting in better expected limits for the aTGC parameters, but allows unitarity to be violated.

LEP Constraint

Additional constraints can be placed on the aTGC parameters to reduce the amount of free parameters. One of these constraints is the LEP constraint [40], which requires $SU(2) \times U(1)$ invariance in the effective Lagrangian and disregards all operators with dimensions eight or higher. The LEP constraint is given by:

$$\Delta\kappa^Z = \Delta g_1^Z - \Delta\kappa^\gamma \tan^2\theta_W; \qquad \lambda^Z = \lambda^\gamma. \tag{1.30}$$

It reduces the number of free parameters from five to three: $\lambda(=\lambda^Z=\lambda^\gamma)$, $\Delta\kappa^\gamma$, and Δg_1^Z.

1.5.1 Effective Field Theory Approach

A different approach to calculate the effect of anomalous couplings that has been advocated by theorists is the Effective Field Theory (EFT) approach [42]. The advantages of the EFT approach are that it never violates unitarity and is constructed with $SU(2) \times U(1)$ gauge invariance. EFT expands the Standard Model Lagrangian by denoting the SM to be a low-energy EFT that is part of a higher energy theory with an energy scale for new physics denoted as Λ. The new Lagrangian can be written as

$$\mathcal{L} = \mathcal{L}_{SM} + \sum_i \frac{c_i}{\Lambda^2}\mathcal{O}_i + ...^{13} \tag{1.31}$$

where $\mathcal{O}_i$ denotes dimension six operators and c_i are dimensonless coefficients that parametrize the strength in which the SM couples to new physics. In this Lagrangian, there are only three independent dimension six operators which affect the electroweak gauge boson self-interaction. The choice of which operators are independent is flexible. This analysis follows the procedure outlined in reference [42] and denotes the three operators as

$$\begin{aligned} \mathcal{O}_{WWW} &= Tr[W_{\mu\nu}W^{\nu\rho}W_\rho^\mu] \\ \mathcal{O}_W &= (D_\mu\Phi)^\dagger W^{\mu\nu}(D\nu\Phi) \\ \mathcal{O}_B &= (D_\mu\Phi)^\dagger B^{\mu\nu}(D\nu\Phi) \end{aligned} \tag{1.32}$$

[13] Higher Order terms are not shown.

where Φ is the Higgs doublet field and $W_{\mu\nu}$ and $B_{\mu\nu}$ are a combination of derivatives of the gauge boson fields. The coefficients related to the three operators are c_{WWW}, c_W, and c_B. The EFT coefficients follow a linear relationship with the aTGC parameters when utilizing the LEP constraint and can be written as

$$\begin{aligned}\frac{c_W}{\Lambda^2} &= \frac{2}{m_Z^2}\Delta g_1^Z \\ \frac{c_B}{\Lambda^2} &= \frac{2}{m_W^2}\Delta\kappa^\gamma - \frac{2}{m_Z^2}\Delta g_1^Z \\ \frac{c_{WWW}}{\Lambda^2} &= \frac{2}{3g^2 m_W^2}\lambda\end{aligned} \tag{1.33}$$

where m_Z and m_W are the masses of the Z and W respectively, and g is the electroweak coupling constant. These relationships between the aTGC and EFT parameters only hold if there is no form factor used for the aTGC parameters, as is the case for this analysis. For this analysis, limits on anomalous couplings will be given for both the aTGC and EFT approach.

1.6 Previous Measurements

Previous cross section and aTGC measurements have been done on diboson WW and WZ production for both the fully leptonic channels, $WW \to \ell\nu\ell\nu$ and $WZ \to \ell\nu\ell\ell$, and semi-leptonic channels, $WW/WZ \to \ell\nu q\bar{q}$. This section gives a summary of these experimental results.

The first direct evidence of WW/WZ production was done by the DZero and CDF experiments using the Tevatron $p\bar{p}$ collider at a center-of-mass energy ($\sqrt{s}$) of 1.96 TeV. Measurements were performed in both the leptonic [43–46] and semi-leptonic [47, 48] channels and a summary of their latest results can be found in table 1.4.

Channel	Experiment	Result [pb]	$\mathcal{L}[fb^{-1}]$
WW+WZ$\to \ell\nu q\bar{q}$	DZero	$19.6^{+3.2}_{-3.0}$ [47]	4.3
	CDF	$18.1 \pm 3.3(\text{stat}) \pm 2.5(\text{syst})$ [48]	4.3
WW$\to \ell\nu\ell\nu$	DZero	$11.5 \pm 2.1(\text{stat+syst}) \pm 0.7(\text{lumi})$ [44]	1
	CDF	$14.0 \pm 0.6(\text{stat})^{+1.6}_{-1.3}(\text{syst}) \pm 0.8(\text{lumi})$ [43]	9.7
WZ$\to \ell\nu\ell\ell$	DZero	$4.50^{+0.63}_{-0.66}$ [45]	8.6
	CDF	$3.9^{+0.8}_{-0.7}$ [46]	7.1

Table 1.4: Summary of WV (V=W,Z) diboson cross section results measured by the DZero and CDF collaborations. The SM NLO predictions for WW and WZ at a $\sqrt{s} = 1.96$ TeV are $\sigma(WW) = 11.7 \pm 0.8$ pb [25] and $\sigma(WZ) = 3.5 \pm 0.3$ pb [25], respectively.

The ATLAS and CMS collaboration have also measured the cross section for WW/WZ decaying into the fully leptonic final state [49–52], and CMS has shown results for the semi-leptonic [53] final state, using the LHC pp collider at a center of mass energy of 7 TeV. Cross section measurements for the fully leptonic final state [27, 28, 52, 54] have also been done

at $\sqrt{s} = 8$ TeV by the LHC experiments. A summary of all these results can be found in table 1.5.

It is interesting to point out that the majority of the DZero and CDF cross section results measure a larger central value for the WW and WZ cross sections, but these results are within one standard deviation from the SM prediction. Likewise, the more sensitive fully leptonic final state measurements performed by ATLAS and CMS, all show an excess in the WW cross section results. In the case of the WW measurements, the deviations are as far as two standard deviations away from the SM prediction. More data is needed to see if this is just a statistical fluctuation or the first sign of new physics.

Channel	Experiment	Result [pb]	$\mathcal{L}[fb^{-1}]$
$\sqrt{s} = 7$ **TeV, 2011 Results**			
WW+WZ$\rightarrow \ell\nu q\bar{q}$	CMS	$68.9 \pm 8.7(\text{stat}) \pm 9.7(\text{syst}) \pm 1.5(\text{lumi})$ [53]	5
WW$\rightarrow \ell\nu\ell\nu$	ATLAS	$51.9 \pm 2.0(\text{stat}) \pm 3.9(\text{syst}) \pm 2.0(\text{lumi})$ [49]	4.6
	CMS	$52.4 \pm 2.0(\text{stat}) \pm 4.5(\text{syst}) \pm 1.2(\text{lumi})$ [50]	4.9
WZ$\rightarrow \ell\nu\ell\ell$	ATLAS	$19.0^{1.4}_{-1.3}(\text{stat}) \pm 0.9(\text{syst}) \pm 0.4(\text{lumi})$ [51]	4.6
	CMS	$20.76 \pm 1.32(\text{stat}) \pm 1.13(\text{syst}) \pm 0.46(\text{lumi})$ [52]	4.9
$\sqrt{s} = 8$ **TeV, 2012 Results**			
WW$\rightarrow \ell\nu\ell\nu$	ATLAS	$71.4 \pm 1.2(\text{stat})^{5.0}_{-4.4}(\text{syst})^{+2.2}_{-2.1}(\text{lumi})$ [27]	20.3
	CMS	$69.9 \pm 2.8(\text{stat}) \pm 5.6(\text{syst}) \pm 3.1(\text{lumi})$ [54]	5.3
WZ$\rightarrow \ell\nu\ell\ell$	ATLAS	$20.3^{+0.8}_{-0.7}(\text{stat})^{+1.2}_{-1.1}(\text{syst})^{+0.7}_{-0.6}(\text{lumi})$ [28]	13
	CMS	$24.61 \pm 0.76(\text{stat}) \pm 1.13(\text{syst}) \pm 1.08(\text{lumi})$ [52]	19.6

Table 1.5: Summary of WV (V=W,Z) diboson cross section results measured by the ATLAS and CMS collaborations at $\sqrt{s}$ =7 and 8 TeV. The SM NLO predictions for WW and WZ at a $\sqrt{s} = 7$ TeV are $\sigma(WW) = 44.9 \pm 2.2$ pb [26] and $\sigma(WZ) = 18.5 \pm 1.3$ pb [26], respectively. The SM NLO predictions for WW and WZ at a $\sqrt{s} = 8$ TeV are $\sigma(WW) = 58.7^{+3.0}_{-2.7}$ pb [27] and $\sigma(WZ) = 20.3 \pm 0.8$ pb [28], respectively.

In regards to limits on anomalous triple gauge couplings, several experiments including ATLAS [49, 51, 55], CMS [50, 53, 56], DZero [57], and a combined result [58] from the four LEP experiments have measured the 95% confidence level limits for aTGCs using the LEP constraint. Other than the DZero combination ($\Lambda = 2$ TeV), all results shown in figure 1.6 are measured using no form factor ($\Lambda = \infty$ in regards to equation 1.29) for the aTGC parameters.

1.7 Analysis Overview

The semi-leptonic decay mode offers an advantage over the leptonic counterpart (WW$\rightarrow$ $\ell\nu\ell\nu$ or WZ$\rightarrow$ $\ell\nu\ell\ell$) due to the higher branching ratios for the W and Z bosons to decay hadronically to quarks. Unfortunately, this decay mode also has two very significant challenges.

The first challenge for this analysis is that the semi-leptonic decay channel contains several background processes with high production cross sections that have the same final state or can potentially fake the same final state in the detector. These background processes

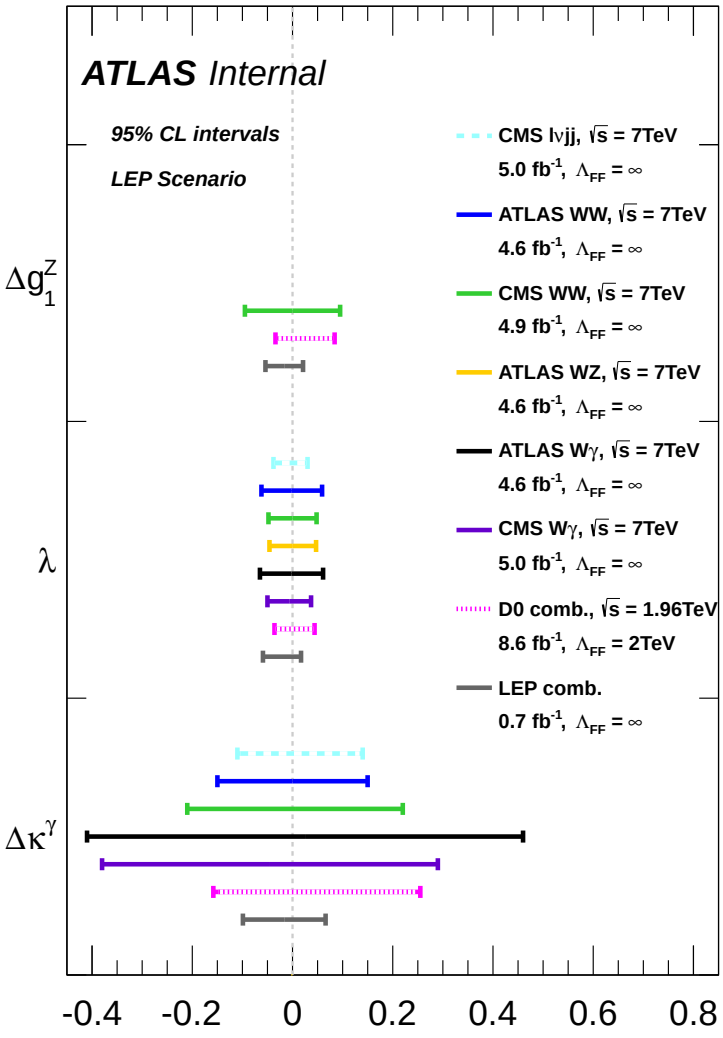

Figure 1.6: Comparison of aTGC limits between different experiments and/or in different channels. All limits are given at 95% CL, and calculated within the LEP scenario. The form factor Λ used in each analysis is listed; $\Lambda = \infty$ is equivalent to no form factor. The limits for each parameter are obtained by fixing the other two parameters to zero. In the CMS $\ell\nu jj$ analysis and the ATLAS and CMS $W\gamma$ analyses, no limits on Δg_1^Z were given. The ATLAS WW and WZ analyses gave limits on Δg_1^Z, but with $\Delta\kappa^Z = 0$ rather than $\Delta g_1^Z = 0$, so they are not comparable with the other results and are thus excluded. For the ATLAS WW result, the published limits on $\Delta\kappa^Z$ are converted to limits on $\Delta\kappa^\gamma$ using the formula $\Delta\kappa^Z = -\Delta\kappa^\gamma \tan^2\theta_w$. The ATLAS WZ analysis published $\Delta\kappa^Z$ limits which can also be converted to $\Delta\kappa^\gamma$, but the limits are much worse than the other limits in this figure, and so are not shown.

include single W+jets and Z+jets production, top ($t\bar{t}$ and single top) production, and QCD multijet production. The largest background contribution comes from single W production with associated jets (W+jets), in which the W decays leptonically and the jets come from

partons scattered or radiated in the interaction. The W+jets inclusive cross section is over a 150 times larger than the combined WW+WZ cross section.

The cross section measurement therefore requires optimization of the event selection and background modeling in order to extract the signal events over a significantly larger background contribution. Event selection criteria are chosen that enhance the signal to background ratio and improve the event modeling in respect to the data. Furthermore, the topology of the WW+WZ signal can be exploited because unlike the majority of the background processes the WW/WZ$\rightarrow \ell\nu jj$ process contains a hadronically decaying boson with a resonant mass that can be reconstructed from the resulting jets. The invariant mass M for two particles (1 and 2) with energy E, momentum $\vec{p}$, and mass m is defined as

$$M = \sqrt{m_1^2 + m_2^2 + 2(E_1 E_2 - \vec{p_1} \cdot \vec{p_2})} \tag{1.34}$$

The invariant mass of the resulting jets coming from the W/Z$\rightarrow q\bar{q}$ decay will have an approximate mass equal to the mass of the parent W or Z boson (80.3 GeV and 91.2 GeV, respectively). This will result in a Gaussian-like peak in the dijet invariant mass, m_{jj}, distribution for the WW+WZ process. On the other hand, backgrounds not containing a hadronically decaying W or Z boson like the W+jets background will show a falling distribution in m_{jj}. Utilizing the fact that the signal shape in the m_{jj} distribution is uniquely shaped compared to the other background processes, a likelihood fit is constructed to extract the small number of WW+WZ signal events from the total set of data that passes the event selection. The extracted number of signal events is then used to calculate the cross section corresponding to the fiducial phase space in which the measurement was performed. The total cross section can be extrapolated from the fiducial cross section and compared to the SM theoretical prediction.

The second major challenge of the semi-leptonic final state are the jets themselves. Jets are intrinsically harder to measure than electromagnetic elementary particles like electrons and muons due to the jets being a reconstructed object derived from a composition of many particles. From an experimental point of view, the resolution to measure a jet is significantly worse than that of a lepton. The jet energy resolution is smeared by roughly 8 to 20 percent depending on the transverse momentum of the jet [59], with the larger uncertainty attributed to jets with a lower transverse momentum (approximately 35 GeV)[14]. At low energies (<50 GeV), the uncertainty of the jet resolution and that of the jet energy scale results in systematic uncertainties that are significantly larger than those observed for leptons in the same energy range. Additionally, these uncertainties are propagated to the invariant mass of the dijet system and smear out the width of the W and Z mass peaks. The m_{jj} distributions for the hadronically decaying W and Z boson are therefore smeared significantly to the point that it is effectively impossible to differentiate between a hadronically decaying W or Z boson from the invariant masses of their dijet system. The jet resolution therefore dictates that the diboson measurement in the semileptonic channel is performed as a combination of both diboson processes.

For both these reasons the WW/WZ$\rightarrow \ell\nu jj$ process can be very difficult to measure

[14]Jet resolution improves as the energy of the jet increases.

compared to the significantly cleaner[15] fully leptonic final states. Regardless, the semi-leptonic channel is an important cross check for the SM, since it tests the hadronic component of the WW/WZ decays and is the first precision measurement in this final state done with the ATLAS detector. The larger branching fraction also means that the channel will observe new physics sooner, but with larger associated uncertainties due to the jet reconstruction. In addition, this analysis can provide a stepping stone for other analyses that may want to use the semi-leptonic channel in the future to probe other aspects of the EWK sector and SM. For example, in WW vector boson scattering[16] or as a background for future Higgs analyses that want to look at the H$\rightarrow WW$ semi-leptonic final state in order to reconstruct the full invariant mass of the Higgs[17] in this particular Higgs decay channel.

Lastly, expected anomalous Triple Gauge Coupling (aTGC) limits are comparable to other WW and WZ final states and are calculated in this analysis using a similar event selection as used for the cross section measurement. The transverse momentum of the dijet system coming from the W/Z decay is used to calculate the aTGC limits using a binned maximum likelihood fit. The semi-leptonic channel is sensitive to both the WWZ and WWγ vertices and limits are performed using the LEP constraint and the effective field theory approach.

[15]These processes are cleaner due to more precise measurements of the lepton candidates and because multiple leptonic final states are easier to distinguish from background processes.

[16]Future analyses will look at the longitudinal component of WW scattering to test if the discovered Higgs particle completely solves unitarity violation in VBS and if not it signifies new physics phenomena.

[17]Using the W mass constraint to determine the Z component of the neutrino momentum.

Chapter 2

Experimental Apparatus

2.1 Introduction to Particle Accelerators

Particle accelerators are a tool used to accelerate and direct a focused beam of charged particles within an electromagnetic field. They are used to better understand and study the desired properties through the interaction of that beam of particles, or its radiation, with matter. Since the 1930s when the first cyclotrons were developed, scientists have been using particle accelerators to study a variety of fundamental and applied research topics. In particle physics, accelerators are used to probe the basic building blocks of matter by accelerating energetic particles into fixed targets or other oncoming accelerated particles at specific interaction points. Particle detectors are located at interaction points where they can be used to study the remnants of these energetic collisions. By increasing the center of mass energy ($\sqrt{s}$) at the interaction point it is possible to produce higher mass particles than the particles that were originally collided, due to the fusion/scattering of particles and/or the radiation of vector bosons. The possible particle interactions are in general governed by the Standard Model (see Sec.1.1), but it is possible that new particles and interactions will be discovered as we continue to test the limits of this theory. Particularly, as accelerator technology improves and higher energy colliding beams are achieved it will be possible to probe energy regimes of the SM that aren't yet well understood.

Currently, the newest and most energetic particle accelerator in the world is the Large Hadron Collider (LHC), designed to reach a center-of-mass energy of 14 TeV. The following sections will give a detailed look at the LHC and the ATLAS[1] particle detector which is located on one of the LHC's interaction points. The data collected from the ATLAS detector is used to perform the cross section analysis of this dissertation.

2.2 Large Hadron Collider

The LHC is a proton-proton collider that accelerates beams of protons along a 27 km ring that crosses the borders of France and Switzerland. Located in the tunnels that previously housed the LEP experiment(1989-2000), construction finished in 2008. The accelerator and

[1] ATLAS is short for "A Toroidal LHC Apparatus."

the adjoining labs of the same name are ran by the European Organization for Nuclear Research (CERN).

The LHC [60] was designed as a high energy, high luminosity (see section 2.3.2) machine that would allow researchers to probe new regimes of the electroweak sector, particularly electroweak symmetry breaking. It is designed to reach a peak center-of-mass energy of 14 TeV ($\sqrt{s} = 14$ TeV) and a luminosity of 10^{34} cm^{-2}s^{-1}. The LHC began full operation in 2010 when it began data-taking at a center-of-mass energy of 7 TeV.

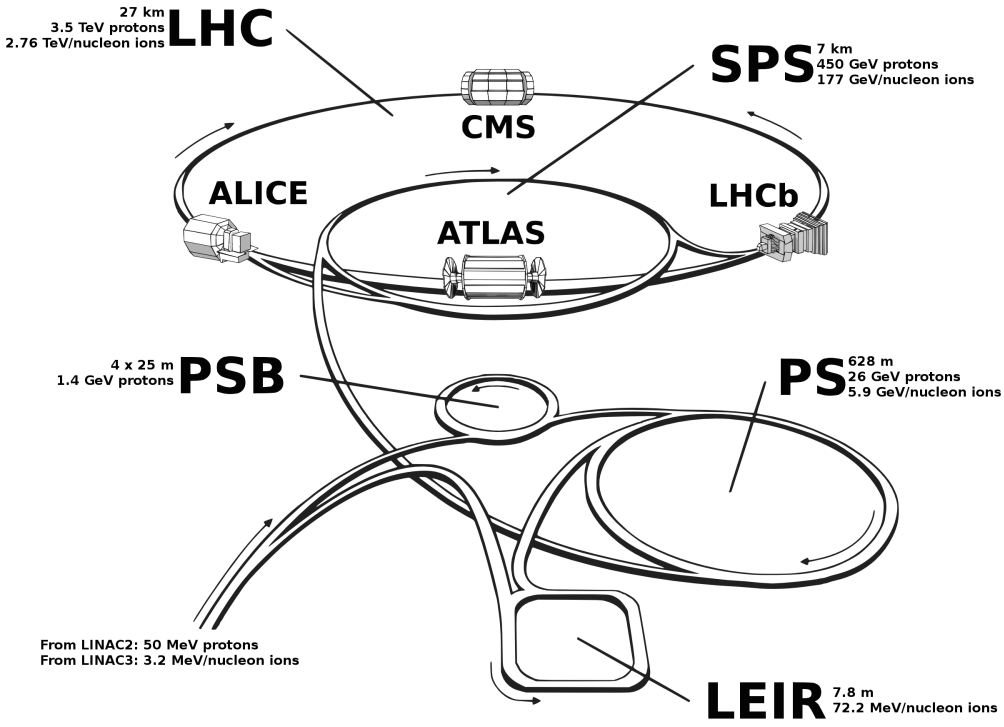

Figure 2.1: Diagram depicting the different accelerators that accelerate and provide high energy proton beams to the LHC ring. The four main detector experiments located on the LHC ring are also shown. Figure 2.1 in reference [4].

Before protons can be collided at an intersection point, the beams must be produced, accelerated and focused to reach the desired energies. The LHC is the fifth and final stage in this process, illustrated in figure 2.1, which begins at one end of the linear accelerator 2 (Linac 2). The process starts by first injecting hydrogen gas into a duoplasmatron device seen in figure 2.2. The hydrogen gas is pumped into the plasma chamber where the hydrogen atoms are stripped of their electrons by thermionically[2] emitted electrons coming from a heated cathode. These electrons collide with the hydrogen atoms due to the electric field produced by the discharge power supply. The remaining positive ions/protons are then accelerated out of the chamber through a small hole in the anode into the expansion cup before being extracted as a beam of protons. The beam is accelerated down the Linac 2 using radio-frequency (RF) cavities until the beam reaches an energy of 50 MeV and enters the Proton

[2]Meaning the thermal energy given to the electron overcomes the binding energy.

Synchrotron Booster (PSB). The PSB consists of 4 superimposed rings that take the protons and accelerates them to 1.4 GeV, passing them along to the Proton Synchrotron (PS). The PS will bring the particles up to 26 GeV and inject them into the Super Proton Synchrotron (SPS) in bunch packets that are spaced by 50 ns and have a typical bunch population of 1.2×10^{11} protons. Finally, SPS will bring the bunches to 450 GeV where they will enter into the LHC to get accelerated to 3.5 TeV before being steered by magnets and collided at intersection points where detectors are located.

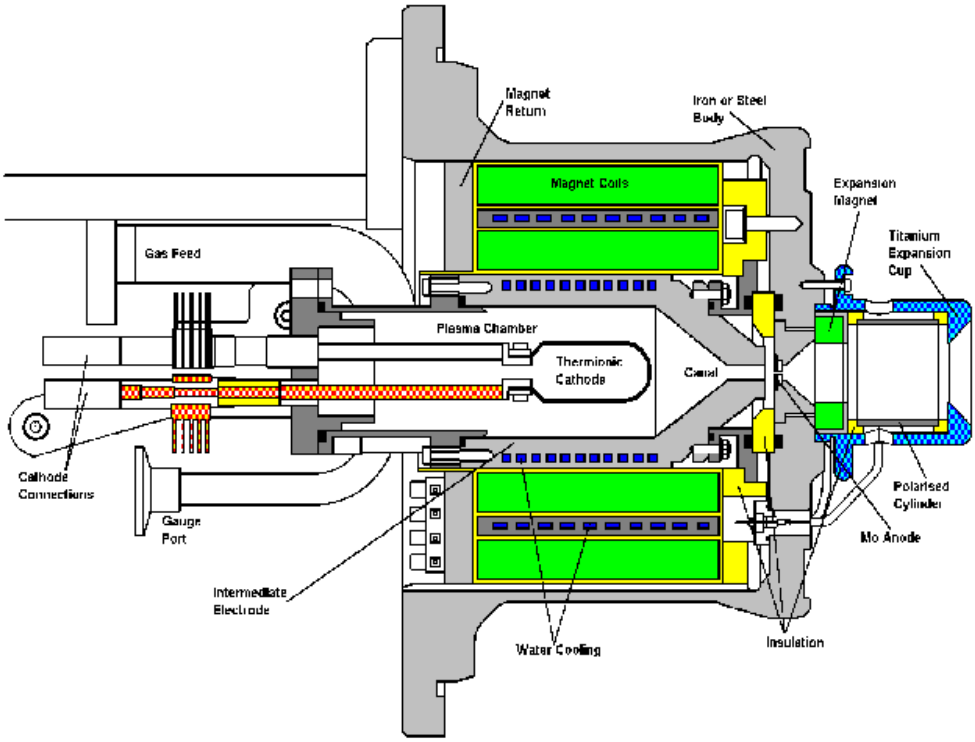

Figure 2.2: Diagram showing the duoplasmatron proton ion source that is used to inject protons into one end of the Linac2, which accelerates the protons to 50 MeV. Figure from [5].

2.3 The ATLAS Detector

The ATLAS detector [61] is one of two general purpose particle detectors located on the LHC's ring, built by an international collaboration of 38 countries and over 3000 scientists and engineers. As a general purpose detector, its goal is to be able to resolve as many physics objects coming from a pp collision, or event, as possible in order to reconstruct and ultimately understand a breadth of different event topologies. The detector, seen in figure 2.3, stands at a height of 25 m and a length of 44 m. The design of the detector allows it to process the high rate of pp collisions produced in the LHC and collect a significant amount of the energy generated in each collision within the volume of the detector.

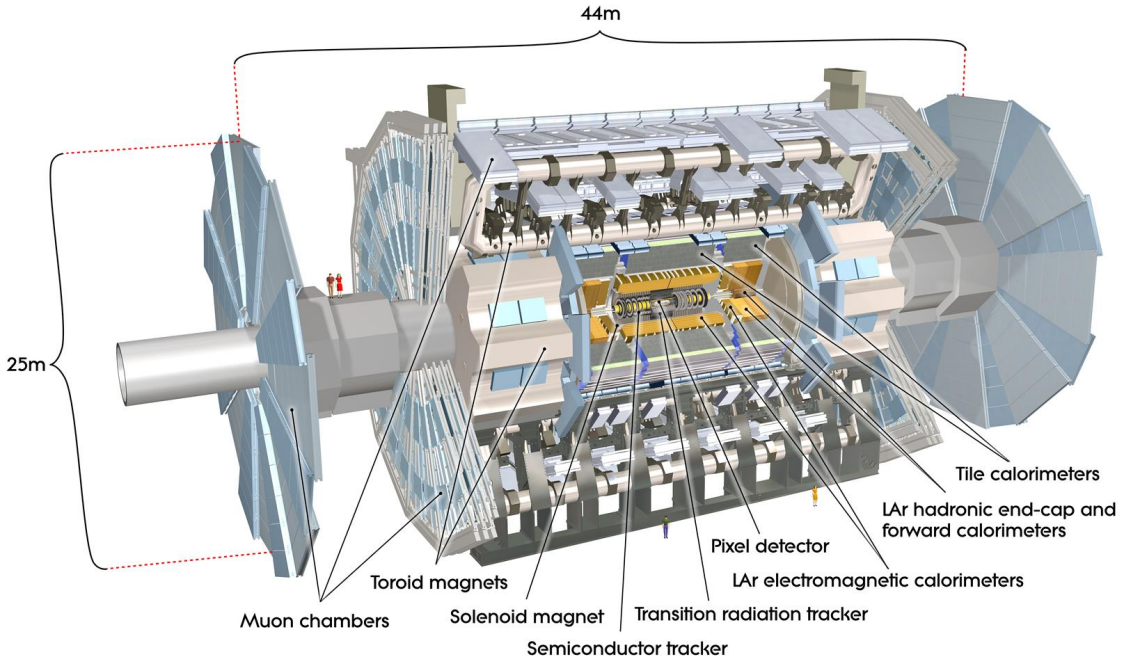

Figure 2.3: A drawing of the ATLAS detector with all its subsystems labeled. Two people are represented on the left side for scale. Figure from [6].

2.3.1 ATLAS Coordinate System

The coordinate system used by the ATLAS experiment is a right-handed coordinate system with the x-axis pointed towards the center of the LHC ring, the y-axis directed upwards with a slight tilt (0.704° from vertical) due to the general tilt of the LHC tunnel, and the z-axis along the direction of the tunnel/beam. Figure 2.4 shows the coordinate system superimposed on the detector. There are two angles of importance, θ and ϕ, where θ is the angle in the xz-plane with respect to the positive z-axis and ϕ is the angle in the xy-plane with respect to the x-axis. Additionally, we define pseudorapidity, η, in equation 2.1. η is generally used over θ since it closely resembles the quantity of rapidity, y defined in equation 2.2, which is invariant under Lorentz boosts[3]. η itself is invariant under boosts along the z-axis and is equivalent to rapidity in the approximation that an object approaches the speed of light or has approximately zero mass.

$$\eta = -\ln(\tan(\frac{\theta}{2})) \tag{2.1}$$

$$y = \frac{1}{2}\log\frac{E + p_z}{E - p_z} \tag{2.2}$$

[3]Invariant under Lorentz boost means that regardless of the reference frame in which something (a particle) is observed the observation will give the same result. A helpful reference for understanding this and the relationship between η and y can be found in ref [62].

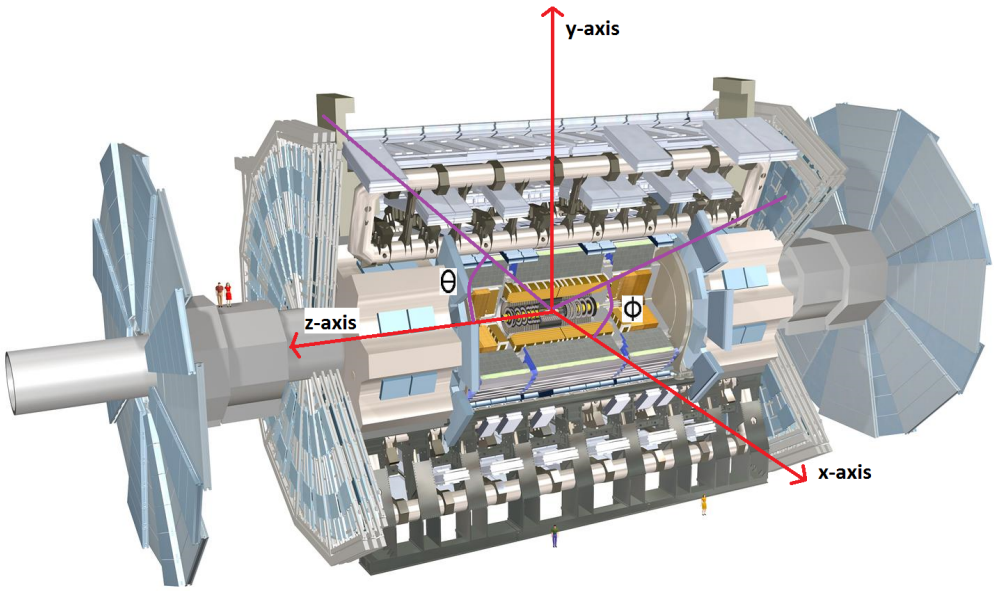

Figure 2.4: The ATLAS detector with the coordinate system overlayed is shown. The x-axis is directed towards the center of the LHC ring, y-axis points vertically, and the z-axis is along the beam direction. The ϕ and θ angles are also shown. Figure from [7].

2.3.2 Luminosity Detectors

From a physics point of view, the two most important aspects related to an accelerator are its center-of-mass energy, $\sqrt{s}$, and its luminosity, $\mathcal{L}$. Luminosity is defined as the number of inelastic collisions that are produced in a detector per cm^2 every second. It can be expressed as

$$\mathcal{L} = \frac{R_{inel}}{\sigma_{inel}} \tag{2.3}$$

where R_{inel} is the rate of inelastic collisions and σ_{inel} is the total proton-proton (pp) inelastic cross section. In a particle accelerator with proton bunches rotating around the ring at a certain frequency, f_r, and a certain number of bunches, n_b, colliding per machine revolution, the equation can be written as

$$\mathcal{L} = \frac{\mu n_b f_r}{\sigma_{inel}} = \frac{\mu_{vis} n_b f_r}{\sigma_{vis}}, \tag{2.4}$$

where μ is the average number of inelastic pp interactions per bunch crossing. Due to detector limitations, it is only possible to observe a fraction of the total inelastic pp interactions per bunch crossing. Equation 2.4 can therefore be rewritten as shown on the far right-hand side to calculate the luminosity as a function of the visible cross section, σ_{vis}, and the visible

interactions per bunch crossing, μ_{vis}. The total and visible quantities are related by an efficiency ϵ such that

$$\mu_{vis} = \epsilon\mu;\ \sigma_{vis} = \epsilon\sigma_{inel} \tag{2.5}$$

ϵ represents a selection efficiency related to the particular detector and algorithms used to calculate μ_{vis} and σ_{vis}. During data-taking, μ_{vis} is observed experimentally in ATLAS using different detectors (discussed later in this section) and is evaluated utilizing an event counting method [63] designed to select bunch crossings with at least one inelastic pp collision. σ_{vis} is determined outside of normal data-taking periods by dedicated van der Meer (vdM) scans, where the value can be calculated through direct measurements of the event rate by varying (scanning over) the beam-beam separation along the x and y plane.

Since the luminosity varies with μ_{vis}, it is calculated for each bunch crossing separately and this is commonly referred to as the instantaneous luminosity. Bunch Crossing Identification (BCID) numbers are used to distinguish between different bunch crossings in the detector. The integrated luminosity, $\mathcal{L}$, is the integral of the instantaneous luminosity over time and represents the total number of inelastic collisions collected or the total dataset.

The details regarding the two luminosity detectors used for this analysis on the 2011 dataset are discussed in the following sections.

Beam Conditions Monitor

The Beam Conditions Monitor [64] (BCM) system's primary goal is to monitor the behavior of the beam near the interaction point and issue beam-abort requests when beam losses have the potential to damage the detector. In addition, it provides a μ_{vis} measurement at $|\eta| = 4.2$ with a time resolution of 0.7 ns. The detector consists of two sets of four diamond sensors on each side of the interaction point at a z = $\pm$1.84 m and a radius of 55 mm. Each sensor is made out of 500 μm thick radiation hard polycrystalline chemical vapor deposition diamonds and are mounted in a cross pattern with a tilt of 45 degrees. The horizontal and vertical pairs of the BCM detectors are read out separately and used as two independent luminosity measurements for cross-checks and redundancy. An image of one BCM station can be seen in figure 2.5.

LUCID

The LUCID detector [65] is the only dedicated detector for measuring online relative luminosity at ATLAS. It is a Cherenkov light detector that consists of 20 aluminium tubes surrounding the beam pipe. Each tube is filled with C_4F_{10} gas at a constant pressure. Cherenkov photons created by charged particles in the gas are reflected in the tube until they reach the photomultiplier tubes at the back end, where if they exceed a given threshold are readout as a hit. Two stations are positioned at opposite sides of the interaction point at a z = $\pm 17m$ with a pseudorapidity coverage of $5.61 < |\eta| < 5.93$. A schematic of one of the stations is shown in figure 2.6.

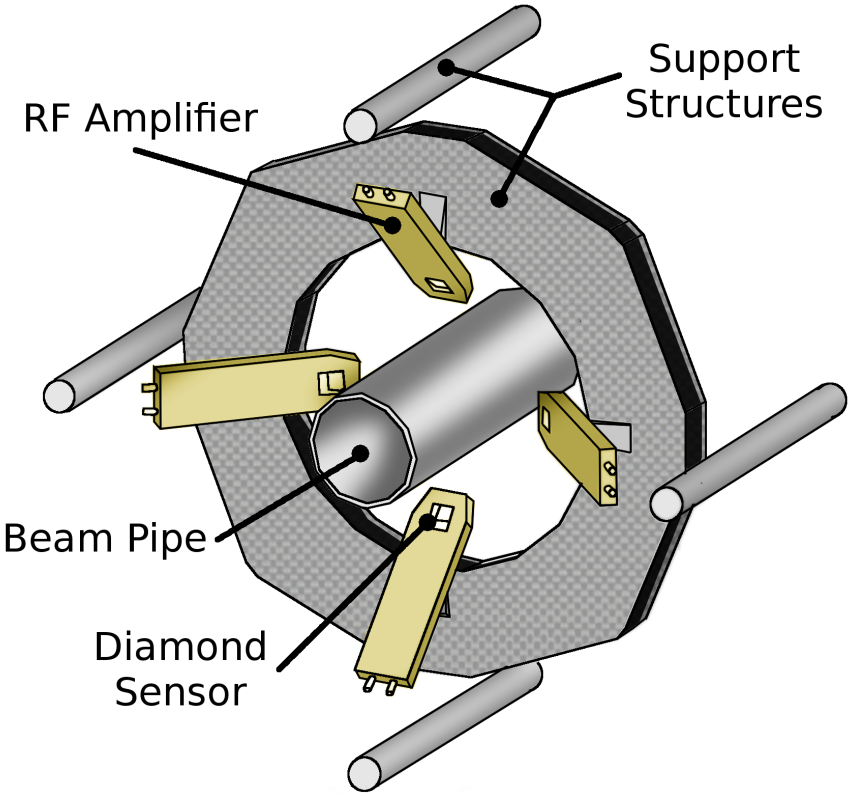

Figure 2.5: Schematic of one of the two BCM stations mounted along the beam pipe on either side of the interaction point. Figure 3.18a from [4].

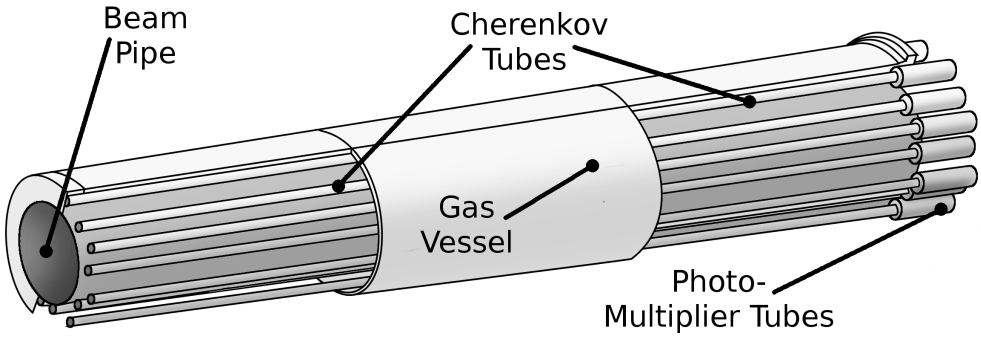

Figure 2.6: Schematic of LUCID detector, the interaction point is along the beam pipe to the left of the schematic.. Figure 3.18c from [4].

2.3.3 Tracking System

The ATLAS inner detector specializes in the detection of tracks coming from charged particles produced at the interaction point. It consists of three subsystems: the pixel detector, Semi-Conductor Tracker (SCT), and the Transition Radiation Tracker (TRT). The detector combines high resolution tracking from the first two subsystems with continuous

tracking from the TRT, all housed within a solenoidal magnetic field of 2T. This allows for precision measurements of particle charge and momentum, with a coverage of up to $|\eta| < 2.5$. The inner detector is depicted in figure 2.7.

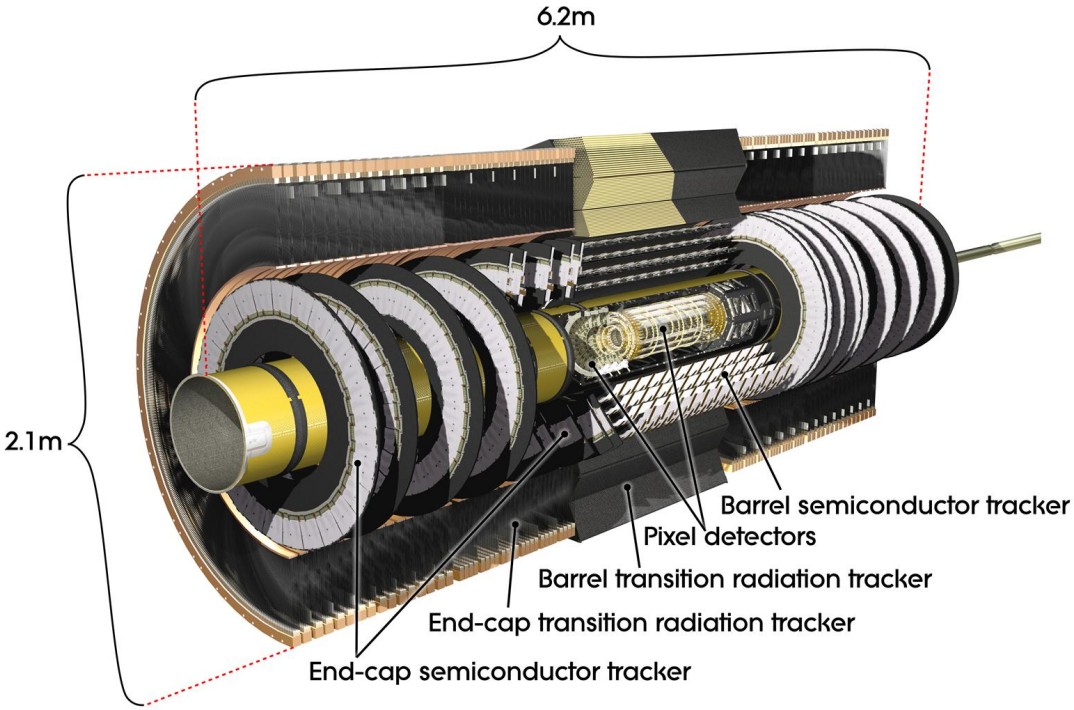

Figure 2.7: A close look at the ATLAS inner detector with the barrel and endcaps labeled for the three subsystems that it comprises of. Figure from [8]

Pixel Detector

The innermost part of the tracking system is the silicon pixel detector [10]. It provides accurate measurements of the collision vertices using very high granularity radiation hard silicon sensors that are very close to the interaction point. This system determines the impact parameter[4] resolution for particle collisions, and has the capabilities to distinguish long-lived particles like B hadrons or τ leptons. The detector, depicted in figure 2.8, is comprised of a barrel and two endcap disk sections, each containing three layers of pixel modules. The three cylindrical barrel layers are located at radial positions of 50.5 mm, 88.5 mm, and 122.5 mm from the interaction point respectively. The barrel layers are made up of 22, 38, and 52 staves respectively, each inclined with an azimuthal angle of 20 degrees to ensure overlap of the active sensor material. Each stave is identical and composed of 13 pixel modules. The three endcap disks on either side of the interaction point are located at distances of 50, 58

[4]The impact parameter is the closest distance along the z or transverse plane between a reconstructed track and where the hard scattering took place (location of a reconstructed vertex).

and 65 cm from the interaction point respectively and are made up of 8 sectors each, with 6 modules in each sector. A pixel module, shown in figure 2.9, contains a pixel sensor, which is a wafer of silicon with dimensions of 16.4 x 60.8 mm, containing 46080 pixels, 50 x 400 μm^2 each. Each sensor is bump-bonded to 16 front-end chips (FEs) [66] which read out 2880 pixels each. The FEs will sample, amplify and discriminate signals from each pixel, compute the time-over-threshold, and then forward that information to the Module Control Chip(MCC) in the case of a triggered event [10]. The intrinsic accuracy of the pixel detector is 10 (R-ϕ) and 115 (z) μm.

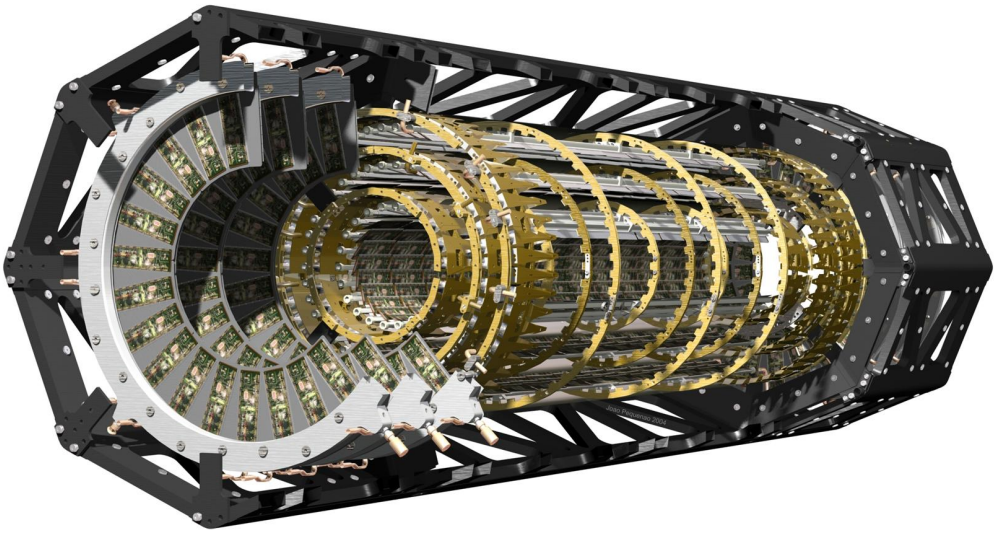

Figure 2.8: The pixel detector is the innermost subsystem of the ATLAS detector. It's composed of three barrel layers surrounding the collision point and three disk layers on each end of the barrel. In black is seen the carbon fiber support structure that the system is encased and mounted on. The whole system has a diameter of 30 cm and a length of 150 cm. Figure from [9]

Semi-Conductor Tracker

Surrounding the pixel detector, the Semi-Conductor Tracker (SCT) contributes to the measurements of the momentum, impact parameter and vertex reconstruction. It consists of a barrel and two endcap regions, with four concentric layers (30 cm < R < 52 cm) making up the barrel and nine disk layers forming each endcap. The barrel provides coverage out to $|\eta|$ <1.1 to 1.4 and the endcaps extend that coverage to $|\eta| < 2.5$. The entire structure houses 4088 silicon strip modules, with 6.2 million readout channels. A silicon strip module is constructed with 4 silicon detectors (6.36 x 6.40 cm^2) with each consisting of 768 readout strips, p-strips on n-type silicon, with a pitch[5] of 80 μm. Two of the detectors are wire-bonded together to form 12.8 cm long sensors and then are glued back to back with the

[5]distance between neighboring strips

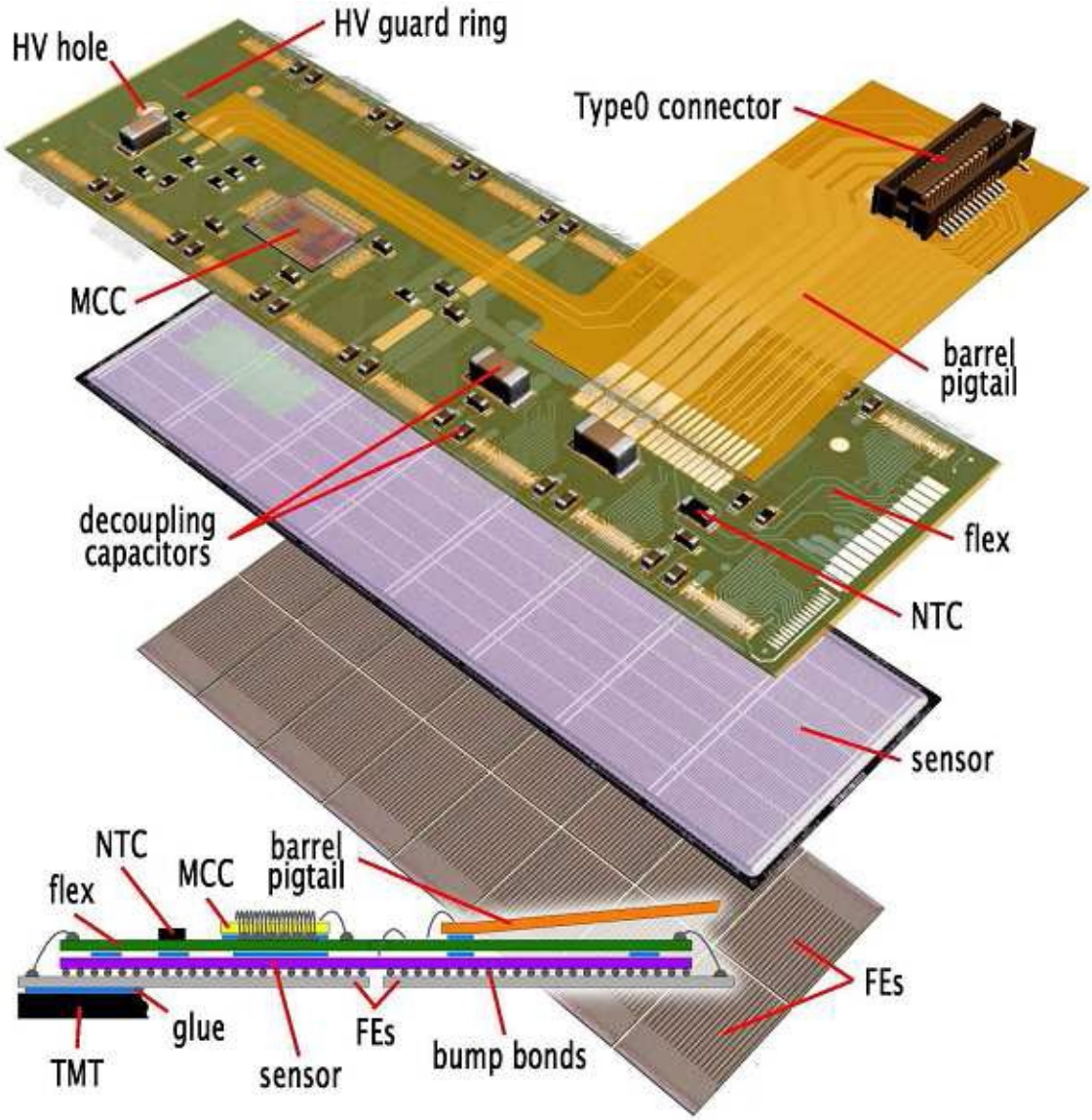

Figure 2.9: Diagram depicting the elements of a Pixel Detector module. Figure from [10]

remaining two detectors (also wire-bonded) at a 40 mrad stereo[6] angle. This setup allows each layer to precisely determine the R-ϕ and z coordinates coming from a particle track. The disk modules are similar to the barrel modules, with strip pitches between 57 and 94 μm that fan out radially with respect to the beam axis[67, 68]. The accuracy achieved by the SCT is 17 (R-ϕ) and 580 (z) μm. An example of a SCT module can be seen in figure 2.10.

[6]Implementation of a slight angle (stereo) between how the long sensors overlap allows for a 3 dimensional representation to be made since the strips between long sensors are no longer parallel with each other and therefore a charged particle traveling in a straight line will interact with each set of strips differently.

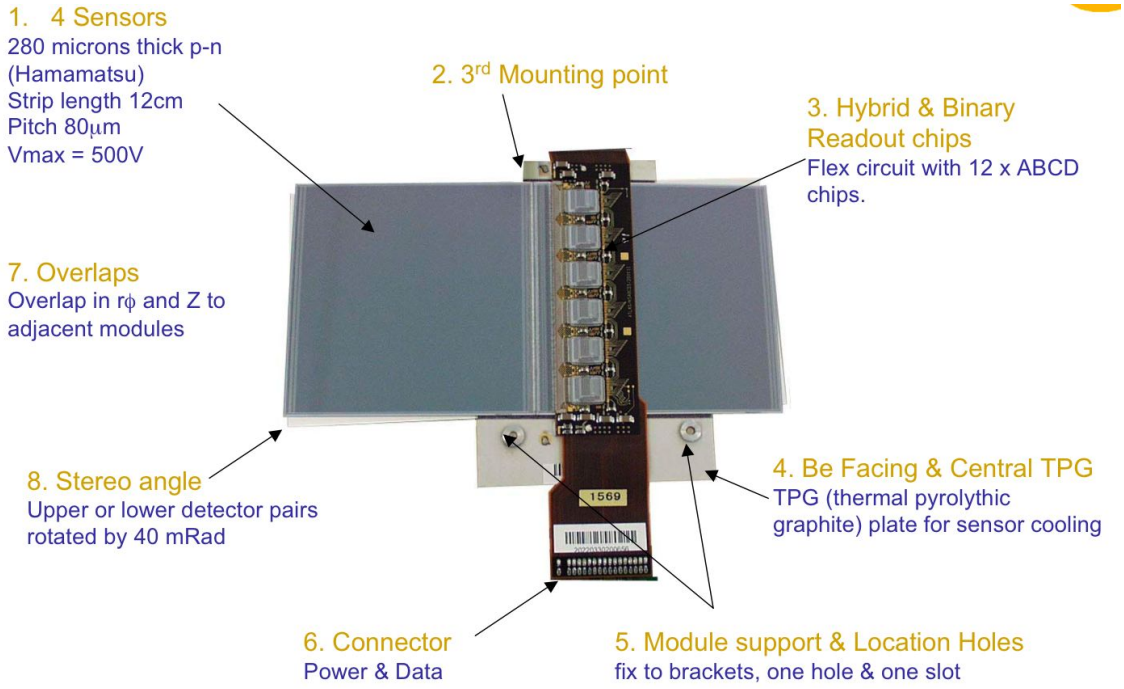

Figure 2.10: Figure showing the elements of a SCT barrel module. Figure from [11].

Transition Radiation Tracker

The final, outermost part of the inner detector, the TRT, is a continuous straw tracker and transition radiation detector. It provides on average 35 two-dimensional measurements ($R\phi$) with a resolution of less than 0.150 mm for charged particles with $p_T > 0.5$ GeV and has a coverage up to $|\eta| < 2.0$. It is composed of approximately 300,000 drift tubes (straws), with lengths of 144 cm (barrel) and 37 cm (endcap), in the barrel ($|\eta| < 1.0$) and endcap ($1.0 < |\eta| < 2.0$) regions. Each straw has a diameter of 4 mm and contains a coaxial gold-plated tungsten anode wire with a diameter of 31 μm. An ionizing gas mixture of 70% Xe, 27% CO_2 and 3% O_2 is used in the straws, with the straw walls lying at a potential of -1.5 kV relative to the wire. The wires are bundled in modules that are completely surrounded by polypropylene-polyethylene fiber matting, a transition radiation material. Figures 2.11 and 2.12 contain a cut-away view of the inner detector with the straws clearly visible in the TRT. In addition to the tracking information, the TRT also helps discriminate electrons from other hadrons due to the transition radiation. Charged particles emit photons as they transverse the TRT (transition radiation) and these photons are typically produced at higher energies (∼5-30 keV) compared to the energy lost due to ionization (∼2 keV) [69]. The number of emitted photons is larger for electrons versus charged hadrons at a given fixed momentum allowing for separation between the two in the detector.

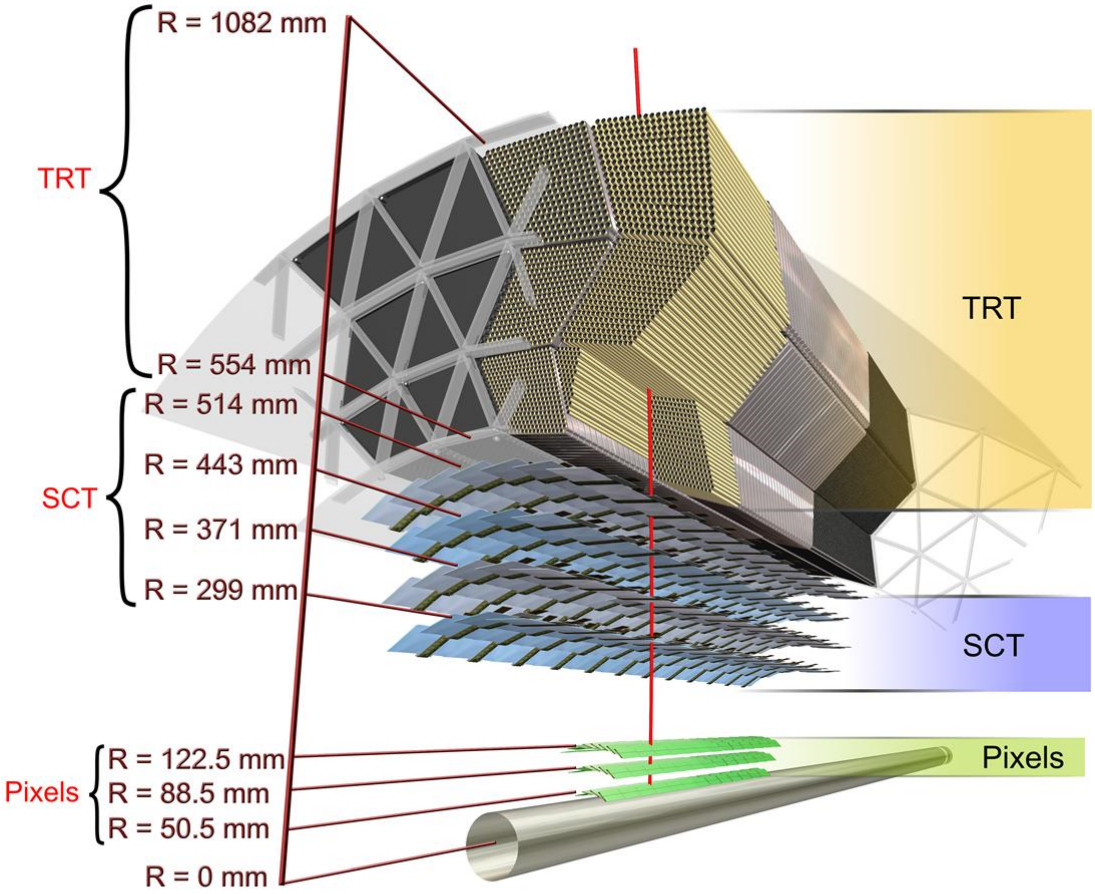

Figure 2.11: Cut-away computer generated image of a particle in red traversing all the subsystems of the ATLAS inner detector. The particle passes through the three layers of the pixel detector, four layers of the SCT, and approximately 25 straw tubes of the TRT. Figure from [8].

2.3.4 Calorimeters

The ATLAS calorimeter systems play the important role of measuring the energy and positions of electrons, photons, and hadronic objects reconstructed as jets. Its systems provide coverage out to $|\eta| < 4.9$ and encompasses a large enough area for the containment of EM and hadronic showers coming from incident particles. An overview of the calorimeter system is shown in figure 2.13. The calorimeter can be separated into two general types of detectors, liquid argon (LAr) and tile calorimeters. Both are a type of sampling calorimeter, in which incident particles will transverse alternating layers of dense absorber material and

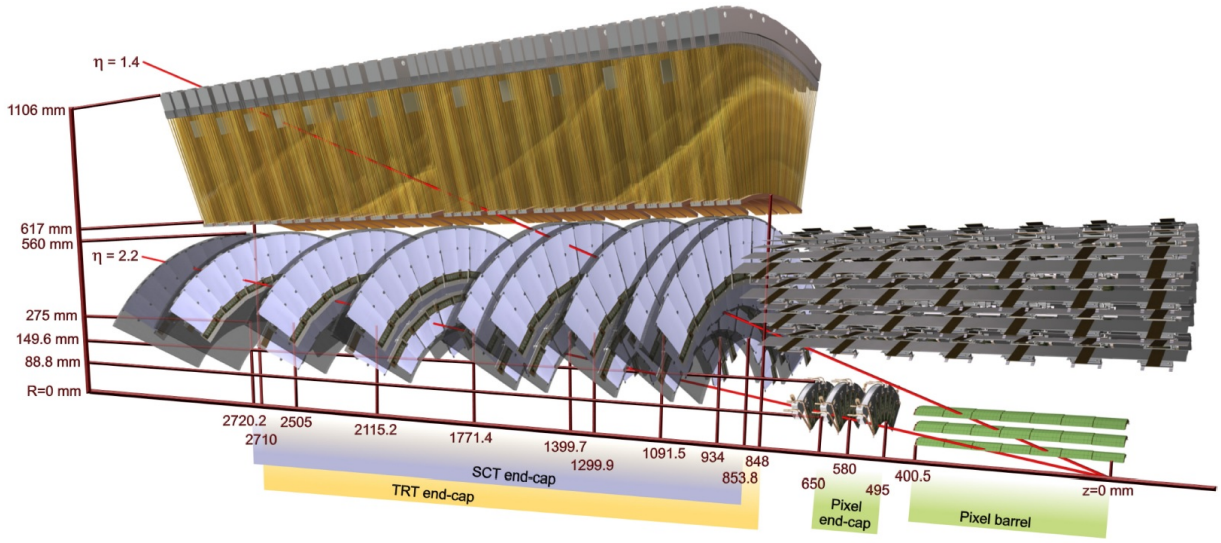

Figure 2.12: View of the inner detector from a perspective almost parallel with the beam axis. Two lines in red, with $\eta = 1.4$ and $\eta = 2.2$, depict particles traveling through the detector. Both the pixel detector and SCT have coverage out to $|\eta| < 2.5$ while the TRT only covers $|\eta| < 2.0$. Figure 3.3 from [12].

active sensor material. The absorber materials are used to facilitate the production of electromagnetic showers as incident particles transverse them, while the active sensor material measures the energy from the resulting showers in between absorber layers. This results in some of the energy being deposited in the absorber layers and not being measured, the sampling calorimeters are therefore calibrated to infer the total energy from the fraction of energy deposited.

Calorimeter systems are intrinsically different from the tracking systems in the inner detector. The tracking system will generally cause minimal disturbance to charged particles as they ionize or excite the instrumentation along their trajectory. Calorimeters are designed to intentionally reduce the energy of incident particles through interactions with the calorimeter material that lead to the development of EM showers. Unlike the tracking system, the calorimeters are therefore sensitive to both neutrally charged and charged particles.

High energy electrons predominantly lose their energy through bremsstrahlung radiation, which is the radiation of photons as electrons experience large accelerations due to the fields around atomic nuclei. The energy loss due to this is parametrized by the radiation length of a material, X_0, which is the mean length of material traversed before an electron's energy is reduced by a factor of $(1 - \frac{1}{e})$ or 63%. For high energy photons, the dominant interaction is through e^+e^- pair production, which has a mean free path of $7/9X_0$. For these reasons, EM calorimeters are generally characterized by the number of radiation lengths traversed by a particle. Prior to reaching the calorimeters, an incident EM particle would have already passed through about 2 (barrel) to 7 (endcap) X_0 worth of material [18]. Hadrons instead lose their energy by inelastic interactions with nuclei through the strong force, characterized by the nuclear interaction length, λ, which is the mean free path of a particle before undergoing

a nuclear interaction in a medium. The higher the density of material, the shorter the interaction length. In general, the showers produced by hadronic showers are broader than EM showers.

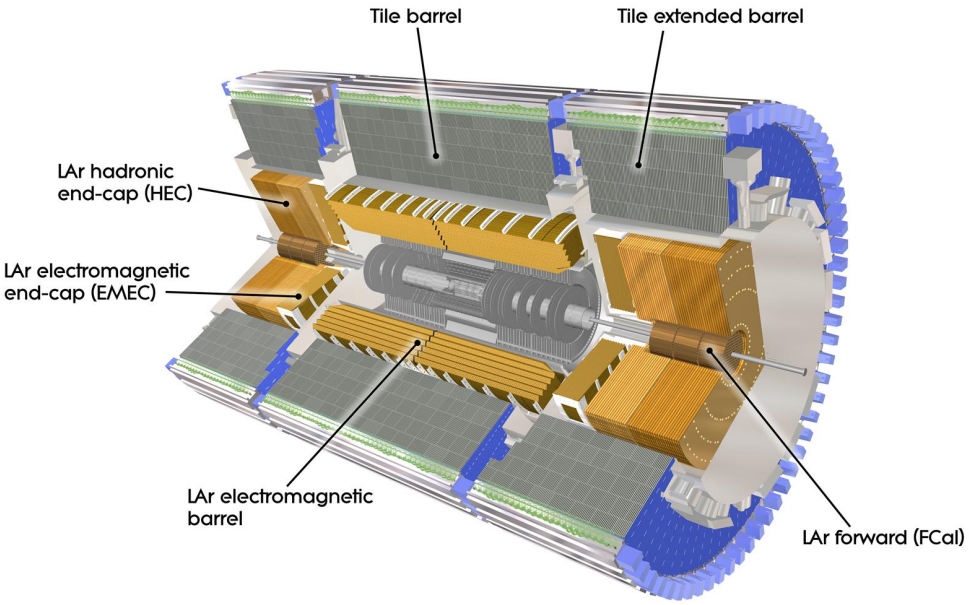

Figure 2.13: Cut-away view of the ATLAS calorimeter system. In orange are the LAr calorimeters and in gray are the tile calorimeters. Figure from [13].

Electromagnetic Calorimeter

The EM calorimeter provides η coverage out to 3.2 and is divided into a barrel ($|\eta| < 1.475$) and endcap part ($1.375 < |\eta| < 3.2$). The barrel is made up of two identical half barrels joined at z = 0 with a gap width of 6 mm. The endcap consists of two coaxial wheels with eta coverage of $1.375 < |\eta| < 2.5$ and $2.5 < |\eta| < 3.2$. Both the barrel and endcap calorimeters are comprised of liquid argon active material with lead absorber plates which provide full ϕ coverage using an accordion-shaped geometry and read out provided by kapton electrodes. A cut-away view of the barrel calorimeter geometry can be seen in figure 2.14. The calorimeter cells are mostly uniform in η and ϕ and therefore have a finer granularity and longitudinal segmentation as they get closer to the interaction point. The total thickness of the EM calorimeter is a minimum of 24 X_0 in the barrel and 26 X_0 in the endcaps.[14, 18]. Table 2.1 shows the eta coverage and granularity of the different sections of the EM calorimeter.

The calorimeter located within $|\eta| < 2.5$ is segmented into three longitudinal sampling layers. The first layer has a granularity of $\Delta\eta \times \Delta\phi = 0.003 \times 0.1$, where the fine $\Delta\eta$ segmentation allows for differentiation of π^0 and γ/e objects. The second sampling layer has a square segmentation and is the largest layer in the radial direction with a greater than

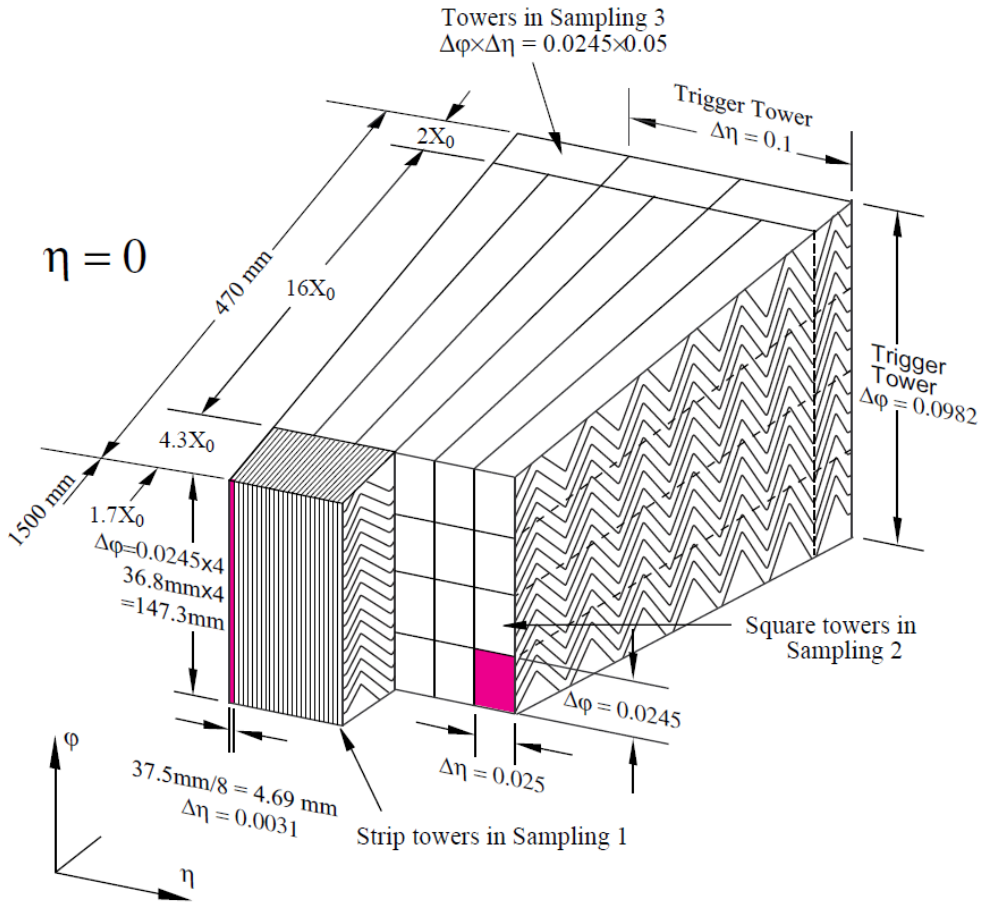

Figure 2.14: Sketch of a segment of the EM calorimeter and the accordion structure that is used. The three sampling layers are shown with the radiation lengths calculated at an $\eta = 0$. Figure 1.2 from [14].

16 X_0 thickness. This layer provides the bulk of the energy measurement for EM particles. The third layer helps distinguish hadronic showers from EM showers as it is likely that most EM showers would not have extended past the second layer. For $|\eta| > 2.5$, the calorimeter is segmented into two longitudinal layers which have a coarser granularity since they are intended to help with the reconstruction of jets and E_T^{miss}, instead of providing precision measurements for electrons and photons. Additionally, there is a presampler calorimeter located at $|\eta| < 1.8$ that is used to correct for energy losses due to the material in front of the calorimeter. It consists of a LAr active layer of thickness 1.1 cm in the barrel and 0.5 cm in the endcaps.

Hadronic Calorimeter

The hadronic calorimeter provides η coverage out to 4.9 and utilizes both LAr and scintillating-tile techniques depending on the expected radiation environment and energy measurement requirements. The total thickness including the hadronic calorimeter and its

EM Calorimeter	**Barrel**	**Endcap**	
Coverage	$\|\eta\| < 1.475$	$1.375 < \|\eta\| < 3.2$	
Granularity ($\Delta\eta \times \Delta\phi$)			
Sampling 1	0.003×0.1	0.025×0.1	$1.375 < \|\eta\| < 1.5$
		0.003×0.1	$1.5 < \|\eta\| < 1.8$
		0.004×0.1	$1.8 < \|\eta\| < 2.0$
		0.006×0.1	$2.0 < \|\eta\| < 2.5$
		0.1×0.1	$2.5 < \|\eta\| < 3.2$
Sampling 2	0.025×0.025	0.025×0.025	$1.375 < \|\eta\| < 2.5$
		0.1×0.1	$2.5 < \|\eta\| < 3.2$
Sampling 3	0.05×0.025	0.05×0.025	$1.5 < \|\eta\| < 2.5$
Presampler	**Barrel**	**Endcap**	
Coverage	$\|\eta\| < 1.52$	$1.5 < \|\eta\| < 1.8$	
Granularity ($\Delta\eta \times \Delta\phi$)	0.025×0.1	0.025×0.1	

Table 2.1: .Granularity of the EM calorimeter and presampler according to their coverage in $|\eta|$ [18].

support structure is 11 λ (9.2 λ without the support structure) at $\eta = 0$, enough to sufficiently contain hadronic showers from penetrating into the muon systems. For the barrel and extended barrel region ($|\eta| < 1.7$) an iron scintillating tile technique is used in which iron is utilized as the absorber and scintillating tiles are the active material. The tile calorimeter is broken up into three sampling layers with granularity of $(\Delta\eta \times \Delta\phi) = 0.1 \times 0.1$ (0.2×0.1) for layers 1 and 2 (3). The layers have approximate interaction lengths of 1.4, 4.0, and 1.8 λ. Each tile is read out by wavelength shifting fibers placed on either side of the tiles that feed into photomultiplier tubes.

The hadronic calorimeter used in the endcaps (HEC in figure 2.13) is a LAr calorimeter with copper plate absorbers. It consists of two wheels with an outer radius of 2.03 m and provides eta coverage out to $1.5 < |\eta| < 3.2$. The inner (outer) wheel contains copper plates with a thickness of 25 (50) mm and a LAr gap of 8.5 mm between the plates, which contain three parallel electrodes that divide the gap into 1.8 mm drift spaces. Table 2.2 shows the eta coverage and granularity of the HEC and tile calorimeter.

Lastly, the LAr forward calorimeter (FCAL) is used in the region $3.1 < |\eta| < 4.9$. The forward calorimeter is required to withstand high amounts of radiation due to its close proximity to the interaction point, as well as be able to accommodate approximately 9 interaction lengths worth of material in a rather small longitudinal area. To accomplish this, high density metal matrices are used to measure and absorb the EM and hadronic showers. The FCAL is divided into three layers, the first layer using a copper metal matrix and the other two layers using tungsten. Each matrix consists of regularly spaced longitudinal(along the beam pipe) channels filled with rods and tubes, with liquid argon filling the gaps between them. The rods are kept at a positively high voltage while the tubes/matrix are grounded. A diagram of the FCAL structure can be seen in figure 2.15 and design parameters are shown

Hardonic Tile	**Barrel**	**Extended Barrel**	
Coverage	$\|\eta\| < 1.0$	$0.8 < \|\eta\| < 1.7$	
Granularity ($\Delta\eta \times \Delta\phi$)			
Sampling 1 and 2	0.1×0.1	0.1×0.1	
Sampling 3	0.2×0.1	0.2×0.1	
Hadronic LAr Endcap		**Endcap**	
Coverage		$1.5 < \|\eta\| < 3.2$	
Granularity ($\Delta\eta \times \Delta\phi$)			
		0.1×0.1	$1.5 < \|\eta\| < 2.5$
		0.2×0.2	$2.5 < \|\eta\| < 3.2$

Table 2.2: Granularity of the hadronic calorimeters according to their coverage in $|\eta|$ [18].

in table 2.3. A summary of the energy resolution for all the calorimeter systems can be found in table 2.4.

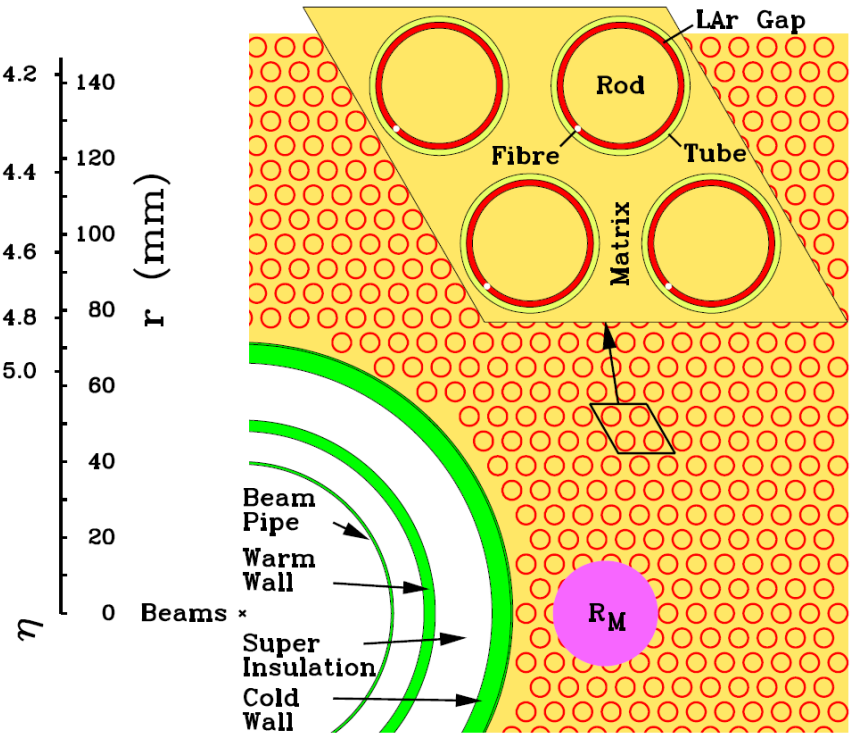

Figure 2.15: Cross section view of the FCAL with a zoomed in view of the calorimetry structure. Liquid Argon is used in the gaps between the rod and tube as the ionizing agent while the very dense metal matrix acts as the absorber. Figure 1.9 from [14].

Section	FCAL 1	FCAL 2	FCAL 2
Material	Copper	Tungsten	Tungsten
η Acceptance	$3.0 < \|\eta\| < 4.9$	$3.1 < \|\eta\| < 4.9$	$3.2 < \|\eta\| < 4.9$
Rod diam./LAr gap	4.75 mm / 0.25 mm	4.75 mm / 0.375 mm	5.50 mm / 0.50 mm
Thickness (λ)	2.6	3.5	3.4

Table 2.3: Summary of the FCAL design values [29].

Calorimeter	Resolution (σ_E /E)
Electromagnetic (LAr)	$10\%/\sqrt{E} \oplus 1.0\%$
Hadronic (LAr and Tile)	$50\%/\sqrt{E} \oplus 3.0\%$
Forward (LAr)	$100\%/\sqrt{E} \oplus 3.0\%$

Table 2.4: Summary of the energy resolution design requirements for the ATLAS calorimeter. The actual resolution is dependent on the sub-system and η [29].

2.3.5 Muon Spectrometer

Muon momentum is measured in both the inner detector (described in section 2.3.3) and the Muon Spectrometer (MS). The MS lies outside the calorimeter system and utilizes the fact that muons do not interact with material very much (high penetration capabilities), allowing them to bypass the majority of the detector with minimal energy losses while the bulk of other particles would have been stopped by the calorimeter. Therefore, the MS can exploit this and provides both a high precision muon momentum measurement, as well as triggering capabilities for muons. The MS, shown in figure 2.16, is divided into four subsystems with a combined coverage of $|\eta| < 2.7$, the Monitored Drift Tubes (MDT) and Cathode Strip Chambers (CSC) provide the precision measurements, while the Resistive-Plate Chambers (RPC) and Thin-Gap Chambers (TGC) provide the triggering capabilities. The system operates in a toroidal magnetic field (described in section 2.3.6) that curves the trajectories of charged particles and is designed such that particles coming from the interaction point will traverse three layers of the tracking subsystems [18]. A sideview of one quadrant of the MS can be seen in figure 2.17. For particles with $|\eta| < 1.4$, passing through the barrel, the middle layer is within the toroidal magnetic field and therefore three points of curvature are present in order to measure the sagitta and calculate the momentum. For $|\eta| > 1.4$, in the endcaps, the magnet cryostats prevent a layer from being placed in the field and therefore the muon measurement is done using a point-angle measurement.

Monitored Drift Tubes

The MDT subsystem consists of three precision measurement layers in the barrel and endcaps out to $|\eta| < 2.0$ and two layers for $2.0 < |\eta| < 2.7$. The drift tubes used in the MDT are constructed out of 30 mm diameter aluminium tubes with a 400 μm wall thickness and a 50 μm diameter central Tungsten-Rhenium wire. The tubes are filled with 93% Ar and 7% CO_2 gas at 3 bar pressure. The resolution is approximately 80 μm for a single wire

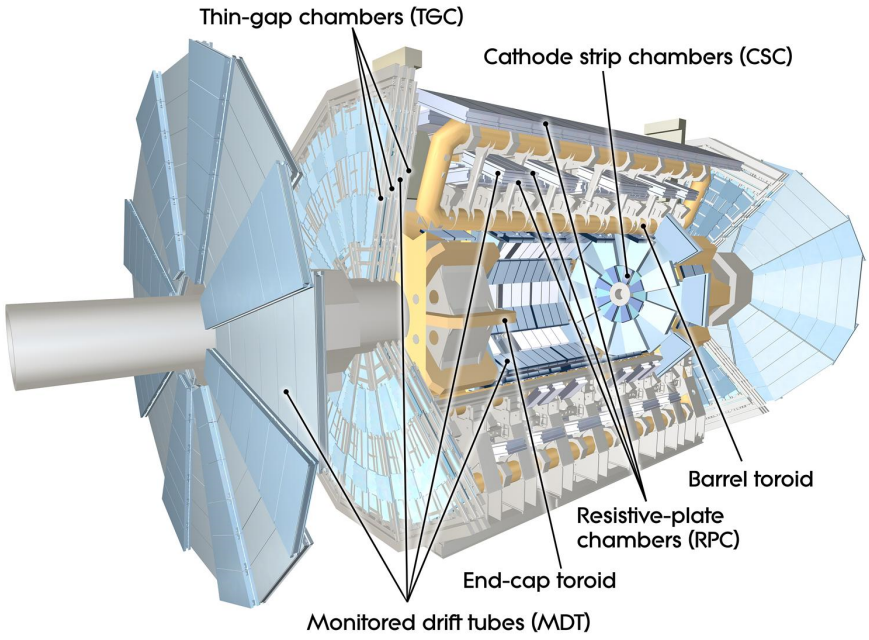

Figure 2.16: Diagram depicts the four different subsystems of the muon spectrometers as well as the toroid magnets used in the barrel and endcaps. Figure from [15].

and is improved to approximately 40 μm by creating MDT chambers which consist of 3-4 monolayers of tubes on two sides of a support structure [18] [16]. The tubes are aligned in order to precisely measure the η coordinate, the direction in which the majority of the bending from the magnetic field occurs.

Cathode Strip Chambers

In the inner endcap region, $2.0 < |\eta| < 2.7$, where particle fluxes are highest the CSC provides precision muon measurements using multiwire proportional chambers with a cathode strip readout. The measurement is obtained by measuring the charge induced on segmented cathodes by the avalanche formed on the anode wires. The anode pitch and anode-to-cathode distance is equal to 2.54 mm, with the pitch between cathode segments being twice that at 5.08 mm. The CSC are arranged in four layers with the second cathode layer arranged orthogonally to the other three layers (parallel to the anode wires) in order to measure the transverse coordinate, ϕ. The resolution obtained for one track measured four times in the bending direction (y-z plane) is 40 μm and 0.5 cm for a single point resolution in the transverse plane.

Resistive-Plate Chambers

The RPC makes up the barrel portion of the trigger chambers for the MS. The chambers are formed by two parallel resistive bakelite plates with a thin gas gap in between containing tetrafluoroethane ($C_2H_2F_4$) . The read out is done using strips that are orthogonal to each

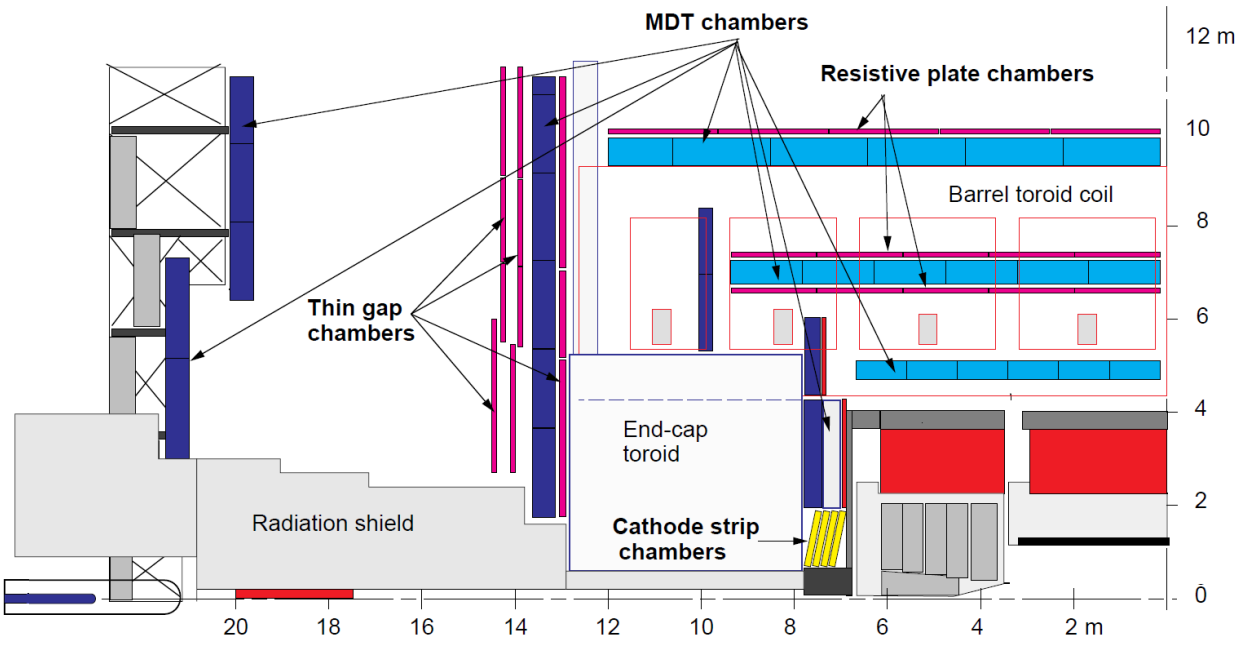

Figure 2.17: A sideview of one quadrant of the ATLAS detector with the subsystems of the MS highlighted. The MDT chambers are highlighted in light blue for the barrel and dark blue for the endcap chambers. The CSC is shown in yellow and provides coverage between $2.0 < |\eta| < 2.7$. The trigger chambers consisting of the RPC and TGC are shown in red. Figure from [16].

other, allowing for a measurement of η and ϕ. Each chamber has two detector layers and combined with three RPC layers a particle traversing through the barrel will provide up to six RPC measurements. The RPC has a time resolution of 1.5 ns for a single layer, much lower than the design requirement of 25 ns which is the designed LHC bunch crossing spacing and the spatial resolution is 6 mm with six measurement points in the RPC [16].

Thin-Gap Chambers

The TGC provides the muon trigger for the endcaps, out to an $|\eta| < 2.4$. The design is similar to the CSC with the anode wire pitch being larger than the cathode to anode distance. Etched copper strips on the back of the cathodes provide the readout with the strip orientation either parallel or orthogonal to the MDT wires. This allows for measurements of both spatial coordinates of a track [16].

2.3.6 Magnet System

The ATLAS magnet system, shown in figure 2.18, is composed of three systems, the Central Solenoid (CS), the barrel and endcap toroids. They provide magnetic fields in the inner detector and muon systems to facilitate accurate particle identification and momentum measurements for charged particles.

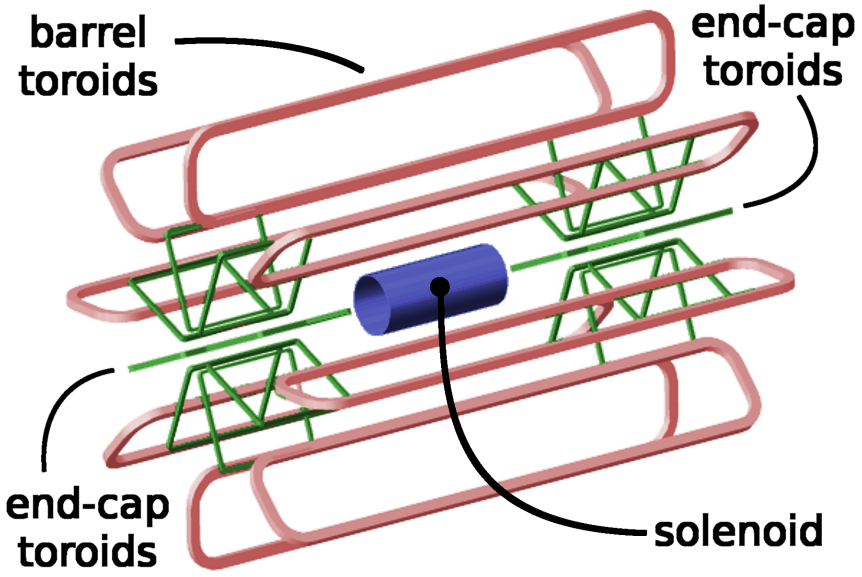

Figure 2.18: The ATLAS magnet system depicting the central solenoid that encases the inner detector and the two toroidal magnet systems that apply a field to the muon spectrometer. Figure 3.19 from [4].

The CS is positioned in front of the EM calorimeter and encapsulates the majority of the inner detector, providing a central magnetic field of 2 T with a peak of 2.6 T pointing in the z direction. It has a total axial length of 5.283 m and an inner radius of 1.247 m. The field is produced using a single layer superconducting coil of Al:Cu:NbTi that is wound up around the support cylinder 1173 times with a current of 7730 A. At $\eta = 0$ the structure has a radiation length of 0.64 X_0 and an interaction length of 0.13 λ [70] [71]. The magnetic field itself is not particularly uniform across the entire length of the solenoid. Figure 2.19 shows distribution of the measured magnetic field as a function of z at different radial lengths [17].

The toroidal magnets for the muon spectrometer are three air-core superconducting toroids, one for the barrel and two for the endcaps. The toroids each consist of eight race-track type coils that are radially and symmetrically around the beam axis. The barrel toroid is located outside the hadronic calorimeter and has an axial length of 25.3 m with a inner radius of 4.7 m. The endcap toroids are located inside the barrel at each end, they have an axial length of 5 m and a inner radius of 1.65 m. The endcap toroid coils are rotated at an angle of 22.5 degrees with respect to the barrel toroids to improve the bending power of the toroids in the transition region between the barrel and endcaps. The typical bending power of the toroid system is 3 Tm in the barrel and 6 Tm in the endcaps. A more detailed look at the distribution of the magnetic bending power of the toroids can be seen in figure 2.20[16].

2.3.7 Trigger System

The trigger system utilized by ATLAS is a three level system that filters and selects events to save for future physics analysis. The LHC, if running at design specifications, would have

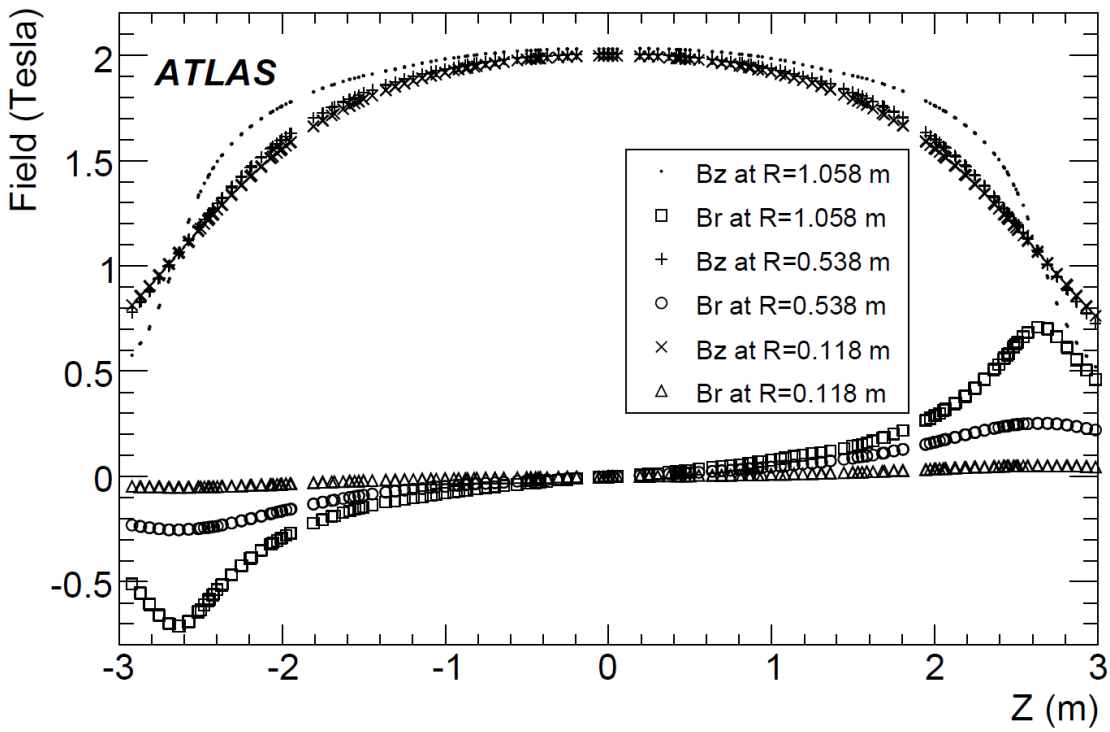

Figure 2.19: Graph showing measurements of the magnetic field axial and radial components in the central solenoid at different radial positions as a function of the axial distance. The data points show the non-uniformity of the field as one moves away from the center of the solenoid. Figure 2 from [17].

a collision rate of 40 MHz for a bunch crossing every 25 ns. At a design luminosity of 10^{34} $cm^{-2}s^{-1}$, the average number of pile-up events at each crossing would be about 23, resulting in a total interaction rate of ∼1 GHz. It would be completely infeasible to read out all the information from all the detectors at this time scale and then write that information into a data storage big enough to handle this rate of data-taking for years. Fortunately, most of these interactions are QCD events which are not prioritized from a trigger or physics perspective on ATLAS. It is the responsibility of the trigger system to filter out these events and reduce the rate down from ∼1 GHz to a read out rate of ∼100 Hz of only potentially interesting events. A diagram depicting the trigger system can be seen in figure 2.21 and is described in the following paragraphs.

The first trigger level (L1) is a hardware trigger that selects events based on coarse calorimeter and muon spectrometer information. For muon identification, only the RPC and TGC trigger chambers are utilized. In the case of the calorimeter, a subset of the detectors using a coarse granularity is used to look for high p_T electrons, photons, jets, taus, missing and total transverse energy. These triggering subsystems send results to the Central Trigger Processor (CTP) and the CTP makes a decision whether to keep the event. If the CTP decides that there is an event of interest it sends out an *L1 accept* signal to the front-end electronic systems of all the detectors in order to hold on to the event information. The

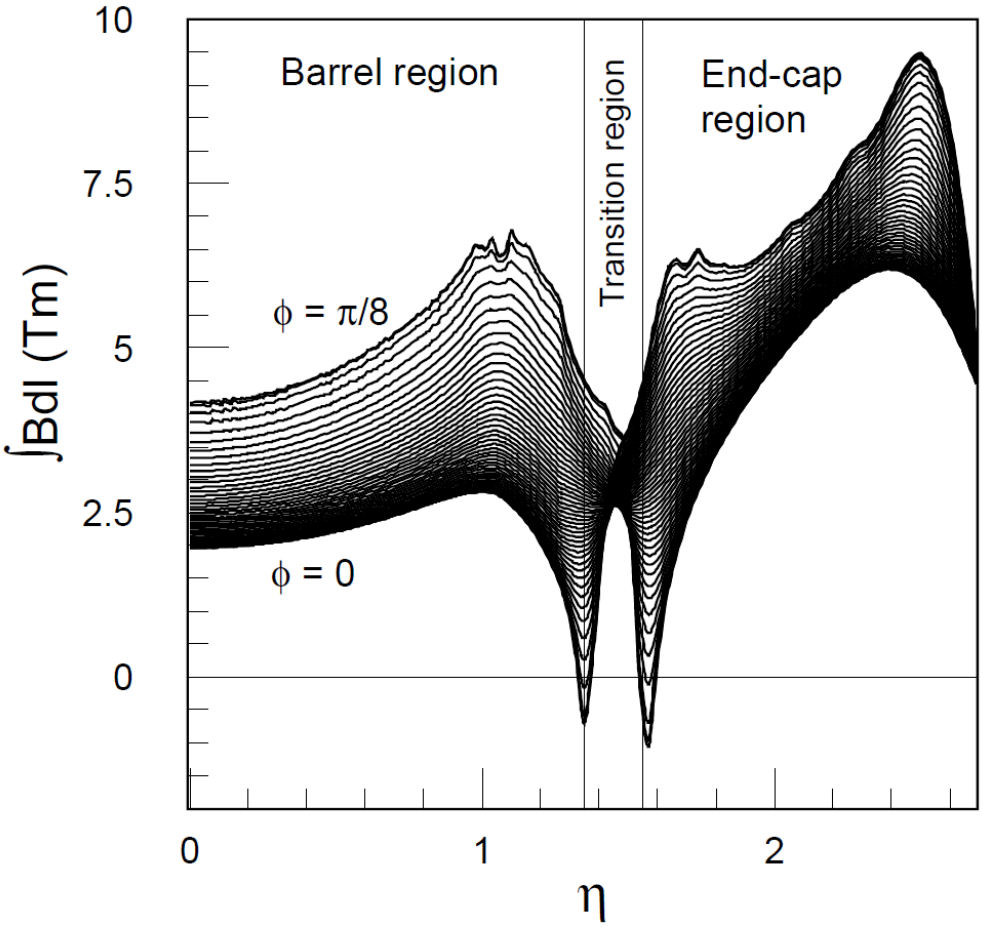

Figure 2.20: The toroid bending power of the azimuthal magnetic field component as a function of η. The curves correspond to azimuthal angles equally spaced between the barrel and endcap toroids. The transition region is where the barrel and endcap fields overlap. Figure 1.5 from [16].

highest rate at which the front-end systems can accept a L1 trigger is estimated at 75 kHZ, thus dictating the raw rate reduction required by the L1 trigger. In addition, the time it takes for a pp collision to occur and a trigger decision to reach all the front-end systems has to be less than 2.5 μs in order to make sure that the event of interest can be read out[18].

Events passing the L1 trigger have the data from the front-end systems read out into readout drivers (RODs) and then into readout buffers (ROBs). Data is held there until the second trigger level (L2) either accepts or rejects the event. The L2 trigger is a software trigger that utilizes region-of-interest[7] (RoI) information given to it by the L1 trigger to make a decision. The L2 trigger has access to the full event data, but generally will make a decision only considering the designated RoIs by only unpacking the full data for a small section in η and ϕ around each RoI. This has an intrinsic advantage that the L2 trigger will

[7]The trigger only looks at detector elements related to the region in which the L1 trigger was fired and makes its division using this limited information

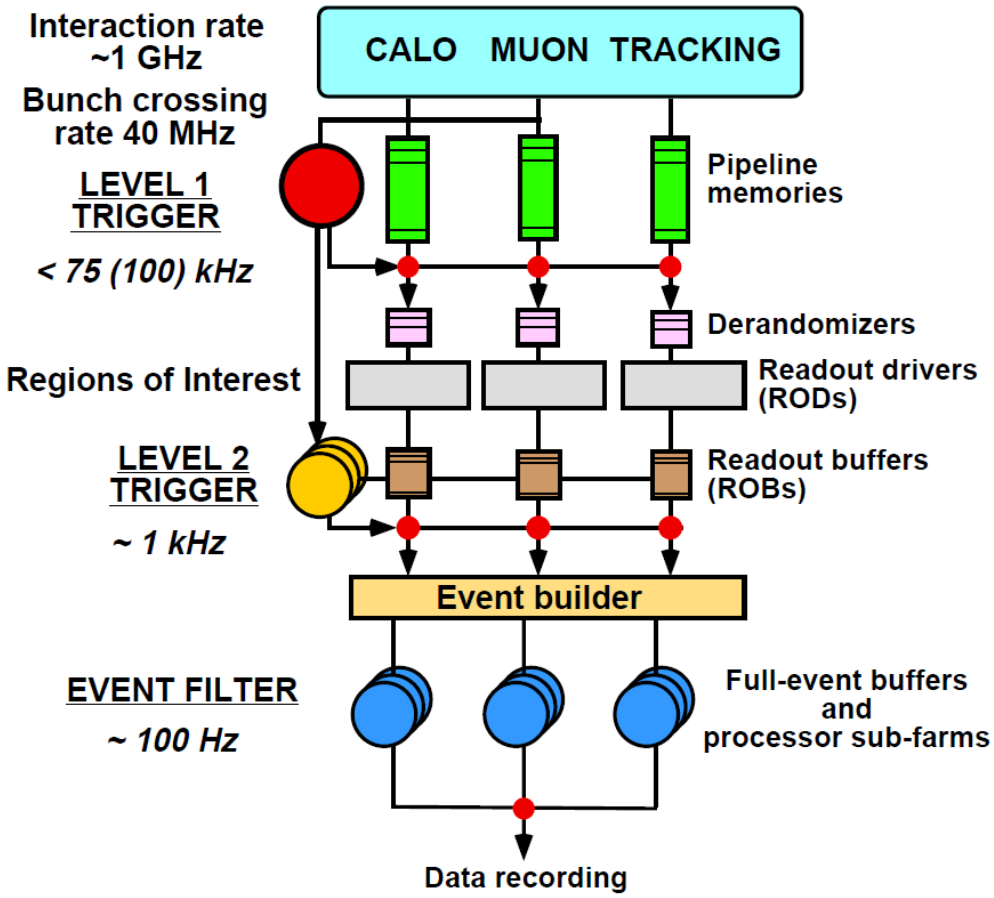

Figure 2.21: Diagram of the ATLAS three level trigger/DAQ system depicting how the interaction rate is reduced to readout rate of $\sim 10^2$. Figure from [18].

only look at roughly a few percent of the full event and therefore can save valuable time. The L2 trigger reduces the rate to ∼1 kHz and has a latency in the range of 1-40 ms.

If an event passes the L2 trigger, the data enters the event builder which merges all the data fragments from the subsystems into one unique full event that gets passed to the final trigger layer, the event filter (EF). The EF uses adapted up-to-date offline reconstruction algorithms to make the final selection on the event. Upon passing this final selection the event is written to mass storage for later offline analysis. The final rate is $\sim$ 100 Hz which corresponds to $\sim$ 100 MB/s of recorded data. The latency at the EF level is about 4 seconds due to the fact that the event has to go through the event-building process.

2.4 Data Acquisition

Events that pass the trigger system are recorded as data in short data-taking periods called *runs*, which usually last a few hours. Each *run* is further split into Luminosity Blocks (LBs) that last for approximately one minute. The luminosity blocks represent a time interval

where all detector and accelerator elements are taken to be fixed which is helpful for offline (post-*runs*) data quality assessments.

A collection of runs represent a data *period* and periods represent a time period when the detector configuration and trigger system are unchanged. A list of the data periods with a summary depicting the differences between each are shown in table 2.5.

Period	Description	$\mathcal{L}_{Max}$ [10^{30} cm^{-2}s^{-1}]	$\langle\mu\rangle_{Max}$
D	50 ns Bunch trains	659	7.3
E	LAr Hole	832	7.6
F	After technical stop	1100	8
G	New trigger cache	1263	7.9
H	Fixed L1 muon trigger	1264	6.8
I	After TS; Partial fix of LAr	1887	9.1
J	Increased beam current; New trigger menus	1995	9.6
K	New trigger menus	2328	11
L	New trigger menus	3252	16
M	No special features	3848	32

Table 2.5: Table of the ten data periods used in this analysis. A short description is shown depicting the differences between each period and the previous one. The maximum instantaneous luminosity, $\mathcal{L}_{Max}$, and maximum average number of interactions per crossing, $\langle\mu\rangle_{Max}$, are also shown. TS stands for technical stop.

Chapter 3

Event Reconstruction

This chapter describes the basic particle reconstruction and identification methods used by ATLAS to interpret the measurements done by the detector subsystems described in Chapter 2. The goal is to take these individual measurements and associate them to objects that can be used for physics analyses. This first involves taking the charge particle hits from the Inner Detector (ID) and building tracks describing their trajectories. Then extrapolating those tracks to common vertices or points of collision. Clusters of energy deposited in the calorimeters are reconstructed into electrons, photons, and jets with the electrons matched with tracks in the ID. Finally hits in the Muon Spectrometer (MS) can be matched with tracks in the ID to identify potential muons.

3.1 Tracks

The reconstruction of tracks describing a charged particle's trajectory through the detector is one of the first stages of event reconstruction. It can be divided into two main sequences or series of algorithms, the first being an inside-out track reconstruction approach and then a subsequent outside-in approach [72]. For the inside-out track reconstruction, three-dimensional space points are first created using hits in the pixel and SCT detectors. In the case of the pixel detector this is quite simple due to the two-dimensional measurements given from individual pixels and the use of the pixel's known surface relative to the beam pipe to set the third dimension. For the SCT, space point objects are constructed using pairs of silicon modules which are laid directly on top of each other and are separated by a stereo angle to get the initial two dimensions.

Using a z vertex constraint[1], track seeds are identified by utilizing space points in the pixel detector which are matched depending on compatible momentum and transverse impact measurements. These track seeds, which consist of two to three pixel hits are then extrapolated to the SCT. Using a Kalman filter formalism [73], the track fitting algorithm continually adds potential ID hits to different track seeds and recalculates the covariance matrix and χ^2, updating and throwing away outliers until it progressively constructs a track across the pixel and SCT layers. Due to the high number of track candidates that are produced at this point, it is important to distinguish between real and fake particle tracks, which

[1] Constrained to a particular value along the z-axis (beam direction)

may be incomplete or share detector hits. An ambiguity processor algorithm is employed that uses a track scoring strategy to score individual tracks and rank them based on a set grading rubric [74]. Tracks passing minimum quality requirements are then extended to the TRT where the iterative fitting and re-scoring process is repeated.

Due to a potential for some tracks to be missed, an outside-in track reconstruction approach is also necessary. The inside-out approach relies on a track seeds being found in the pixel detector, but this can be an issue for tracks coming from secondary decay vertices or photon conversions that may only be present in ID layers further from the interaction point. In addition, the ambiguity processor may have incorrectly rejected the initial track seed or substantial energy loss in the ID may have caused incorrect track building in the SCT and TRT. The outside-in approach instead creates track segments in the TRT and then back-tracks into the SCT and pixel subsystems. The hits in the TRT can not be reconstructed in three dimensions, so tracks segments are reconstructed based on hits (constructed using the straw centers) being projected in the r-ϕ plane in the TRT barrel and r-z plane in the TRT endcaps. Particle tracks with a transverse momentum of greater than 500 MeV appear in the TRT as roughly straight lines and using a Hough Transform [75] these hits can be parameterized and clustered into lines that satisfy the same intial azimuthal angle ϕ_0 and inverse momentum parameter c_T, along different slices of η. At which point, it is possible to find the local maximum in the resulting two dimensional histogram to extract the hits associated to the same tracks. These tracks are then refitted using the TRT drift time information and a Kalman filter-smoothing formalism to get a collection of track segments. Segments that were used in the initial inside-out approach are removed from the collection in order to save CPU time and then a iterative re-fitting and re-scoring process is done to extrapolate the remaining TRT track segments into the SCT and pixel subsystems.

3.2 Vertices

The tracks built in the previous section are used to construct common vertices or points of collisions. Due to the high instantaneous luminosity, the average number of collisions in any given bunch crossing is quite high, resulting in a significant amount of additional interactions[2] and therefore vertices that need to be reconstructed. For this analysis and in general, the primary vertex is the vertex with the largest sum of track transverse momenta, $\sum p_T^2$, associated with it. Furthermore, secondary vertices that are displaced along the transverse direction are important in determining hadronic jets originating from b quark decays and other displaced particle decays. Figure 3.1 shows the average number of interactions per bunch crossing in the 2011 ($\sqrt{s}$ = 7 TeV) dataset. Figure 3.2 shows the average number of reconstructed vertices as a function of the average number of inelastic pp interactions per bunch crossing, μ. For this 2011 analysis, we have a $\langle\mu\rangle = 9.1$ which corresponds to reconstructing an average of five vertices per recorded event.

ATLAS uses the AdaptiveMultiVertexFinder (AMVF) algorithm, a 'finding-through-fitting' approach, for identifying and reconstructing primary vertices [76]. This approach starts by first associating a set of tracks believed to come from the interaction region into

[2]Additional interactions other than from the hard scattering process are called *pile-up*, a description of pile-up can be found in section 4.2.1.

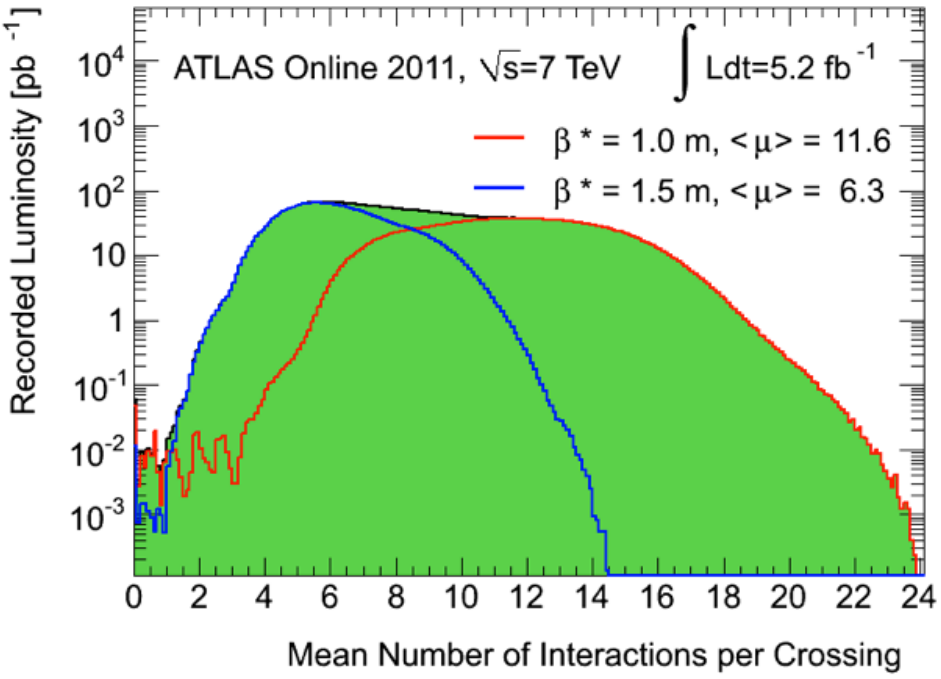

Figure 3.1: Shows the luminosity weighted distributions of the mean number of pp interactions per crossing for the full 2011 data. The red and blue lines represent when the β^* paramter was changed from 1.5 m to 1.0 m during the technical stop between periods E and F. β^* is a beam parameter that represents the amplitude function of the beam at the interaction point, a smaller β^* is equated with a more focused beam. Figure from [19].

a single vertex. Each track in the vertex is then fitted using an adaptive multi-vertex fitter and any outliers are discarded to form a second vertex. At this point the fitter is ran again simultaneously on the two vertices, using any outlier tracks to form additional vertices that compete to associate tracks to them. This process continues until a complete set of vertices are reconstructed for the event. The vertex resolution depends on the number of tracks associated to it and is 10-12 (35-55) μm in the transverse (longitudinal) direction.

3.3 Electrons

Electrons are identified in the detector by a narrow clustered energy deposition in the EM calorimeter coming from the interaction point and an associated track in the inner detector pointing to the cluster. In addition, high threshold hits in the TRT signify transition radiation photons which come from charged particles passing through the TRT and can be calibrated for electrons. There are three algorithms used by ATLAS to cluster calorimeter cells and reconstruct electrons. The main one uses a sliding window algorithm [77] which is seeded by clusters in the EM calorimeter and is used for high-pt isolated electrons. The second algorithm uses a track-based seeding from the ID and is used to identify low p_T

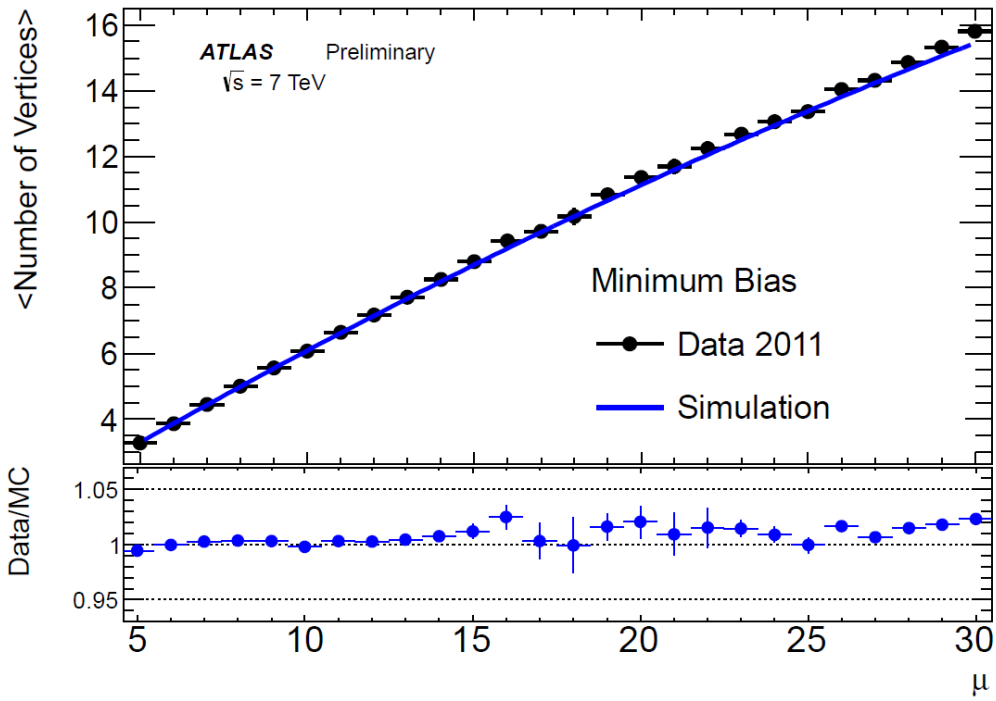

Figure 3.2: Figure shows the average number of vertices reconstructed as a function of the average number of pp interactions per bunch crossing, μ, for the 2011 data run. Figure from [20].

electrons and electrons in jets. The last algorithm reconstructs electrons in the forward region where only the forward calorimeter information is available and is beyond the scope of this analysis.

The sliding window algorithm first starts by building calorimeter towers with $\Delta\eta \times \Delta\phi$ sizes equal to 0.025×0.025 based on the middle EM calorimeter layer's granularity. These towers extend in the longitudinal direction encompassing all the EM calorimeter layers within the given tower size. EM cells that fall in between towers have their energy depositions shared between towers depending on their relative volume occupying each tower. A fixed sliding window of tower size 3×5 (or 0.075×0.125) is used to locate preliminary seed clusters with a local maximum in transverse energy that is above an E_T threshold of 2.5 GeV [78]. Seed clusters that overlap go through a set of energy comparisons and the less likely cluster is removed from the seed cluster collection. The middle calorimeter layer of each cluster is then matched to tracks in the ID, where a given track must fall within a $\Delta\eta < 0.05$ and $\Delta\phi < 0.1(0.5)$ of a given cluster seed. The 0.1 looser requirement in $\Delta\phi$ is used for the side of the track in which the electron is bending to account for bremsstrahlung energy losses. For tracks only present in the TRT, only the ϕ is used for matching. In the case of multiple tracks pointing to the same cluster, the track in which the $\Delta R(track, cluster) = \sqrt{\Delta\eta^2 + \Delta\phi^2}$ is smallest is used. Any seed clusters that are matched to tracks are considered electron candidates and their cluster size is recomputed to an optimized value of $3 \times 7(5 \times 5)$ towers in the barrel (endcap) with the initial seed constituting a portion of the new cluster. Finally, the

four momentum of the electron candidate is calculated using the combined track momentum and cluster energy of the candidate. The electron energy scale has been calibrated using the known Z boson mass.

The track-based electron reconstruction is used to find low p_T electrons. The tracks must fulfill several quality cuts and have hits in all three layers of the ID. Tracks are then matched to 3×7 clusters in the middle EM layer and an overlap removal between these clusters is performed. In the case of an electron being reconstructed by both algorithms, the cluster-based algorithm is used by default.

These reconstruction algorithms are designed to have a high acceptance rate for electrons, but are poor in rejecting backgrounds like photon conversions and low p_T electron-like jets. To be able to identify electrons coming from the primary interaction, a set of three baseline identification cuts have been developed that provide good signal to background separation. These set of cuts are labeled as *Loose++*, *Medium++*, and *Tight++* where the '++' is used to separate the selections from what was recommended in the previous 2010 dataset. A list and description of all the electron quality variables [78] is shown below and table 3.1 lists the different requirements for each selection.

- R_{had1}, R_{had} : Ratio of the E_T in the hadronic calorimeter to the E_T of the EM cluster. R_{had} is used over the η range $0.8 < |\eta| < 1.37$. R_{had1} is used over the η range $0.8 < |\eta| > 1.37$ and only considers the first layer of the hadronic calorimeter.[1]
- R_{η} : The ratio in η of cell energies from using a 3×7 tower cluster versus 7×7 tower cluster.[1]
- $\omega_{\eta 2}$: Lateral width of the shower.
- $\omega_{s,tot}$: Total shower width.
- E_{ratio} : The ratio of the energy difference associated with the largest and second largest energy deposit over their sum.
- N_{blayer} : Number of track hits in the b-layer of the pixel detector.
- N_{pixels} : Number of track hits in the pixel detector.
- N_{pixSCT} : Number of track hits in the pixel and SCT detector.
- N_{TRT} : Number of track hits in the TRT.
- R_{htTRT} : The ratio of the number of high-threshold hits to the total number of hits in the TRT.
- d_0 : Transverse impact parameter of the matched track.
- $\Delta\eta_1$: $\Delta\eta$ between the cluster and the matched track.

[1]Shower shape and scale variables that are used in the *Loose++* and *Medium++* criteria are used as inputs into a multi-variate analysis program in bins of η and E_T in order to take into account correlations between variables and determine if the electron candidate is likely to be real. Therefore these variable do not have explicit cuts listed in the table [78].

- $\Delta\phi_2$: $\Delta\phi$ between the cluster and the matched track.
- E/p : Ratio of the cluster energy to the track momentum.
- $Conversions$: Electron candidates which match to reconstructed photon conversions.

Loose++
Detector Acceptance, $\|\eta\| < 2.47$
Shower Properties : R_{had1}, R_{had}, R_{η}, $\omega_{\eta 2}$[1]
Medium++
Includes Loose++
Shower Properties : $\omega_{s,tot}$ and E_{ratio}[1]
Track Quality: $N_{pixels} \geq 1$, $N_{pixSCT} \geq 7$, $d_0 < 5mm$, and $\Delta\eta_1 < 0.01$
Tight++
Includes Medium++
Track Quality: $N_{blayer} \geq 1$, $\Delta\phi_2 < 0.02$, E/p, $\Delta\eta_1 < 0.005$, $d_0 < 1mm$
TRT : N_{TRT} and R_{htTRT}
Pass Conversion

Table 3.1: Definitions of the three main selection criterias for electron identification used to reconstruct electron candidates in the ATLAS experiment.

3.4 Muons

Muon reconstruction is done using both the ID and MS tracking information to identify potential muons that are produced from the interaction point or secondary vertices from decays. Tracks in the MS are identified using a 'standalone' muon algorithm and extrapolated backwards into the ID and then combined to form the complete muon object. For this analysis the combined muon reconstruction algorithm used is called Staco.

The standalone tracking algorithm called "Muonboy" is used to construct the particle tracks in the MS [79]. The algorithm looks at regions of interest designated by the muon trigger chambers and uses an outside-in iterative fitting approach similar to the track reconstruction in the ID to produce track candidates. The fits use the available magnetic field, material and hit information to construct the tracks and extrapolate them back to the interaction point taking into consideration energy losses from the calorimeter material. The particle track trajectories are represented by these five track fit variables: impart parameters (d_0 and z_0), charge inverse momentum (q/p), and the track angles (ϕ and η).

The combined tracking algorithm Staco uses the standalone tracks produced by Muonboy and extrapolates them to the track candidates already reconstructed in the ID, described in section 3.1. The two sets of tracks are combined using a statistical combination that utilizes

the five track fit parameters and their covariance matrices [80]. For two separate tracks in the ID and MS we can define each a vector, P_{ID} and P_{MS}, containing their five track parameters and a covariance matrix, C_{ID} and C_{MS}, respectively. The combined parameter vector of both tracks, P, and covariance matrix C can be described by equations 3.1 and 3.2. The χ^2_{match} of these combined tracks can be defined as in equation 3.3. Each MS track candidate is combined with all ID tracks within a crude η and ϕ window. The tracks which have the lowest χ^2_{match} are kept as muon candidates assuming they pass a minimum cut (of $\chi^2_{match} < 30$).

$$(C_{ID}^{-1} + C_{MS}^{-1}) \times P = C_{ID}^{-1} \times P_{ID} + C_{MS}^{-1} \times P_{MS} \tag{3.1}$$

$$C = (C_{ID}^{-1} + C_{MS}^{-1})^{-1} \tag{3.2}$$

$$\chi^2_{match} = (P_{ID} - P_{MS})^T (C_{ID} + C_{MS})^{-1} (P_{ID} - P_{MS}) \tag{3.3}$$

3.5 Jets

Jet reconstruction is a more complicated process when compared to the other objects that are reconstructed in an event. Due to jets not being fundamental particles, but rather a collection of different hadrons and leptons, the ability to calibrate and understand the inner-complexities of a jet are somewhat limited by the fact that a subset of jets may have very different internal properties (e.g. gluon-jet vs quark-jet), but physicists as observers are mostly only able to see the final outcome of the hadronization process. From the perspective of the detector, a jet is observed by energy deposited in both the EM and hadronic calorimeters with ID tracks pointing towards the respective calorimeter cells. Unlike electrons, the hadronic shower of particles from jets can penetrate into the hadronic calorimeter and the shower shape itself is broader when compared to electrons due to the longer radiation length.

The reconstruction of jets begins by first clustering the energy deposited in the calorimeter cells using topological clusters. Unlike the tower clusters used for electrons which combines the energy from all cells along the same longitudinal direction, topological clusters are built by following the hadronic shower development on a cell-by-cell basis, and thus form dynamic three-dimensional objects. The clustering algorithm starts by first searching for seed cells in which the signal-to-noise (S/N) ratio is greater than 4 [22, 81, 82]. The noise is determined by the RMS of the cell's energy distribution for a random sampling of events. Once a cluster seed has been found, all neighboring cells, including neighbors of neighbors, with a $|S/N| > 2$ are added to the cluster. Then all nearest-neighbor cells surrounding the current cluster regardless of S/N are added to the topological cluster. At this point the clusters go through a splitting algorithm in which any local maxima in the cluster are used as seeds for their own topological clusters. Energy deposits in the shared cells are distributed among these overlapping topological clusters depending on the cluster energy and each cell's distance to the cluster cell containing the local maximum. Each topological cluster is defined to have zero mass and the reconstructed direction is based on a weighted average of the ϕ and η components of the included cells.

These topological clusters are used as inputs for jet finding algorithms. For this analysis, the anti-k_T [21] jet algorithm is implemented and is the default sequential recombination jet finder algorithm used by ATLAS. The algorithm is defined by two distance equations, d_{ij} (Eqn. 3.4) and d_i (Eqn. 3.5),

$$d_{ij} = min(k_{t,i}^{-2}, k_{t,j}^{-2})\frac{\Delta_{ij}^2}{R^2} \tag{3.4}$$

$$d_i = k_{t,i}^{-2} \tag{3.5}$$

where $\Delta_{ij}^2 = (\eta_i - \eta_j)^2 + (\phi_i - \phi_j)^2$ and $k_{t,i}$ is the transverse momentum of the ith object or input. The parameter R is analogous to the cone size of the jet being reconstructed and for this analysis, an $R = 0.4$ is used. The algorithm works by calculating all the distances, d_{ij} and d_i, between all individual inputs that went into the algorithm. If the minimum distance, $d_{min} = min(d_{ij}, d_i)$, was found to come from a d_{ij} calculation then the ith and jth object used to compute d_{min} are merged into one object (see equations 3.6 - 3.8) and d_{min} is recalculated using the newly merged object instead of the ith and jth object.

$$k_{t,k} = k_{t,i} + k_{t,j} \tag{3.6}$$

$$\eta_k = [k_{t,i}\eta_i + k_{t,j}\eta_j]/k_{t,k} \tag{3.7}$$

$$\phi_k = [k_{t,i}\phi_i + k_{t,j}\phi_j]/k_{t,k} \tag{3.8}$$

If d_{min} is calculated from a d_i value, then the ith object can not be merged anymore and therefore is removed from the list of inputs and is labeled as a jet. The algorithm keeps repeating this process until there are no more objects in the list of inputs. An example result of this iterative process can be seen in figure 3.3 in which an R=1 value is used. Due to the anti-k_T algorithm's dependence on k_t^{-2}, it is able to mostly ignore the effect of soft particles when it comes to their influence on the shape of the jet boundary that is being reconstructed, while other hard particles that are reconstructed as separate jets can still influence the jet boundaries of neighboring jets. This results in anti-k_T jets being very cone-like regardless of soft radiation, the shape of the jet is only strongly modified when nearby hard particles overlap with each other.

The jets that have been reconstructed are built using electromagnetic calibrated measurements from the calorimeter or what is defined as the EM scale. The true jet energy is different due to hadrons from jets having a lower detector response when compared to EM showers. A Jet Energy Scale (JES) calibration scheme is therefore necessary to bring the reconstructed jet energies closer to their true values. The JES calibration [22] is applied to the jets in four steps using a combination of corrections derived from both data and Monte Carlo[3] (MC).

The first correction is due to the pile-up offset, the correction is derived from MC and is based on the energy offset in the detector caused by additional energy deposited in the

[3]MC are generated events that have been run through a detector simulation and are discussed in detail in Chapter 4.

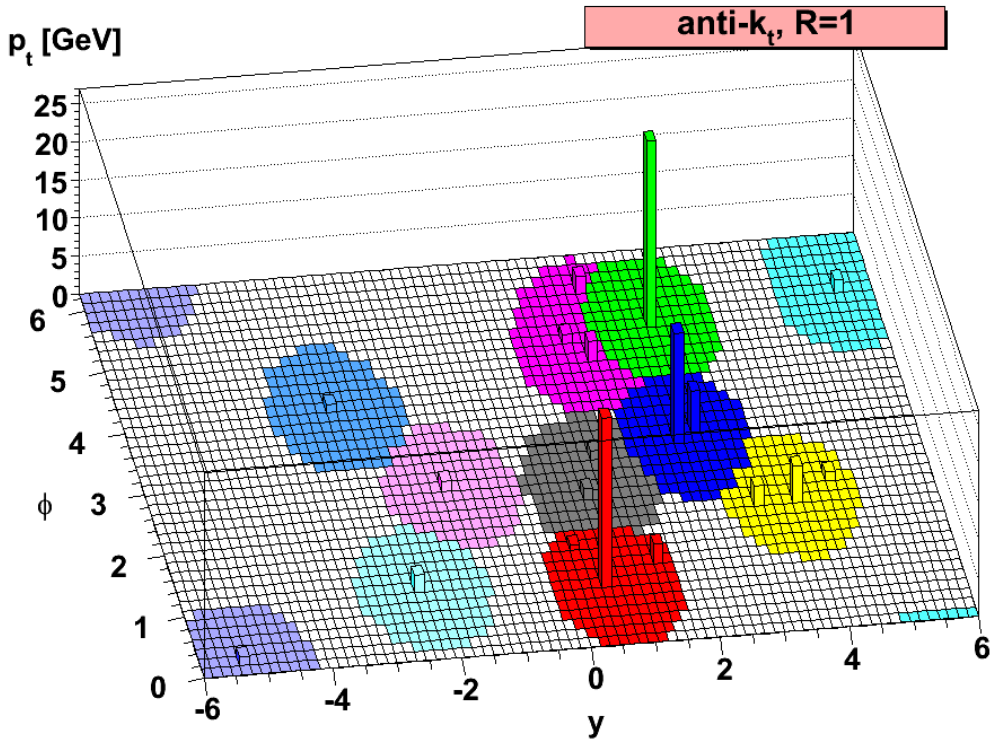

Figure 3.3: Simulation of an event's jet reconstruction using the anti-k_T jet algorithm with an R value of 1. Each solid color designates a unique jet from by the reconstruction algorithm. The jets found by the anti-k_T algorithm are generally centered around an energy peak and are conical in shape. Figure from [21].

calorimeter by minimum bias events. The correction is calculated as a function of the number of reconstructed primary vertices and the expected average number of interactions per event in bins of η and the transverse momentum of the jet. The next correction changes the jet direction to point to the primary vertex instead of the center of the ATLAS detector, there are no changes done to the jet energy. Next, the jet energy is scaled to the true jet energy which is derived from MC as a function of the reconstructed jet energy and η. Lastly, residual in situ derived corrections from comparing data to MC are used to finish correcting the jets to the jet energy scale. The different components of this JES correction scheme are discussed further in chapter 7, where the JES systematics are discussed in more detail.

For the derivation of the missing transverse energy (E_T^{miss}) described in the next section, this analysis also uses jets in which the initial topological clusters are first calibrated using a local cluster weighting (LCW) scheme. The LCW method improves on the initial EM scale clusters, by reducing the fluctuations due to the calorimeters non-compensation[4] to hadronic showers. LCW classifies clusters as either hadronic or EM depending on the energy density

[4]Non-compensation refers to the different detector response the calorimeter has between photons and hadrons.

and longitudinal shower depth of the cluster and then applies MC corrections accordingly to each cluster. These LCW scaled clusters are used as inputs into the anti-k_T algorithm and then are calibrated to the same JES scale as jets derived from topological clusters. In effect it supplies inputs into the jet algorithm that are more consistent with the true jet produced in the event and thus provides for a more accurate basis for the jet reconstruction.

3.6 Missing Transverse Energy

The Missing Transverse Energy(E_T^{miss}) in the event is a depiction of the energy that escaped the detector undetected. In this analysis, it is in direct reference to the single neutrino produced when the W boson decays leptonically. The E_T^{miss} is reconstructed by the negative transverse vector sum of all energy contributions recorded by the detector in the event.

When the proton beams collide in the interaction point there is no transverse component to the initial incoming particles, therefore conservation of momentum dictates that the total transverse momentum of the system after the collision should still be equal to zero. In order to use this conservation law it is necessary to contain as much of the event as possible in the detector and this is done by utilizing calorimeters that extend out to $|\eta| < 4.9$ and providing full ϕ coverage over the collision point.

The E_T^{miss} algorithm used for this analysis is MET_refFinal [83] and is built using all the objects discussed previously in this chapter and additionally reconstructed photons and taus. The contributions to the E_T^{miss} can be broken down into

$$MET = MET^{Electrons} + MET^{Jets} + MET^{Photons} + MET^{Taus} + MET^{Muons} + MET^{Soft} \quad (3.9)$$

The algorithm loops over all objects (leptons within $|\eta| < 2.7$ and jets within $|\eta| < 4.9$) and iterates over their individual calorimeter cells, applying weights to add/remove corrections to the given object and accounting for calorimeter cells that overlap among physics objects to avoid any double counting. For jets, the cluster cells used for the building of the E_T^{miss} have the LCW scheme applied. Calorimeter cells that were not assigned to physics objects during reconstruction within $|\eta| < 4.5$ are also added as the MET^{Soft} contribution. The sum of all these contributions is the E_T^{miss} .

Chapter 4

MC Event Generation

In order to perform measurements using particle detectors it is important to model correctly the results measured from the recorded data. In general there are two analysis approaches taken by physicists to understand the data, usually both are employed in tandem within the same analysis, that is to model data processes using Monte Carlo (MC) event generation methods or to use data-driven[1] techniques to reproduce the data. This chapter will concentrate on the former.

MC event generation is the generation of data-like events using the probabilistic nature of particle interactions in order to model and predict a large range of physics processes. MC utilizes the abundance of current knowledge we have about particle physics and varies the parameters in a given process based on the current uncertainties related to it. Two important points to make here is that due to the statistical nature of MC it is possible, with enough computing power, to generate an over-abundance of events making it possible to have much more statistics than the data sample that is being modeled. This leads to the second point, that MC generation is a iterative process. Since MC events can in principle be only systematically limited, data driven approaches can be utilized to understand if the MC models predict the data appropriately and, if not, additional corrections can be done to improve on the data-MC agreement. These MC corrections can be applied during the production of new MC samples or post-production as will be discussed in section 4.4.

MC generators, discussed in the following section 4.1, produce events starting from the pp interaction all the way to the final state particles. These final state particles then pass through a simulation of the ATLAS detector, discussed in section 4.2, resulting in a detector-level output of the event that looks identical to the readout given by the detector during data-taking. Finally the events are reconstructed utilizing the same reconstruction algorithms as were described for data in chapter 3 and any MC corrections, described in section 4.4, are applied to the MC events.

[1]Data-driven is a general-term, but put simply it the utilization of the data to constrain a driven physics process that can be used later on for a given measurement

4.1 MC Generators

The main task of MC generators is the evaluation of the pp cross section (shown in equation 1.25) for a particular hard scattering process. This integral is dependent on the proton's PDF used, the factorization/renormalization scale, and the partonic cross section calculation (i.e. leading-order (LO), next-to-leading order (NLO), etc) that describes the hard scattering process using perturbative QCD. In addition, the generators can model the underlying event[2] (UE), initial/final state radiation, parton showering (fragmentation), hadronization, and the final state decays of the particles. Other than a few general purpose MC generators that can do all of these things listed above, most MC programs specialize on a particular aspect of the MC generation and then interface with another MC program to provide the missing parts. Several generators for example just perform the matrix element (ME) calculations used to determine the hard process cross section and then pass their results to another generator to complete the parton showering and UE.

The final output in this event generation chain is in the form of particle collections with their accompanying four vectors. These MC samples are denoted as event generation only or *truth* samples. In regards to this analysis, the definition of the fiducial cross section is calculated using the truth information in the MC samples and some systematics (W/Z+jets modeling) utilize or are evaluated using only the event generation level information. This is acceptable when the systematic being evaluated are not adversely affected when going from the truth information to the fully reconstructed event.

Since several of the event generation steps require theoretical inputs and computational cutoffs in the calculations, the algorithms used to model collisions can be inherently different between generators. In general, the MC generator that models a given process the best when compared to data is chosen and systematics are evaluated by varying the input parameters of that MC generator and/or comparing the results with other generators. The remainder of this section will go over the general characteristics of the different MC generators used in this analysis to produce MC samples.

PYTHIA

PYTHIA [84] is a general purpose MC generator that models the hard scattering, parton showering, UE, hadronization and subsequent decays. PYTHIA contains a LO subprocess library that contains hundreds of $2 \to n$ subprocesses, where n is 1, 2, or 3. Unstable decays coming from final state particles of each subprocess include full spin correlations. Final State Radiation (FSR) from partonic processes are accurate to leading-log and are evolved forward in time using a decreasing time-like virtuality depending on the mass of the parent particle. Initial State Radiation (ISR) is backwards evolved in time from the hard scattering and uses a decreasing Q^2 ordering to dictate the showering. The UE is modeled with perturbation theory using $2 \to 2$ scatterings and has a cutoff at the order of 2 GeV. The Lund string model [85, 86] is used to model the hadronization and subsequent decays.

[2] Additional soft interactions that are not part of the hard scattering.

HERWIG

HERWIG [87] is a general purpose MC generator that like PYTHIA models the hard scattering, parton showering, UE, hadronization and subsequent decays. The decays from unstable resonances includes the full spin correlations. The parton showering in HERWIG is ordered based on the parent particle's energy and the angle of emission. The UE is modeled using a minimum bias pp event generator, and an external package named JIMMY [88] is interfaced to HERWIG and used to simulate the multiple scattering interactions in the UE. The hadronization is performed using a cluster hadronization model based on the color pre-confinement property of the parton shower.

ALPGEN

ALPGEN [89] is a matrix element generator that calculates exact LO partonic MEs. Its emphasis is on producing MEs for collisions with final states containing large parton/jet multiplicities. Spin correlations in top quark and gauge bosons are also taken into account. ALPGEN is generally interfaced with HERWIG or PYTHIA in order to provide the parton showering and hadronization of the events.

ACERMC

ACERMC [90] is a tree-level ME generator like ALPGEN that is used for a small selection of background processes in pp collisions. The advantage of ACERMC is that it provides fast and efficient event generation that can be interfaced with either PYTHIA or HERWIG.

MC@NLO

MC@NLO [38] is a NLO ME generator which provides higher precision in the cross section measurement and modeling of the hard subprocesses. MC@NLO is interfaced to HERWIG to provide showering and hadronization. MC@NLO applies a negative weight to some events in order to subtract the contribution of the NLO estimations done during the parton showering of the interfaced generator.

4.2 Detector Simulation

For MC samples, the ATLAS detector's response to traversing particles or particle interactions with the detector is simulated using the GEANT4 [91] software toolkit. Output of the MC generators in the form of particle collections are provided to GEANT4, which simulates the passage of those particles through the detector material using a MC statistical method to calculate interactions with said material. GEANT4 contains a digital map of the ATLAS detector geometry, including any subsystem misalignments, read-out electronics, cables, and dead material. Particles moving through the simulated detector in steps will take into account interactions with the magnetic field, ionization/showering of new particles, and energy depositions into the sensitive detector material, or hits. All hits are later digitized and

recorded in the same format as would be read out from the detector during data-taking and are subsequently passed through the event reconstruction algorithms described in chapter 3.

In order to produce the MC statistics necessary for processes that have large cross sections it is essential that large MC samples are produced, thus requiring immense computing times. A typical event simulated with GEANT4 can take from 10 to 50 minutes [92] depending on the process, which quickly leads to a computing bottleneck. To address this issue, several physics processes in this analysis that require a significant amount of statistics have been simulated with the Atlfast-II fast simulation software [93]. Atlfast-II uses the FastCaloSim software package to simulate the calorimeter response of the detector, which constitutes the majority of the GEANT4 processing time during event simulation. FastCaloSim parameterizes the longitudinal and lateral energy profiles of single particle showers that deposit their energy in the calorimeter. The result is a factor of 10 to 30 times faster processing per event, but with the disadvantage of having an intrinsically less accurate representation of the detector. Though less accurate, the MC can be later tuned against data to correct for disagreements.

4.2.1 Pile-up

Pile-up is a general term to describe the multiple interactions within the detector either before or after (denoted as *out-of-time pile-up*), and during (denoted as *in-time pile-up*) the triggered bunch crossing. Out-of-time pile-up is a result of triggered events being readout within a certain time window in order to account for the drift times of particles in the detector. Interactions from neighboring bunch crossings may therefore contaminate a given recorded event. The probability of this grows significantly as the instantaneous luminosity (section 2.3.2) of the accelerator grows.

In-time pile-up is usually the dominant pile-up source and like out-of-time pile-up is predominantly made up of additional minimum bias interactions within the same bunch crossing. Minimum bias interactions are defined by processes that are selected using a loose trigger setup intended to select inelastic collisions with as little bias as possible [94]. In addition, there is a constant cavern background produced from neutrons and photons interacting with the cavern wall and shielding that enters into the events.

In order to simulate this in Monte Carlo, a constant number of events simulating cavern background are added to each Bunch Crossing ID (BCID) dependent on the rate of interaction per bunch crossing,$\langle\mu\rangle$ in the event. Likewise, a number of minimum bias events are added to the hard scatter event randomly selected from a Poisson distribution with a mean of $\langle\mu\rangle$ [95]. The $\langle\mu\rangle$ value is determined from a large range of possible values in order to later reweight each MC event based on the $\langle\mu\rangle$ distribution recorded from the data, see section 4.4.1 for details. Events may be offset from the recorded event times in order to simulate the out-of-time pile-up as well. These pile-up events are added in the digitization step of the event, prior to reconstructing any objects in the event.

Process	Generator	cross section σ (pb) ($\times$ BR)
$W \to \ell\nu$	ALPGEN	$(10.46 \pm 0.42)\times 10^3$ [96]
$Z/\gamma^* \to \ell\ell$ ($m_{\ell\ell} > 40$ GeV)	ALPGEN	$(10.70 \pm 0.54)\times 10^2$ [96]
$Z/\gamma^* \to \ell\ell$ ($10 < m_{\ell\ell} < 40$ GeV)	ALPGEN	3.9×10^3 [96]
$t\bar{t}$	MC@NLO	177^{+10}_{-11}
Single top Wt	MC@NLO	$15.74^{+1.17}_{-1.21}$
Single top s-channel	MC@NLO	$4.63^{+0.20}_{-0.18}$
Single top t-channel	ACERMC	$64.57^{+2.63}_{-1.74}$
WW	MC@NLO	43.7 ± 2.1
WZ	MC@NLO	17.4 ± 1.2
ZZ	HERWIG	5.96 ± 0.3 [26, 38]
$\gamma W \to \gamma\ell\nu(\ell = e, \mu, \tau)$	PYTHIA,MADGRAPH [97]	135.4
Wbb	ALPGEN	723.0
Zbb	ALPGEN	25.8
Wcc	ALPGEN	256.9
Wc	ALPGEN	914.4

Table 4.1: List of generators used to produce the MC samples in this analysis with corresponding cross sections at the center-of-mass energy of $\sqrt{s} = 7$ TeV. Further details about the MC samples used are given in Appendix A.

4.3 Data and Monte Carlo Samples

This section goes into details on all the MC samples used for the analysis, including samples produced and used for the assessment of the systematic uncertainties. Table 4.1 lists the SM processes, their given cross sections, and the generators used to produce their given samples. A more explicit list of the samples with ATLAS sample nomenclature, efficiencies and cross sections can be found in Appendix A.

4.3.1 Diboson Processes: WW, WZ, and ZZ production

The simulation of the signal samples, WW and WZ, are generated with MC@NLO [38], which simulates $q\bar{q} \to WW/WZ$ events using Next-To-Leading Order (NLO) calculations. The CT10 [39] set of parton distribution functions (PDFs) is used to model the initial parton momentums. The subsequent parton showering, hadronization and underlying event are modeled with HERWIG [87] and JIMMY [88]. Additionally, the ZZ samples are generated using HERWIG interfaced with JIMMY with an $m_{ll} > 60$ GeV requirement. The diboson samples are generated to NLO with cross sections of 43.7 $\pm$ 2.1 pb, 17.4 $\pm$ 1.2 pb, and 5.96 $\pm$ 0.3 pb for WW, WZ, and ZZ respectively. The WW and WZ cross section central values are derived using MC@NLO with CT10 PDFs. The ZZ cross section is estimated using MCFM [26] with the MSTW2008NLO [98] PDFs. The uncertainties for the diboson samples are calculated using MCFM by varying independently the factorization and renormalization scales up and down by a factor of 2, and varying the 68% Confidence Level (CL) PDF+α_s uncertainties by one standard deviation using the procedure described in reference [99].

The MC@NLO generator allows for the calculation of aTGC weighting factors to reweight

events based on a particular set aTGC value. In effect, this reweighting scheme allows for the transformation of the SM MC@NLO samples to any sample produced at a particular aTGC value and vice versa. The MC signal samples were produced using two different configurations. The first set of samples were produced using the Standard Model configuration, with no anomalous couplings present. This SM sample, though having high statistics, lacks statistical power in the high energy tails of the kinematic distributions (lepton p_T, $p_{\mathrm{T}}(jj)$, etc), which provide the most sensitivity to anomalous couplings. Therefore, a second set of signal samples were produced at a large aTGC point[3] in order to fill the kinematic tails necessary for setting the aTGC limits. For the nominal SM signal distributions, these aTGC samples are reweighted to the SM and combined with the original SM samples in order to increase the MC statistics. Details on the validation of this reweighting scheme are shown in section 10.3.

Systematic samples for the WW/WZ signal processes are also produced using PYTHIA [84] and HERWIG interfaced with JIMMY. Additionally, event generation only MC@NLO systematic samples have been produced with varying factorization and renormalization scales.

4.3.2 W/Z+jets Processes: W/Z with associated jets production

The W+jets and Z+jets samples are generated using ALPGEN v2.13 [89], with CTEQ6L1 PDFs [100], interfaced to HERWIG v6.510 [87] and JIMMY v4.31 [88]. Each set of MC samples are composed of four exclusive samples each with zero to four additional partons (np with n =0−4) and one inclusive sample with five or more additional partons present in the event. The cross sections for each sample are computed using the ALPGEN cross sections and are scaled such that the sum of the np sample cross sections is equal to the QCD Next-to-Next-to-Leading Order(NNLO) inclusive cross section times branching fraction for a single lepton channel calculated using FEWZ [101]. This equates to a total W$\to \ell\nu$ cross section of 10.46 ± 0.42 nb and a Z/$\gamma^* \to ll$ cross section of 1.070 ± 0.054 nb for a lepton invariant mass of greater than 40 GeV [102, 103]. An additional Drell−Yan Z/$\gamma^* \to ll$ sample is produced for lepton invariant masses between 10 and 40 GeV.

Exclusive samples of W/Z+Heavy Flavor (HF) quarks were also produced with ALPGEN, where charm and bottom quarks are explicitly included in the matrix element calculation. The following samples were produced: Wc+np (n=0−4), Wcc+np (n=0−3),Wbb+np (n=0−3), and Zbb+np (n=0−3). These samples were merged with the existing W/Z+jets nominal samples by first applying a heavy flavor event veto to the nominal samples on any events with additional charm or bottom partons in order to avoid double counting of heavy flavor parton events[4]. The nominal W/Z+jets samples with this veto applied are commonly referred to in this analysis as W/Z+LF jets where LF stands for light flavor.

In addition samples were produced with very high statistics using the Atlfast-II (AFII) simulation software [93] in order to reduce the systematic due to MC statistics in the cross section fit. For this analysis, the distribution shapes derived from these samples are used while the normalization/rate are taken from the Full Simulation (FS) samples. A comparison

[3]The aTGC samples generated correspond to the following aTGC point: $\Delta g_1^Z = -0.3$, $\Delta\kappa^Z = 1.0$, and $\lambda^Z = 0.3$.

[4]The nominal W/Z+jets samples make no distinction between heavy and light flavor partons, therefore heavy flavor partons from the matrix element are included in the nominal samples

of the dijet invariant mass shape between AFII and FS can be seen in figure 4.1 and is shown to have good agreement.

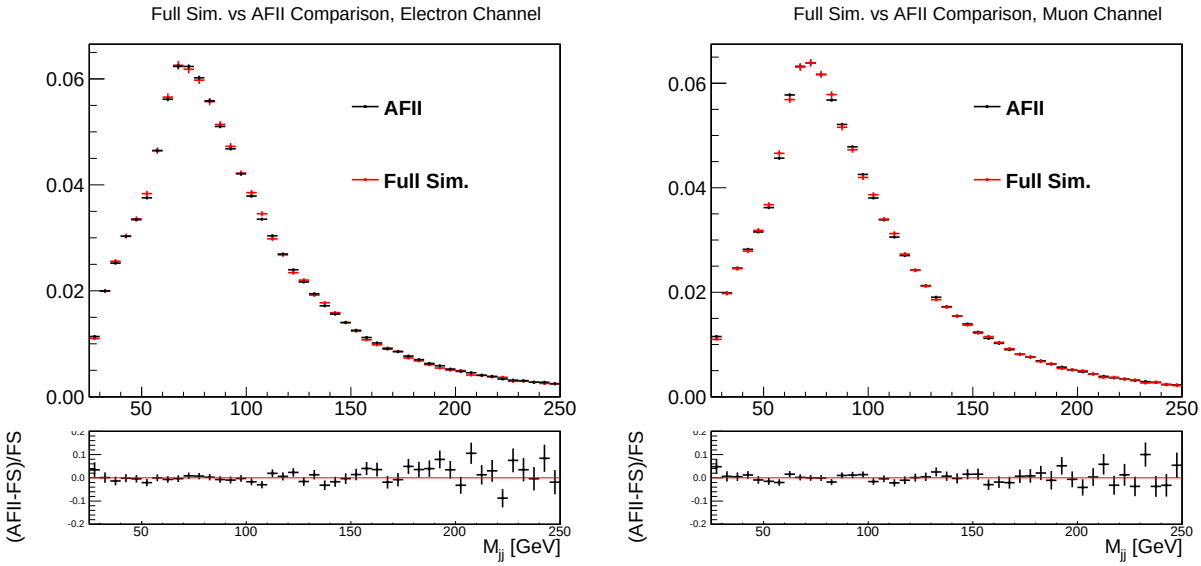

Figure 4.1: Figures show a comparison of the m_{jj} distribution in the electron channel (left) and muon channel (right) between the W/Z+jets distributions using only fully simulated samples and samples using the AFII simulation. Both distributions are normalized to the same area. The lower plots show the relative change with respect to the FS distribution.

Various systematic samples for W+jets were produced with varied ALPGEN parameters at the event generation (Evgen) level. The varied ALPGEN parameters are described below:

- iqopt - Renormalization and factorization scales. The nominal value of 1 equates to $m_W^2 + \sum p_T^2$, varied values 2 and 3 equate to m_W^2 and $m_W^2 + p_{T,W}^2$ respectively.
- qfac - The multiplicative scale factor to the renormalization and factorization scales (qfac×iqopt). The nominal value is 1, the varied values are 0.5 and 2.
- ktfac - The multiplicative scale factor for α_s (see section 1.3). The nominal value is 1, the varied values are 0.5 and 2.
- Minimum p_{T} − The minimum p_{T} of the jets used in the MLM jet-parton matching algorithm [104]. The nominal value is 20 GeV, the varied value is 25 GeV.
- ΔR(jet,parton) - Angular distance between the jet from the parton shower and the partons coming from the matrix element calculation [105] using the MLM matching (cone scheme). The nominal value is 0.7, the varied values are 0.4 and 1.0.

A preliminary study of these different samples, showed that the largest systematic effects to this analysis came from the ΔR(jet,parton) and qfac samples. AFII samples for these two parameter variations were produced. Additionally, samples with these varied parameters

using the $p_T(W)$ method described below were produced using AFII for the ΔR(jet,parton) parameter and event generation (Evgen/truth) only for the qfac parameter.

In order to set aTGC limits (see chapter 10) on this analysis it was necessary to generate enough MC statistics to populate the tails of the dijet p_T distribution. ALPGEN AFII samples were produced with a event generator-level filter requiring a high p_T leptonically decaying W boson. Figure 4.2 shows that $p_T(W)$ is highly correlated to the dijet p_T after event reconstruction and thus a high $p_T(W)$ event filter is quite effective in populating the p_{Tjj} tails. Samples were produced in four $p_T(W)$ slices: [200−300] GeV, [300−400] GeV, [400−500] GeV, and larger than 500 GeV. A requirement on the event generated $p_T(W)$ <200 GeV of the nominal light flavor AFII samples makes it possible to stitch the five different $p_T(W)$ regions together. Likewise, for the heavy flavor AFII samples, the stitching occurs at event generated $p_T(W)$ =250 GeV between the nominal AFII samples and the 200-300 GeV $p_T(W)$ sample. An example of this sample stitching can be seen in figure 4.3.

Lastly, samples for Wγ were generated with PYTHIA, but studies showed the effect of this process was negligible for this analysis and results are not included in the contribution to the W/Z+jets background.

4.3.3 Top Processes: $t\bar{t}$ and single top production

The $t\bar{t}$ samples are produced using MC@NLO [38] with the CT10 PDF set [106] interfaced to HERWIG. The $t\bar{t}$ cross section used for this analysis is 177^{+10}_{-11} pb [107] for a top quark mass of 172.5 GeV. It is calculated using the NNLO QCD prediction including resummation of next-to-next-to-leading logarithmic (NNLL) soft gluon terms with top++2.0 [108–113]. The PDF and α_S uncertainties were calculated using the PDF4LHC prescription [114] with the MSTW2008 68% CL NNLO [2, 99], CT10 NNLO [106, 115], and NNPDF2.3-5F FFN [116] PDF sets, added in quadrature to the scale uncertainty.

Single top events are generated using MC@NLO for the Wt and s-channels, and ACERMC [90] for the t-channel. The cross sections used for this analysis with there uncertainties are $15.74^{+1.17}_{-1.21}$, $4.63^{+0.20}_{-0.18}$ and, $64.57^{+2.63}_{-1.74}$ for Wt, s-channel, and t-channel respectively [117–119].

Systematic samples for $t\bar{t}$ and single top production are generated with varied ISR/FSR simulation using ACERMC.

4.4 Monte Carlo Corrections

Monte Carlo samples are in general generated prior to or during the data collection period in order to conduct sensitivity studies for a given process or to be able to immediately compare with data as it becomes available. This being the case, many aspects of the MC samples can not be modeled accurately without knowing the properties of the partial/full dataset and instead best guess estimates must be done a priori or with limited experimental results. Specialized performance groups continually update the object calibrations for the MC as more data is collected. Updated calibration tools are put in place to increase the MC agreement with data and accompanying systematics (discussed in section 7) are derived for use by analysis groups. The following sections describe the major calibration tools used on

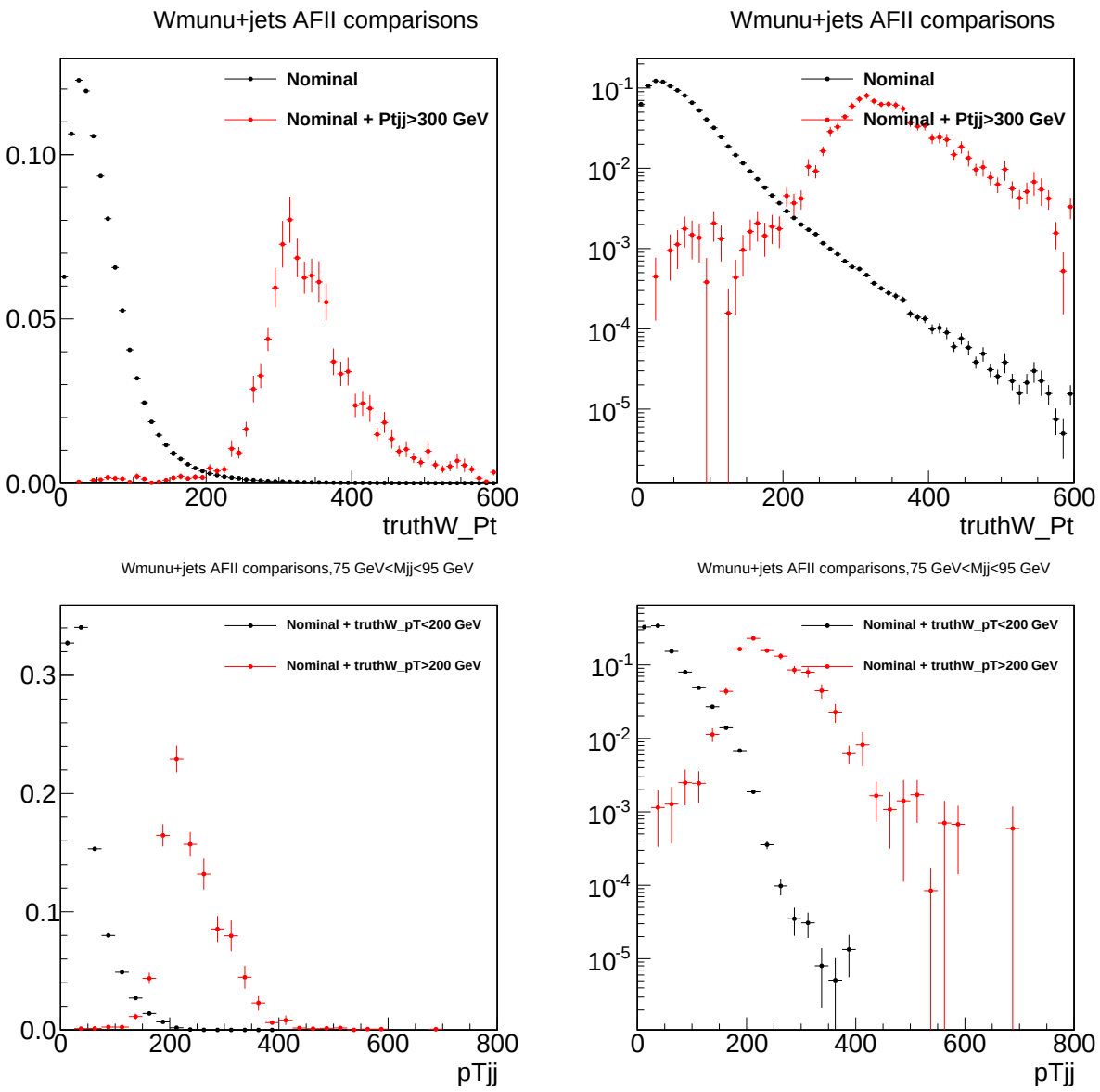

Figure 4.2: **Top**: The true $p_{\mathrm{T}}(W)$ distribution for $W(\rightarrow \mu\nu)$+jets ALPGEN MC, for all events passing the nominal selection (black) and for only the subset of events that have $p_{\mathrm{T}}(jj)$ > 300 GeV (red). **Bottom**: The reconstructed $p_{\mathrm{T}}(jj)$ distribution for W+jets ALPGEN MC, after applying a cut on the true W of $p_{\mathrm{T}}(W)$ less than (black) and greater than (red) 200 GeV. In addition to the nominal selection, the bottom plots require events to be within an m_{jj} window of 75 GeV and 95 GeV as required by the aTGC selection. The right-hand plots are log-scale versions of the left−hand plots.

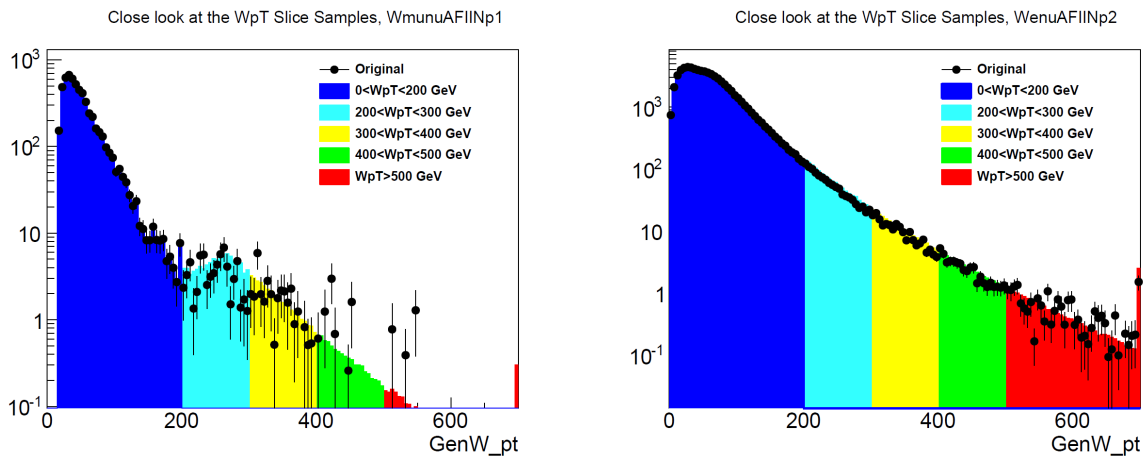

Figure 4.3: The overall $p_{\mathrm{T}}(W)$ distribution for $W \to \mu\nu + 1\mathrm{p}$ (left) and $W \to \nu + 2\mathrm{p}$ (right) events, obtained by stitching together different Alpgen MC samples generated in slices of $p_{\mathrm{T}}(W)$. For comparison, the original/nominal samples generated without a $p_{\mathrm{T}}(W)$ filter are also shown. The bump in $W \to \mu\nu + 1\mathrm{p}$ plot is due to the event selection requiring exactly two jets, but the sample only has 1 additional parton so an extra jet must come from pile-up or the underlying event.

the MC to improve the data-MC agreement. Table 4.2 shows the list of official ATLAS tool packages used in this analysis and their corresponding version tags.

4.4.1 Pile-up Reweighting

It is impossible to predict and simulate the pile-up conditions of the data in MC with complete accuracy prior to having the data available. Instead MC events are generated with a wide array of different pile-up conditions based on the best estimates of what the pile up conditions will be during the data run. This involves simulating MC events with a varying amount of minimum bias interactions (pile-up) overlaid on top of the hard scattering event, and then later reweighting the MC such that it agrees with the pile-up conditions of the data. For the 2011 dataset, the MC is reweighted based on the data's μ distribution, where μ is the average number of proton-proton collisions averaged across all bunch crossings in a given luminosity block (see section 2.4) of data and is calculated directly using the luminosity detector subsystems described in section 2.3.2.

4.4.2 Vertex Reweighting

MC samples in 2011 were generated with one of two different beam widths along the z direction (z-beam spot) for the hard interaction, either with a wide z-beam spot ($\sigma(z) \approx 90$ mm) or with a narrow z-beam spot ($\sigma(z) \approx 75$ mm). The MC reweighting scheme is taken from the 2011 data and is derived from a full $Z \to ee$ selection[120]. Figure 4.4 shows the data-MC agreement of the z vertex position before and after reweighting the events passing the full selection for the cross section measurement.

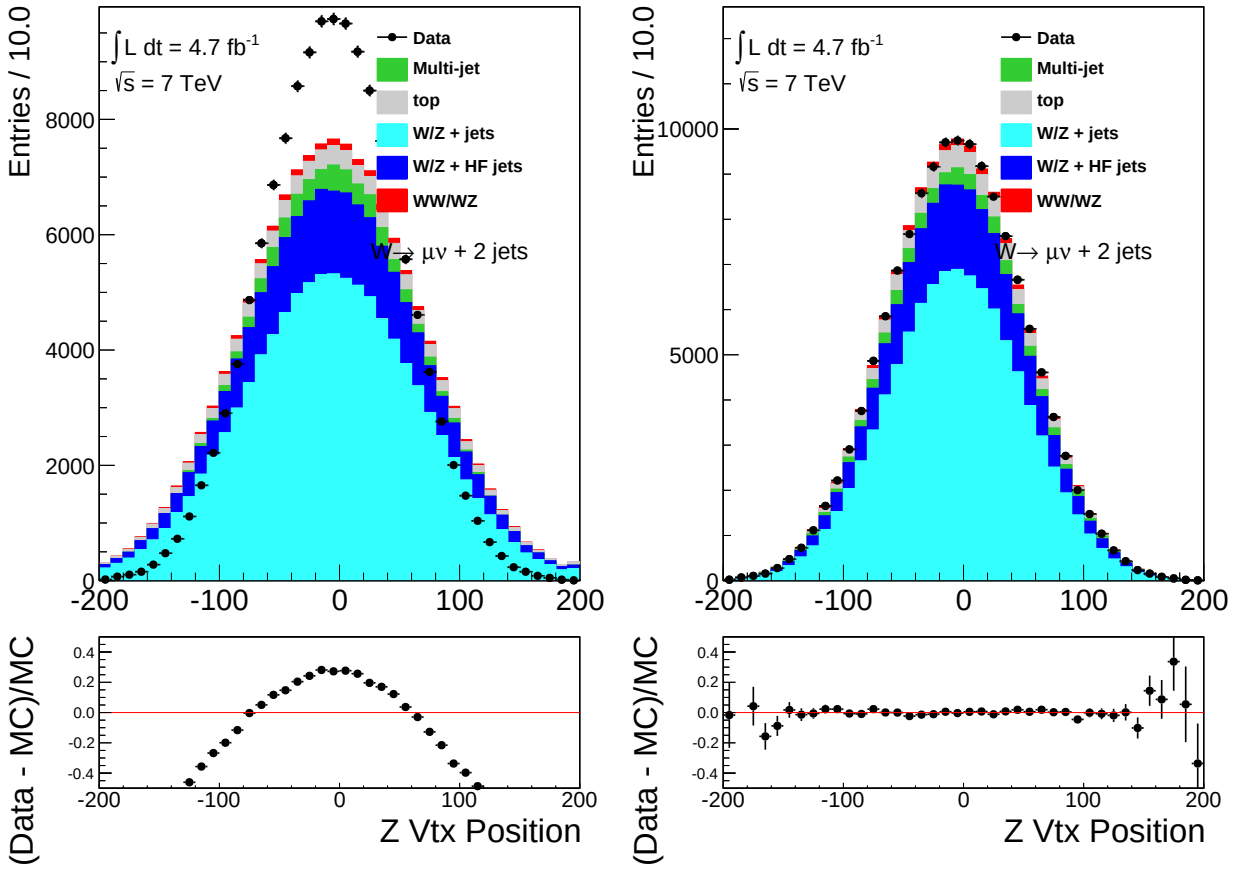

Figure 4.4: Distributions of the Z vertex position for events passing the analysis event selection in the muon channel. MC events not weighted by the Z vertex event weight shown on the left and with the weight on the right. The lower distributions show the relative difference between data and MC.

Package Name	Version Tags
GoodRunsLists	00-00-98
TrigMuonEfficiency	00-02-08
MuonEfficiencyCorrections	02-01-03
MuonMomentumCorrections	00-05-03
MuonIsolationCorrection	01-01
EgammaAnalysisUtils	00-03-39
PileupReweighting	00-02-03
ApplyJetCalibration	00-01-06
egammaEvent	03-06-20
JetUncertainties	00-08-06
JetResolution	01-00-00
CalibrationDataInterface	00-01-02
MissingETUtility	01-01-03

Table 4.2: Table of the official ATLAS tool packages used on MC and data for this analysis, and the corresponding version tags.

4.4.3 Electron Object Corrections

The electron object corrections discussed in the following section are separated into three Scale Factors (SF) that are used to weight the MC event and three energy corrections to the reconstructed electron candidate. The scale factors are derived by the ratio of the efficiencies calculated in data and MC (SF= $\epsilon_{Data}/\epsilon_{MC}$) and are implemented as functions of η and the electron E_T, ranging from approximately 0 to 3% away from unity.

Electron Selection Efficiency

The electron selection efficiency (ϵ_{el}) can be separated into the reconstruction (ϵ_{reco}), identification (ϵ_{ID}), and trigger ($\epsilon_{trigger}$) efficiencies.

$$\epsilon_{el} = \epsilon_{reco} \times \epsilon_{ID} \times \epsilon_{trigger} \tag{4.1}$$

The efficiencies are determined in the data and MC using a tag-and-probe method. This entails using a standard candle process (like $Z \rightarrow ee$, which has a very clean and well-measured mass peak) and first utilizing a strict selection criteria to define a "tag" object that enables the creation of an unbiased sample of "probe" objects which are defined by a set of looser criteria. The sample of probes can then be tested by requiring additional selection criteria in order to calculate the efficiency of the additional criteria. As an example, using $Z \rightarrow ee$ events the tag can be defined as a well-reconstructed electron and the probe is another electron satisfying a looser selection criteria that reconstructs the Z invariant mass peak. The efficiency is then defined as the ratio of probes passing the given test selection criteria over all selected probes. The efficiency in the MC is done using dedicated samples of the given process ($Z \rightarrow ee$ in the example case), while for the data it is first necessary to do some form of background subtraction.

The reconstruction efficiency is the efficiency of the reconstruction algorithm to reconstruct a cluster into an electron and match an inner detector track to the same cluster. ϵ_{reco} is determined from $Z \to ee$ events using Tight++ defined electrons as the tag and other potential EM clusters as the probe [121, 122].

The identification efficiency is the efficiency of the electron to pass identification criteria (i.e. loose, medium, and tight) relative to the reconstructed electron. The efficiency is determined from a combination of $W \to e\nu$, $Z \to ee$, and $J/\psi \to ee$ samples in order to measure the efficiency over a wide E_T range. With the tag object being either the E_T^{miss} (W sample) or a tight electron (Z and J/ψ samples), and the probe being the remaining electron. The trigger efficiency is calculated on a per-trigger basis and is determined using a $Z \to ee$ sample, requiring that the probe offline electron be matched to an electron candidate which fired the given trigger [123]. Each of the efficiencies build on the previous one, the ϵ_{ID} measurement for example can not be performed without first reconstructing the electron which depends on ϵ_{reco}.

Electron Energy Scale and Resolution

The electron energy scale corrections are applied in three steps to the data and/or MC. First, electrons in data are corrected by applying the energy scales obtained in MC from $Z \to ee$ and $J/\psi \to ee$ resonances, and $W \to e\nu$ E/p studies [121]. The scale correction, α is applied as a function of η and calculated using

$$E^{\text{measured}} = E^{\text{true}}(1 + \alpha), \tag{4.2}$$

where E^{true} is the true electron energy and E^{measured} is the energy measured in MC by the calorimeter after MC-based energy corrections. The scale correction lies within $\pm 2\%$ for electrons in the barrel.

The second correction fixes the reconstructed energy scale near the transition region ($1.42 < |\eta| < 1.55$) of the EM calorimeter and is applied to both data and MC. Simulations showed that the electron energy was underestimated by 5–10% in this region [124]. The last scale correction is applied to only MC samples simulated with Atlfast and corrects for a 0.1–1% difference in reconstructed electron energy seen between Atlfast and Geant4 MC samples.

The fractional electron resolution (σ_E/E) measured in the calorimeter is denoted as

$$\frac{\sigma_E}{E} = \frac{a}{\sqrt{E}} \oplus \frac{b}{E} \oplus c, \tag{4.3}$$

where a is the sampling term, b is the noise term, c is the constant term, and $\oplus$ signifies adding the terms in quadrature. The sampling term contributes mostly at low energies and its design value is $9\%/\sqrt{E[GeV]}$ at small $|\eta|$ and then grows as η increases due to an increase in detector material. The noise term has a value of about $350\times \cosh(\eta)$ MeV [125] for an electron cluster assuming a mean number of interactions per bunch crossing of $\mu = 20$. At higher energies the energy resolution tends asymptotically to the constant term with a design value of 0.7% [125]. Using a $Z \to ee$ sample, the electron resolution in the MC was shown not to reproduce the resolution in the data. A small smearing procedure is applied to the electron energy in MC in order to correct for this.

Calorimeter Isolation Correction

The calorimeter isolation quantity for an electron is the amount of energy that is collected in the calorimeter within a cone around a given electron candidate after excluding the electron cluster. Ensuring that a lepton candidate is isolated from other objects is important in obtaining accurate measurements of the object's energy and momentum, as well as reducing the likelihood that the cluster is a by product of a jet.

The calorimeter isolation variable, ETconeXX, where XX[5] denotes the cone size must be corrected for energy leakage and pile-up effects in both data and MC. Leakage occurs when some of the electron object's energy is deposited outside the designated electron cluster and thus contributes positively to the calorimeter isolation variable. Pile-up corrections are calculated based on the number of primary vertices in the event which also increases the value of the calorimeter isolation variable. These corrections amount to approximately 2.3 GeV being subtracted from the ETcone30 variable, which is the variable used in this analysis's selection criteria [126].

4.4.4 Muon Object Corrections

The object corrections applied to muon candidates are constructed similarly to electrons, there are two scale factors applied to MC from efficiency measurements and a correction to the muon resolution and isolation variables. The following sections go more into detail on how each are measured.

Muon Selection Efficiency

The muon selection efficiency (ϵ_{mu}) is made up of two components, the full reconstruction (ϵ_{reco}) efficiency and the trigger ($\epsilon_{trigger}$) efficiency.

$$\epsilon_{mu} = \epsilon_{reco} \times \epsilon_{trigger} \tag{4.4}$$

The full reconstruction efficiency is a product of the reconstruction efficiency in the inner detector, the reconstruction efficiency in the muon spectrometer, and lastly the matching efficiency between the two subsystems. The efficiencies are calculated using a tag-and-probe method, described in section 4.4.3, using $Z \to \mu^+\mu^-$ decays in which two oppositely charged isolated tracks are used that have an invariant mass close to the Z boson. The tag muon object is a combined Staco muon, and the probe is either a Standalone muon if measuring the inner detector reconstruction efficiency or an inner detector track if the MS and matching efficiency is being measured [127]. The measured scale factor applied to the MC is approximately 0–2% as a function of η and muon p_T. The muon trigger efficiency is calculated the same way as in the electron channel using $Z \to \mu^+\mu^-$ events on a per trigger basis.

[5]For this analysis, ETcone30 is used as recommended by the performance group, denoting a $\Delta R = 0.3$ cone size.

Muon Energy Resolution

The fractional muon resolution ($\sigma_\mu(p)/p$) for a given η can be parametrized as a function of the p_T and denoted as

$$\frac{\sigma_\mu(p)}{p} = \frac{p_0^{Det}}{p_T} \oplus p_1^{Det} \oplus p_2^{Det}\dot{p}_T, \tag{4.5}$$

where p_0^{Det}, p_1^{Det}, p_2^{Det} are related to the energy loss due to the calorimeter material, multiple scattering, and the intrinsic resolution terms, respectively [128]. Det stands for either the inner detector or the muon spectrometer, since both systems have independent resolutions. For the inner detector resolution, there is no p_0^{Det} term. The muon resolution is measured from the Z mass peak width in $Z \to \mu\mu$ decays and from $W \to \mu\nu_\mu$ decays in which momentum measurements in the ID and MS are compared. The muon resolution in MC was shown to not reproduce the data [128], therefore a smearing correction is applied to MC to address this difference in simulation.

Calorimeter Isolation Correction

The muon calorimeter isolation variable is corrected for effects due to pile-up as is done for electron candidates. The correction is applied for a given isolation cone size (the analysis uses ETCone30) as a function of η and the number of primary vertices present in the event.

4.4.5 Excluded Calorimeter Region

During one of the runs in 2011, a crate controller failed in the EM calorimeter resulting in six front-end boards being completely lost which affected a region between $-0.1 < \eta < 1.5$ and $-0.9 < \phi < -0.5$. The resulting so-called 'LAr hole' in the calorimeter was eventually repaired, but the lost of these boards was present through the data taking periods E through H (runs 180614–185352). The consequence was a significant underestimation of the energy resolution for both electrons and jets, resulting in a poor E_T^{miss} reconstruction as well. A subset of all events in each MC sample, corresponding proportionally to the percentage of the data effected by the LAr hole, is generated with the LAr hole resolution degradation simulated. For this portion of the MC and data, a simple veto method is used to remove all events in which a calorimeter jet falls in the vicinity of the LAr hole with a p_T greater than a given threshold [129]. The details of the veto are described in the event selection section (sec. 5.4).

4.4.6 Jet Calibrations

The same JES calibration scheme discussed in section 3.5 is used on jets produced in MC to modify the jet kinematics from the EM scale to the JES scale. Measured differences between the data and MC simulated jets are taken into account during this process, as well as differences between using fully simulated MC samples and samples produced using Atlfast-II.

Chapter 5

Selection Criteria

5.1 Data and Good Runs List

The 2011 dataset collected by the ATLAS detector at $\sqrt{s} = 7$ TeV corresponds to approximately a total integrated luminosity, $\mathcal{L}_{int}$, of 5 fb^{-1} collected over 10 data periods. Only data collected in luminosity blocks which pass a set of data quality requirements is used for this analysis. The criteria requires that all detector subsystems are properly functioning, the LHC beams are stable and that the colliding bunches contain protons in order to have collisions. The data quality of each luminosity block is stored in a Good Runs List (GRL)[1] which is used offline for this analysis. The total integrated luminosity for data passing the GRL is 4.64 fb^{-1}, table 5.1 shows a breakdown of each data periods $\mathcal{L}_{int}$ contribution.

Period	$\mathcal{L}_{int}^{Collected}$ $[pb^{-1}]$	$\mathcal{L}_{int}^{GRL}$ $[pb^{-1}]$
D	182	164
E	52	48
F	156	131
G	566	502
H	283	257
I	406	333
J	237	224
K	676	583
L	1599	1387
M	1160	1015

Table 5.1: Breakdown of the total integrated luminosity collected for each data period, $\mathcal{L}_{int}^{collected}$, and the amount of integrated luminosity passing the GRL used for this analysis,$\mathcal{L}_{int}^{GRL}$.

[1]The GRL used for this analysis is $data11\_7TeV.periodAllYear\_DetStatusv36pro10\_CoolRunQuery00$-$0408\_WZjets\_allchannels\_DtoM.xml$

Period	e Channel	μ Channel
D - I	EF_e20_medium	EF_mu18_MG
J	EF_e20_medium	EF_mu18_MG_medium
K	EF_e22_medium	EF_mu18_MG_medium
L - M	EF_e22vh_medium1	EF_mu18_MG_medium

Table 5.2: List of un-prescaled single lepton triggers used in the analysis depending on the data period.

5.2 Triggers

This analysis uses the lowest p_T un-prescaled[2] single lepton triggers available during each corresponding data period. As the instantaneous luminosity increased during data taking in 2011, the p_T threshold for un-prescaled triggers also increased due to the growing amount of pile-up events causing a drop in the trigger acceptance. Table 5.2 lists the triggers used for each channel depending on the data period.

The un-prescaled single electron triggers include EF_e20_medium, EF_e22_medium, and EF_e22vh_medium1. The values after EF_e in each trigger name represents the electron candidates p_T threshold in GeV for that trigger. The suffix 'medium' or 'medium1' refer to the tightness of the electron identification requirement and 'vh' signifies that the trigger has an η-dependent p_T threshold and a requirement on the hadronic leakage cut at the L1 trigger. The electron trigger efficiencies are measured using a $Z \to ee$ tag-and-probe method and plateau at approximately 90-98% depending on the electron candidate's p_T and which trigger is used [123].

The single muon triggers consist of EF_mu18_MG and EF_mu18_MG_medium. Both triggers have a nominal p_T threshold of 18 GeV. The suffix 'medium' denotes a change at the L1 trigger thresholds from L1_MU10 to L1_MU11 (from 10 GeV to 11 GeV). The muon trigger efficiencies are measured using a $Z \to \mu\mu$ tag-and-probe method are equal to approximately 70% in the barrel and 90% in the endcaps [130].

5.3 Object Selection

The general object reconstruction algorithms discussed in Chapter 3 do an adequate job in identifying and accepting potential objects of interest to be later analyzed. The large acceptance of these reconstruction algorithms leads to the possibility for fake or misidentified (e.g. an electron being reconstructed as a jet) objects to be reconstructed. Therefore, additional requirements, discussed in the following sections, on electron, muon, and jet candidates are imposed prior to the event selection in order to increase the purity of true objects. As a reminder, all data and MC corrections discussed in section 4.4 are applied before applying any selection criteria through out the rest of this thesis unless otherwise

[2]The trigger prescale denotes the probability that an event that passes the trigger will be recorded or passed to the next higher level trigger system. An un-prescaled trigger will always record or pass the accept signal.

Muon Selection

- STACO Muons, Author == 6
- p_{T}> 25 GeV, $|\eta| < 2.4$
- MCP cuts
- $|d_0/\sigma(d_0)| < 3$ and $z_0 < 1.0$ mm
- $\frac{pTcone30}{p_T} < 0.15$
- $\frac{ETcone30}{p_T} < 0.14$

Electron Selection

- Author == 1 or 3, OTX cleaning
- Tight++ Id criteria
- p_{T}> 25 GeV, $|\eta| < 2.47$, exclude crack
- $|d_0/\sigma(d_0)| < 10$ and $z_0 < 1.0$ mm
- $\frac{pTcone30}{E_T} < 0.13$
- $\frac{ETcone30}{E_T} < 0.14$

Jet Selection

- Anti−kt TopoEM, $\Delta R = 0.4$
- p_{T}> 25 GeV, $|\eta| < 2.8$
- Looserbad Jet Cleaning
- $\Delta R(lepton, jet) > 0.5$
- JVF> 0.75 for $|\eta| < 2.5$

MET Selection

- MET_refFinal
- MET Cleaning

Table 5.3: For ease of viewing, a list of the important object selection cuts for each object are shown above. For more details please see the relevant sections.

noted. For easy viewing, table 5.3 lists the important object selection criteria for each object, see the relevant sections below for specific details.

5.3.1 Electrons

An electron's author variable which defines the electron reconstruction algorithm used is required to be equal to 1 or 3, which represents that the electron candidate must be reconstructed from an EM cluster that is associated to a track (standard method). Candidates, which are reconstructed using EM calorimeter clusters known to have dead or poorly functioning detector hardware are excluded, el_OQ&1446 != 0[3]. Electron candidates are required to satisfy the ATLAS tight++ identification criteria and have a transverse energy $E_T > 25$ GeV to be well within the trigger plateau[4]. Additionally they are required to be

[3]Variable requires that the electron Object Quality (OQ) is good (==0) according to an object quality bit mask that checks that the electron was not reconstructed using dead cells, cells that have read out problems due to missing front end boards, or in general the cells are known to badly reconstruct particle energies.

[4]The energy threshold in which the trigger acceptance is constant.

within $|\eta| < 2.47$, excluding the crack region between the barrel and endcap EM calorimeter, $1.37 < |\eta| < 1.52$. In order to ensure that the candidate is consistent with originating from the primary vertex, cuts on the impact parameter[5] are required. The transverse impact parameter significance, $|d_0/\sigma(d_0)|$, must be less than 10 and the impact parameter along the beam (z) direction, z_0, must be less than 1 mm. To ensure that the electron candidate is well isolated from other objects, particularly jets and non-prompt electrons, calorimeter and tracking isolation requirements are necessary:

- $\frac{pTcone30}{p_T} = \frac{\sum_{\Delta R<0.3}(p_T^{track})}{p_T} < 0.13$;
- $\frac{ETcone30}{E_T} = \frac{\sum_{\Delta R<0.3}(E_T^{cells})}{p_T} < 0.14$.[6]

where pTcone30 (ETcone30) is the sum of the transverse momentum (energy) of all tracks (calorimeter cells) within a cone of size $\Delta R = 0.3$ around the electron candidate, excluding the momentum or energy of the candidate.

5.3.2 Muons

A muon's author variable which defines the muon reconstruction algorithm used is required to be equal to 6 corresponding to the mu_staco combined reconstruction algorithm. Muon candidates are required to have a transverse momentum $p_T > 25$ GeV and lie within $|\eta| < 2.4$. Like electrons, impact parameter requirements are imposed to ensure the candidate is consistent with originating from the primary vertex and not from cosmic rays or heavy flavor decays. The transverse impact parameter significance, $|d_0/\sigma(d_0)|$, must be less than 3 and the impact parameter along the beam(z) direction, z_0, must be less than 1 mm. Several cuts on the ID track are used following recommendations from the Muon Combined Performance(MCP) group to reduce muon mis-identification and improve the momentum resolution. The criteria is listed below:

- Require 1 hit in the b-layer of the pixel detector
- Number of pixel detector hits + Number of crossed dead pixel sensors > 5
- Number of SCT hits + Number of crossed dead SCT sensors ≥ 5
- Number of pixel holes + Number of SCT holes < 3
- Defining TRT_{hits} = Number of TRT hits + Number of TRT outliers(TRT_{out}):
  - If $|\eta| < 1.9$ **then require** $TRT_{hits} \geq 5$ and $TRT_{out} < (0.9)TRT_{hits}$
  - If $|\eta| \geq 1.9$ and $TRT_{hits} \geq 5$ **then require** $TRT_{out} < (0.9)TRT_{hits}$

The muon candidate's calorimeter and tracking isolation requirements are:

- $\frac{pTcone30}{p_T} = \frac{\sum_{\Delta R<0.3}(p_T^{track})}{p_T} < 0.15$;
- $\frac{ETcone30}{E_T} = \frac{\sum_{\Delta R<0.3}(E_T^{cells})}{p_T} < 0.14$[7]

[5] Impact parameter is defined as the closest distance in the plane transverse to the beam line.
[6] Corrected for p_T leakage and pile-up, see section 4.4.3
[7] Corrected for pile-up, see section 4.4.4

, where pTcone30 (ETcone30) is the sum of the transverse momentum (energy) of all tracks (calorimeter cells) within a cone of size $\Delta R = 0.3$ around the muon candidate, excluding the candidate.

5.3.3 Jets

Jets are reconstructed using the anti-k_T algorithm with a cone size of $\Delta R = 0.4$. Jets are required to have a transverse momentum $p_T > 25$ GeV and lie within a $|\eta| < 2.8$. Any jet that overlaps with a good lepton passing the object selection criteria within a cone of $\Delta R < 0.5$ is removed from the event. A set of cleaning criteria is used to identify jets which are not associated to real energy deposits in the calorimeters. These misidentified jets can come from various sources including hardware malfunctions, accelerator beam conditions, and cosmic-ray showers [131]. Any jet that fulfills any of the following *bad* jet criteria listed below is removed from the event:

- (HECf > 0.5 and |HECQ| > 0.5 and LArQmean > 0.8)
- $E_{jet}^{negative} > 60GeV$
- ($Jet_{EMF} > 0.95$ and |LArQ| > 0.8 and LArQmean > 0.8 and $|\eta| < 2.8$)
- ($Jet_{EMF} < 0.05$ and $Jet_{chf} < 0.05$ and $|\eta| < 2.0$)
- ($Jet_{EMF} < 0.05$ and $|\eta| \geq 2.0$)
- ($Jet_{FMax} > 0.99$ and $|\eta| < 2.0$)

where:

- HECf - The energy fraction in the Hadronic Endcap Calorimeter(HEC).
- LArQ - Jet Reconstruction Quality, the fraction of energy corresponding to LAr cells with a cell Q-factor > 4000.
- Q-factor - Difference between the measured pulse shape (a_i^{meas}) and the predicted pulse shape (a_i^{pred}) used to reconstruct the calorimeter cell energy. Computed as $\sum(a_i^{meas} - a_i^{pred})^2$.
- HECQ - Same as LArQ but only considering HEC cells.
- LArQmean - Normalized LArQ, computed as the energy squared cells mean quality.
- $E_{jet}^{negative}$ - Negative energy in the jet.
- Jet_{EMF} - The energy fraction in the EM calorimeter.
- Jet_{chf} - The jet charge fraction, ratio of the sum p_T from tracks associated with the jet over the calibrated jet p_T.
- Jet_{FMax} - The maximum energy fraction in one calorimeter layer.

In order to suppress jets coming from pile-up interactions and not from the primary vertex a Jet Vertex Fraction(JVF) cut is applied to jets that fall within the η acceptance of the inner detector. All jets within $|\eta| < 2.5$ are required to have a $|\text{JVF}| > 0.75$. The JVF is defined as the sum p_T of all jet-matched tracks from a given primary vertex divided by the sum of all jet-matched track p_T. A JVF close to 1 means the majority of matched tracks originate from the primary vertex, while a JVF value close to 0 signifies that the matched tracks do not. A JVF value equal to -1 is given to jets in which there are an insufficient number of tracks matched to it. The JVF cut has been studied and is shown to be 95% efficient out to $|\eta| < 2.5$, see appendix D.1 for details.

5.3.4 Missing Transverse Energy

The E_T^{miss} is reconstructed using the MET_refFinal algorithm discussed in section 3.6. All data and MC corrections that are applied to physics objects are propagated to the E_T^{miss} calculation prior to the event selection. Due to the E_T^{miss} being reconstructed using the total energy deposited in the calorimeters, MET cleaning is necessary to exclude events in which reconstructed jets pass the bad jet criteria. This avoids having events pass event selection that have poorly reconstructed E_T^{miss} due to possible detector issues that cause energy spikes in the calorimeter cells that later get reconstructed into misidentified jets. Events are rejected if a jet passing the bad jet criteria (described in the previous section) has a $p_T > 20$ GeV and is separated from all leptons passing the object selection by a $\Delta R > 0.3$.

5.4 Event Selection

This section lists and motivates the cuts used for the cross section measurement. The following event selection assumes all the criteria discussed previously in this chapter (GRL, trigger, and object selection). To measure the WW/WZ$\rightarrow l\nu jj$ process, we require one high p_T lepton (muon or electron), high E_T^{miss} , and two jets. The different lepton channels are analyzed separately for this analysis, but follow the same basic selection criteria and strategy.

First, events are required to contain a primary vertex that is reconstructed using at least 3 tracks, each with a $p_T^{track} > 400$ MeV. In the case of multiple vertices satisfying this criteria, the vertex with the largest $\sum(p_T^{track})^2$ is defined as the primary vertex. For data only, events that have been flagged due to the LAr Calorimeter experiencing a noise burst are removed[8].

Events are required to contain exactly one reconstructed lepton candidate (electron or muon). Events containing more than one lepton are rejected in order to suppress the Z+jets and $t\bar{t}$ backgrounds. The lepton candidate is required to be matched to the event trigger, the ΔR between the electron (muon) candidate and the η-ϕ detector triggering region needs to be within a ΔR of 0.15(0.10).

A simple veto method [131] is used to veto events in which a jet falls within the region ($-0.1 < \eta < 1.5$ and $-0.9 < \phi < -0.5$) affected by the LAr hole issue during the effected

[8]Noise bursts are reported when calorimeter cells in a region give large signals with distorted shapes for a very short amount of time $< 5\mu s$. Events are vetoed around a short time window around a given noise burst. The cut in ATLAS terminology is defined as larError>1.

data period or MC sample equivalent. Events are vetoed if a given jet may have deposited a significant amount of energy in the LAr hole. This is determined by requiring that the

$$\text{Jet } p_T > (\text{LArHole } p_T^{threshold}) * \frac{1 - BCH\_CORR\_JET}{1 - BCH\_CORR\_CELL}, \tag{5.1}$$

where the LArHole $p_T^{threshold}$ is taken to be 25 GeV for this analysis. BCH_CORR_CELL is the fraction of jet energy coming from a correction to dead calorimeter cells in which the energy density of the dead cells is taken to be the same as neighboring active cells. BCH_CORR_JET is the fraction of the jet energy after reconstructing the jet using the corrected dead cells and dead tile modules.

Events must have a $E_T^{\text{miss}} > 30$ GeV to account for the neutrino coming from the leptonic W$\rightarrow \ell\nu$ decay. The transverse mass, m_T, calculated using the E_T^{miss} and lepton candidate is defined as

$$m_T = \sqrt{2 \cdot E_T^{\text{miss}} \cdot p_T(\ell) \cdot [1 - \cos(\Delta\phi(E_T^{\text{miss}}, \ell))]} \tag{5.2}$$

and must be greater than 40 GeV. Both the E_T^{miss} and m_T cuts highly suppress the QCD multijet background and increase the probability of identifying a leptonically decaying W candidate.

Events are required to have exactly two jets passing the object selection. Resulting in a event veto for any event with 3 or more jets with a $p_{\text{T}} > 25$ GeV and $|\eta| < 2.8$. Both selected jets are required to be within an $|\eta| < 2.0$ and the leading jet is required to have a $p_{\text{T}} > 30$ GeV. The jet veto requirement greatly reduces the $t\bar{t}$ contribution in the signal region and the requirement to keep the selected jets located in the central region of the detector suppresses the QCD multijet background and W/Z+jet.

The azimuthal angular separation, $\Delta\phi$, between the leading jet and the E_T^{miss} is required to be greater than 0.8 and the $\Delta\eta$ between the leading and sub$-$leading jet must be less than 1.5. The $\Delta\phi$ cut is used to reduce and shape the QCD multijet background, while the $\Delta\eta$ improves on the signal to background ratio. The relevant $\Delta\phi$ and $\Delta\eta$ shape distributions without their respective cuts applied can be seen in figures 5.1 and 5.2.

Additionally, there is a cut on the $\Delta R(Jet_1, Jet_2)$ or $\Delta R(jj)$ between the leading and sub$-$leading jet, requiring that the $\Delta R(Jet_1, Jet_2) > 0.7$ or that the $p_{\text{T}}(jj) > 250$[9] GeV. This cut is done in order to select a phase space that is modeled correctly by the ALPGEN generator which generates the W/Z+jets MC samples, the largest and most important background in this analysis. The ALPGEN samples avoid the double counting of jets during the event generation step by applying a minimum ΔR(jet,parton) requirement of 0.7 between matrix element and the parton shower. This generator requirement results in only the jets from the parton showers being kept in regions where two jets lie within $\Delta R(Jet_1, Jet_2) < 0.7$. Data on the other hand has no such requirement and therefore this difference in selection leads to a mis-modeling between the data and MC. This mis-modeling in the $\Delta R(Jet_1, Jet_2)$ distribution can be seen clearly in figure 5.3. This discrepancy is also very noticeable in the low m_{jj} region as seen in figure 5.4. Applying the ($\Delta R(Jet_1, Jet_2) > 0.7$ or $p_{\text{T}}(jj) > 250$ GeV) cut to both data and MC greatly improves the data/MC agreement for the m_{jj} distribution as seen in figure 5.8. The choice to drop the $\Delta R(Jet_1, Jet_2)$ cut for high values

[9] $p_{\text{T}}(jj)$ stands for the transverse vector sum of the two leading jets in the event, or $p_T(Jet_1, Jet_2)$.

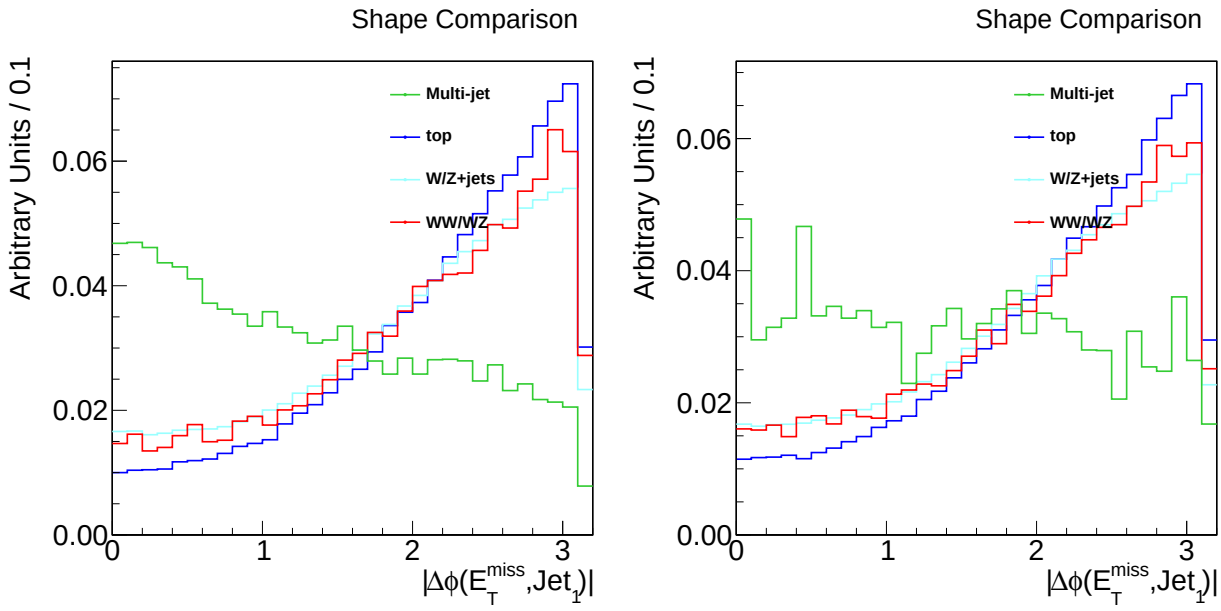

Figure 5.1: The $\Delta\phi(E_T^{\text{miss}}, Jet_1)$ distributions for all processes, for the electron (left) and muon (right) channels after applying all selection criteria but the $\Delta\phi(E_T^{\text{miss}}, Jet_1) > 0.8$ cut. The distributions are normalized to the same area.

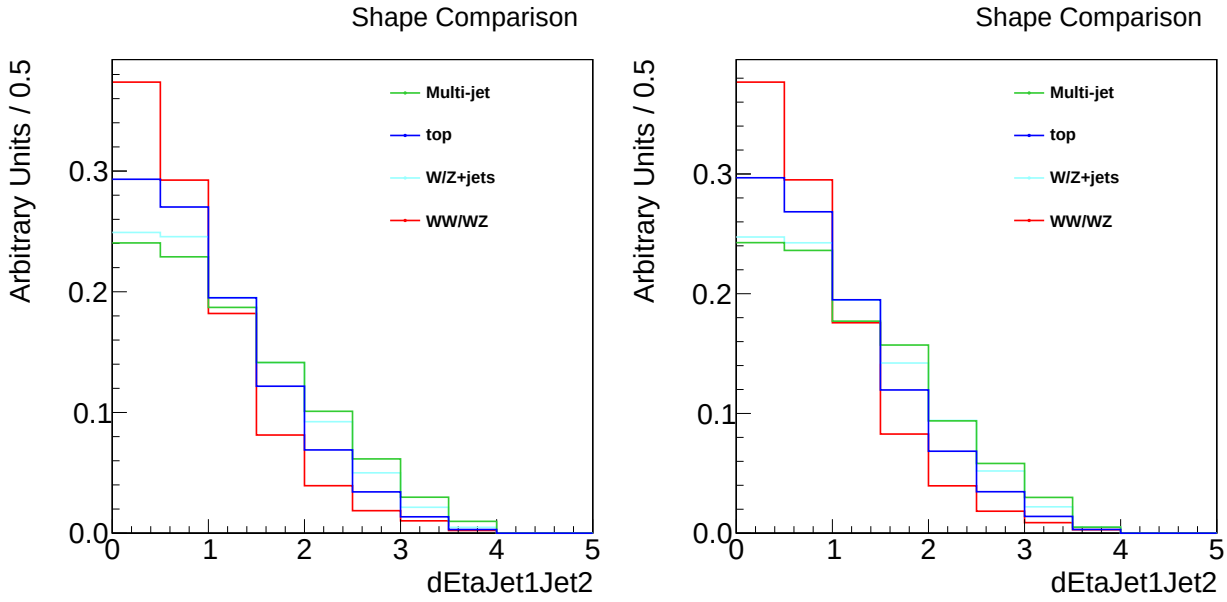

Figure 5.2: The $\Delta\eta(Jet_1, Jet_2)$ distributions for all processes, for the electron (left) and muon (right) channels after applying all selection criteria but the $\Delta\eta(Jet_1, Jet_2) < 1.5$ cut. The distributions are normalized to the same area.

of $p_{\mathrm{T}}(jj)$ is done to ensure adequate statistics in the tail of the $p_{\mathrm{T}}(jj)$ distribution for the setting of the aTGC limits. Due to the angular separation of boosted jets decreasing in the lab frame as the p_{T} of the jets increases it becomes nearly impossible for any events to survive the $\Delta R(Jet_1, Jet_2)$ cut in the high $p_{\mathrm{T}}(jj)$ tails where the majority of the aTGC limit sensitivity lies. Additional systematic uncertainties are taken into account to cover any remaining modeling discrepancies.

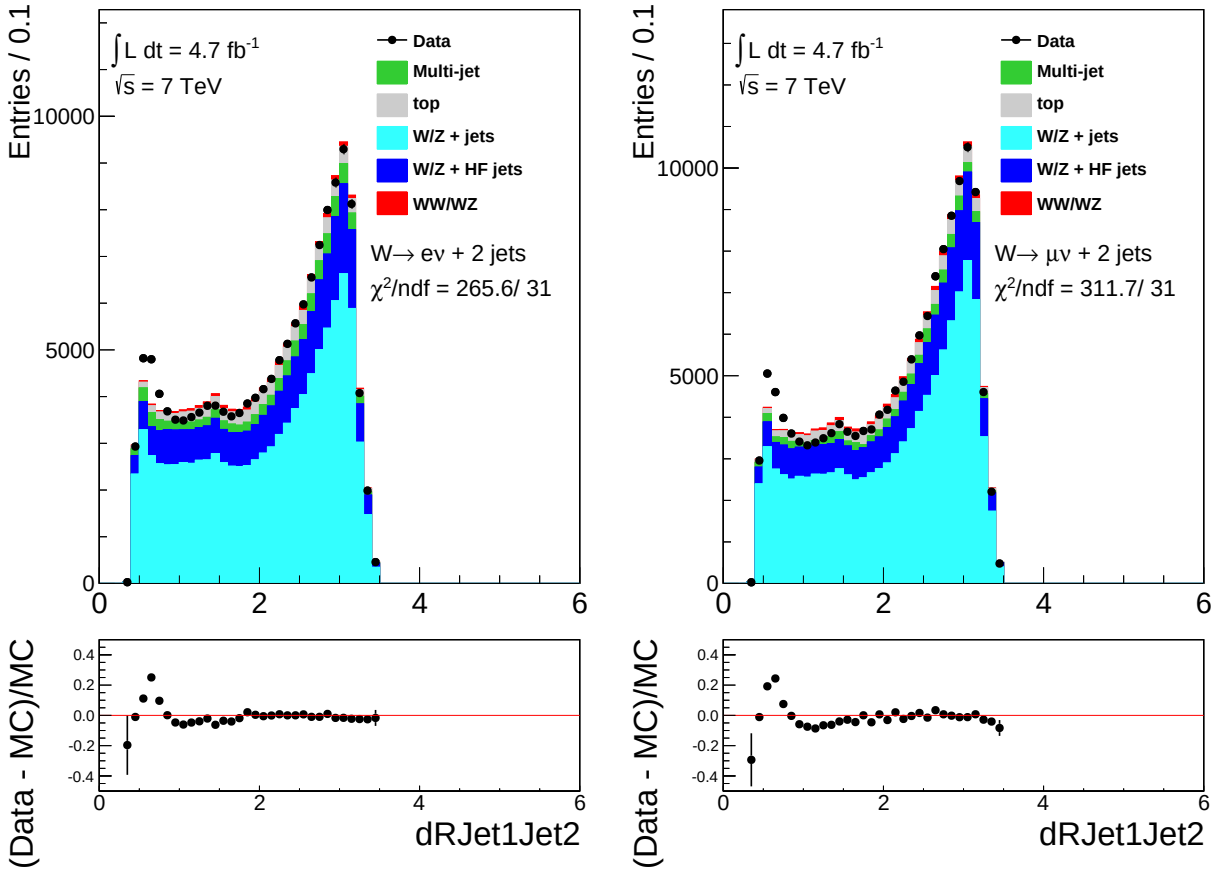

Figure 5.3: Comparison of the $\Delta R(Jet_1, Jet_2)$ distributions for data (solid circles) and MC (histograms) for the electron (left) and muon (right) channel after applying all selection criteria but the $\Delta R(Jet_1, Jet_2) > 0.7$ cut. The plots in the lower panel show the percent difference between data and the MC prediction with respect to the MC(solid circles).

Lastly, for the cross section fit to the m_{jj} distribution only the mass range of $25 < m_{\mathrm{jj}} < 250$ GeV is considered. Therefore after applying all object and event selection criteria there are 127650 events found in the electron channel and 134846 events in the muon channel.

For easy viewing, a list is provided below of the event selection criteria.

Event Selection

- Apply GRL

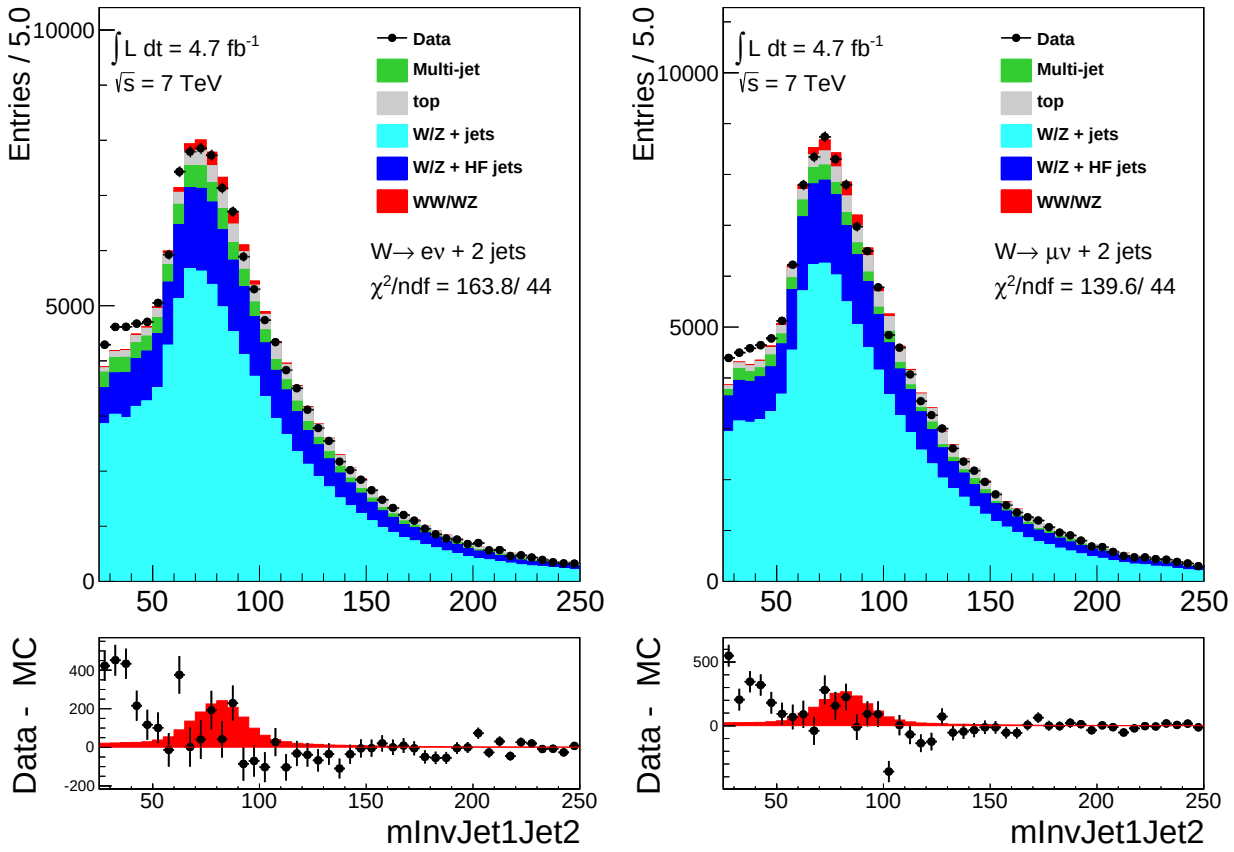

Figure 5.4: Comparison of the m_{jj} distributions for data (solid circles) and the SM predictions shown as stacked histograms for the electron (left) and muon (right) channel after applying all selection criteria but the $\Delta R(Jet_1, Jet_2) > 0.7$ cut. The right−most bins include events in the overflow. The plots in the lower panel show the difference between data and the MC background prediction (solid circles) overlaid on the signal (red histogram).

- Require at least 1 primary vertex
- Data Only, remove noise bursts: larError >1
- Pass single lepton trigger requirements
- Require exactly 1 lepton (electron or muon) to pass object selection
- Require lepton to be matched to the fired trigger
- LArhole veto
- $E_T^{\text{miss}} > 30$ GeV
- $m_{\text{T}} > 40$ GeV
- Require exactly two jets to pass object selection
- Jet_1 p_{T}> 30 GeV and $|\eta| < 2.0$
- Jet_2 p_{T}> 25 GeV and $|\eta| < 2.0$
- $\Delta\phi(E_T^{\text{miss}}, Jet_1) > 0.8$
- $\Delta\eta(Jet_1, Jet_2) < 1.5$
- $\Delta R(Jet_1, Jet_2) > 0.7$ or $p_{\text{T}}(jj) > 250$ GeV
- 25< m_{jj} <250 GeV

5.5 Signal and Background Estimation

The signal and background SM predictions are obtained using a combination of the MC sample predictions and data driven techniques. These signal and background estimations are used to validate the data/MC agreement and later implemented as the initial templates for the cross section fit and the aTGC limit setting.

For each MC sample, the event yields for all events that pass the event selection, N_i^{passed}, are normalized based on their sample cross section σ_i to the total integrated luminosity $\mathcal{L}_{int}$ using:

$$N_i^{Normalized} = \mathcal{L}_{int} \cdot \sigma_i \cdot \frac{N_i^{passed}}{N_i^{total}}, \tag{5.3}$$

where i is a given MC sample and N_i^{total} is the total number of initial events in that sample prior to imposing any selection criteria. The normalization rates and shapes for the $t\bar{t}$, single top, and diboson WW/WZ signal samples are taken directly from the MC predictions. For the W+jets , Z+jets , and very small ZZ contribution only the shape prediction is taken directly from the MC, while the production rates along with the QCD multijet background shape and production rate predictions are calculated using a data-driven technique explained in the following section.

Table 5.4 gives a summary of the methods used to calculated the normalization rates and shapes for each given signal and background process.

Process	Normalization	Shape
W+LF jets, W+HF jets	NLO prediction, E_T^{miss} fit correction	ALPGEN
Z+LF jets, Z+HF jets	NLO prediction, E_T^{miss} fit correction	ALPGEN
ZZ	NLO prediction	HERWIG
Top, Single-top	NLO prediction	MC@NLO
QCD multijet electron	E_T^{miss} fit	Data-driven
QCD multijet muon	E_T^{miss} fit	Data-driven
WW/WZ	NLO prediction	MC@NLO

Table 5.4: Summary of the methods used to obtain the SM predictions for the normalization and shape of each signal and background process.

5.5.1 QCD Multijet Background Estimation: Fit to E_T^{miss}

For this analysis the QCD multi-jet (MJ) background is estimated using a data driven approach. In the muon channel the MJ background is dominated by semi-leptonic heavy flavor decays and for the electron channel there is an additional component from jets faking electrons that pass the event selection. Due to the enormous rate of QCD MJ production that takes place at the LHC it is very difficult to generate MC with enough statistics that adequately replicates the shape and rate of the MJ background seen in data, particularly for the subset of MJ events that pass the event selection criteria. Instead control regions (CR) are used that modify the lepton selection in order to create a control sample dominated by QCD MJ production and kinematics that closely resemble those of the signal region. The shape of the MJ background is taken from these control regions and fitted in the signal region to extract the MJ rate.

For the muon channel, the QCD CR differs from the signal region by reversing the d_0 significance cut on the muon candidate, $|d_0/\sigma(d_0)| > 3$. This leads to a control sample where the muon candidate is not pointing back to the primary vertex and therefore has a higher likelihood of the muon coming from a heavy flavor decay. The electron channel QCD CR requires that the electron candidate passes the Medium++ identification criteria (see sec. 3.3) without passing the Tight++ criteria. This results in a sample of poorly reconstructed electron candidates that are likely to be jets that have been misidentified. In both cases, the contribution from ElectroWeaK (EWK) processes are calculated using the MC samples that pass the QCD CR selection and these contributions are subtracted from the events that pass the selection in the data in order to obtain the final shape of the QCD MJ distribution for each lepton channel. A breakdown of the EWK contributions in the QCD CR can be seen in appendix D.2.

The normalization of the QCD MJ and the W/Z+jets contributions are determined using a binned negative log likelihood fit to the E_T^{miss} spectrum in data over the range $0 < E_T^{\text{miss}} < 400$ GeV (no E_T^{miss} cut is applied for the fit), in bins of 5 GeV. This E_T^{miss} fit is done separately for each lepton channel. The E_T^{miss} variable is chosen to determine the QCD MJ normalization because it provides the best discrimination between the QCD and W/Z+jets processes as seen in figure 5.5. Due to the large uncertainty in the W/Z+jets cross section, the W/Z+jets normalization, N_{float}, is allowed to float in the fit and an overall scale factor is

calculated and applied to the W/Z+jets background in the signal region. The contribution from the ZZ diboson background is very small and its negligible contribution is added to the W/Z+jets background. Contributions from the signal and top backgrounds are held fixed, N_{fixed}, in the fit. The likelihood fit takes the form

$$L(f) = \sum_i \int_{x_{min}}^{x_{max}} \Gamma[N^i_{Data}, N^i_{Bkg}(f)] \cdot \frac{e^{\frac{(x-N^i_{Bkg}(f))^2}{2\sigma}}}{\sqrt{2\pi}} dx \tag{5.4}$$

where Γ is the gamma function, given by

$$\begin{aligned} \Gamma[N^i_{Data}, N^i_{Bkg}(f)] &= \frac{1}{(N^i_{Data}-1)!} \int_0^{N^i_{Bkg}(f)} t^{N^i_{Data}-1} e^{-t} dt, \text{ for } N^i_{Data} > N^i_{Bkg}(f) \\ &= 1.0 - \frac{1}{(N^i_{Data})!} \int_0^{N^i_{Bkg}(f)} t^{N^i_{Data}} e^{-t} dt, \text{ for } N^i_{Data} < N^i_{Bkg}(f) \end{aligned} \tag{5.5}$$

and σ is the statistical uncertainty in the MC, x_{min}/x_{max} represent 10 standard deviations in statistical uncertainty from the MC prediction, N^i_{Data} is the number of data events in bin i, and $N^i_{Bkg}(f)$ is the number of background events in bin i given by

$$N^i_{Bkg}(f) = (N^i_{Data} - N^i_{fixed})[N^i_{float} - f(N^i_{float} - N^i_{QCD})] + N^i_{fixed}. \tag{5.6}$$

The fit minimizes the negative log likelihood by calculating it over a 1000 points in f, the qcd fraction, from 0 to 0.999.

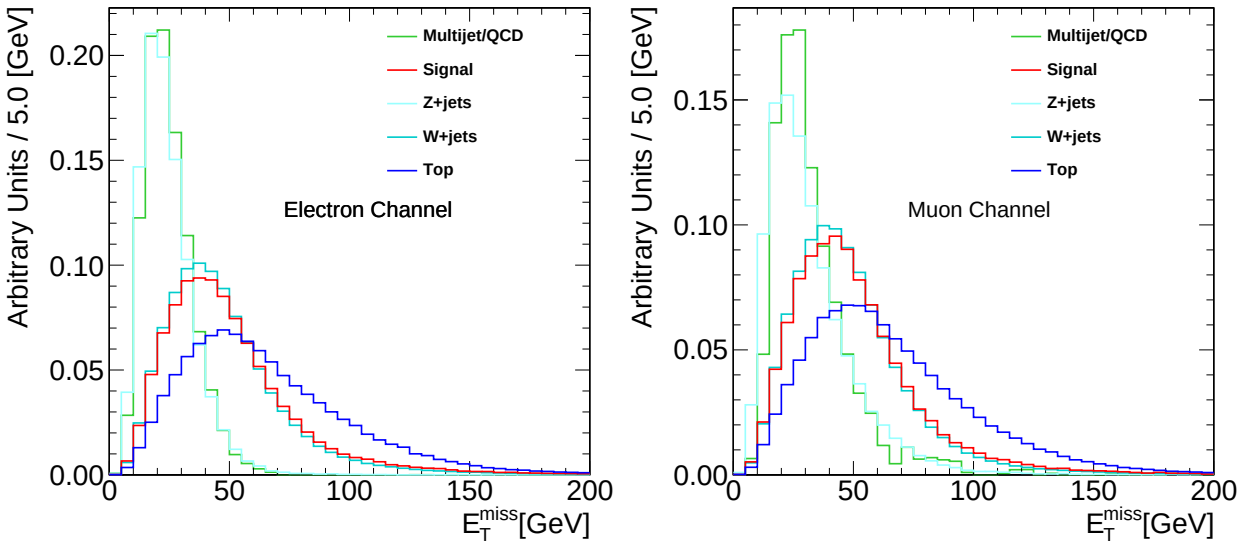

Figure 5.5: E_T^{miss} distributions for all processes for the electron (left) and muon (right) channels after applying all selection criteria but the $E_T^{\text{miss}} > 30$ GeV cut. The distributions are normalized to the same area.

Figure 5.6 shows the negative log likelihood distribution used to calculate the QCD normalization and W/Z+jets scale factor as a function of the QCD fraction. The minimum of the negative log likelihood is the fraction of reduced data events (the data yield after substraction of the fixed backgrounds) that represents the multijet background after all selection criteria, not including the E_T^{miss} cut. Figure 5.7 shows the E_T^{miss} distribution for the data after requiring all selection criteria, overlaid with the result of the fit for the electron channel (left) and muon channel (right).

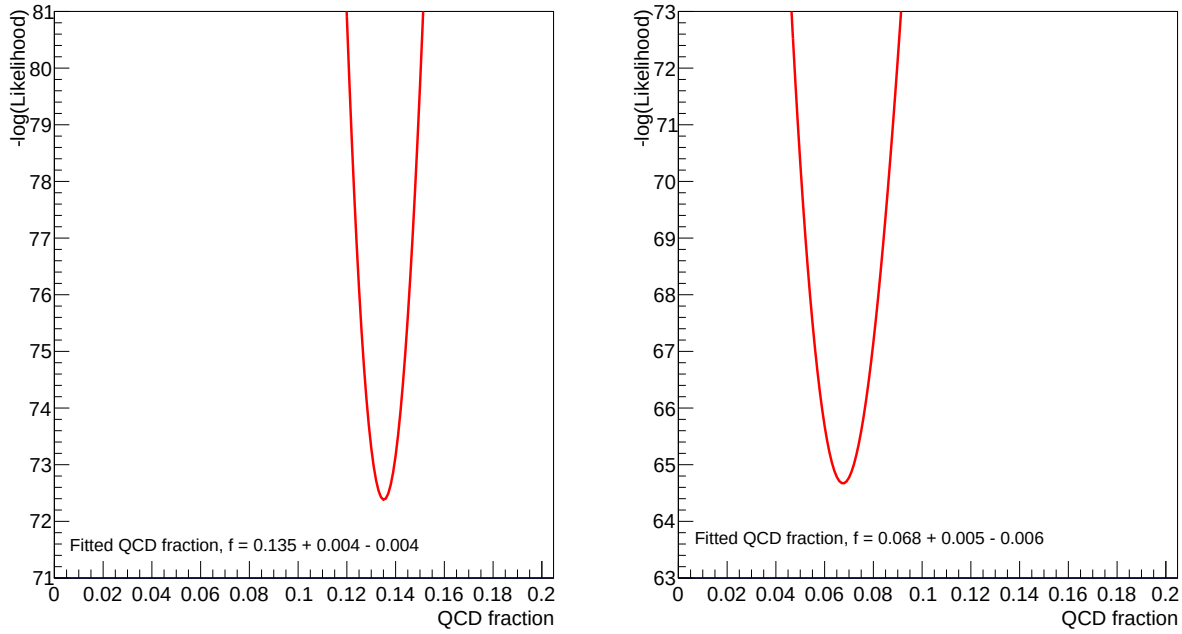

Figure 5.6: Distributions showing the negative log likelihood fit to the full E_T^{miss} spectrum used to obtain the total fraction of multijet events in the signal region for the electron (left) and muon (right) channels. The fitted QCD fraction represents the total fraction of multijet events in the data after applying all selection criteria except for the E_T^{miss} cut and after substracting the fixed backgrounds (signal and top).

The fraction of the QCD MJ contribution in the signal region ($E_T^{\text{miss}} > 30$ GeV) is found to be 5.3% and 3.7% for electron and muon channels respectively. The correction factors applied to the W/Z+jets processes are 0.993 ± 0.005 for the electron channel and 0.965 ± 0.006 for the muon channel.

It should be noted that the MET likelihood fit only takes into consideration the statistical uncertainty of the data and MC samples, and does not include any of the normalization and/or template shape systematics associated with the W/Z+jets and QCD MJ processes, resulting in poor goodness-of-fit results. In section 7.4, shape systematics and validation studies on the QCD contribution for the cross section fit have been conducted and show that the estimate for the QCD process with the inclusion of its systematics is in good agreement within systematic uncertainties. Additionally, it should be stated that since the

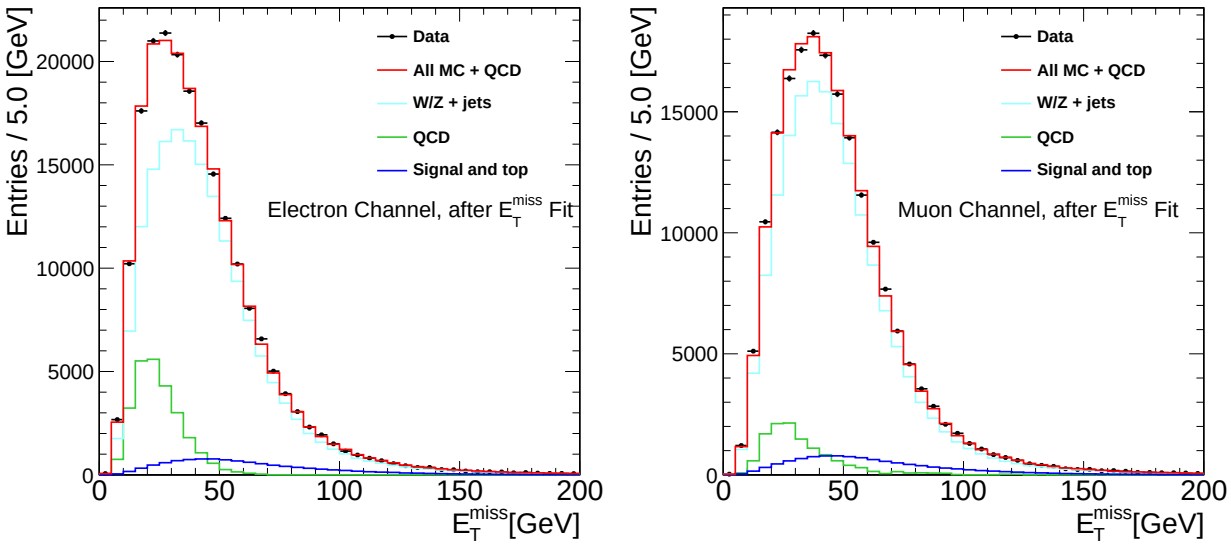

Figure 5.7: E_T^{miss} distributions shown after applying the scale factor corrections to W/Z+jets and the QCD multijet normalization given by the E_T^{miss} likelihood fit for the electron (left) and muon (right) channels.

E_T^{miss} distribution shapes for the W/Z+jets and signal processes are very similar, that the presence of the signal at a percent level does not affect the QCD normalization result due to allowing the W/Z+jets normalization to float.

5.5.2 Selection Yields

Table 5.5 shows the expected numbers of events for the signal and background processes after the full selection (including the E_T^{miss} cut) has been applied. The number of events observed in data, the signal to background ratio and signal efficiency in the range $60 < m_{\text{jj}} < 120$ GeV are also listed. The signal efficiency is defined as the ratio of the number of WW+WZ events passing all selection criteria and in the region $60 < m_{\text{jj}} < 120$ GeV over the total number of generated events for the WW+WZ processes. The m_{jj} distribution after applying all selection criteria is shown in figure 5.8.

5.6 Pre-fit Distributions

This section contains kinematic distributions that show the level of agreement between MC and data that is obtained prior to the cross section fit to m_{jj} . The systematic uncertainty bands are composed of the Jet Energy Scale (JES), Jet Energy Resolution (JER), ΔR(jet,parton), and qfac systematics which are described in chapter 7. The χ^2/ndf is calculated only using the statistical uncertainty and therefore does not reflect the level of agreement that is achieved once the systematic bands are considered. Figure 5.9 shows the dijet invariant mass distribution for both lepton channels, the level of agreement between

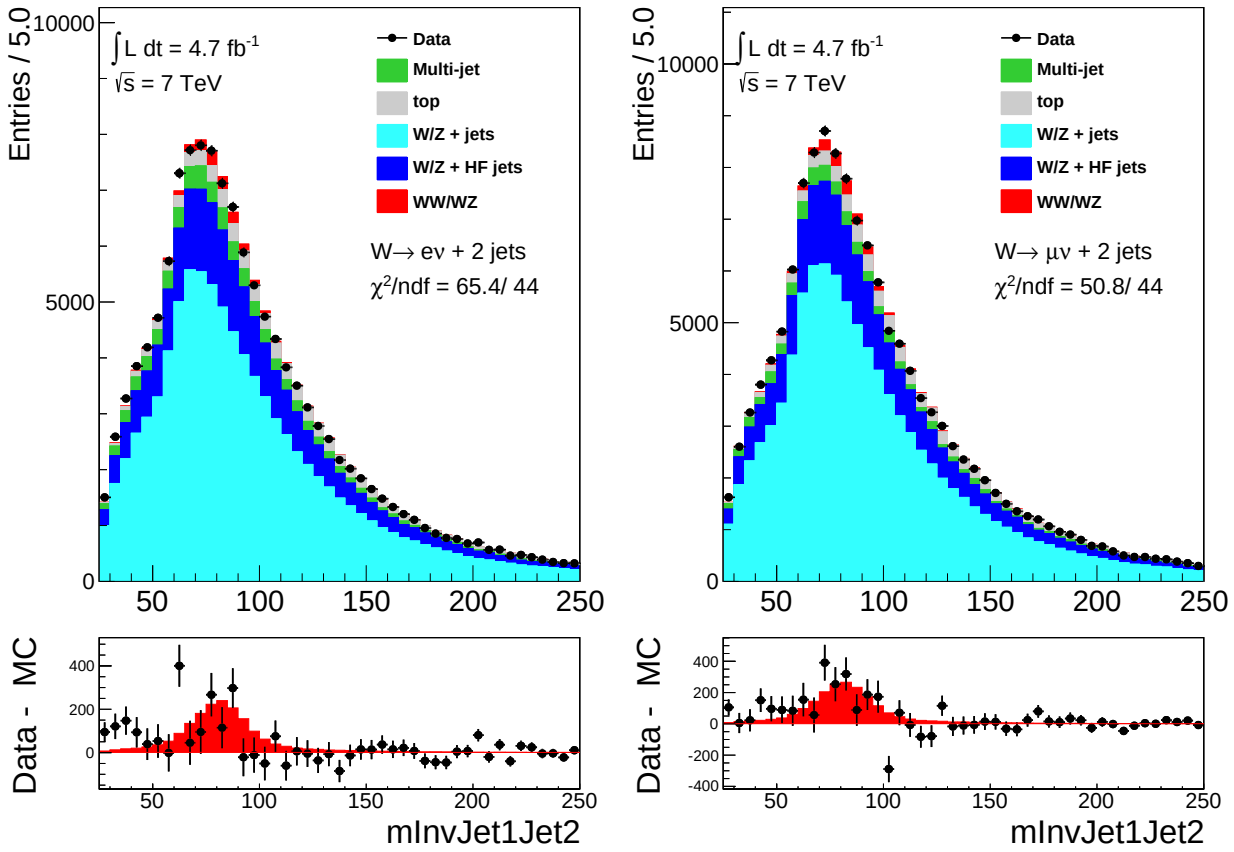

Figure 5.8: Comparison of the m_{jj} distributions for data (solid circles) and the SM predictions shown as stacked histograms for the electron (left) and muon (right) channels. The right−most bins include the overflow. The plots in the lower panel show the difference between data and the MC background prediction (solid circles) overlaid on the signal (red histogram).

Process	e	μ
WW	1435 ± 70	1603 ± 79
WZ	334 ± 23	370 ± 26
W+ jets	$(107 \pm 21) \times 10^3$	$(116 \pm 23) \times 10^3$
Z+ jets	$(55.4 \pm 11.1) \times 10^2$	$(46.3 \pm 9.3) \times 10^2$
$t\bar{t}$	$(47.2 \pm 7.1) \times 10^2$	$(47.2 \pm 7.1) \times 10^2$
Single top	$(20.2 \pm 3.0) \times 10^2$	$(20.5 \pm 3.1) \times 10^2$
Multijet	$(67.3 \pm 10.1) \times 10^2$	$(50.5 \pm 7.6) \times 10^2$
ZZ	19.2 ± 3.8	21.1 ± 4.2
Total SM prediction	$(128 \pm 17) \times 10^3$	$(135 \pm 19) \times 10^3$
Total Data	127650	134846
Signal efficiency for 60 $< m_{\mathrm{jj}} <$ 120 GeV	1.9%	1.6%
Signal to background ratio for 60 $< m_{\mathrm{jj}} <$ 120 GeV	2.02%	2.13%

Table 5.5: Total number of events in data and expected yields for each process. The multijet and W/Z+jets yields are obtained from the fit to the E_T^{miss} distribution as explained in Section 5.5.1. Uncertainties for the expected signal yields are based on the corresponding cross section uncertainties, while for QCD multijet and the other backgrounds the uncertainties correspond to the assumed normalization uncertainty discussed in chapter 7. The last two rows list the signal efficiency and signal to background ratio for the two channels.

data and MC is very good and within the systematic bands. The $\Delta R(Jet_1, Jet_2)$ is shown in the top half of figure 5.11 and shows that the data-MC uncertainties lie within W/Z+jets modeling systematics. The few points below $\Delta R(Jet_1, Jet_2) < 0.7$ represent events with a $p_{\mathrm{T}}(jj)$ greater than 250 GeV. The remaining plots are for validating the object kinematics of the $\ell\nu jj$ selection. Distributions of the leading and second-leading jet transverse momentums can be seen in figure 5.10. The lepton p_T, E_{T}, and transverse invariant mass are shown in figures 5.11 and 5.12, respectively.

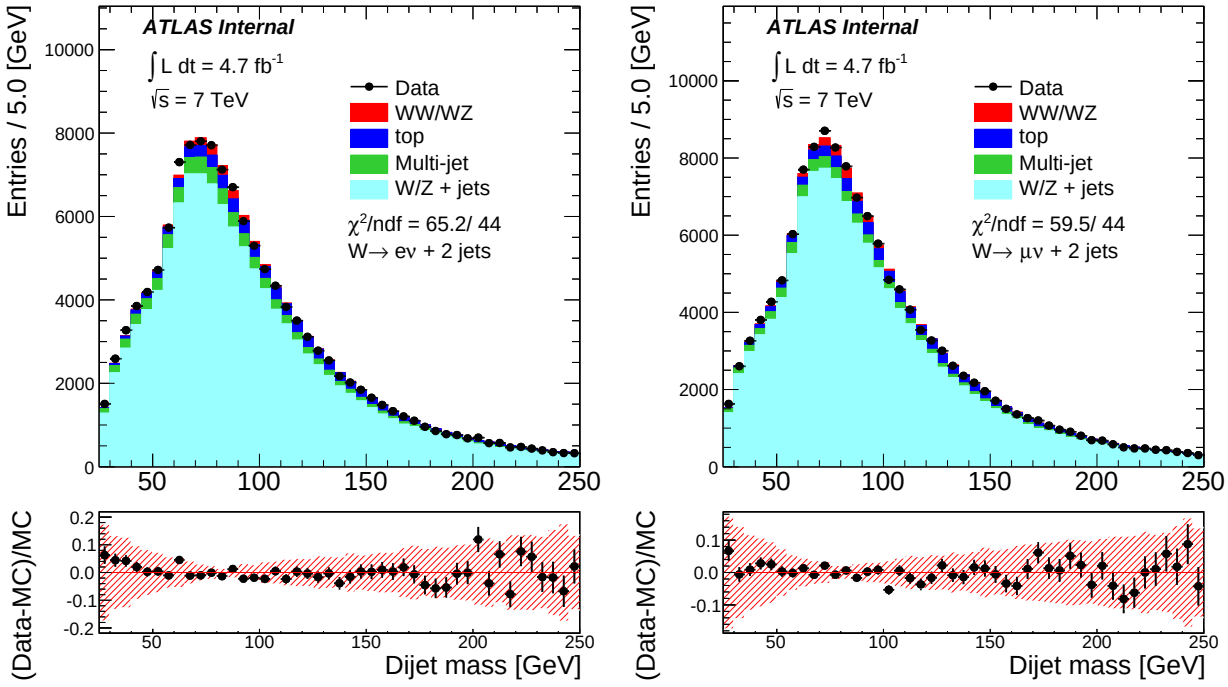

Figure 5.9: Distributions of dijet invariant mass m_{jj} for electron (left) and muon (right) channels. The points are data and the stacked histograms are SM predictions. In each plot, the lower panel displays the relative difference between the data and the MC expectation. The systematic band only contains systematics due to JES, JER, ΔR(jet,parton), and qfac.

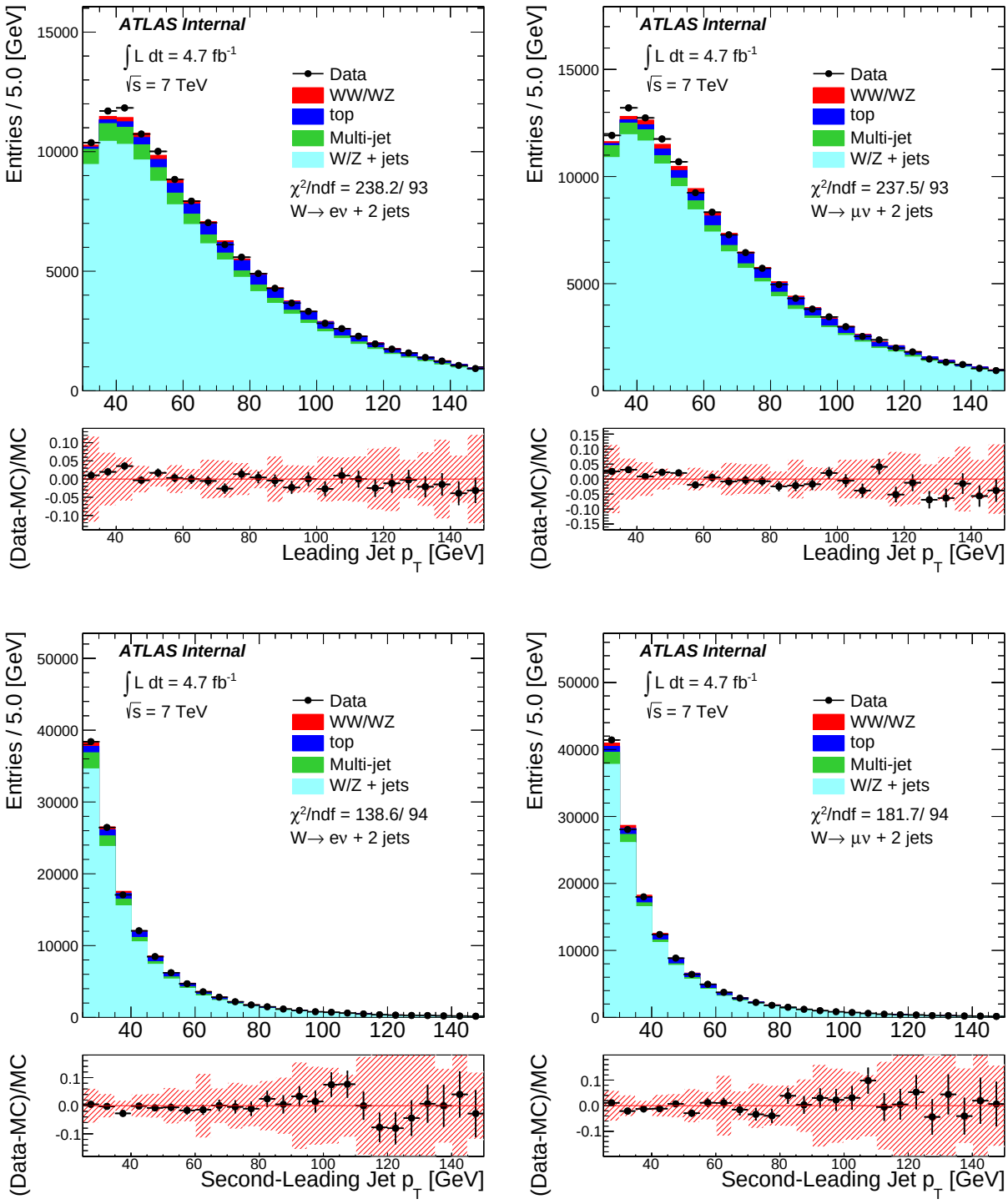

Figure 5.10: Distributions of the leading (top) and sub-leading (bottom) jet transverse moment for electron (left) and muon (right) channels. The points are data and the stacked histograms are SM predictions. In each plot, the lower panel displays the relative difference between the data and the MC expectation. The systematic band only contains systematics due to JES, JER, ΔR(jet,parton), and qfac.

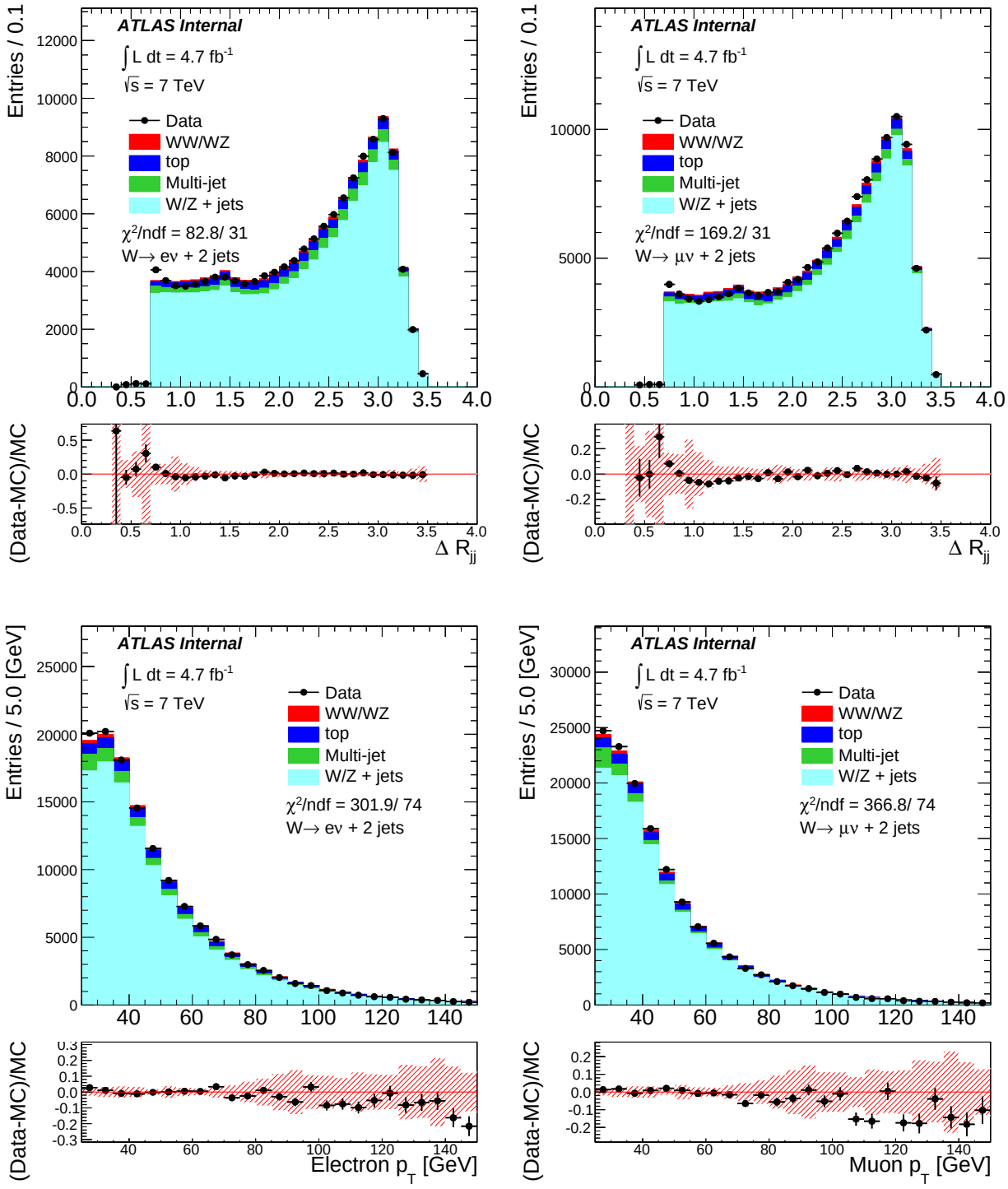

Figure 5.11: Distributions of the angular distance ΔR between the leading and subleading jets (top) and lepton p_T (bottom) for electron (left) and muon (right) channels. The points are data and the stacked histograms are SM predictions. In each plot, the lower panel displays the relative difference between the data and the MC expectation. The systematic band only contains systematics due to JES, JER, ΔR(jet,parton), and qfac.

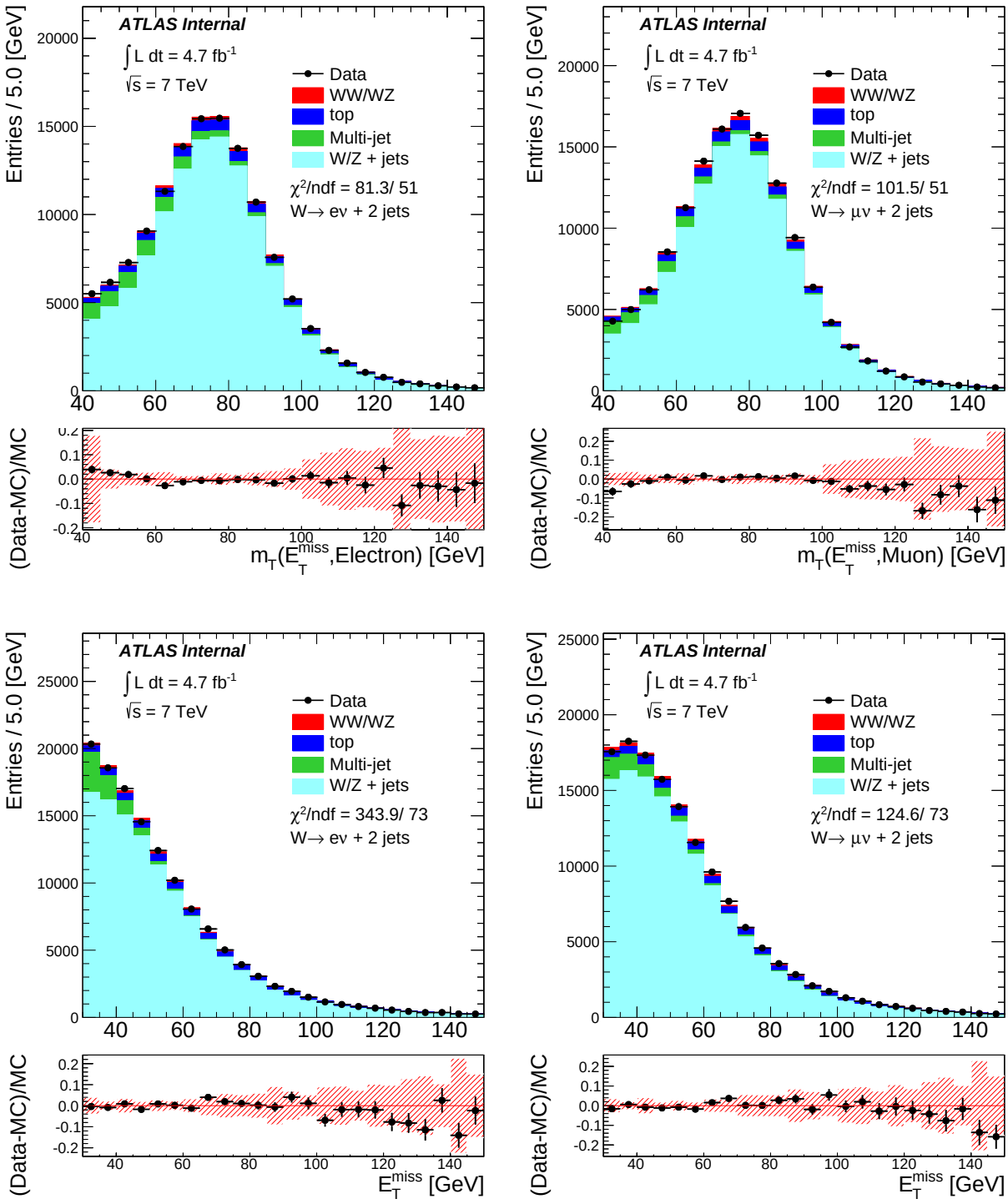

Figure 5.12: Distributions of the transverse mass m_{T} (top) and the missing transverse energy E_T^{miss} (bottom) for electron (left) and muon (right) channels. The points are data and the stacked histograms are SM predictions. In each plot, the lower panel displays the relative difference between the data and the MC expectation. The systematic band only contains systematics due to JES, JER, ΔR(jet,parton), and qfac.

Chapter 6

Procedure for the Cross Section Measurement

The measured signal yield is extracted from a binned maximum likelihood fit to the m_{jj} distribution of the data. Four templates representing the WW+WZ, W/Z+jets, top ($t\bar{t}$ and single top), and the QCD MJ processes are constructed and normalized to the integrated luminosity as detailed in section 5.5 to provide the initial SM prediction for the fit. The parameter of interest returned by the fit is a multiplicative factor, β, also known as the signal strength.

The likelihood combines the muon and electron channels into one likelihood function in order to correctly account for correlations between the two channels. The function is expressed as:

$$\mathrm{L}(\beta,\vec{\alpha}) = \prod_{\ell=e,\mu}\prod_{b=1,45} \mathrm{Pois}(n_{\ell b}|(v_{\ell b}^{bkg} + \beta v_{\ell b}^{sig})(\vec{\alpha})) \cdot \prod_{\mathrm{p=parameters}} f_p(\alpha_p) \tag{6.1}$$

where $n_{\ell b}$ is the number of data events in bin b and channel ℓ, with $b = 1$ to 45 and $\ell = e, \mu$. $v_{\ell b}^{bkg}$ and $v_{\ell b}^{sig}$ are the expected number of events in bin b for channel ℓ for the background and signal processes respectively. $f_p(\alpha_p)$ is the functional constraint on the nuisance parameters α_p. More details about the likelihood and how the nuisance parameters are handled will be discussed in chapter 8. It is important to note at this time that the extracted β value multiplied with the expected signal normalization ($N_\ell^{expected}$) gives the total number of signal events in data (N_ℓ^{meas}) for a given lepton channel ℓ as shown in equation 6.2.

$$N_\ell^{meas} = \beta N_\ell^{expected}; N_\ell^{meas} = \beta \sum_{b=1,45} v_{\ell b}^{sig} \tag{6.2}$$

Likewise, for this analysis the signal strength multiplied with the predicted SM total cross section for WW+WZ returns the measured SM total cross section.

$$\sigma_{tot}^{meas} = \beta \sigma_{tot}^{predicted} \tag{6.3}$$

Its important to note that the cross section fit is being done in a region of phase space that corresponds to the imposed event selection, therefore the returned β extracted by the fit applies directly to a particular fiducial volume which is a subset of the total phase space.

The total cross section can be calculated by extrapolating the measured fiducial cross section to the total phase space using theoretical predictions. This extrapolation is performed by first calculating the theoretical cross section in the fiducial volume defined in the following section.

6.1 Fiducial Volume Selection

A common fiducial volume is defined for the electron and muon channels. All selection criteria is applied at the particle level (event generation) against truth objects and represents a selection that closely resembles the event selection applied on reconstructed events.

First, the fiducial selection requires that the event decays semileptonically, $WW/WZ \to \ell\nu jj$, with ℓ being either a muon or electron[1]. The lepton coming directly from the leptonic W decay has the four momentum of all photons lying within a $\Delta R < 0.1$ of the selected lepton added to the lepton's four momentum in order to take into account final state QED radiation. The newly 'dressed' lepton is then required to have a $p_{\mathrm{T}} > 25$ GeV and $|\eta| < 2.47$. The neutrino coming from the $W \to \ell\nu$ decay represents the E_T^{miss} and is required to be greater than 30 GeV. The transverse mass m_{T} constructed using the dressed lepton and neutrino from the leptonically decaying W is required to be greater than 40 GeV.

Events are required to have exactly two particle−level anti−kt jets with a $p_{\mathrm{T}} > 25$ GeV, $|\eta| < 2.8$, and be separated from the dressed lepton by $\Delta R > 0.5$. The leading jet is required to have a $p_{\mathrm{T}} > 30$ GeV and both jets must be within $|\eta| < 2.0$. Additionally the same angular cuts applied in the event selection are applied to these particle−level objects: $|\Delta\phi(E_T^{\mathrm{miss}}, Jet_1)| > 0.8$, $|\Delta\eta(Jet_1, Jet_2| < 1.5$, and $\Delta R(Jet_1, Jet_2) > 0.7$ or $p_{\mathrm{T}}(jj) > 250$ GeV. Lastly the dijet invariant mass of the particle-level jets must satisfy the m_{jj} window of the cross section measurement, $25 < m_{\mathrm{jj}} < 250$ GeV.

A cutflow of the fiducial selection can be found in the figure C.4 of the appendix.

6.2 Extrapolation to the Total Cross section

The standard cross section formulas that relate the measured signal yield N^{meas} to the fiducial (σ_{fid}) and total (σ_{tot}) cross section are:

$$\sigma_{fid} = \frac{N^{meas}}{\mathcal{L}_{int} \cdot C} \tag{6.4}$$

$$\sigma_{tot} = \frac{\sigma_{fid}}{A \cdot B} \tag{6.5}$$

where $\mathcal{L}_{int}$ is the integrated luminosity, B is the branching ratio for $WW/WZ \to \ell\nu jj$, A is the signal acceptance of events passing the fiducial volume selection, and C is the correction factor accounting for the differences in yields between the event selection and the fiducial

[1]Tau decays are not included

volume selection. The equations for A and C are

$$A = \frac{N_{fid}^{truth}}{N_{Gen}^{WW/WZ\to\ell\nu jj}}; \qquad C = \frac{N_{fid}^{reco}}{N_{fid}^{truth}} \tag{6.6}$$

where N_{fid}^{truth} is the number of events passing the fiducial volume selection, $N_{Gen}^{WW/WZ\to\ell\nu jj}$ is the total number of generated $WW/WZ \to \ell\nu jj$ events, and N_{fid}^{reco} is the number of events passing the event selection at reconstruction-level[2]. The relevant values used to calculate A and C for both lepton channels and samples are shown in appendix C.

The above general equations for the fiducial and total cross section only take into account a single process. In this analysis, the cross section measurement is performed over two processes[3], WW and WZ, which contain their own unique cross section, branching ratio, and correct factors (A and C). Therefore a new generalization of equations 6.4 and 6.5 for two processes is required. The fiducial cross section can be rewritten as

$$\sigma_{fid} = \frac{N^{meas}}{\mathcal{L}_{int} \cdot D_{fid}} \tag{6.7}$$

where D_{fid} is defined as:

$$D_{fid} = f_{fid}^{WW} \cdot C^{WW} + (1 - f_{fid}^{WW}) \cdot C^{WZ} \tag{6.8}$$

$$f_{fid}^{WW} = \frac{1}{1 + \frac{\sigma_{WZ,\mathrm{MC@NLO}} \cdot A^{WZ} \cdot B^{WZ}}{\sigma_{WW,\mathrm{MC@NLO}} \cdot A^{WW} \cdot B^{WW}}} \tag{6.9}$$

and the factor f_{fid}^{WW} is the ratio between the WW fiducial cross section and the WW+WZ fiducial cross section, and B^{WZ} and B^{WW} are the semileptonic branching ratios to a single lepton flavor for the given process. A similar generalization for the total cross section equation can be written as

$$\sigma_{tot} = \frac{N^{meas}}{\mathcal{L}_{int} \cdot D_{tot}} \tag{6.10}$$

where D_{tot} is defined as:

$$D_{tot} = f_{tot}^{WW} \cdot (C \cdot B \cdot A)^{WW} + (1 - f_{tot}^{WW}) \cdot (C \cdot B \cdot A)^{WZ} \tag{6.11}$$

$$f_{tot}^{WW} = \frac{1}{1 + \frac{\sigma_{WZ,\mathrm{MC@NLO}}}{\sigma_{WW,\mathrm{MC@NLO}}}} \tag{6.12}$$

The theoretically calculated values for D_{fid} and D_{tot} used in this analysis are shown in table 6.1, separately for the electron and muon channels. The fiducial cross section is calculated separately for each lepton channel and then summed together to calculate the full fiducial cross section.

[2]This includes non $WW/WZ \to \ell\nu jj$ events, as well as tau decays

[3]Technically we have three processes: WW, W^-Z, and W^+Z so the following generalization is redone for three processes in the calculation for D_{fid} and D_{tot}

	MC@NLO SM+aTGC
Muon	
D_{fid}	0.683
D_{tot}	7.01E-03
Electron	
D_{fid}	0.622
D_{tot}	6.29E-03

Table 6.1: Table shows the calculated values for D_{fid} and D_{tot} in both channels using the SM and aTGC (reweighted to SM) samples combined. The values calculated using the SM signal samples and the aTGC signal samples separately are shown in figure C.3 of the appendix.

Systematic uncertainties on the fiducial and total cross section are calculated by summing in quadrature the uncertainites evaluated on the signal yield N^{meas}, the factors D_{fid} and D_{tot}, and lastly the integrated luminosity. The sources of the systematic uncertainties are discussed in chapter 7, while their implementation into the fit are discussed in chapter 8.

Chapter 7

Evaluation of the Systematics

The systematic uncertainties for this analysis are discussed in the following sections. For the cross section measurement, uncertainties are considered for N_{meas}, D_{fid}, D_{tot}, and the luminosity calculation. As introduced briefly in chapter 6, the number of signal events N_{meas} is extracted from a likelihood fit to the m_{jj} distribution. Therefore, systematic sources that may affect N_{meas} consist of effects that alter the normalization and/or modeling of the nominal background and signal m_{jj} templates. Systematics in this chapter are discussed individually for the four composite processes (templates) used in the m_{jj} fit: WW+WZ signal, W/Z+jets (includes ZZ), top (including $t\bar{t}$ and single top processes), and the QCD multijet background. Each systematic is either handled as a nuisance parameter in the cross section fit or evaluated using pseudo-data produced through the use of toy datasets. Their treatment in regards to their implementation in the fit and the total measurement uncertainty are discussed further in chapter 8.

Normalization uncertainties for the signal are evaluated through the D_{fid} and D_{tot} factors (discussed in chapter 6) and are propagated to the cross section measurement assuming that they are uncorrelated to the N_{meas} extracted from the fit.

The aTGC study uses a very similar, yet reduced set of systematics than what are considered for the cross section measurement. Only systematics that have a significant effect on the $p_{\mathrm{T}}(jj)$ normalization and shape distribution, particularly in the distribution's tail, are considered. Further discussion on the differences in the systematic evaluations are discussed in section 10.2.

7.1 Uncertainty on the Jet Measurement

The uncertainties due to changes in the Jet Energy Scale (JES) and the Jet Energy Resolution (JER) are estimated independently from one another. The JES uncertainty corresponds directly to the calibration scheme utilized for jet objects discussed in section 3.5. Their evaluation is based on a detailed study [22] considering uncertainties due to the calorimeter energy scale, dead material in the detector, cluster reconstruction algorithm, fragmentation, underlying event, and the pile-up modeling. The total uncertainty on the transverse momentum of the jet ranges from 1 to 6% dependent on the η and p_{T} of the jet candidate. As an example, figure 7.1 shows the total fractional jet energy scale uncertainty

as a function of jet p_{T} for an η value of 0.5.

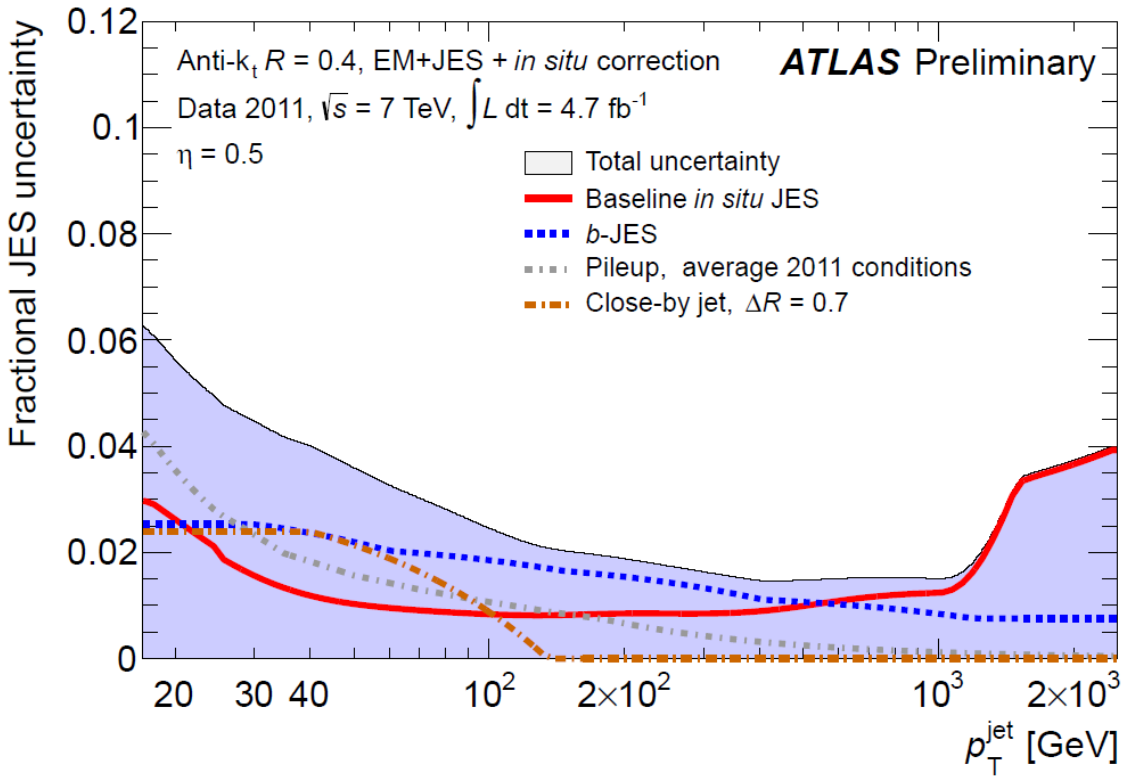

Figure 7.1: Fractional jet energy scale systematic uncertainty as a function of the transverse momentum of the jet for jets with an $\eta = 0.5$. Figure from [22]

Evaluation of the uncertainty on the jet objects for the signal and MC background processes are handled similarly, therefore to avoid any unnecessary repetition this important systematic will be discussed jointly in the following sections. Additionally, the JES and JER uncertainties affect both the shape and the normalization of the templates. Due to several systematic contributions also affecting the normalization for each process and no easy way to disentangle their correlations, a single global normalization or production rate uncertainty based on the cumulative systematic effects of each source is used in the cross section fit for the different templates and discussed in the relevant sections of this chapter corresponding to the individual processes.

7.1.1 Jet Energy Scale Uncertainty

The JES uncertainty is decomposed into sixty-four baseline nuisance parameters [22, 30]. From this a combined and reduced set of sixteen parameters is identified in which the correlations between the composite parameters are minimized and considered independent. These 16 components, labeled JES1–JES16, are described briefly in table 7.1 and are used to evaluate the JES uncertainty in this analysis. From the reduced set of sixteen components,

JES component	Description
JES1-6[1]	Effective *in situ* component 1-6
JES7	Eta intercalibration: stat uncertainties
JES8	Eta intercalibration: MC generator modelling uncertainty
JES9	High Pt term (temporary, 2010 uncertainty) **(N.A.)**
JES10	Closure of the calibration, relative to MC11b **(N.A.)**
JES11	NPV pile-up
JES12	Mu pile-up
JES13	Close-by jet
JES14	Flavor composition of jets
JES15	Flavor response
JES16	b-jet uncertainty

Table 7.1: Description of the sixteen different JES components corresponding to the reduced set of components mentioned in Ref. [30], plus the flavor and topology uncertainties mentioned in the same reference. JES9 and JES10 do not apply to this analysis, and so are not used. The effective *in situ* components describe the uncertainties from the *in situ* calibration of the JES, including correlations.

two of the uncertainties (JES9 and JES10) are not applicable to this analysis, so only fourteen components are considered.

The effect of each of these JES components are considered by reevaluating the effect of the event selection in all MC processes after applying an upward or downward shift to the jet objects dependent on a single varied JES component. The size of the variation corresponds to one standard deviation on the measurement of each JES component. Any changes to the jet 4-vector is propagated to the E_T^{miss} calculation prior to the event selection. The end results are a total of twenty-eight systematically varied distributions of the m_{jj} spectra corresponding to the up and down one sigma variations of the remaining fourteen JES components. These templates are each normalized to the nominal event yield in order to take into account only the shape variations caused by each JES component (normalization uncertainties handled separately). An example of one of these sets of templates for the JES13 component in the muon channel can be seen in figure 7.2. The additional templates can be found in appendix B.1. The general consensus is that the shape effect of each JES component is small and mostly has an effect on the low m_{jj} region.

7.1.2 Jet Energy Resolution Uncertainty

The JER uncertainty is measured in data and MC with QCD dijet events using in-situ techniques (dijet balance and bi-sector method) [59]. The agreement with the MC simulation jet resolution is within 10%, dependent on the jet p_{T} and η. The JER uncertainty in this analysis is done by scaling each jet by a random factor pulled from a Gaussian distribution with a mean of 1 and a sigma equal to the square root of the quadratic difference between the MC resolution measurement and its measured uncertainty [132]. Like the JES uncertainty, these variations are propagated until the end of the event selection and JER varied systematic

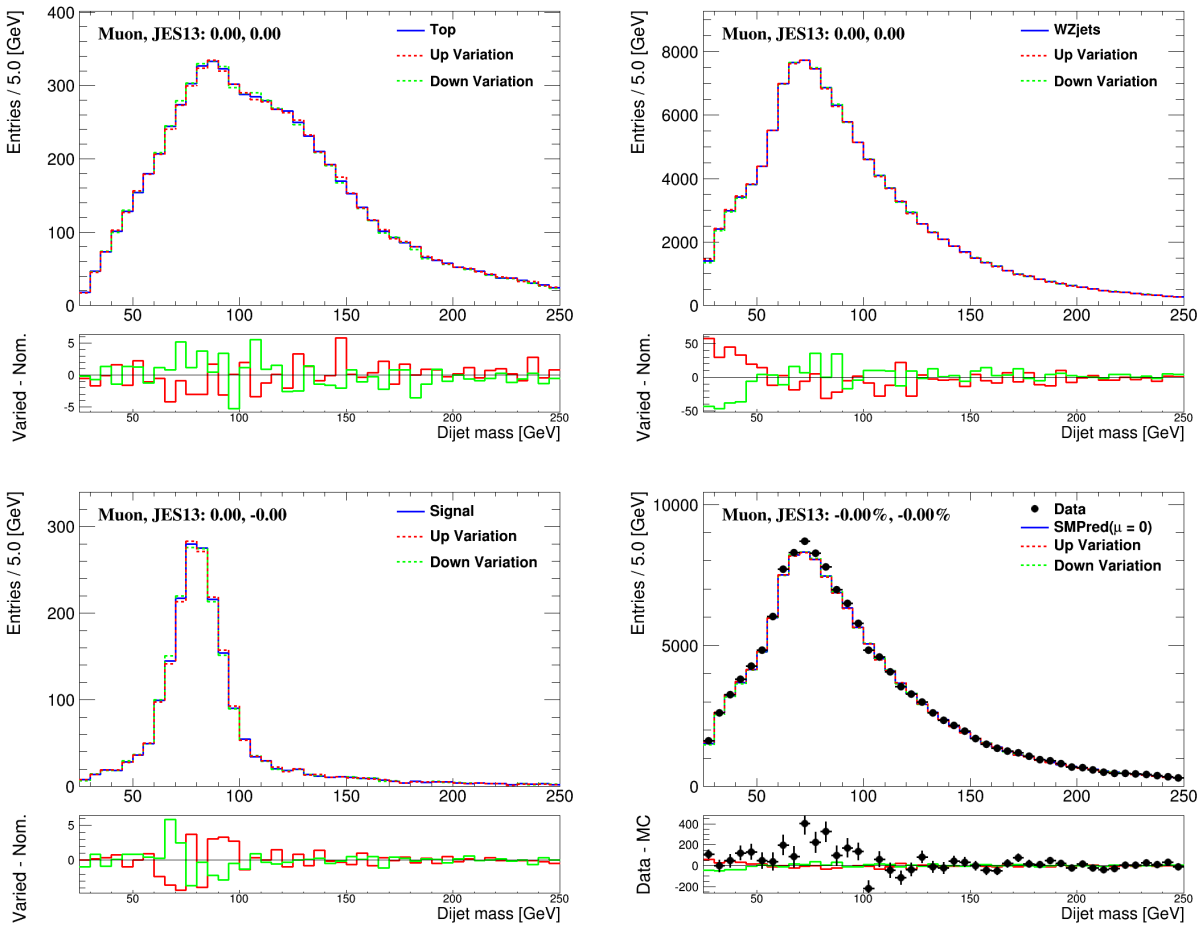

Figure 7.2: Muon Channel: m_{jj} templates for the top (top left), W/Z+jets (top right), and signal (bottom left) processes are shown. For the top panels, the nominal (blue) templates are compared with the up and down systematically varied templates corresponding to the JES13 component. The bottom panels show the difference between each varied template and the nominal template. The bottom right plot contains all the data passing the event selection overlayed with the nominal and varied templates assuming a signal yield of 0 ($\beta = 0$). The bottom panel of the bottom right plot contains the difference between the data and the nominal prediction ($\beta = 0$) in black and the difference between the systematic variation and the nominal prediction in green/red.

templates (shape only) are produced. In order to implement the JER variation into the fit, the systematically varied template is symmetrized with respect to the nominal template to make an up and down varied template similarly to what is done for the JES uncertainty. This can be seen in figure 7.3 for the electron channel[2].

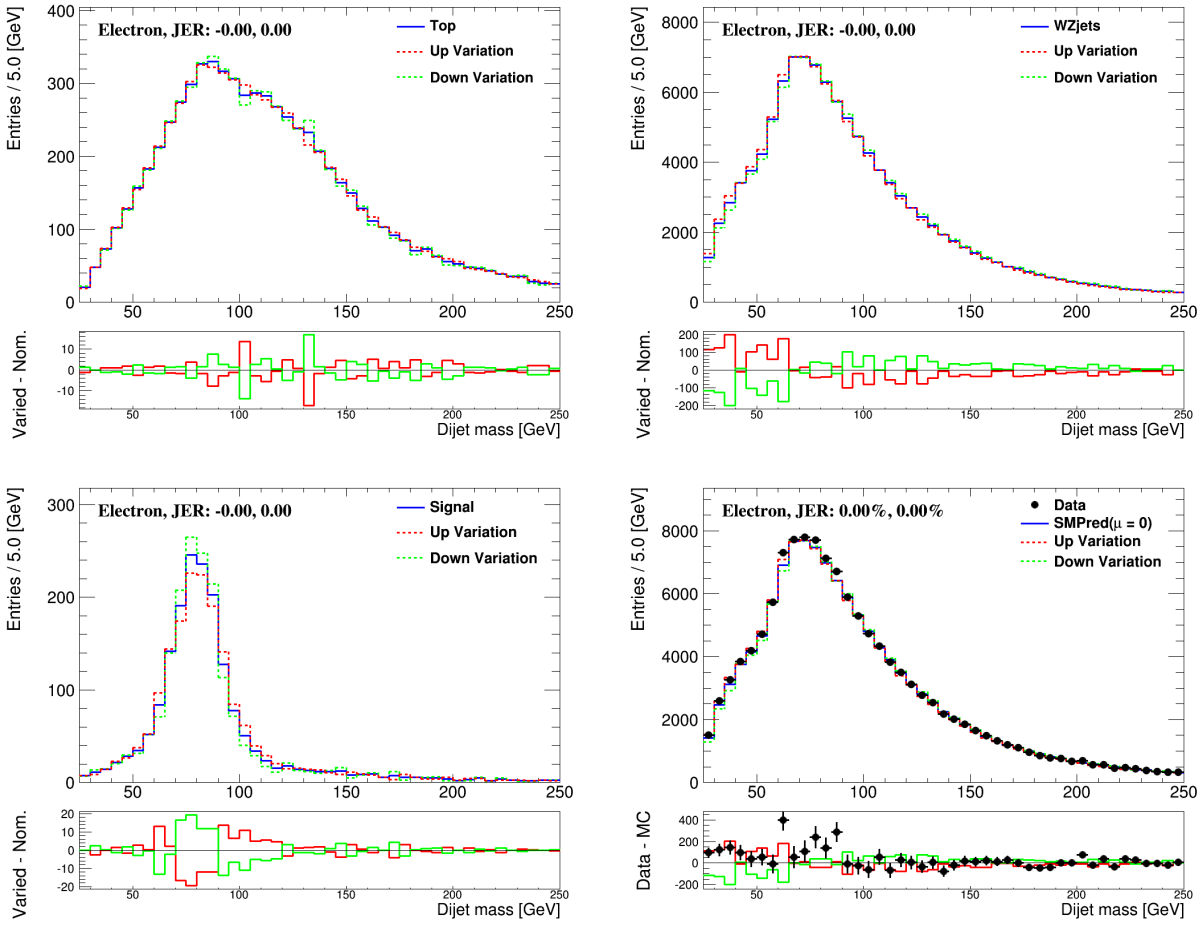

Figure 7.3: Electron Channel: m_{jj} templates for the top (top left), W/Z+jets (top right), and signal (bottom left) processes are shown. For the top panels, the nominal (blue) templates are compared with the up and down systematically varied templates corresponding to the JER component. The bottom panels show the difference between each varied template and the nominal template. The bottom right plot contains the data passing event selection overlayed with the nominal and varied templates assuming a signal yield of zero ($\beta = 0$). The bottom panel of the bottom right plot contains the difference between the data and the nominal prediction ($\beta = 0$) in black and the difference between the systematic variation and the nominal prediction in green/red.

[2]muon channel shown in figure 7.3 of appendix B.1

7.1.3 JES/JER Normalization Uncertainty: W/Z+jets and top processes

The production rate effect (difference in yields after event selection) of each JES and JER component to the W/Z+jets (tables B.1, B.2) and top (tables B.3, B.4) processes can be found in appendix B.1 for each lepton channel. The total normalization uncertainty due to JES and JER are calculated to be approximately 8% and 6%, for W/Z+jets and top respectively. This is taken into consideration when determining the global normalization uncertainty for each template used in the fit.

7.1.4 JES/JER Normalization Uncertainty: WW/WZ processes

Normalization uncertainties that affect the signal processes are considered as systematics for the cross section through the D_{fid} and D_{tot} factors. The effect of the JES and JER uncertainty variations have been calculated for D_{fid} by varying each JES component and JER by their uncertainties for all factors that enter into D_{fid} definition. The effect of each component is shown in Tables 7.2 and 7.3 for the electron and muon channels respectively. The total uncertainty considered for D_{fid} is 6%. Since the JES and JER variations only enter into the reconstruction acceptance, C, the uncertainty calculated in D_{fid} is by definition the same systematic uncertainty as would be calculated in D_{tot} .

Muon Channel	**MC@NLO SM samples only**			
JES/JER Systematic on D_{fid}	$+\sigma$	**% Diff.**	**-σ**	**% Diff.**
Nominal Values	**0.679**	**N/A**	**0.679**	**N/A**
Effective JES Unc.Component 1	0.684	0.7	0.674	-0.7
Effective JES Unc.Component 2	0.668	-1.6	0.686	1.1
Effective JES Unc.Component 3	0.682	0.5	0.675	-0.6
Effective JES Unc.Component 4	0.678	-0.1	0.679	0.1
Effective JES Unc.Component 5	0.679	0.0	0.679	0.0
Effective JES Unc.Component 6	0.680	0.1	0.678	-0.1
Eta Intercalibration: Stat Unc.	0.681	0.3	0.677	-0.3
Eta Intercalibration: MC Gen. Modelling Unc.	0.683	0.6	0.676	-0.5
NPV Pile-up Uncertainty	0.678	-0.1	0.679	0.0
Mu Pile-up Uncertainty	0.677	-0.2	0.679	-0.0
Close-by Jet Uncertainty	0.679	-0.0	0.678	-0.1
Flavor Comp. Uncertainty	0.700	3.1	0.654	-3.7
Flavor Response Uncertainty	0.690	1.7	0.665	-2.0
b-jet Uncertainty	0.679	0.0	0.679	-0.0
JER	0.666	**-1.9**	0.666	**-1.9**
JES components added in quadrature		**3.9**		**5.1**
JES and JER		**4.4**		**5.4**

Table 7.2: Calculated values for D_{fid} in the muon channel for the SM MC@NLO signal samples after varying the JES components and JER by $\pm\sigma$. % Diff. shows the relative percent difference with respect to the nominal value.

Electron Channel	**MC@NLO SM samples only**			
JES/JER Systematic on D_{fid}	$+\sigma$	**% Diff.**	$-\sigma$	**% Diff.**
Nominal Values	**0.620**	**N/A**	**0.620**	**N/A**
Effective JES Unc.Component 1	0.623	0.4	0.615	-0.8
Effective JES Unc.Component 2	0.610	-1.7	0.626	1.0
Effective JES Unc.Component 3	0.622	0.2	0.616	-0.7
Effective JES Unc.Component 4	0.618	-0.3	0.620	-0.03
Effective JES Unc.Component 5	0.620	-0.1	0.619	-0.1
Effective JES Unc.Component 6	0.620	-0.03	0.619	-0.3
Eta Intercalibration: Stat Unc.	0.621	0.1	0.618	-0.4
Eta Intercalibration: MC Gen. Modelling Unc.	0.621	0.1	0.614	-1.0
NPV Pile-up Uncertainty	0.619	-0.3	0.619	-0.2
Mu Pile-up Uncertainty	0.618	-0.4	0.618	-0.4
Close-by Jet Uncertainty	0.623	0.5	0.618	-0.4
Flavor Comp. Uncertainty	0.639	3.1	0.595	-4.1
Flavor Response Uncertainty	0.630	1.6	0.606	-2.3
b-jet Uncertainty	0.620	0.1	0.620	-0.03
JER	0.605	**-2.5**	0.605	**-2.5**
JES components added in quadrature		**3.9**		**5.1**
JES and JER		**4.7**		**5.7**

Table 7.3: Calculated values for D_{fid} in the electron channel for the SM MC@NLO signal samples after varying the JES components and JER by $\pm\sigma$. % Diff. shows the relative percent difference with respect to the nominal value.

7.2 W/Z+jets Uncertainties

7.2.1 W/Z+jets Modeling Uncertainty

The modeling uncertainties for the W/Z+jets process are evaluated on generated $W \rightarrow \mu\nu + Np$ AFII samples that vary the renormalization/factorization scale (qfac) and the ΔR(jet,parton) ALPGEN parameters as discussed in section 4.3.2. Additionally, for the ΔR(jet,parton) parameter only, high statistics $p_T(W)$ slice samples were produced and are combined with the existing $W \rightarrow \mu\nu + Np$ samples to create a more robust set of ΔR(jet,parton) varied samples. The variations on the shape of m_{jj} in the signal region are derived by calculating a ratio of each parameter variation over the nominal sample m_{jj} template (e.g. [varied qfac = 0.5 template]/[nominal qfac = 1.0 template]). The resulting four ratios corresponding to qfac = 0.5, 2.0 and ΔR(jet,parton) = 0.4, 1.0 are fitted by a polynomial function to smooth any statistical fluctuations. The smoothed systematic ratio distributions calculated from these $W \rightarrow \mu\nu + Np$ samples are then applied to the full nominal W/Z+jets templates as up and down variations for both lepton channels[3]. The shape

[3]Note that for processes in which there are available exclusive systematically varied AFII simulated samples, as in the case for the ΔR(jet,parton) parameter in $W \rightarrow \mu\nu + Np$ samples, those samples are used directly. The fitted ratios are only applied to processes in which there exists no samples with the corresponding systematically varied parameter.

variations for these modeling systematics are shown in figure 7.4.

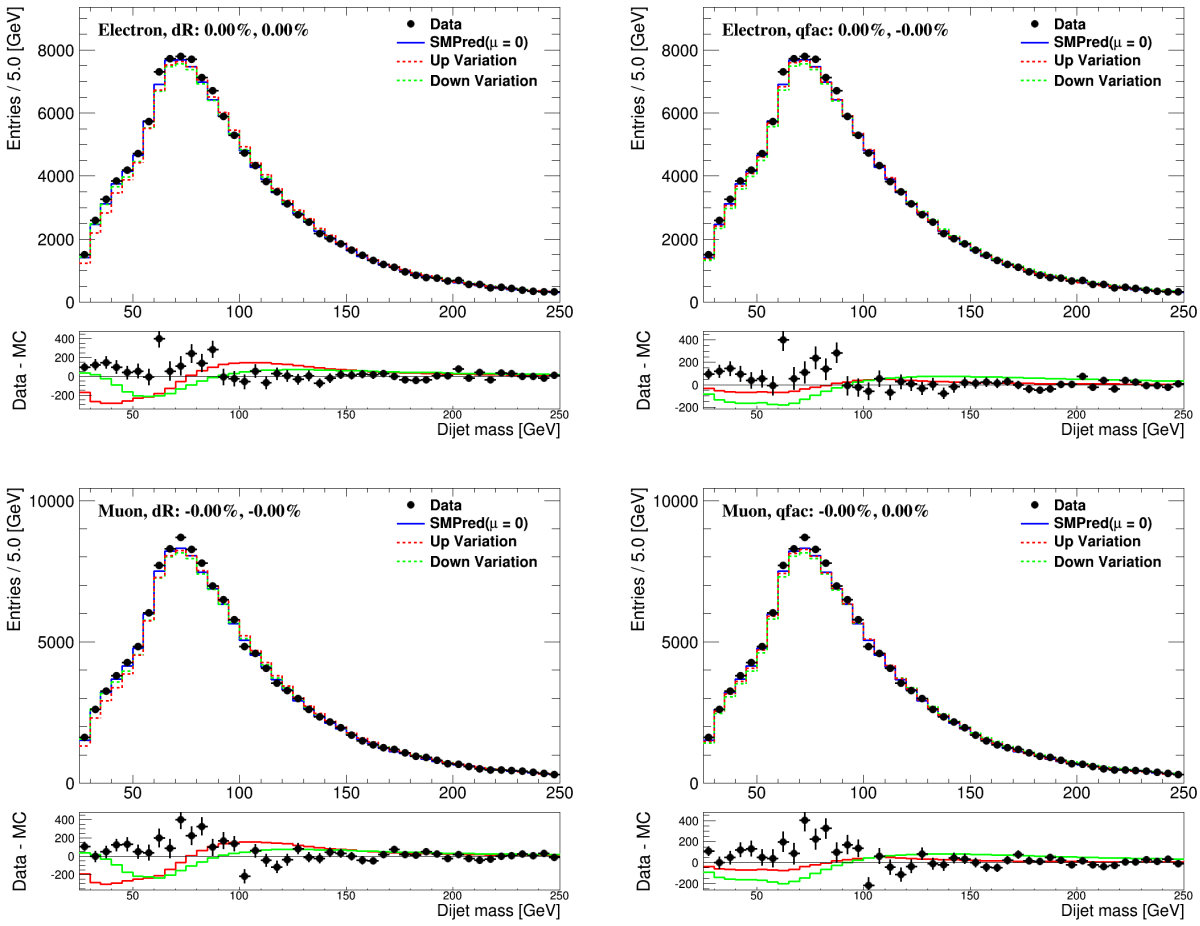

Figure 7.4: A comparison of the m_{jj} distribution in data with the SM prediction assuming zero signal ($\beta = 0$) is shown for the electron (top) and muon (bottom) channel. The figures also show the SM prediction with the included W/Z+jets shape systematics for ΔR(jet,parton) (left) and qfac (right) up and down variations. The bottom panels contain the difference between the data and the nominal prediction ($\beta = 0$) in black and the difference between the systematic variation and the nominal prediction in green/red.

7.2.2 W/Z+jets Normalization Uncertainty

The global normalization uncertainty for W/Z+jets is conservatively calculated to be 20% and is based on the individual normalization uncertainties of the JES, JER, and qfac variations. The effect of this uncertainty in the signal region is seen in figure 7.5. For the cross section fit, the normalization uncertainty for W/Z+jets is considered to be completely correlated among the two lepton channels. Additionally, it should be noted that due to the large contribution of W/Z+jets events in the signal region across the entire m_{jj} distribution, the W/Z+jets production rate will be highly constrained by the cross section fit.

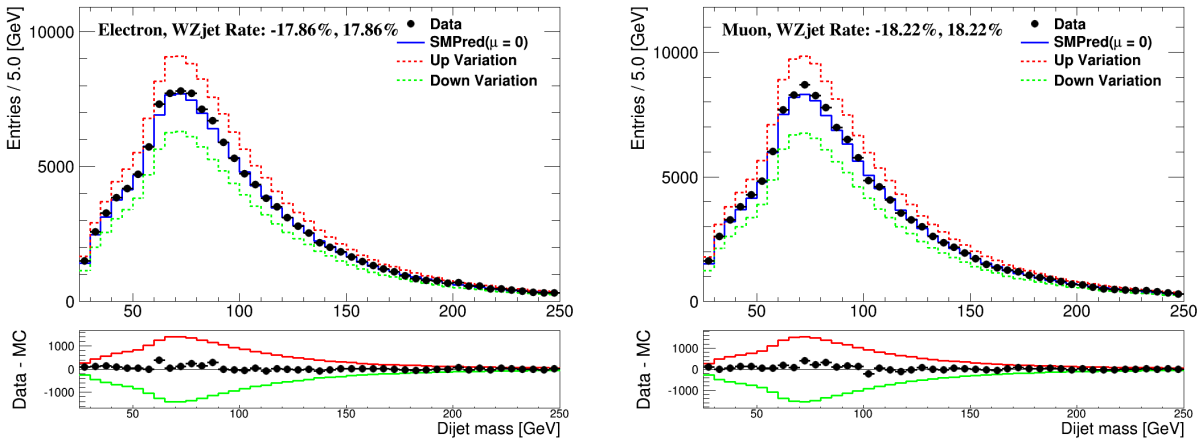

Figure 7.5: m_{jj} distributions for the electron (left) and muon (right) channel are shown for the data (black dots) and SM prediction ($\beta = 0$) assuming zero signal. The up (red) and down (green) templates represent shifting the W/Z+jets process up and down by its entire normalization uncertainty of 20%. The bottom panels contain the difference between the data and the nominal prediction ($\beta = 0$) in black and the difference between the systematic production rate variation and the nominal prediction in green/red.

7.3 $t\bar{t}$ and Single Top Uncertainties

The production rate uncertainty for the top processes is calculated to be 15% and is calculated by summing in quadrature the rate uncertainty from JES, JER, and the theoretical uncertainties on the cross sections. The theoretical cross section uncertainties vary between 5% and 10% for the different top contributions ($t\bar{t}$, single top s/t/Wt channels). A conservative value of 10% is used and summed with the approximately 6% from JES/JER, resulting in a conservative estimate of 15%.

The uncertainty due to ISR/FSR is evaluated using ACERMC generated samples (different from the nominal MC@NLO top samples) with varied ISR/FSR contributions. The uncertainty on the m_{jj} nominal shape and normalization due to these ISR/FSR varied samples is shown in figure 7.6 for both lepton channels.

7.4 QCD Multijet Normalization and Shape Uncertainties

The QCD Multijet shape uncertainty is derived using an alternatively defined QCD MJ enriched systematic control region obtained with a data driven method. The control region is defined by slightly modifying the nominal event selection by:

- $E_T^{\mathrm{miss}} < 25$ GeV (Nominal selection is $E_T^{\mathrm{miss}} > 30$ GeV);
- $m_{\mathrm{T}} > 10$ GeV (Nominal selection is $m_{\mathrm{T}} > 40$ GeV).

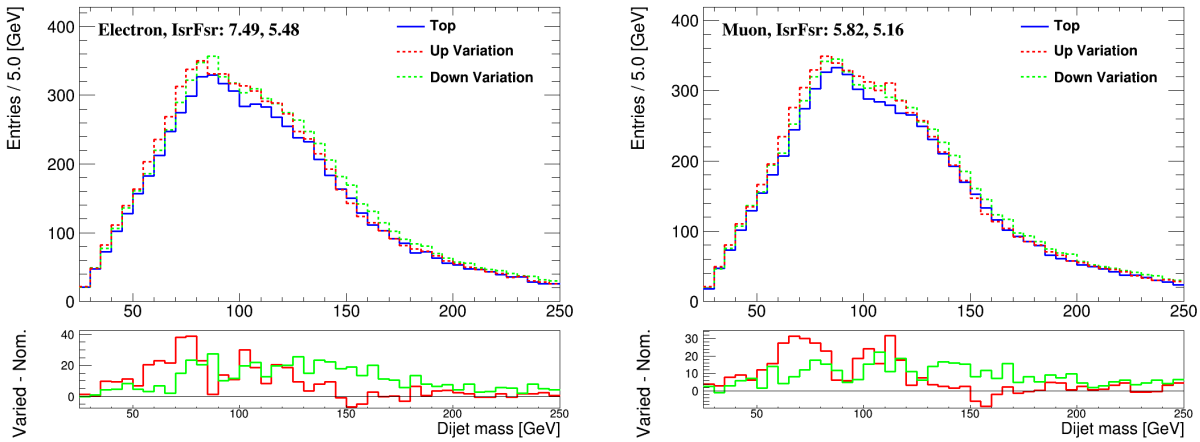

Figure 7.6: m_{jj} distributions for electron (left) and muon (right) channels are shown for the top processes ($t\bar{t}$ and single top) using the nominal samples (blue) and the ISR/FSR varied samples (red/green). The bottom panels contain the difference between the ISR/FSR varied templates and the nominal top prediction.

Process	Muon Channel	Electron Channel
WW+WZ	558	592
W/Z+jets	47k	82k
top	1041	1155
QCD multijet	30k	69k
QCD multijet/All(%)	38%	45%
Data	79470	150215

Table 7.4: Number of expected events for the QCD multijet Systematic control region selection for the various processes in the electron and muon channels.

The total number of events that pass this selection criteria after the likelihood fit to the full E_T^{miss} distribution are shown in table 7.4. Plots of the m_{jj} and E_T^{miss} distributions for both lepton channels are shown in figures B.9; B.10 of the appendix. The shape systematic is derived in this QCD systematic CR by taking the ratio of the data template minus all Non-QCD MC templates over the QCD template derived the standard way (described in section 5.5.1). This ratio is then applied to the nominal QCD template in the signal region and symmetrized with respect to the nominal QCD template to produce an up and down variation to be used in the cross section fit. Figure 7.7 shows the effect of this shape systematic on the m_{jj} distribution for the electron and muon channels.

The QCD Multijet normalization uncertainty is assumed to be 15% and uncorrelated between the lepton channels. A fit to the m_{jj} distribution akin to what is done to extract the WW+WZ signal (see chapter 8) is done as a crosscheck to validate this chosen normalization uncertainty. The fit is performed in the QCD MJ systematic Control region (defined above)

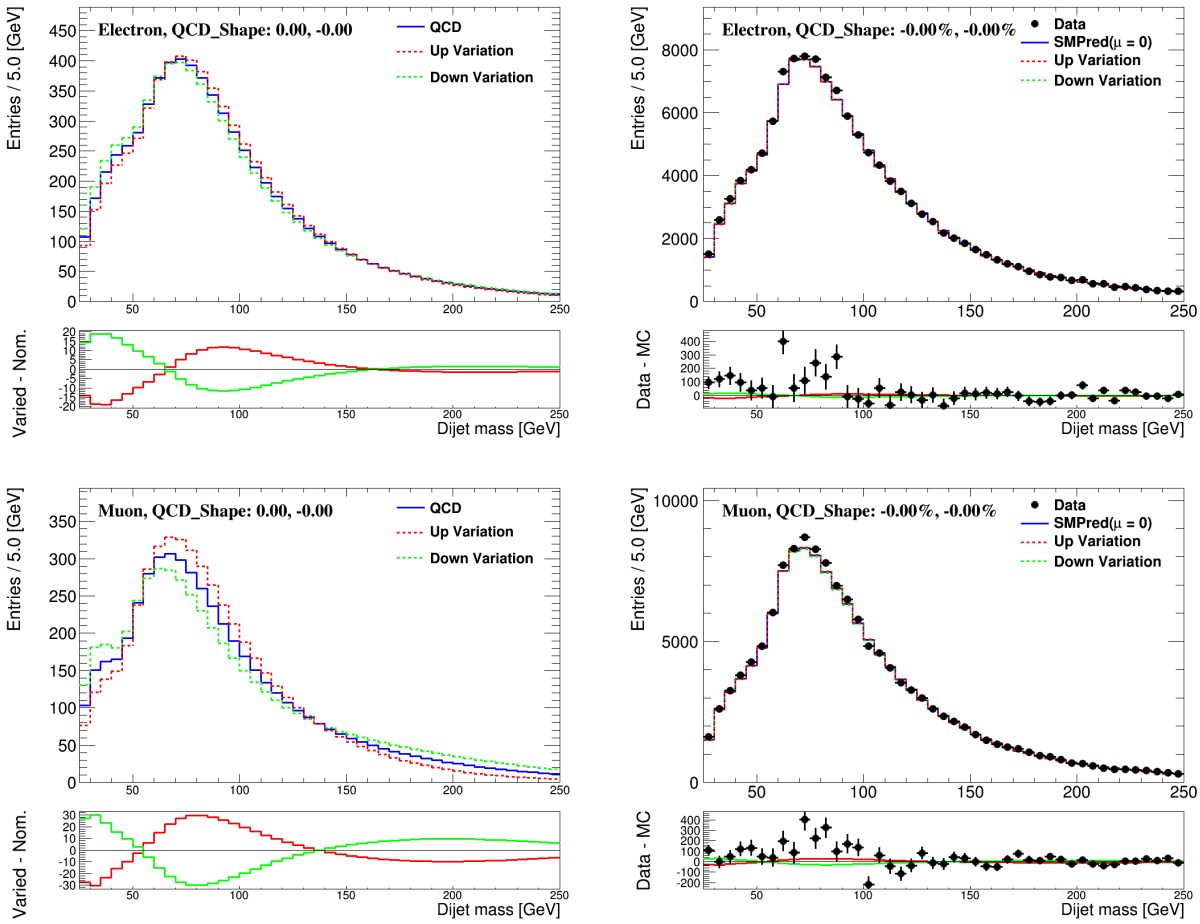

Figure 7.7: Nominal m_{jj} templates for the QCD multijet process overlaid with the systematically varied QCD templates are shown for the electron (top left) and muon (bottom left) channels. The lower panels show the difference between the varied templates and the nominal templates. The figures on the right show the m_{jj} templates for the data overlaid by the SM prediction assuming zero signal ($\beta = 0$) for all processes (black dots) and with QCD varied templates (red/green lines). The bottom panels contain the difference between the data and the nominal prediction ($\beta = 0$) in black and the difference between the systematic variation from the QCD and the nominal prediction in green/red.

and the signal considered in the fit is the QCD MJ process. All relevant systematics are allowed to float within their uncertainties in the fit. The measured signal strengths of the QCD process for the electron and muon channels are calculated to be $\beta_{ele} = 1.02 \pm 0.01$ and $\beta_{\mu} = 1.12 \pm 0.08$. The fitted results show that a QCD MJ normalization uncertainty of 15% is within the projected systematic uncertainty.

7.5 Signal Shape Uncertainties

The signal modeling uncertainty considers systematic effects due to the fragmentation and ISR/FSR modeling, and the choice of PDF. The JES and JER shape uncertainties were discussed previously in this chapter.

7.5.1 Shape Uncertainty due to Fragmentation Model

To estimate the shape uncertainty due to different fragmentation models for the signal the nominal MC@NLO interfaced with HERWIG samples are compared to samples produced with a LO PYTHIA generator. A template using the PYTHIA samples is produced after applying the full event selection and the shape is symmetrized with respect to the nominal signal template to produce an up and down shape variation to the signal. The resulting shape uncertainty can be seen in figure 7.8.

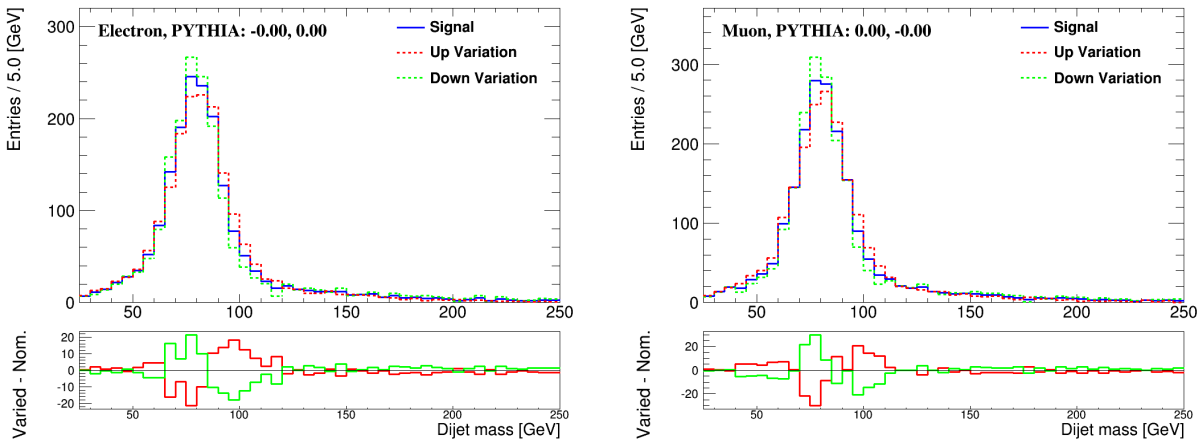

Figure 7.8: m_{jj} distributions for electron (left) and muon (right) channels are shown for the signal processes (WW+WZ) using the nominal samples (blue) and the PYTHIA varied sample(red/green). The bottom panels contain the difference between the PYTHIA varied templates and the nominal signal prediction.

This systematic uncertainty also covers the shape uncertainty due to the use of the MC@NLO generator to produce semi-leptonic decays. MC@NLO does not directly support semi-leptonic diboson decays, instead the W's and Z's must be produced by MC@NLO on−shell and passed to HERWIG to generate the leptonic and hadronic decay products.

This results in a distorted line shape for the decay bosons since the boson width does not contain the Breit-Wigner component. This small effect ends up being negligible for this analysis, since the dijet mass resolution is significantly larger than the actual width of the W and therefore this zero width assumption can be folded into the current modeling uncertainty discussed above.

7.5.2 Normalization Uncertainty due to Fragmentation Model

The normalization uncertainty on the cross section measurement due to fragmentation and ISR/FSR has been assessed as a systematic on D_{fid} and D_{tot} . The effect has been calculated by applying the nominal selection to a PYTHIA generated and HERWIG generated sample and then taking the relative difference in the event yields as the uncertainty. Table 7.5 shows the calculated values for D_{fid} and D_{tot} for each sample and channel. Table C.6 shows the breakdown of the event yields and the calculated A and C values for the fiducial/total cross section. The total uncertainty considered for D_{fid} and D_{tot} is 4% and 5%, respectively.

	Herwig	Pythia	% Diff.
Muon Channel			
D_{fid}	0.713	0.743	4.03
D_{tot}	0.0196	0.0205	4.70
Electron Channel			
D_{fid}	0.658	0.683	3.70
D_{tot}	0.0180	0.0186	3.47

Table 7.5: Calculated values for D_{fid} and D_{tot} in both lepton channels calculated using the systematic signal samples. % Diff. shows the percent relative difference with respect to the average of the 2 values.

7.5.3 Renormalization and Factorization Scale Dependence for the WW+WZ Processes

The systematic uncertainty due to the choice of the renormalization and factorization scale was evaluated by producing varied event-generation-only (truth) MC@NLO samples, which varied either one or both scales by two times or one half the nominal scale value. The samples with the largest variations to the m_{jj} distribution were implemented into the cross section fit as a systematic and were calculated to have a negligible effect to the measurement. The production rate uncertainty due to the scale choice was at most 1% and thus was also ignored for this analysis.

7.5.4 Jet Veto Scale Dependence for the WW+WZ Processes

The systematic uncertainty introduced by the scale dependence of the jet veto has been assessed comparing the jet veto efficiency with MC@NLO+HERWIG and HERWIG. In order

to do access this, D_{tot} has been calculated for the standard signal selection and for the standard signal selection but without applying the jet veto ($D_{tot}^{no\ Veto}$). The quantities D_{tot} and D_{tot}^{noVeto} have been calculated with MC@NLO+HERWIG and HERWIG. The ratio between D_{tot} and D_{tot}^{noVeto} for each generator is shown in table 7.6 as a percentage. The difference between the ratios is taken as the systematic on the jet veto dependence, this translates to 3.56 % (4.61 %) for the muon (electron) channel. We take a conservative value of 5 % for both channels.

	MC@NLO+HERWIG (%)	HERWIG (%)	Difference (%).
Muon Channel D_{tot}/D_{tot}^{noVeto}	71.7	75.3	3.56
Electron Channel D_{tot}/D_{tot}^{noVeto}	70.1	74.7	4.61

Table 7.6: The percent effect on D_{tot} due to removing the third jet veto is shown for MC@NLO interfaced with HERWIG and HERWIG only in the first two columns for each channel. The difference of the two percentages is taken as the systematic due to the jet veto scale. 5% is used as a conservative estimate on the systematic for both channels. The values for D_{tot} and D_{tot}^{noVeto} can be found in table C.5.

7.5.5 Boson Spin Correlations

As discussed in section 7.5.1, the fact that the MC@NLO signal samples do not explicitly do diboson semileptonic decays also results in the spin correlations between the hadronic parents and the HERWIG produced decays to be lost in the interface between the two generators. The neglect of the spin−correlation effect is studied at truth−level to determine the size of the uncertainty. The study was conducted by generating $WZ \to e\nu\mu^+\mu^-$ decay samples using MC@NLO with and without the spin correlations present. As a proxy for this analysis's hadronic boson decay, the $Z \to \mu^+\mu^-$ decay was used in replacement of $Z \to jj$. Selection criteria similar to the event selection applied for this analysis was used and showed that for the cross section measurement, a production rate difference of 3% was observed between the different samples[4]. The difference is considered as an uncertainty to D_{tot} since this is a systematic only on the signal acceptance. Additional studies for this systematic in regards to its effect on the $p_{\mathrm{T}}(jj)$ shape for the aTGC limit setting are done and discussed in section 10.2.

7.5.6 PDF Uncertainties for the WW+WZ Processes

The effect of varying the Parton Distribution Functions (PDFs) for the signal samples has been evaluated as a systematic for both the signal normalization and shape. The PDF set used for the MC@NLO MC samples is CT10 [39], which uses a flexible PDF parametrization to allow for PDF reweighting on an event-by-event basis. The PDFs for the signal events are reweighted by $\pm 1\sigma$ in regards to the central value given by the 68% confidence level

[4]The sample without spin correlation had the higher acceptance

CT10 PDF set. The PDFs are varied separately for the WW, WmZ and WpZ samples. The normalization uncertainty is then calculated for each sample separately by calculating the ratio between the nominal event yield and the PDF varied yields (up and down). In order to be conservative, the maximum production rate deviation among all samples and variations is reported. The shape uncertainty in the m_{jj} shape is also calculated separately for each sample. To evaluate the shape uncertainty, the ratio between the nominal m_{jj} distributions and the varied PDF distributions are calculated. The final shape uncertainty is taken to be the maximum deviation among shapes in each bin seen among all samples. To remain as conservative as possible, the normalization and shape uncertainty have been calculated separately for each lepton channel. Additionally, using a similar procedure to what is done to vary the CT10 PDF, the signal events are all reweighted to the central value of the MSTW2008NLO [98] PDF set and compared with the central CT10 value.

Channel	CT10 Uncertainty (%)		MSTW2008NLO Uncertainty (%)
Muon	2.3	1.4	−0.8
Electron	2.5	1.8	1.4

Table 7.7: Normalization Uncertainties due to varying the PDF set for the signal samples for the electron and muon channel are shown. The central CT10 PDF values are varied between the uncertainty in CT10 and the central MSTW2008 NLO PDF set. The normalization uncertainty is calculated separately for each samples and only the maximum normalization uncertainty for each channel is shown.

The normalization uncertainty due to PDFs is reported for D_{tot} by calculating the effect on the product of $A \cdot C$, the results are shown in table 7.7. The maximum deviation is shown to be 2.5% in the electron channel, therefore this is reported as the normalization uncertainty for D_{tot} . Similarly, the PDF normalization systematic has been evaluated on D_{fid} and the maximum deviation from the nominal normalization was calculated to be 0.75% in the muon channel and 0.8% in the electron channel. The conservative value of 0.8% is reported for D_{fid} for the final systematic.

The maximum shape uncertainty due to the PDFs is shown for the m_{jj} distribution in figure 7.9. From the figure it can be seen that the shape deviation below $m_{\mathrm{jj}} < 120GeV$ is less than 0.5% and slowly rises to less than 2% at higher values of m_{jj} . In the high mass region the signal samples have very low statistics and are dominated by large statistical fluctuations. The shape uncertainty due to PDFs in m_{jj} is seen to be small compared to other systematics and therefore is neglected in the final systematic assessment. Additionally, the maximum shape uncertainty in the $p_{\mathrm{T}}(jj)$ spectrum is also evaluated for the aTGC limits and is neglected as well due to having a small effect on the distribution.

7.6 Lepton Reconstruction

The uncertainty due to the lepton reconstruction and identification efficiencies was done by varying the event weights for these MC correction factors up and down by their uncertainties and then propagating these changes through the event selection. This study [133]

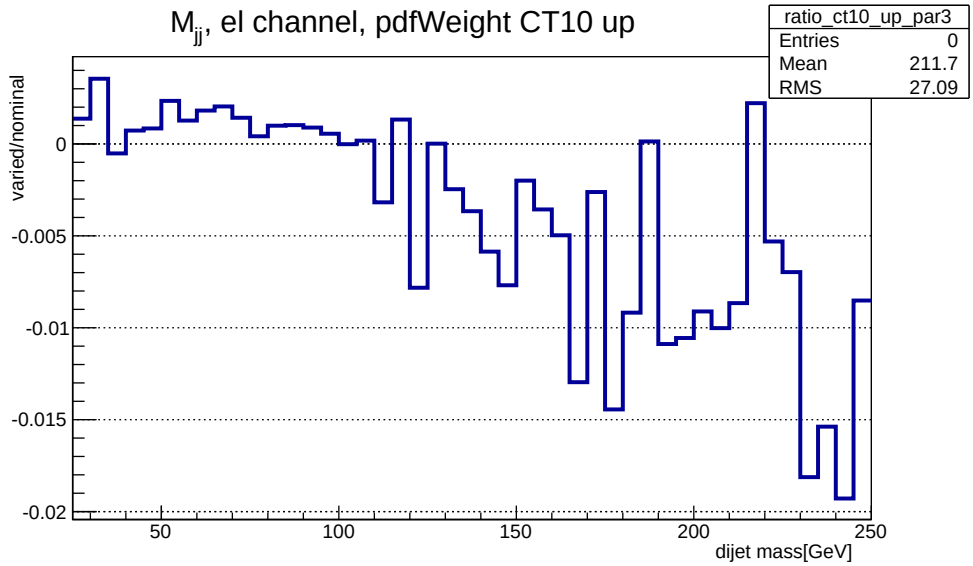

Figure 7.9: Distribution of the ratio in shapes between the PDF varied and nominal m_{jj} distribution. The varied PDF template is produced from the maximum observed variation per bin per signal sample.

concluded that the uncertainty was within 1% for both the electron and muon channels and therefore is quite negligible in this analysis.

7.7 MC Statistical Uncertainty

The MC statistical uncertainty comes from the binned statistical precision of the input templates used in the cross section fit. Prior to the generation of the high statistics AFII W/Z+jets samples discussed briefly in section 4.3.2, the systematic uncertainty due to the MC statistics for the reported cross section in this analysis's old conference note [133] was 18%. This uncertainty accounted for approximately 60% of the total uncertainty in the final measurement. The MC uncertainties were mostly due to a lack of statistics in the low parton W/Z+jets samples, since those samples were produced with an integrated luminosity far below the amount of integrated luminosity recorded in the data. This resulted in these large cross section samples with only a few events passing the selection (due to not satisfying the jet requirement) to have to be scaled up to the integrated luminosity of the data. Causing the uncertainty to grow by the same factor as the scaling and since m_{jj} templates are binned distributions the uncertainty was even larger since the poor statistics/uncertainties were distributed among several bins.

In order to reduce this uncertainty, a careful look at the W/Z+jets samples contributing the largest effect was conducted. New samples simulated with AFII were produced with enough statistics that would result in the MC statistical uncertainty being equivalent to the uncertainty due to JES/JER and thus any further reduction in the uncertainty would not have a significant effect on the total systematic uncertainty for the cross section measurement.

A list of the samples and the requested statistics are shown in table 7.8 It has been estimated with the addition of these new samples that if additional samples with an infinite amount of statistics were produced that the total uncertainty in the cross section would only differ by 2%.

Process	Statistics	% Increase
WenuNp0	40483970	582
WenuNp1	11565494	231
WenuNp2	23766976	631
WenuNp3	5008490	496
WenuNp4	1074498	144
WenuNp5	999998	238
WmunuNp0	40458469	581
WmunuNp1	11493491	230
WmunuNp2	23760472	631
WmunuNp3	5008496	497
WmunuNp4	974497	129
WmunuNp5	1000000	239
WbbNp1	645000	315
WccNp1	2999499	286
WccNp2	800000	152
WcNp1	6069994	293
WcNp2	1998499	384

Table 7.8: A list of the requested W+jets samples that contained the biggest contribution to the MC statistical uncertainty and the remaining W/Z+jets AFII samples. Statistics represents the total number of events in each AFII samples and % increase shows the precent increase in relation to the original full simulated samples. More details about the samples used can be found in appendix A

As previously discussed in section 4.3.2 and shown in figure 4.1, the kinematic distributions for the AFII generated W/Z+jets samples are consistent with the fully simulated (FS) samples. Only the shape and the uncertainties for the AFII samples are utilized to create the templates, the production rates are taken directly from the FS samples.

The bin-by-bin uncertainty due to the MC statistics is evaluated using pseudo-data generated toys (discussed in section 8.2) which are produced by fluctuating each templates bin contribution within the statistical uncertainty of that bin. This results in a 12% uncertainty, which is in agreement with the expected reduction calculated when taking into account the additional samples.

7.8 Integrated Luminosity Measurement Uncertainty

The integrated luminosity uncertainty was calculated to be 1.8% [63] by the Luminosity working group for the 2011 dataset collected by the ATLAS detector. This uncertainty is added in quadrature to the final cross section results.

Source of Systematic	Type	xSec assessment	used for aTGC
W/Z+jets normalization	Norm.	PR	•
W/Z+jet modeling	Shape	PR	•
$t\bar{t}$+single t normalization	Norm.	PR	•
ISR/FSR for $t\bar{t}$	Norm. and Shape	PR	
multijet normalization	Norm.	E	•
multijet shape	Shape	PR	
PDF signal	Norm.	O	
JES uncertainty (but JES15) all processes but multijet	Shape	PR	•
JES flavor uncertainty (JES15) all processes but multijet	Shape	O	•
JES uncertainty signal	Norm.	O	•
JER uncertainty all processes except multijet	Shape	PR	•
JER uncertainty signal	Norm.	O	•
lepton reconstruction signal process	Norm.	O	
Signal modeling	Shape	PR	
Signal normalization	Norm.	O	•
MC statistics all processes	N.A.	E	•
Luminosity	Norm.	–	•

Table 7.9: Summary of the systematic sources considered and of the method to estimate their effect on the cross section measurement. The third column indicates if the systematic is included in the likelihood definition (PR=profiled) for the cross section fit, if its effect is estimated using pseudo-experiments (E) or if it is estimated with other methods (O) as explained in the text. The pseudo-experiment method is explained in Section 8.1. Except for JES15 (the jet flavor response uncertainty, see Table 7.1), all the JES systematic contributions have been profiled in the likelihood fit. JES15 has instead been evaluated using pseudo-experiments. In the last column the systematics that have been used also for setting the aTGC limits in Chapter 10 are marked with a •.

7.9 Summary on Systematic Uncertainty Treatment

A quick summary of the different systematic uncertainties and how they are evaluated in this analysis is shown in table 7.9. The systematics are for the most part either profiled in the cross section likelihood fit or estimated using pseudo-data, both methods are discussed in the following chapter 8. The last column of the table signifies whether the given systematic is used for the aTGC limit setting, further discussion of the systematics affecting the aTGC limit calculation are discussed in section 10.2.

Chapter 8

Fitting Procedure for the Cross Section Measurement

As was defined in chapter 6, the extraction of the WW/WZ signal yield (N^{meas}) is done by performing a binned maximum likelihood fit to the observed m_{jj} distribution in the range of 25 to 250 GeV. The fit returns the signal strength (β) which is the ratio of the measured cross section over the theoretical NLO SM cross section given by the MC. In this way, β multiplied with the predicted signal cross section given in table 4.1 provides the measured total cross section for the WW+WZ process. This chapter discusses the details of how the likelihood fit is performed.

8.1 Template Fit Method

The cross section fit is performed simultaneously in both the electron and muon channel. Four templates for each channel consisting of the WW+WZ signal, W/Z+jets[1], top[2], and the QCD multijet processes are used to fit to the observed data in each channel. Figure 8.1 shows the nominal m_{jj} templates used for both channels, normalized to unity. It is important to note that the WW/WZ template has a different shape when compared to the other templates, this in turn allows for the likelihood fit to discriminate between the signal and the other background processes in an environment that has such a high background rate and associated uncertainties.

The likelihood function is minimized using MINUIT [134], which is implemented through HistFactory, a standard package of ROOSTATS [135], for fitting both the background-only and signal-plus-background hypotheses. All normalization and shape systematics that are used in the fit (see table 7.9) are introduced into the fit as 'nuisance' parameters. As a reminder the likelihood function is represented by

$$\mathrm{L}(\beta,\vec{\alpha}) = \prod_{\ell=e,\mu}\prod_{b=1,45}\mathrm{Pois}(n_{\ell b}|v_{\ell b}(\vec{\alpha}))\cdot\prod_{\mathrm{p=parameters}} f_p(\alpha_p) \tag{8.1}$$

[1] includes the ZZ contribution

[2] includes $t\bar{t}$ and single top production

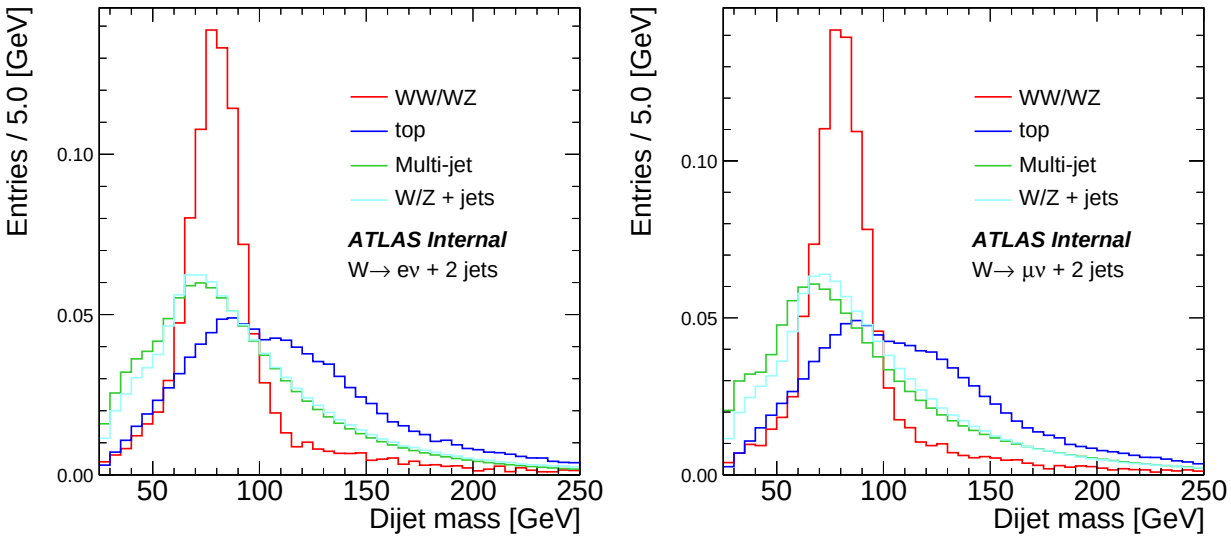

Figure 8.1: The m_{jj} nominal templates for the WW+WZ, W/Z+jets , top, and QCD MJ processes are shown for the electron (left) and muon (right) channels. The templates are obtained after the event selection as described in chapter 5. All templates are normalized to unit area.

where $n_{\ell b}$ is the number of data events in bin b and lepton channel ℓ, and

$$\mathrm{Pois}(n_{\ell b}|v_{\ell b}(\vec{\alpha})) = \frac{(v_{\ell b}(\vec{\alpha}))^{n_{\ell b}} \cdot e^{-v_{\ell b}(\vec{\alpha})}}{n_{\ell b}!}, \tag{8.2}$$

and $f_p(\alpha_p)$ is the Gaussian functional constraint for a nuisance parameter p, stated as

$$f_p(\alpha_p) = \frac{1}{\sqrt{2\pi}} \cdot e^{-\frac{\alpha_p^2}{2}}. \tag{8.3}$$

$v_{\ell b}(\vec{\alpha})$ represents the expected number of total events, signal ($v_{\ell b}^{sig}(\vec{\alpha})$) plus background ($v_{\ell b}^{bkg}(\vec{\alpha})$), in bin b and channel ℓ. Broken into its components

$$v_{\ell b}(\vec{\alpha}) = \beta \cdot v_{\ell b}^{sig}(\vec{\alpha}) + \sum_k v_{\ell bk}^{bkg}(\vec{\alpha}) \tag{8.4}$$

where β is the signal strength and parameter of interest returned by the fit, and k is one of the three background components (W/Z+jets , top, or QCD MJ). The nuisance parameters for the normalization and shape systematics are introduced into the likelihood function through $v_{\ell b}(\vec{\alpha})$ which can be rewritten as

$$v_{\ell b}(\vec{\alpha}) = \beta \cdot N_{\ell b}^{sig,nom} \cdot (h_{\ell b}^{sig}(\vec{\alpha})) + \sum N_{\ell bk}^{bkg,nom} \cdot \eta_k^{bkg} \cdot (h_{\ell bk}^{bkg}(\vec{\alpha})) \tag{8.5}$$

where $N_{\ell b}^{sig/bkg,nom}$ is the number of signal/background events expected for bin b and channel ℓ, and η_k^{bkg} is the normalization scale factor for background component k. It is parametrized

in terms of nuisance parameter α_k as follows:

$$\eta_k^{bkg} = (1+\sigma_k^{bkg})^{\alpha_k}, \text{ for } \alpha_k \geq 1, \tag{8.6}$$

$$= (1+\sum_{i=1}^{6} a_i(\alpha_k)^i), \text{ for } |\alpha_k| < 1 \tag{8.7}$$

$$= (1-\sigma_k^{bkg})^{-\alpha_k}, \text{ for } \alpha_k \leq -1, \tag{8.8}$$

where σ_k^{bkg} is the normalization uncertainty in background component k (ie. 0.20 for the W/Z+jets process), and α_k is a nuisance parameter with a Gaussian constraint of mean 0 and width 1. a_i are the coefficients of the 6th-order polynomial and are determined by requiring continuity in η_k^{bkg} and its first two derivatives at the boundary $\alpha_k = \pm 1$[3]. With this definition, η_k^{bkg} is always positive and for small values of α it approaches $(1+\alpha\sigma)$.

$h_{\ell bk}^{sig}(\vec{\alpha})$ and $h_{\ell bk}^{bkg}(\vec{\alpha})$ represent how the shape systematics are introduced into the likelihood function. The nominal histogram, h_k^0, for the signal/background component k is distorted by systematic j and parametrized by α_j according to :

$$h_{\ell bkj}^{sig/bkg}(\vec{\alpha}) = h_{\ell bk}^0 + \alpha_j(h_{\ell bkj}^+ - h_{\ell bk}^0), \text{ for } \alpha_j > 1, \tag{8.9}$$

$$= h_{\ell bk}^0 + \sum_{i=1}^{6} a_{ijk}(b)(\alpha_j)^i, \text{ for } |\alpha_j| \leq 1, \tag{8.10}$$

$$= h_{\ell bk}^0 + \alpha_j(h_{\ell bkj}^- - h_{\ell bk}^0), \text{ for } \alpha_j < -1, \tag{8.11}$$

where $h_{\ell bkj}^+$ and $h_{\ell bkj}^-$ represent the "up" and "down" systematically varied templates for signal/background component k obtained by varying systematic j by ± 1 σ as discussed in chapter 7. $a_{ijk}(b)$ are histograms that are calculated by requiring that h and its first two derivatives with respect to α_j are continuous at the boundaries, $\alpha_j = \pm 1$.

For the electron and muon channel, the systematic uncertainties that are profiled[4] in the fit due to the same sources are assumed to be 100% correlated ($\alpha_{j,muon} = \alpha_{j,electron}$) except for the QCD MJ shape. Systematic uncertainties due to different sources are assumed to be mutually independent of each other. As described in table 7.9, all background normalizations and background/signal shape variations are profiled in the fit except for uncertainties due to the QCD MJ normalization, JES15, and MC statistics. The QCD MJ normalization is not profiled because attempts to include this systematic in the fit led to stability issues with the fit not converging. The JES15 systematic, representing the jet flavor response uncertainty, is recommended not be profiled because it is based on a comparison between PYTHIA and HERWIG++ [136] and therefore it does not have a real physical meaning in terms of a continuous nuisance parameter. Another way of saying this is that the likelihood fit could possibly decide to heavily constrain the JES15 systematic like is done for the W/Z+jets normalization, but this would be incorrect due to the assumption that the systematic variation is based on a continuous distribution when it is in fact a discrete systematic based on the interpolation between HERWIG++ and PYTHIA[5].

[3]This avoids kinks in the fit due to the boundary transitons.

[4]Systematics which are allowed to float in the likelihood fit are considered "profiled."

[5]As said in reference [137], "Can one really say that the data is best described by ...30% HERWIG + 70% Pythia ($\pm$10%)?"

Source of Systematic	Type	Uncertainty	Comments	Profiled?
W/Z+*jets* rate	Norm.	20%	1 parameter affecting both channels	yes
QCD rate	Norm.	15%	2 parameters (one for each channel)	no
QCD shape	Shape	N.A.	2 parameters (one for each channel)	yes
JES	Shape*	N.A.	14 parameters affecting all of the components except for QCD in both channels	yes, except for JES15
JER	Shape*	N.A.	1 parameter affecting all of the components except for QCD in both channels	yes
Top rate	Norm.	15%	1 parameter affecting both channels	yes
ISR/FSR description	Norm and Shape	N.A.	1 parameter affecting top in both channels	yes
Signal modeling	Shape	N.A.	1 parameter affecting signal in both channels	yes
Norm/Fact scale	Shape*	N.A.	1 parameter affecting W/Z+*jets* in both channels	yes
ΔR parton matching	Shape*	N.A.	1 parameter affecting W/Z+*jets* in both channels	yes

Table 8.1: A list of the nuisance parameters profiled in the template fit and how they are incorporated between components and lepton channels. The type "Shape*" indicates that the normalization uncertainty relative to that systematic is folded into the production rate uncertainty for that given background process as described in the chapter 7.

For both the QCD MJ normalization and JES15 systematics the corresponding α_j values are fixed to zero for the fit and there uncertainty, like the MC statistical uncertainty, is estimated using pseudo-experiments as described in the next section. Table 8.1 summarizes the uncertainties that have been profiled in the fit and how they are handled regarding their different components and the different lepton channels.

8.2 Procedure to Calculate Uncertainties using Pseudo-experiments

A pseudo-experiment is defined as using the likelihood fit (described in the previous section) on a pseudo-dataset[6] which has been generated using MC techniques. Pseudo-datasets are created by taking a random sampling of systematically varied probability density functions (p.d.fs) of the signal and background templates to create a "new" dataset. Each pseudo-dataset is created by first randomly drawing values for each nuisance parameter, α_j, utilizing their Gaussian constraints[7], and then creating new p.d.fs (templates) for the signal and background processes based on these drawn α_j values. From these new p.d.fs, a random sampling of events are "generated" to create a pseudo-dataset. Poisson fluctuations in the number of generated events is also taken into account when generating these pseudo-datasets. The resulting pseudo-datasets will therefore include effects due to systematic uncertainties

[6]Pseudo-datasets are commonly referred to as toy datasets or toys.
[7]Where the Gaussian constraint is given with mean 0 and width 1.

from both normalization and shape in the signal (shape only) and background, as well as statistical fluctuations.

The likelihood fit is then done on each pseudo-dataset in the same way that the fit is done for the real data, as in the α_j from profiled systematics are varied and for non-profiled systematics they are fixed to zero. To calculate the uncertainty in the non-profiled systematic JES15[8], pseudo-datasets are generated from p.d.fs created using randomly drawn α_j values for the profiled systematics and varied α_{JES15} values. These pseudo-datasets that include variations due to JES15 are then fitted in the normal way, with α_{JES15} set to zero. The root mean square (r.m.s) of the fitted signal strengths calculated from these pseudo-datasets is used to estimate the total uncertainty including the JES15 component ($\sigma_{JES15+other}$). To calculate just the uncertainty due to JES15, $\sigma_{JES15+other}$ is subtracted in quadrature from the r.m.s. calculated in pseudo-datasets produced with only the profiled nuisance parameters varied (σ_{other}) and α_{JES15} equal to zero.

$$\sigma_{JES15} = \sqrt{\sigma^2_{JES15+other} - \sigma^2_{other}} \tag{8.12}$$

The results of the pseudo-experiments to calculate σ_{JES15} are shown in figure 8.2 and result in $\sigma_{JES15} = 6\%$. Likewise, a similar approach was taken to calculate the uncertainty in the QCD MJ normalization which came out to 6%. For the MC statistical uncertainty, the pseudo-datasets were generated using p.d.fs in which the bins were fluctuated within the statistical uncertainties of the nominal templates. The "up" and "down" shape systematic templates were also fluctuated along with the nominal templates and these fluctuations were assumed to be 100% correlated. The resulting uncertainty due to the MC statistics is calculated to be 12%.

8.3 Calculating the Expected Significance

The expected significance is estimated by the likelihood ratio λ defined as:

$$\lambda = \frac{L(\beta = 0, \vec{\alpha})}{L(\beta, \vec{\alpha})} \tag{8.13}$$

where β is the signal strength returned from the fit and $\vec{\alpha}$ is the vector of all nuisance parameters varied in the fit. $L(\beta = 0, \vec{\alpha})$ denotes the maximum likelihood value when β is set to zero resulting in zero signal events, and $L(\beta, \vec{\alpha})$ is the maximum likelihood where the signal strength is allowed to float along with the nuisance parameters. Psuedo-datasets are generated with background-only processes and signal+background processes. In both cases the profiled α_j parameters are varied along with the uncertainties due to low MC statistics. $L(\beta = 0, \vec{\alpha})$ and $L(\beta, \vec{\alpha})$ are calculated for each psuedo-dataset and the resulting $-log\lambda$ distributions using the background-only (λ_{bkg}) and signal+background ($\lambda_{sig+bkg}$) psuedo-datasets are shown in figure 8.3. The expected $-log(\lambda)$ value is drawn in purple, denoting where 50% of the entries lie on either side of the vertical line for the $-log(\lambda_{sig+bkg})$ distribution. The p-value is then calculated as the area under the $-log(\lambda_{bkg-only})$ distribution to the right of the expected $-log(\lambda)$ value over the entire $-log(\lambda_{bkg-only})$.

[8]The same process is used for the QCD MJ normalization uncertainty

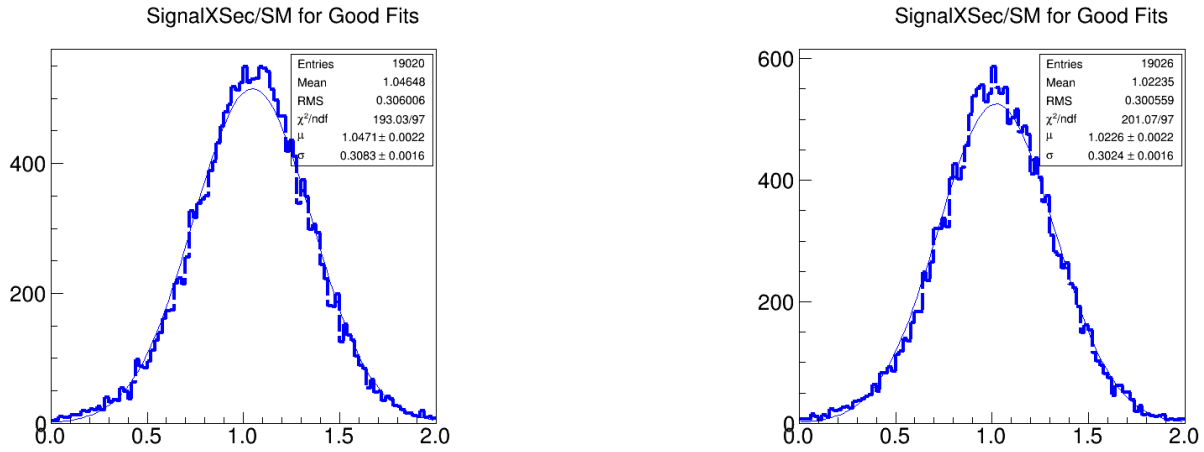

Figure 8.2: Distributions of the fitted signal strengths for psuedo-experiments done on psuedo datasets produced with the nominal profiled systematics plus variations in JES15 (left) and just with the nominal profiled systematics (right). The uncertainty attributed to JES15 only is calculated by subtracting in quadrature the r.m.s. of both distributions. The generated psuedo-datasets include bin-by-bin variations due to limited MC statistics.

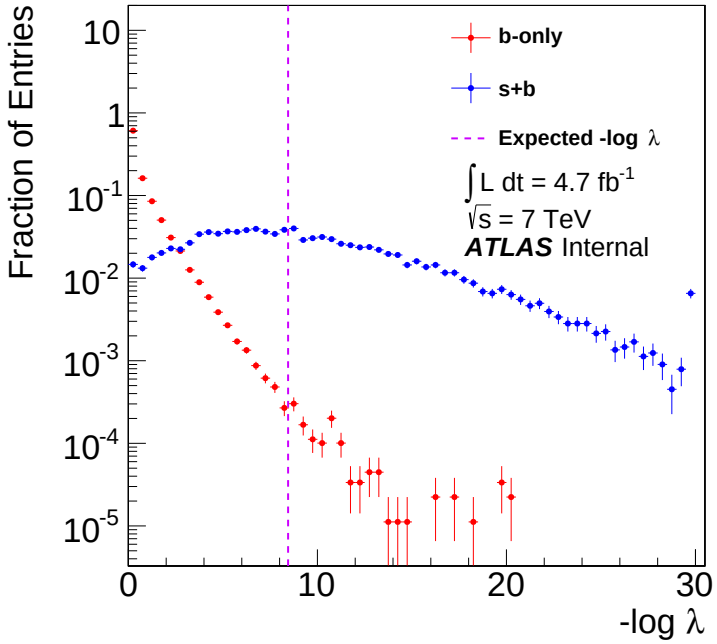

Figure 8.3: Distributions of the negative log likelihood ratio $-log(\lambda)$ for background-only (red points) and signal+background (blue points) pseudo-experiments. The expected value of λ for the signal+background hypothesis is also shown as a dashed purple vertical line and is located at the median of the $-log(\lambda_{sig+bkg})$ distribution.

8.4 Fit Validations

8.4.1 Pull Distributions

In order to understand if the fit contains any bias and that the systematic uncertainties cover the measurement appropriately (not over/under-estimating) the pull distribution for the fit as been studied. A 1000 pseudo-datasets were generated with the signal and background m_{jj} distribution taken from the nominal templates (no systematics were varied in the generation, $\alpha = 0$) and the pull distribution, shown in figure 8.4, was checked. The pull is calculated as:

$$\text{pull}_i = \frac{\beta_i - \beta_{nominal}}{\sigma_i} \tag{8.14}$$

where i corresponds to one of the pseudo-experiments with a signal strength β_i and fit uncertainty σ_i. $\beta_{nominal}$ is equal to 1 since the nominal templates were used to produce the pseudo-datasets so they only contain statistical fluctuations. The fit to the pseudo-datasets were performed allowing the profiled nuisance parameters float in the fit as is done in the normal cross section fit. As can be seen in the top left plot the fit consistently gives a β consistent with 1. The top right plot is the pull distribution and when fitted with a Gaussian has a mean close to zero indicating no bias and a sigma near 1 showing that the uncertainties are handled correctly.

The bottom distribution is the distribution of fitted β values due to performing pseudo-experiments on pseudo-datasets produced by varying all the nuisance parameters[9] (including non-profiled systematics) within their Gaussian constraints. The plot shows that the fit results do not depend on the variations from nuisance parameters around their nominal values.

8.4.2 Linearity of the Returned Fitted Signal Strength

The linearity of the fit was demonstrated by producing pseudo-datasets with varying amounts of injected signal events and then the fit was performed on these generated datasets. All the datasets were generated with the nominal values for the nuisance parameters. The results are shown in figure 8.5, the top left plot shows the fitted β value plotted against the generated β used to produce the pseudo-dataset. A linear fit is performed on the distribution and shows a slope equal to 0.99 with a y-intercept of -0.014. The plot on the top right shows the fit bias on β to be approximately 2% which is negligible compared to the other systematics so no additional systematics are added.

8.4.3 Fit Sensitivity to the Systematic Uncertainties

The fit sensitivity to the systematic uncertainties was studied using pseudo-experiments. Pseudo-datasets were generated with random Gaussian constrained nuisance parameters $\vec{\alpha}$ for all profiled and non-profiled systematics except for the uncertainty due to MC statistics. The normal maximum likelihood fit was then performed on these datasets and the results

[9]The pseudo-datasets do not include variations due to limited MC statistics

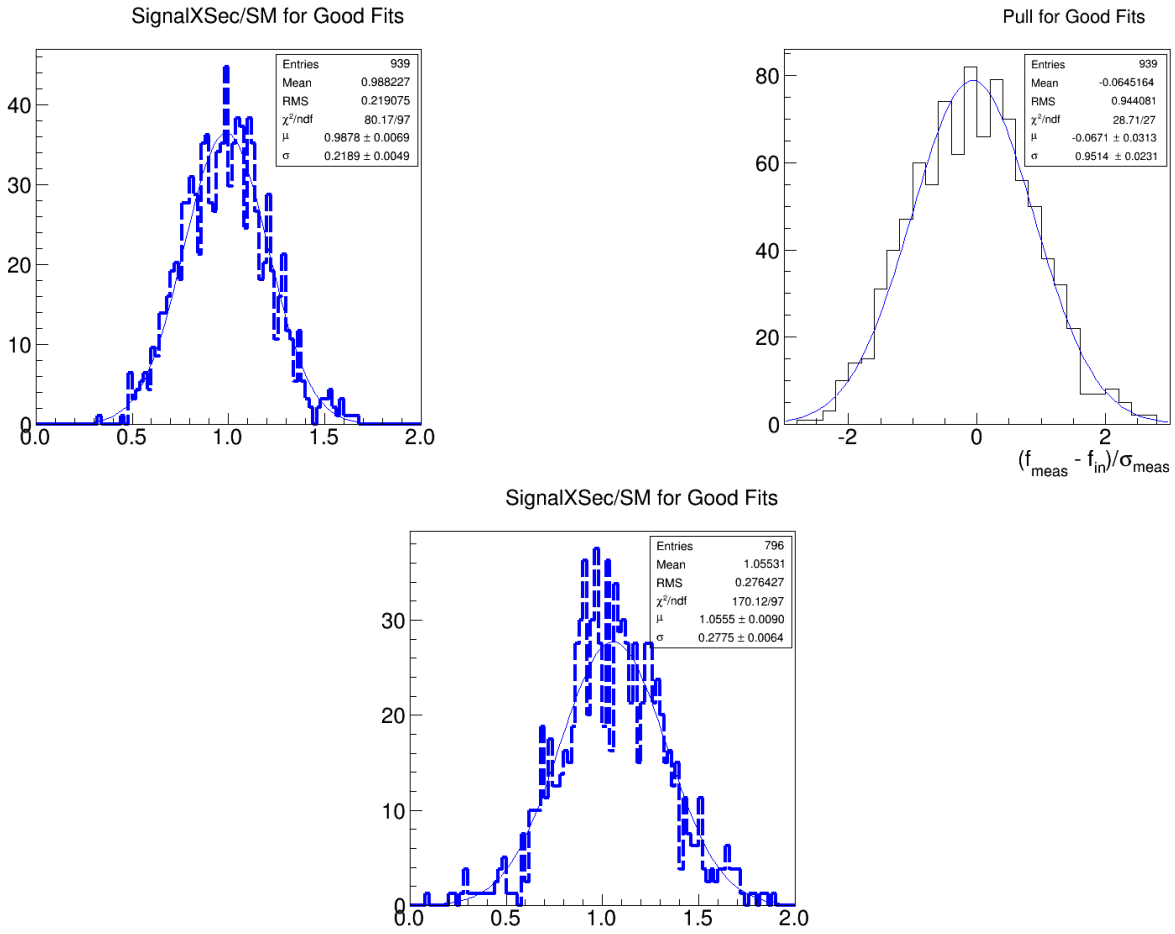

Figure 8.4: The plots on the top show the fitted signal strength (left) and corresponding pull distribution (right) for fits on pseudo-datasets produced using the nominal values from the templates with no systematics included. The bottom plot shows the fitted signal strength for pseudo-datasets produced by varying all nuisance parameters randomly within their gaussian constraints.

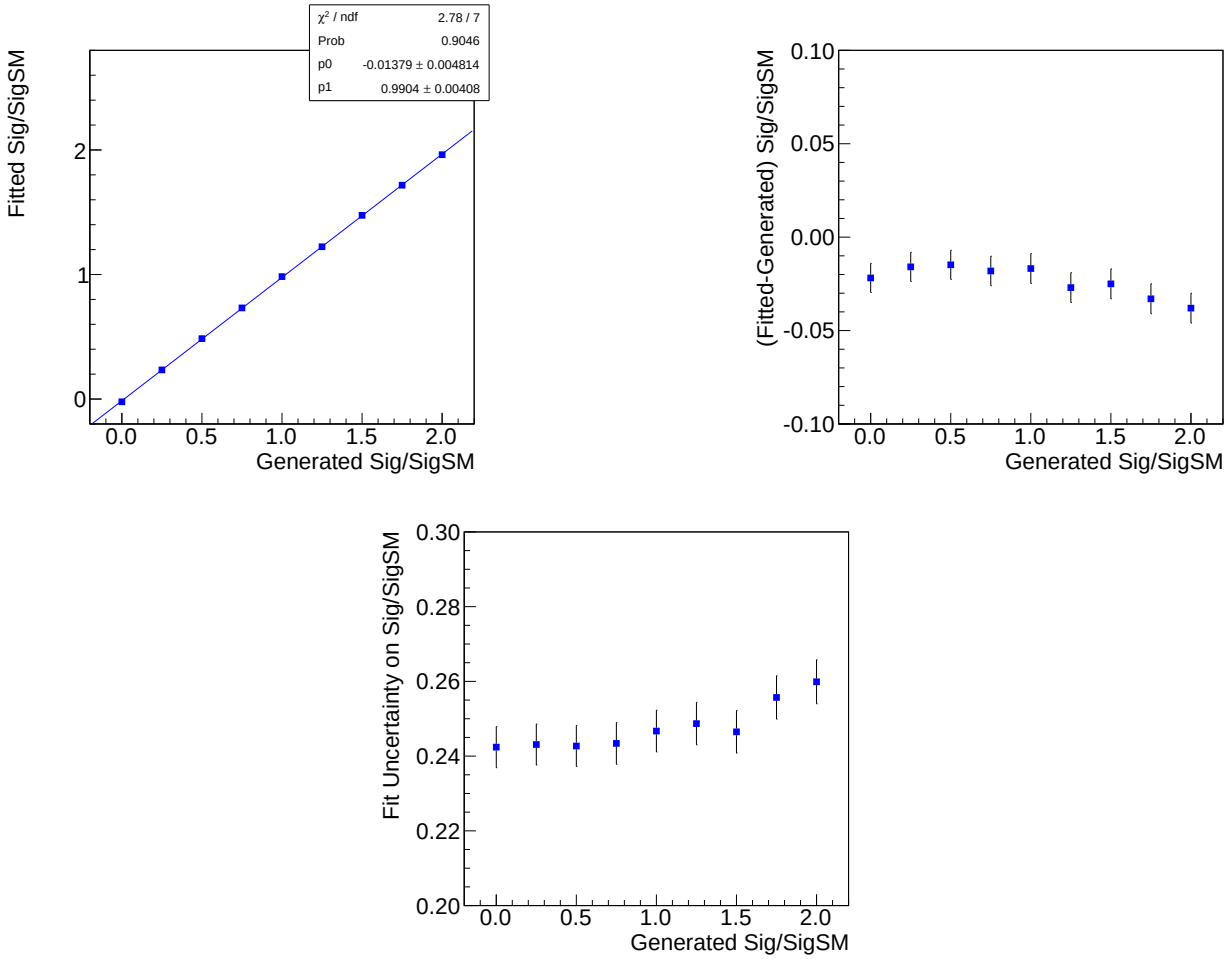

Figure 8.5: Results from the study to show the linearity of the fit in regards to returning the correct signal strength from pseudo-datasets generated with varied amounts of injected signal are shown. Top Left: The fitted β value is plotted against the generated β value with the parameters shown for the best fit line. Top right: The fit bias shown as the calculated fit β minus the generated β is shown. Bottom: The fit error on fitted β is shown as a function of the generated β.

were checked for stability across different values of the generated α values, and by comparing the fitted nuisance parameter with the generated value. Plots for two of the largest contributions to the systematic uncertainty in the measurement, W/Z+jets normalization and JER, can be seen in figure 8.6. The top plots show the dependence of the fitted signal strength with respect to the generated α value for each systematic. The bottom plots compare the fitted nuisance parameter with the generated value. This study shows that the signal strength has little dependence on the seen nuisance parameters and that the fit can accurately determine the correct value for the nuisance parameters across a long range of α values.

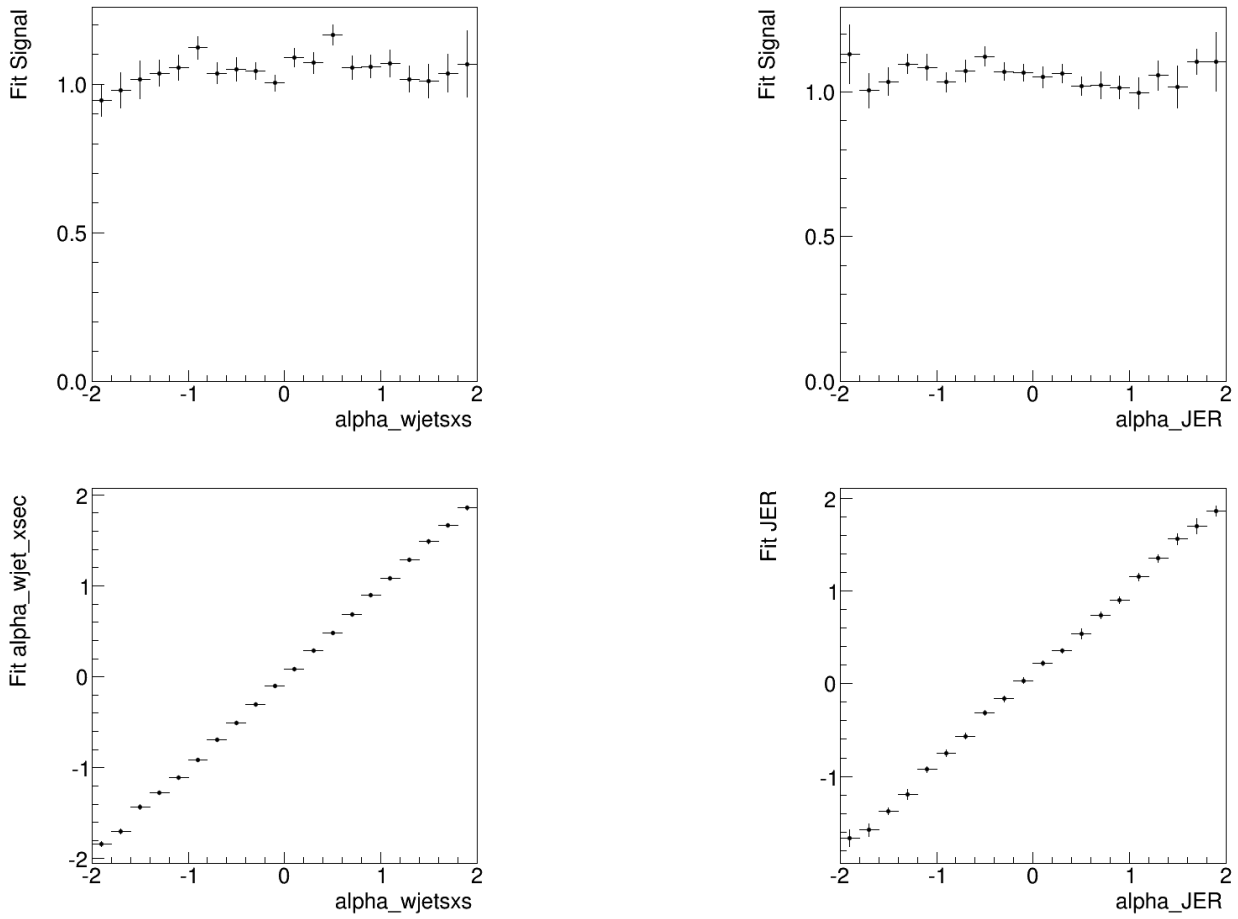

Figure 8.6: Results are shown for the psuedo-experiments done to look at the fit sensitivity while varying the systematic uncertainty nuisance parameters. The top plots show the fitted signal strengths as a function of the W/Z+jets production rate (left) and JER (right) α nuisance parameters used to generate the pseudo-datasets. The bottom plots show the generated W/Z+jets production rate (left) and JER (right) nuisance parameters used to generated the pseudo-datasets compared with the value returned by the fit.

Chapter 9

Results for the Cross Section Measurement

This chapter details the final results for the cross section measurement and additional tests to demonstrate the measurement's stability and reliability.

9.1 Cross Section Results

The fitted results for the likelihood fit to the m_{jj} distribution in data for the m_{jj} range between 25 to 250 GeV for the electron and muon channels are shown in figure 9.1. The distributions are created by applying the fitted α nuisance parameters, corresponding to each systematic, to the appropriate nominal templates as described in section 8.1. The systematic uncertainty band in the lower panel of the figures represents the total uncertainty, including the non-profiled systematics: JES15, QCD MJ normalization, and the bin-by-bin[1] uncertainty. Figure 9.2 shows the data minus the total fit for each lepton channel separately and the sum can be seen in figure 9.3.

The residuals calculated as the difference between the data in bin i and the fitted signal plus background yield in bin i, divided by the total uncertainty in that bin is shown in figure 9.4. The distribution of the residuals contains 90 entries corresponding to the 45 bins used in each channel and shows good agreement (within uncertainties) with a normal distribution with mean 0 and $\sigma = 1$. The lower panel of figure 9.4 shows the distribution of the residuals as a function of m_{jj} for the electron (black) and muon (red) channels.

The most probable signal strength obtained by the fit that maximizes the likelihood function is given by

$$\beta = 1.11 \pm 0.26 \tag{9.1}$$

The total fit uncertainty on β is 23% and is determined from the systematics profiled in the fit and the statistical uncertainty in the data. The statistical uncertainty in the data is calculated by fixing all nuisance parameters to their nominal fitted values and then re-doing the fit, the remaining uncertainty in the fit measurement is attributed to the statistical uncertainty. The fit uncertainty calculated separately for the profiled systematics is 21% and

[1] Uncertainty due to limited MC statistics

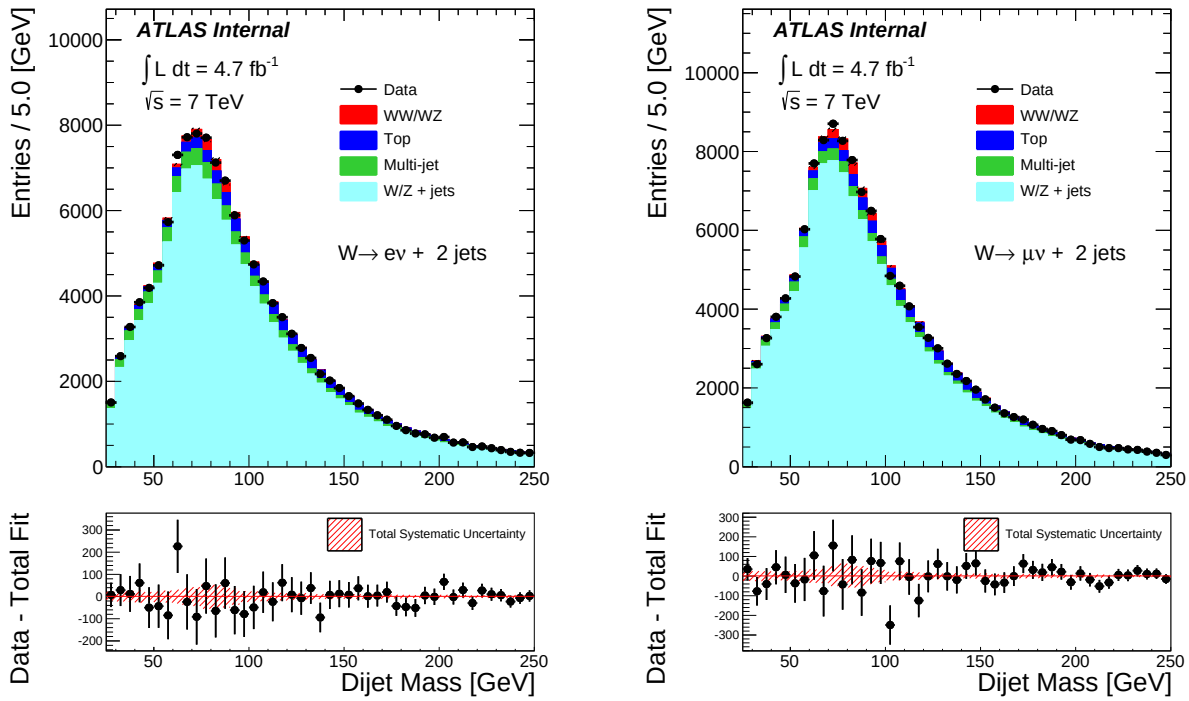

Figure 9.1: m_{jj} distributions for the electron (left) and muon (right) channels for data (black dots) and for the background plus signal distributions obtained from the combined fit. The different processes contributing to the background and signal are shown as stacked histograms. The lower panels show the difference between the data and the signal+background estimation (solid circles), including the WW/WZ signal scaled to the fitted cross section . The red band shows the systematic uncertainty from the fit and the uncertainty due to the non-profiled systematics.

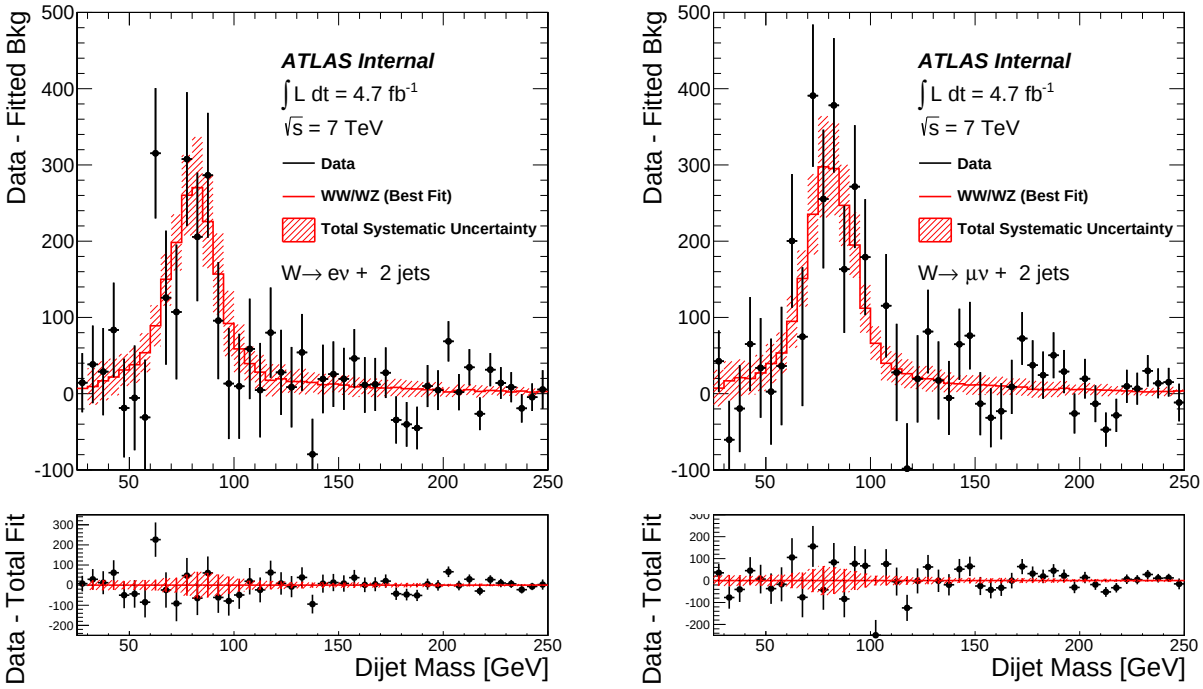

Figure 9.2: Distributions of the data (black dots) after the estimation for the background only distributions has been subtracted for the electron (left) and muon (right) channels. The error bars represent the statistical error for the data. The superimposed red histogram shows the fitted signal and the hatched red bands show the total systematic uncertainty. The bottom panels show the difference between data and MC, where MC includes both the background (including the QCD estimation) and signal.

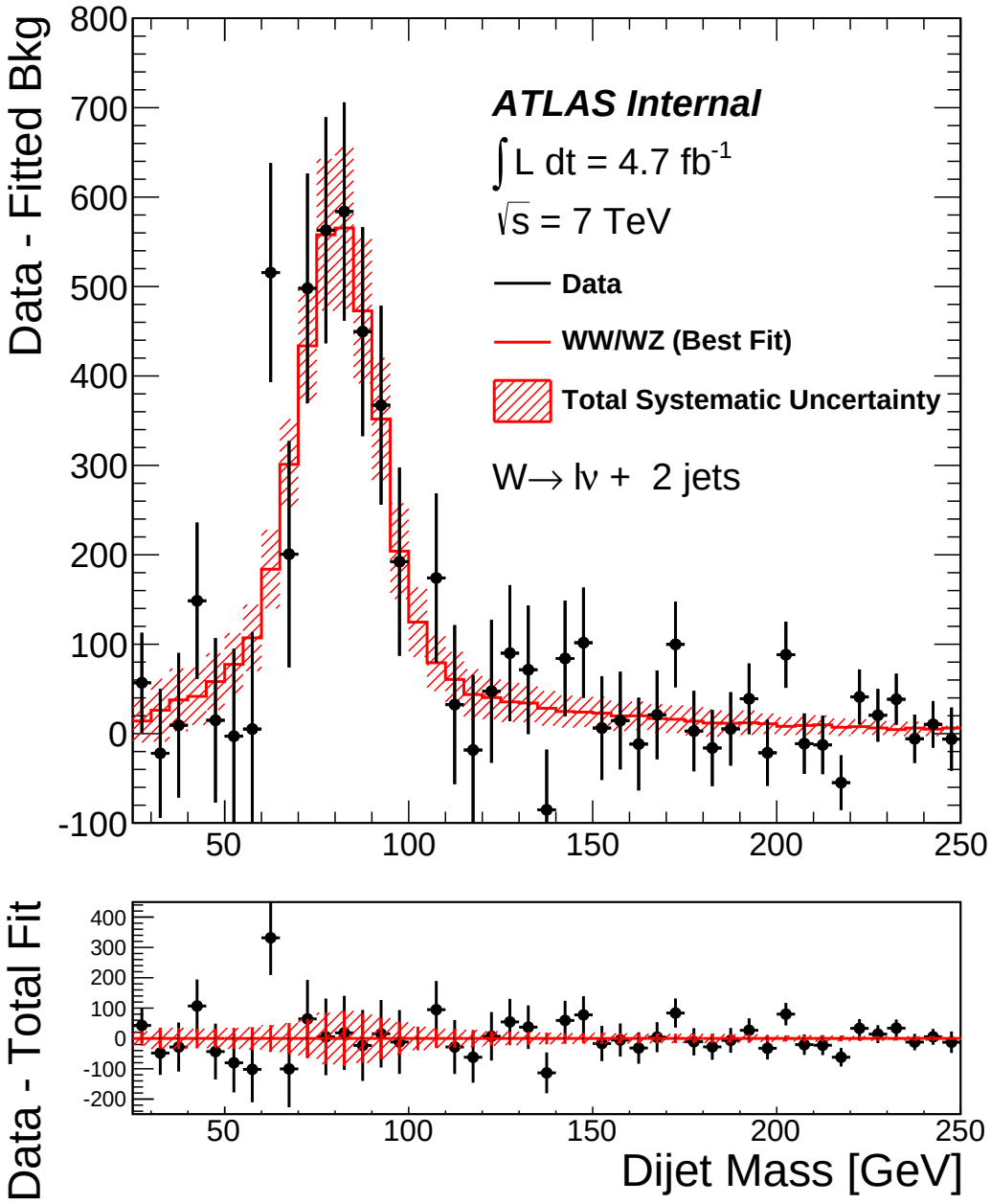

Figure 9.3: Distribution of the data (black dots) after the estimation for the background only distributions has been subtracted from the sum of the electron and muon channels. The error bars represent the statistical error for the data. The superimposed red histogram shows the fitted signal and the hatched red bands show the total systematic uncertainty. The bottom panel shows the difference between data and MC, where MC includes both the background (including the QCD estimation) and signal.

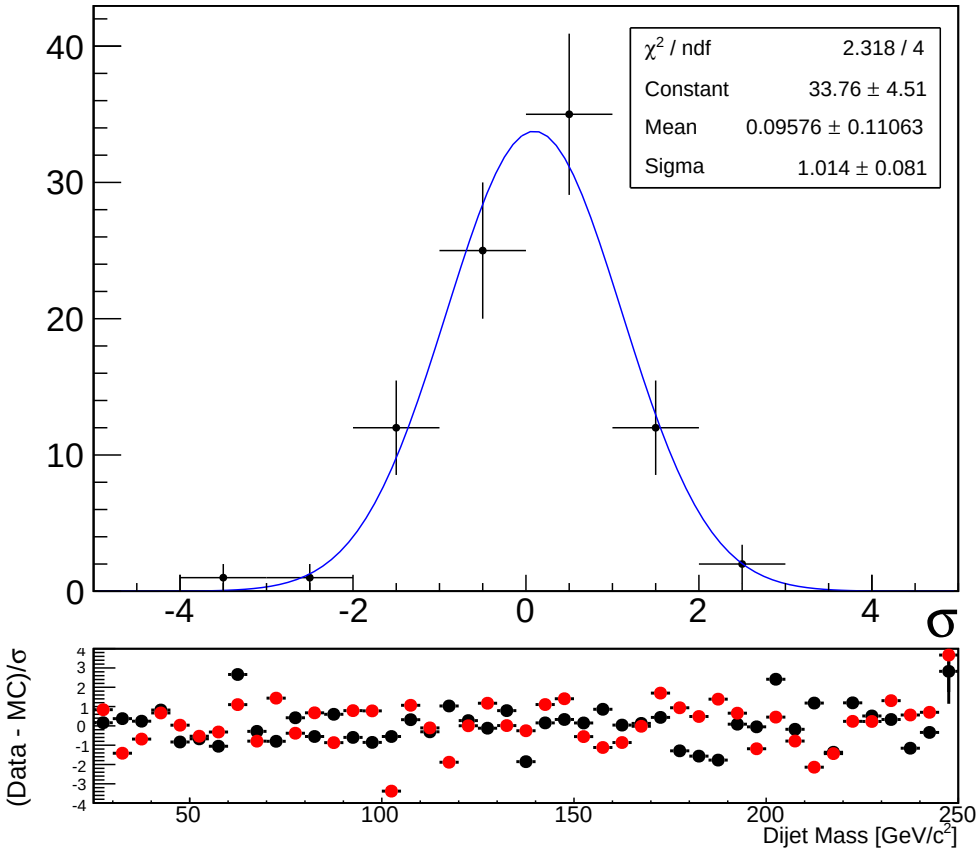

Figure 9.4: The top plot shows the distribution of the differences between data and the fitted signal+background estimations divided by the total uncertainty in each bin of the m_{jj} distributions corresponding to the electron and muon channel. The distribution includes 90 entries (45 bins per channel), one for each bin of the electron and muon channel m_{jj} distribution. The residual distribution is fitted with an overlaid gaussian function. The bottom plot shows the residuals divided by the total uncertainty as a function of m_{jj} for the electron (black) and muon (red) channels.

10% for the data statistics. Summing in quadrature the uncertainty from the non-profiled systematics with the profiled systematics gives a total uncertainty due to just systematics of 26%. Multiplying the fitted β value and its uncertainties with the expected signal yield $N^{expected}$ gives

$$N^{meas}_{electron} = 1965 \pm 197 \text{ (statistical)} \pm 501 \text{ (systematic)}, \tag{9.2}$$

$$N^{meas}_{muon} = 2191 \pm 219 \text{ (stat.)} \pm 599 \text{ (syst.)}, \tag{9.3}$$

A full list of each nuisance parameter fitted value and their uncertainty can be found in table 9.1 and in figure 9.5 (right). The nuisance parameter correlation matrix[2] is also shown in figure 9.5 (left).

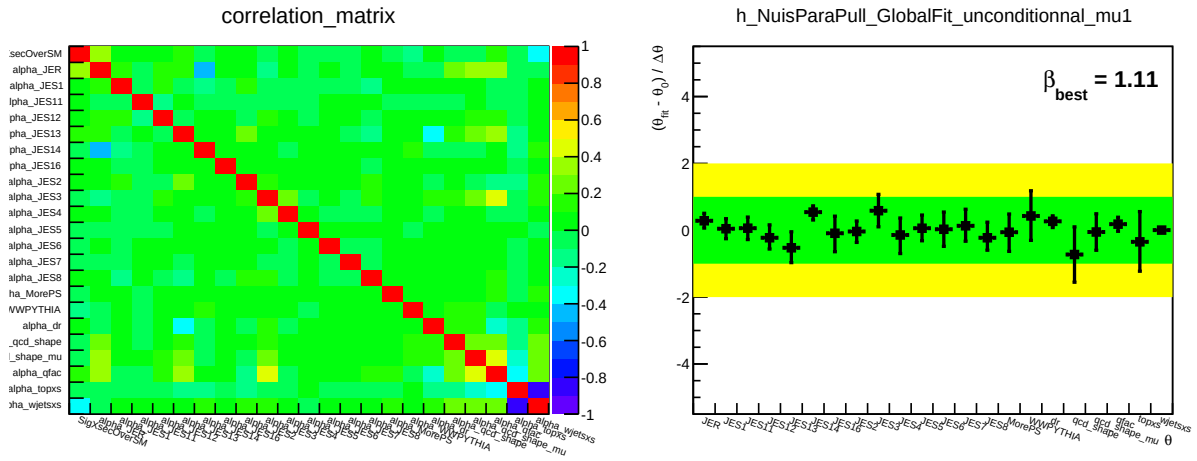

Figure 9.5: The nuisance parameter correlation matrix for all profiled systematics is shown on the left. The shift of each nuisance parameter with respect to their nominal value and their corresponding relative error in units of σ are shown on the right. A value equal to 0 means that the nuisance parameter value after the fit is equal to the nominal value, a value equal to 1 means that the nuisance parameter has been moved by 1 σ. The 1 and 2 σ bands are represented by the yellow and green bands respectively.

The expected signal significance as defined in section 8.3 by the likelihood ratio λ is estimated to be 3.2σ. The observed significance measured in data corresponds to 3.4σ, figure 9.6 shows the likelihood ratio distribution with the measured result. The total cross section (WW+WZ) calculated using equation 6.3 is

$$\sigma_{tot} = 68 \pm 7 \text{ (stat.)} \pm 18 \text{ (syst.) pb}. \tag{9.4}$$

The fiducial cross section (WW+WZ) calculated using equation 6.7 is

$$\sigma_{fid} = 1.35 \pm 0.14 \text{ (stat.)} \pm 0.36 \text{ (syst.) pb}, \tag{9.5}$$

[2]The correlation matrix is calculated by dividing the i^{th} and j^{th} element of the covariance matrix by the multiplication of the uncertainties for the i^{th} and j^{th} element

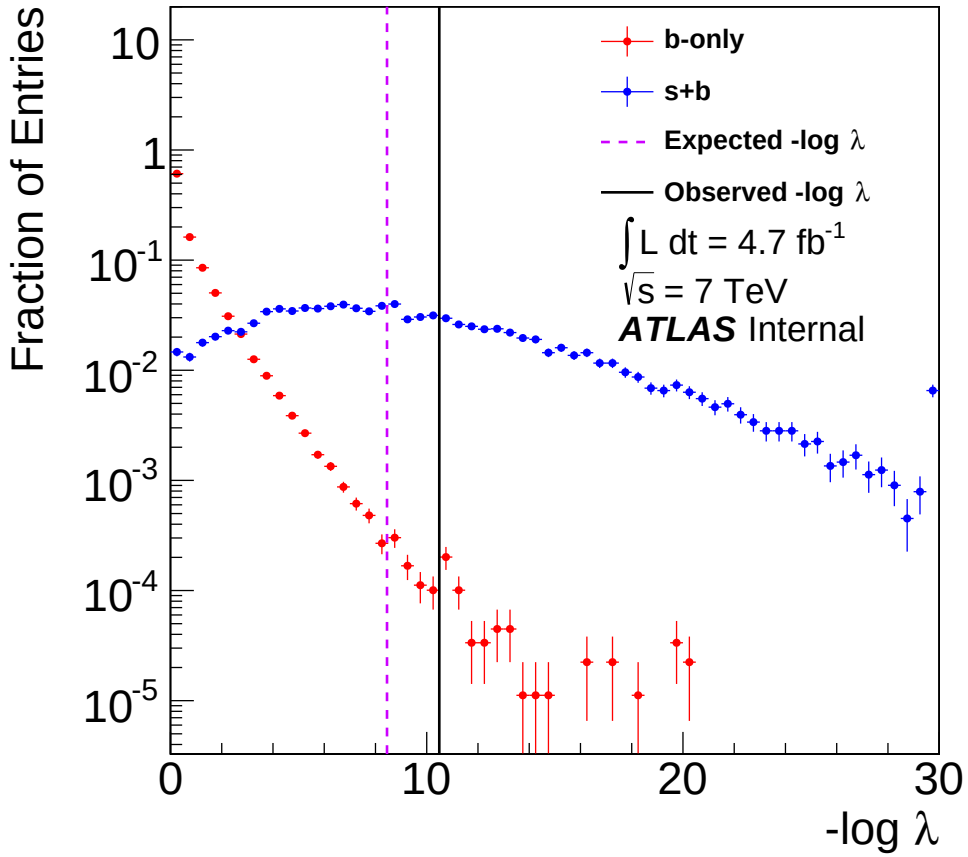

Figure 9.6: Distributions of the negative log likelihood ratio $-log(\lambda)$ for background-only (red points) and signal+background (blue points) pseudo-experiments. The expected value of λ for the signal+background hypothesis is shown as a dashed purple vertical line and is located at the median of the $-log(\lambda_{sig+bkg}$ distribution. The observed value as measured in the data is given by the solid black line.

Nuisance Parameter	Post Fit Value (in σ unit)
μ	$1.11^{+0.26}_{-0.25}$
Jet Energy Resolution uncertainty (JER)	$0.28^{+0.22}_{-0.22}$
Jet Energy Scale uncertainty component JES1	$0.05^{+0.30}_{-0.30}$
Jet Energy Scale uncertainty component JES11	$0.06^{+0.33}_{-0.34}$
Jet Energy Scale uncertainty component JES12	$-0.22^{+0.39}_{-0.34}$
Jet Energy Scale uncertainty component JES13	$-0.53^{+0.48}_{-0.44}$
Jet Energy Scale uncertainty component JES14	$0.54^{+0.19}_{-0.24}$
Jet Energy Scale uncertainty component JES16	$-0.1^{+0.5}_{-0.6}$
Jet Energy Scale uncertainty component JES2	$-0.04^{+0.31}_{-0.33}$
Jet Energy Scale uncertainty component JES3	$0.59^{+0.49}_{-0.48}$
Jet Energy Scale uncertainty component JES4	$-0.1^{+0.5}_{-0.6}$
Jet Energy Scale uncertainty component JES5	$0.06^{+0.39}_{-0.38}$
Jet Energy Scale uncertainty component JES6	$0.0^{+0.5}_{-0.5}$
Jet Energy Scale uncertainty component JES7	$0.13^{+0.50}_{-0.46}$
Jet Energy Scale uncertainty component JES8	$-0.23^{+0.47}_{-0.37}$
Top samples ISR/FSR variations (MorePS)	$-0.1^{+0.5}_{-0.6}$
Signal shape modeling uncertainty (WWPYTHIA)	$0.4^{+0.8}_{-0.7}$
Wjet modeling (matching NLO, shower - dr)	$0.27^{+0.16}_{-0.19}$
Multi QCD shape uncertainty electron (qcd_shape)	$-0.7^{+0.8}_{-0.8}$
Multi QCD shape uncertainty muon (qcd_shape_mu)	$-0.1^{+0.5}_{-0.5}$
Wjet modeling factorization/normalization scale (qfac)	$0.18^{+0.21}_{-0.21}$
ttbar and single top norm. uncertainty (topxs)	$-0.3^{+0.9}_{-0.9}$
W/Z+jet norm. uncertainty (wjetsxs)	$0.005^{+0.046}_{-0.049}$

Table 9.1: The full list of profiled nuisance parameters and their uncertainties as obtained from the simultaneous fit to the electron and muon channels.

where the electron and muon channel contributions to the fiducial cross section are summed together. Both measurements are consistent with the SM prediction of $\sigma_{tot}(WW+WZ) = 61.1 \pm 2.5$ pb for the total cross section and $\sigma_{fid}(WW+WZ) = 1.22 \pm 0.05$ pb for the fiducial cross section. The systematics for the total and fiducial cross section measurement are calculated by summing in quadrature the uncertainty contributions from the signal yield N^{meas}, D_{fid}, D_{tot}, and the integrated luminosity. Table 9.2 gives a summary of the percent error contributions from each systematic source relative to the measured cross section. The values used for the systematic uncertainites that affect D_{fid}, D_{tot}, and the integrated luminosity are described in the appropriate sections of chapter 7. For the uncertainties that affect N^{meas},

Source	σ_{fid}	σ_{tot}
	N_{meas}	
Data Statistics	±10	
MC Statistics	±12	
W/Z+jets Normalization	±15	
W/Z+jets Shape Modeling	±4	
Multijet Shape and Normalization	±8	
Top Normalization/Shape modeling ISR/FSR	±6	
Jet Energy Scale Shape, All Processes	±9	
Jet Energy Resolution Shape, All Processes	±11	
WW/WZ Shape Modeling	±5	
	D_{fid}	D_{tot}
JES/JER Uncertainty	±6.0	±6.0
Fragmentation	±4.0	±5
Jet Veto Scale Dependence	-	±5
Others (spin-corr, lepton reco, PDF)	±1	±4
Integrated Luminosity	±1.8	
Total Systematics	±27	±28

Table 9.2: Table shows the observed statistical and systematic uncertainties as percentages for the measured fiducial and total cross sections. The uncertainties are divided up according to the quantity (N^{meas}, D_{fid}, D_{tot}, Integrated Luminosity) they are affecting.

they are estimated by re-evaluating the fit by first fixing one of the parameters to the central value given by the fit and then comparing the new fit uncertainty with the uncertainty of the nominal fit (where none of nuisance parameters are fixed). The subtraction of these two uncertainties in quadrature gives an estimate of the uncertainty due to the fixed nuisance parameter. As can be seen in the table, the largest source of uncertainty is unsurprisingly from the W/Z+jets normalization, followed by the MC statistics and the JER.

9.2 Additional Validation Checks on the Fit

Several additional checks on the fit results have been performed and are described in the following sections.

9.2.1 Stability of the Fit

The stability of the fit has been checked by repeating the fit results using slightly different event selections. The event selection for this analysis was conducted by studying the Signal-to-Background (S/B) ratios and signal significance ($S/\sqrt{B}$) in the MC. Though due to the small S/B ratio ($< 2\%$) it is necessary to check that the fit results are consistent with respect to small variations in the selection criteria to ensure that the nominal results are not due to a lucky outlier in the fit.

Varied cut	β
Nominal	1.13 ± 0.20
$E_T^{\text{miss}} > 35(30)$ GeV	0.95 ± 0.25
$E_T^{\text{miss}} > 25(30)$ GeV	0.97 ± 0.20
$Jet_1\ p_T > 35(30)$ GeV	1.07 ± 0.22
$Jet_1\ p_T > 25(30)$ GeV	1.00 ± 0.24
$Jet_2\ p_T > 30(25)$ GeV	0.86 ± 0.23
$m_{\text{T}} > 45(40)$ GeV	0.84 ± 0.22

Table 9.3: This table demonstrates the stability of the fit results as slight changes in the selection are made. The first column lists the varied selection criteria with respect to the nominal selection. For each varied value, the nominal value is given in parenthesis. The second column gives the fitted β value for the corresponding selection criteria in the first column. The fit to calculate β was performed with a reduced set of nuisance parameters, all JES and QCD MJ systematics were not profiled in the fit. Therefore, the error given for β only corresponds to the statistical uncertainty in data and the systematic uncertainty due to the JER, W/Z+jets and top normalization, W/Z+jets modeling, signal modeling, and ISR/FSR uncertainty for the top samples.

The fit has been performed on new templates produced with different selection criteria for the E_T^{miss}, leading and sub-leading jet p_{T}, and the m_{T}. It's important to note that the various changes in the selection do not differ wildly from the nominal values (no more than 5 GeV) as small changes in these variables already greatly effect the acceptance of the QCD MJ background and the W/Z+jets background. Each of the fits were performed with only a subset of the nuisance parameters in order to speed up the validation study. Table 9.3 lists the different selection criteria that was used to produce the templates and the measured signal strengths with their uncertainties for each selection. The results show that the signal strength is quite stable across a range of selection criteria around the nominal selection.

9.2.2 Separate Fits to the Electron and Muon Channels

The results shown in section 9.1 were done with performing the fit simultaneously for both lepton channels. This section looks at the results for doing the fit for the electron and muon channels separately to ensure that the fit returns results within the given uncertainties. The calculated signal strengths given by the fit separate lepton fits are

$$\beta_{muon} = 1.13 \pm 0.36, \tag{9.6}$$

$$\beta_{electron} = 1.00 \pm 0.36. \tag{9.7}$$

For both measurements the uncertainty corresponds to only the statistical and systematic uncertainties that are profiled in the fit. Both values are in agreement within the statistical uncertainty of each other and that of the combined measurement. The fitted m_{jj} distributions for each channel are shown in figure 9.7, with the corresponding correlation matrices and

nuisance parameter values shown in figure 9.8. Additionally, figure 9.9 shows the β values for the separate fits and simultaneous fit overlaid on the same figure.

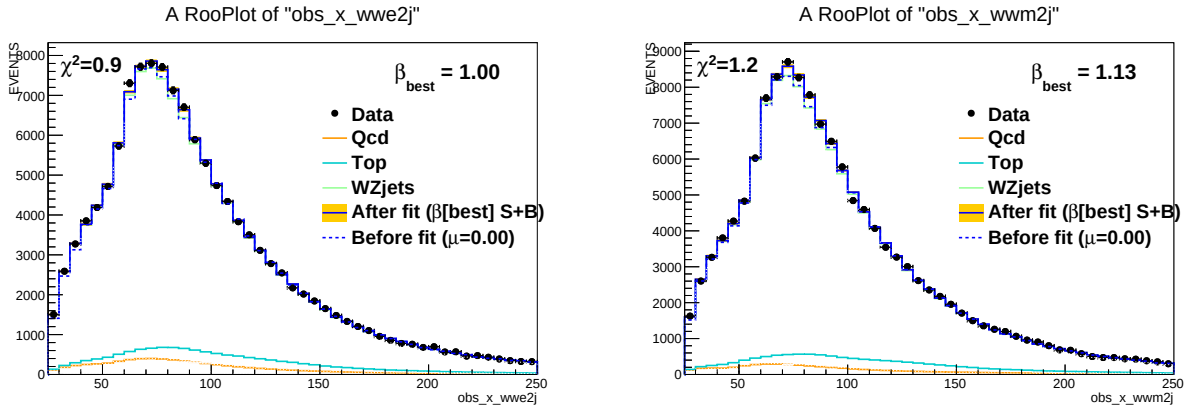

Figure 9.7: m_{jj} distributions for the electron (left) and muon (right) channels for data (solid black dots) and for the background plus signal distributions obtained from the fits to each lepton channel separately.

9.2.3 Performing Fit with Conditional Zero Signal

Lastly, the fit is performed with fixing the signal strength β to a value of zero. This tests if the background distributions can adequately model the m_{jj} distribution in data without the need for any signal events. It should be noted that the sensitivity study discussed in section 8.4.3 is a better metric for judging whether the fit can accurately return a β_{fitted} equivalent to the hypothesis β. The fit using a fixed $\beta = 0$ value is done with the complete nuisance parameter configuration used for the nominal fit. Figure 9.10 shows the difference between the data and the fitted background m_{jj} distributions for the combined electron and muon channels. It is clear from the distribution that the region close to where the signal would be (70 to 100 GeV) has a discrepancy between the data and the fitted background.

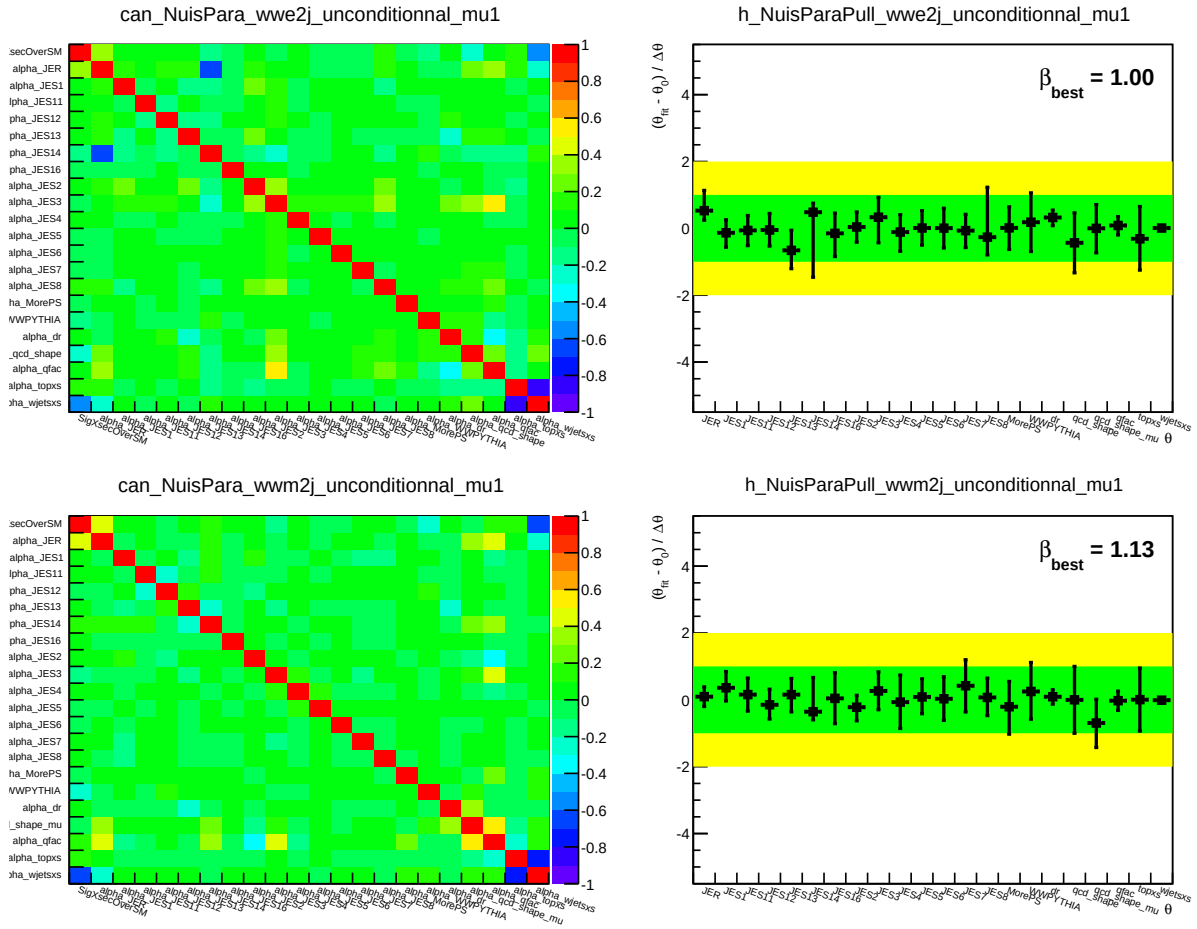

Figure 9.8: The nuisance parameter correlation matrix for all profiled systematics is shown on the left for the separate fits to the electron (top) and muon (bottom) channels. The shift of each nuisance parameter with respect to their nominal value and their corresponding relative error in units of σ are shown on the right due to the separate lepton fits for the electron (top) and muon (right) channels. A value equal to 0 means that the nuisance parameter value after the fit is equal to the nominal value, a value equal to 1 means that the nuisance parameter has been moved by 1 σ. The 1 and 2 σ bands are represented by the yellow and green bands respectively.

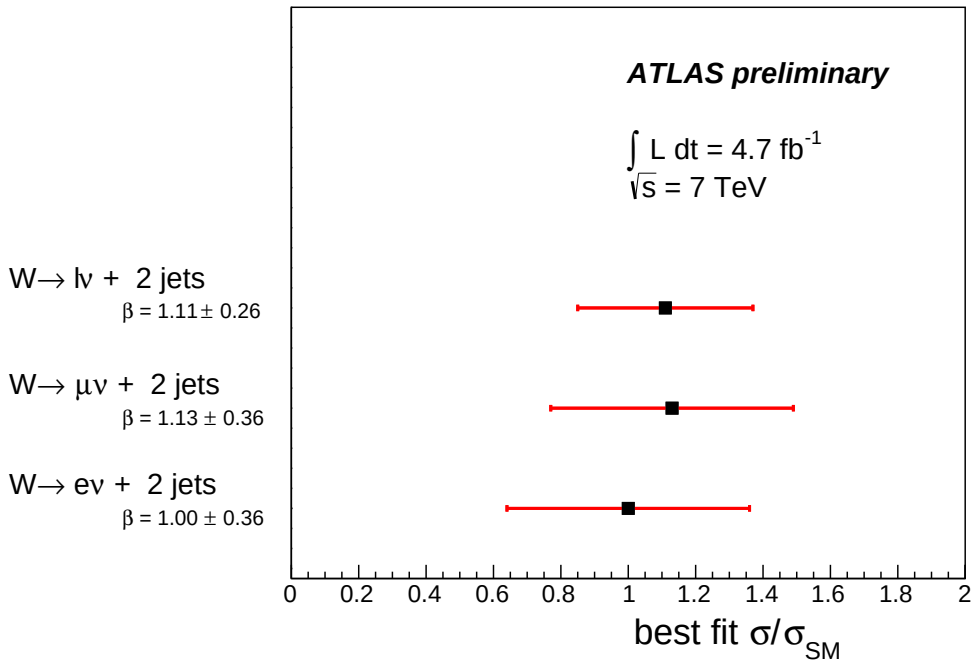

Figure 9.9: This figure gives a summary of the β results returned from the fit using a simultaneous fit to both lepton channels and to each channel separately. The error bars only include the statistical uncertainty and systematic uncertainty due to the profiled systematics in the fit.

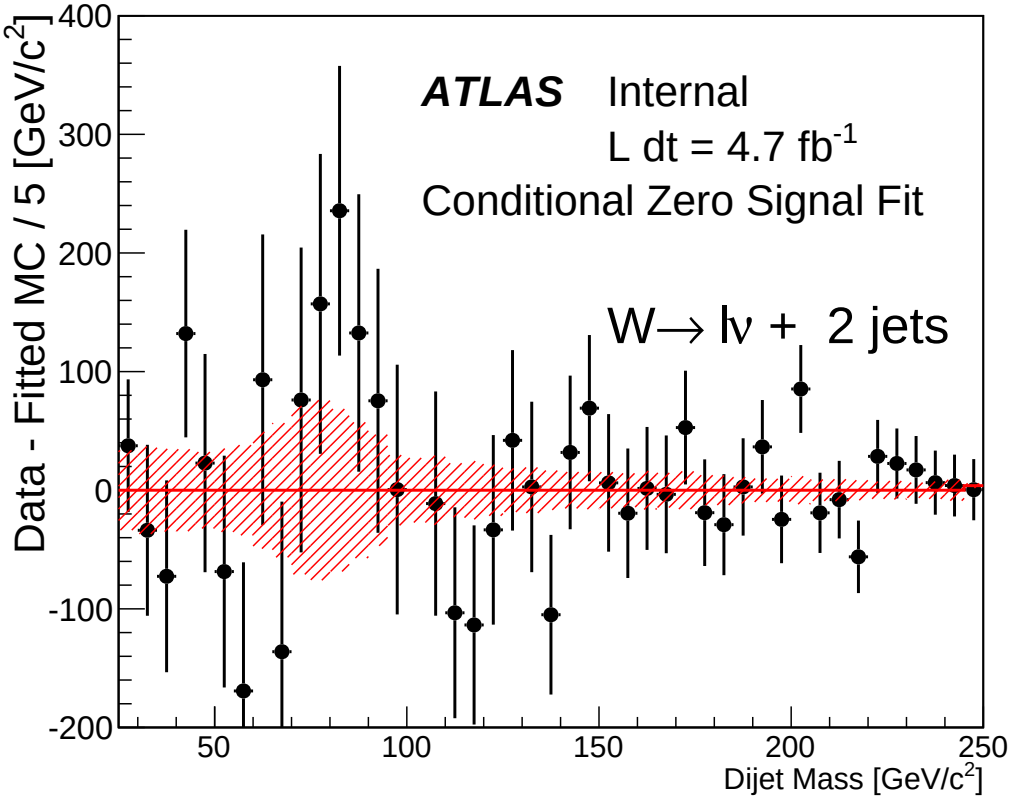

Figure 9.10: This figure shows the difference between data and the fitted distribution for the background, assuming zero signal events, for the combined electron and muon channel. The error bars on the black points represent the statistical error in the data and the red systematic band is the total systematic uncertainty.

Chapter 10

Limit Studies for Anomalous Triple Gauge Couplings

This chapter discusses how the limit studies were performed for possible extensions to the SM through the form of additional anomalous triple gauge couplings (aTGCs). For an introduction to aTGCs and a description of the anomalous coupling parameters of interest please refer back to section 1.5.

The chapter is broken up into several sections. Sections 10.1 and 10.2 discuss the changes to the event selection and to the treatment of the systematic uncertainties for the aTGC limit studies. The aTGC reweighting scheme for MC@NLO is discussed in section 10.3. Section 10.4 describes the limit setting procedure and the binning optimization used for the limit calculations. Final expected and observed results are discussed in section 10.6.

10.1 Event Selection for the aTGC Limits

In order to evaluate the anomalous coupling limits it is necessary to increase the purity of the signal events from what is seen in the cross section selection. Since evidence of aTGCs appears for the most part in the high energy tails of kinematic distributions (e.g. lepton and jet p_{T}) it becomes important to remove as much background as possible to discriminate between possible aTGC related signals and other backgrounds. This increase in the signal-to-background ratio can be efficiently done by requiring a cut on the dijet invariant mass for a mass window around the W and Z boson mass peaks.

Therefore the aTGC selection only differs from the cross section measurement by requiring that m_{jj} be between 75 GeV and 95 GeV. The range of the mass window was optimized by comparing the significance (Signal/$\sqrt{\mathrm{Bkg}}$), calculated as the number of signal events over the square root of background events, for signal samples corresponding to different aTGC values. A list of the aTGC points investigated is seen below[1]:

- aTGC point 1: $\lambda^Z = \lambda^\gamma = 0.35$
- aTGC point 2: $\lambda^Z = \lambda^\gamma = -0.35$

[1]The events were reweighted to the appropriate aTGC point using the standard MC@NLO aTGC reweighting scheme discussed in section 10.3

- aTGC point 3: $\Delta\kappa^{\gamma} = 0.19$
- aTGC point 4: $\Delta\kappa^{\gamma} = -0.19$

The aTGC values for each sample were chosen based on the expected aTGC limit sensitivity for this study. Only events in which the dijet transverse momentum $p_{\mathrm{T}}(jj) > 350$ GeV were considered to restrict the selection to the region with the highest aTGC sensitivity. The SM signal event yield was included as part of the background and only the difference between the aTGC signal yield and the SM signal event for each sample was considered as signal for the significance calculation. The significance was calculated for mass windows of varying sizes between 60 and 120 GeV in steps of 5 GeV. The results showed that the 75 to 95 GeV m_{jj} window had the largest significance across the majority of samples tested.

Additionally, as discussed in the event selection (section 5.4), the cut $\Delta R(Jet_1, Jet_2) > 0.7$ is dropped for events with a $p_{\mathrm{T}}(jj) > 250$ GeV. This selection criteria was initially imposed to correct for the mis-modeling seen in the ALPGEN samples. As can be seen in figure 10.1, the selection greatly reduces the number of events that pass the event selection at the high $p_{\mathrm{T}}(jj)$ tails. This reduction in efficiency results in about a factor of two deterioration in the aTGC limits, therefore this selection criteria was removed for the high $p_{\mathrm{T}}(jj)$ events. This comes at a cost, with the increase in the acceptance there is also an increase in the systematic uncertainty due to the ALPGEN mismodeling for W/Z+jets in that region. It should be noted that unlike the low $p_{\mathrm{T}}(jj)$ region which is systematically limited, the high $p_{\mathrm{T}}(jj)$ region is statistically limited so the effect of a larger systematic due to dropping the ΔR cut would not have as large of an effect on the total uncertainty. This and the other systematics that effect the W/Z+jets modeling for the aTGC limits are discussed further in section 10.2.2.

10.1.1 Choice of aTGC Fit Variable

The choice on which aTGC fit variable to use to set the aTGC limits is discussed here. The addition of aTGCs enhances the diboson cross section for high boson p_{T}, the variables considered were:

- The dijet transverse momentum $p_{\mathrm{T}}(jj)$, which is effectively the p_{T} of the hadronically decaying W or Z candidate.
- The p_{T} of the lepton $p_{T,\ell}$ from the leptonically decaying W candidate.

A priori, it is important to state that the $p_{\mathrm{T}}(jj)$ variable is expected to be more sensitive than $p_{T,\ell}$ without the inclusion of systematics since $p_{\mathrm{T}}(jj)$ probes directly the p_{T} of the boson. This study is to see if the larger jet uncertainties change the expected limits to the point where the $p_{T,\ell}$ variable becomes more favorable to use due to the lepton systematics being considerably smaller. The expected aTGC limits were calculated (see section 10.4) for both variables as shown in table 10.1. In the case of $p_{\mathrm{T}}(jj)$ the expected limits were calculated without systematics and with the inclusion of systematics due to the JES and the background normalizations (20% for W/Z+jets, 10% for top, and 30% for QCD MJ). From this study it can be seen that the limits for $p_{T,\ell}$ without applying any systematics is approximately 25% worse than $p_{\mathrm{T}}(jj)$ with the inclusion of the major systematics due to the

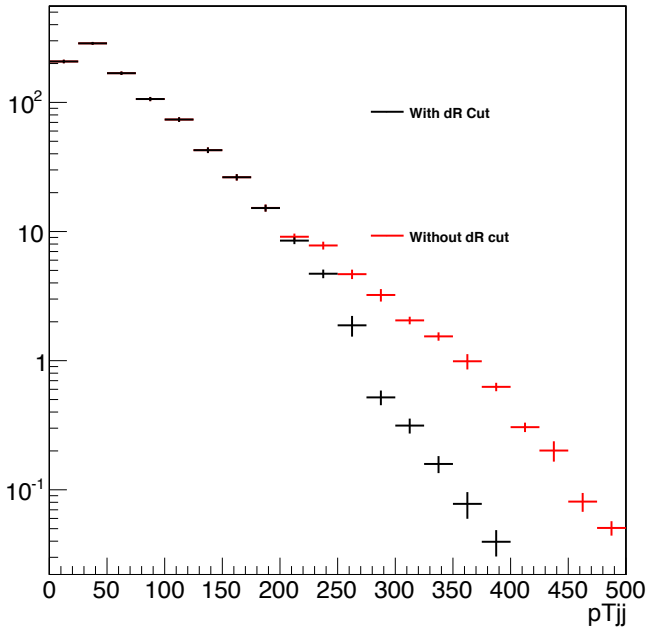

Figure 10.1: Figure shows a comparison of the $p_{\mathrm{T}}(jj)$ distribution after applying the aTGC selection, with (black) and without (red) applying the $\Delta R(Jet_1, Jet_2) > 0.7$ cut. The distribution is shown in log scale to get a better idea of the differences in the tails of the distribution.

jets and normalization. Therefore, the $p_{\mathrm{T}}(jj)$ variable was chosen in this analysis in order to calculate the observed aTGC limits.

Expected 95% Limits on aTGC's			
Variable	Systematics	λ	κ^{γ}
$p_{\mathrm{T}}(jj)$	MC stat.	[−0.0401, 0.0403]	[−0.221, 0.244]
$p_{\mathrm{T}}(jj)$	MC stat., JES, bkg. norm.	[−0.0408, 0.0409]	[−0.225, 0.247]
$p_{T,\ell}$	MC stat.	[−0.0513, 0.0519]	[−0.288, 0.313]

Table 10.1: Calculated expected aTGC limits for the variables $p_{\mathrm{T}}(jj)$ and $p_{T,\ell}$ without including any systematics. Additionally the expected limits for $p_{\mathrm{T}}(jj)$ are calculated including uncertainties due to JES and the background normalizations (20% for W/Z+jets, 10% for top, and 30% for QCD MJ).

10.2 Treatment of Systematic Uncertainties for aTGC Limit Studies

The systematics used for the aTGC limit setting are identical to those used for the cross section measurement except some of the systematics were excluded due to being negligible in regards to the high $p_{\mathrm{T}}(jj)$ tails[2]. The systematics that were neglected include the QCD multi-jet shape, ISR/FSR systematic on top, and JES components 4-8,11,12,and 16. Additionally, the signal modeling systematic calculated by comparing a LO PYTHIA signal sample to the NLO MC@NLO nominal samples was too conservative since the difference between NLO and LO is quite large. Instead the signal modeling systematic was derived by comparing LO PYTHIA to LO HERWIG and the shapes of their $p_{\mathrm{T}}(jj)$ distributions were found to be consistent within their uncertainties so this systematic was also dropped.

As will be described in section 10.4, the remaining systematics are included in the limit setting as nuisance parameters. Since they consist of both the same normalization and shape uncertainties that were described thoroughly in chapter 7, the following sections will emphasize some of the systematics that are of particular interest to the aTGC limit calculation.

10.2.1 Signal Uncertainties

The WW and WZ production rate systematic for the signal is a little different than what was used in the cross section measurement for D_{fid} and D_{tot} due to the addition of the m_{jj} window and the theory uncertainty on the SM cross section (4.1%). The normalization uncertainty effects due to JES, JER[3], signal modeling (7.5%, zero-width approximation, see next paragraph), and the theoretical uncertainty in the cross section were taken into account and summed in quadrature to arrive at a 15% total normalization uncertainty for the signal.

[2]The aTGC limit code takes a fairly long time to calculate limits, dropping unnecessary systematics speeds up this process

[3]Tables breaking down the normalization uncertainties for the JES and JER components in the aTGC selection can be found in appendix B.1.1.

The largest contribution to this uncertainty comes from the JES at 11%-16%, mainly from the JES14 which corresponds to the flavor composition of the jets.

The zero width approximation uncertainty due to the MC@NLO samples being generated with only on-shell bosons was discussed in section 7.5.1 in relation to the cross section measurement. Due to its impact on the m_{jj} distribution, its effect on the aTGC analysis with respect to the use of the m_{jj} window needed to be re-evaluated as a normalization uncertainty. LO PYTHIA (Breit-Wigner) samples were compared to the NLO MC@NLO (on-shell) samples and a production rate difference of 7.5% was calculated within the m_{jj} window.

The effect due to the MC@NLO samples being generated neglecting the spin-correlations between the decaying bosons was discussed in section 7.5.5. In terms of the aTGC analysis, the 3% difference in production rate between the MC@NLO $WZ \to e\nu\mu^+\mu^-$ samples produced with and without spin-correlations is taken into account by the PYTHIA vs MC@NLO systematic. In regards to any uncertainties in the shape distributions, the electron and Z boson η and p_{T} distributions are compared between the two generated truth samples and are shown in figures 10.2 and 10.3. As a reminder, the $p_T(Z)$ is a proxy for the $p_{\mathrm{T}}(jj)$ variable used in the aTGC calculation. As can be seen in the figure, the effect due to neglecting the spin correlations is small and within the uncertainties for the $p_T(Z)$ distribution. No additional systematic due to this uncertainty is added to the aTGC analysis.

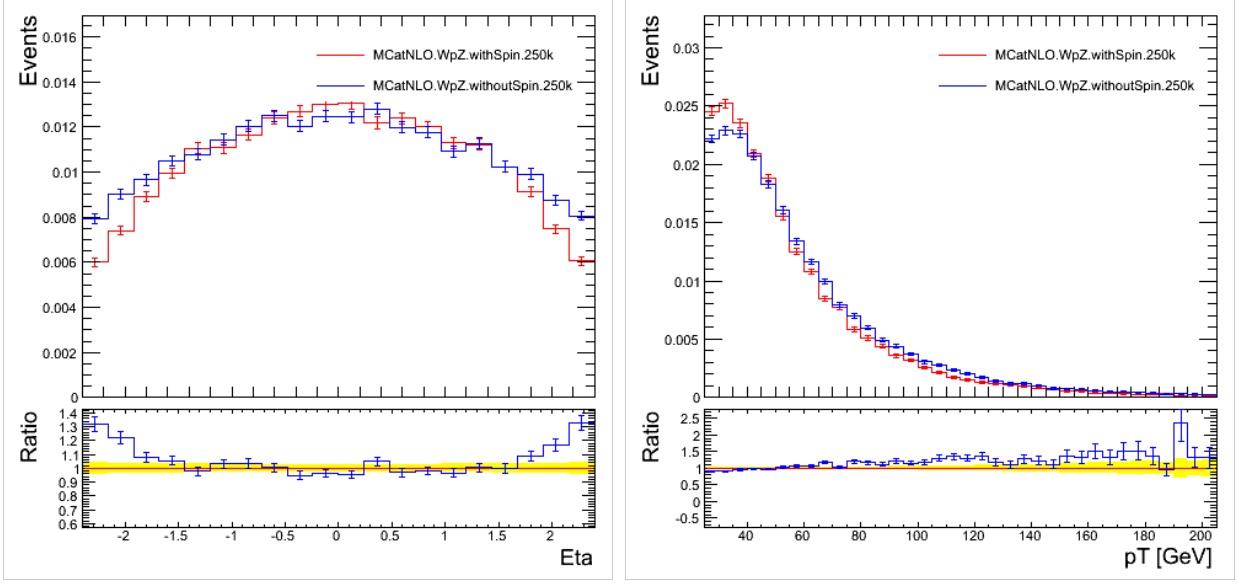

Figure 10.2: Distributions for the electron η (left) and p_{T} (right) are shown for truth generated $WZ \to e\nu\mu^+\mu^-$ samples with (red) and without (blue) including spin-correlations. The distributions are not normalized to the same area since the acceptances differ between both samples. Study and plots from reference [23].

Lastly, the possible p_{Tjj}-dependence based on the renormalization/factorization (μ_R/μ_F) scales of the signal samples were evaluated. As was discussed in section 7.5.3, event-generation-only (truth) MC@NLO samples were produced by varying both scales simultaneously and independently of each other. The largest deviations from the nominal samples

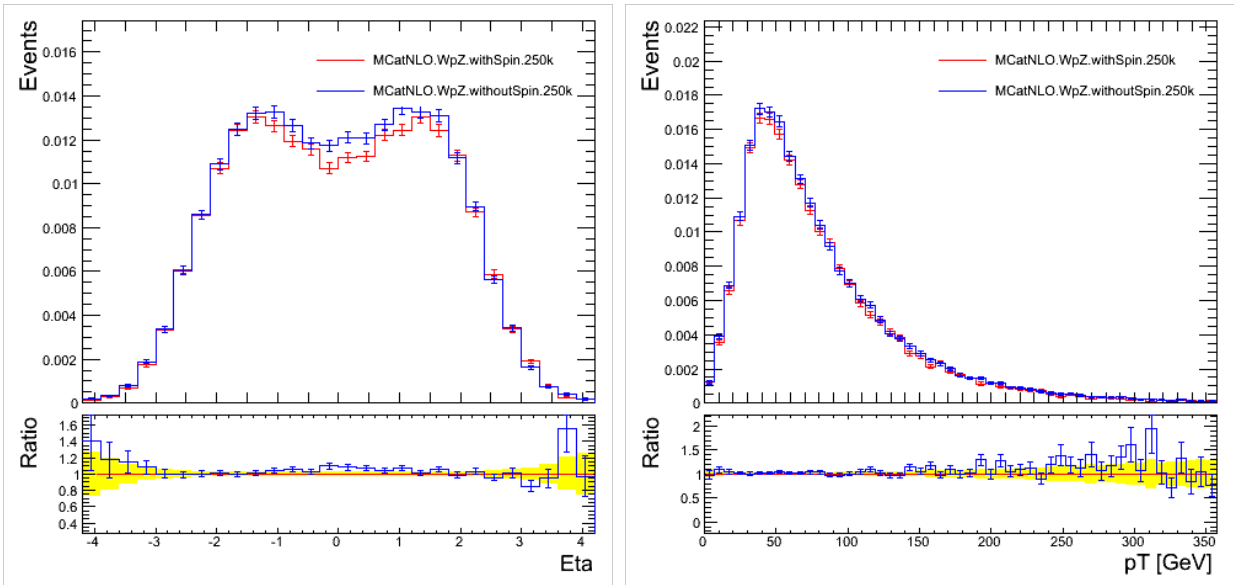

Figure 10.3: Distributions for the Z boson η (left) and p_{T} (right) are shown for truth generated $WZ \to e\nu\mu^+\mu^-$ samples with (red) and without (blue) including spin-correlations. The p_{T} of the Z boson is used as a proxy for the $p_{\mathrm{T}}(jj)$ distribution in the analysis. The distributions are not normalized to the same area since the acceptances differ between both samples. Study and plots from reference [23].

came from varying the scales simultaneously by two times the nominal value (20_20) and half the nominal value (05_05). The effect on the acceptance for these samples in the aTGC selection is less than 2%, comparable to the 1% normalization effect seen in the cross section selection. In order to evaluate the p_{Tjj}-dependence of these scales, particularly in the high $p_{\mathrm{T}}(jj)$ region, new aTGC truth signal samples were produced with high statistics corresponding to the scale choices of 20_20 and 05_05. The aTGC point used to generate the samples is the same as the fully reconstructed aTGC samples used for the signal[4]. The events in these high statistics aTGC samples were reweighted to the SM (discussed in section 10.4) in order to increase the statistics of the high $p_{\mathrm{T}}(jj)$ tails for this study. Figure 10.4 shows the ratios of the $p_{\mathrm{T}}(jj)$ distributions for these varied samples compared to the nominal samples. The ratios are binned coarsely in order to smooth out the statistical fluctuations and are each fitted by a linear polynomial. Each polynomial is then varied by $\pm 1\sigma$ and the variation that deviates most between both varied samples from the nominal template is used as the final shape systematic in order to be conservative. This fit to the ratio is multiplied with the nominal distribution and symmetrized relative to it to create the "up" and "down" systematic templates. The inclusion of these signal scale systematics makes the aTGC limits approximately 2% to 3% worse.

[4]As described in section 4.3.1 and corresponding to the aTGC point: $\Delta g_1^Z = -0.3$, $\Delta\kappa^Z = 1.0$, and $\lambda^Z = 0.3$

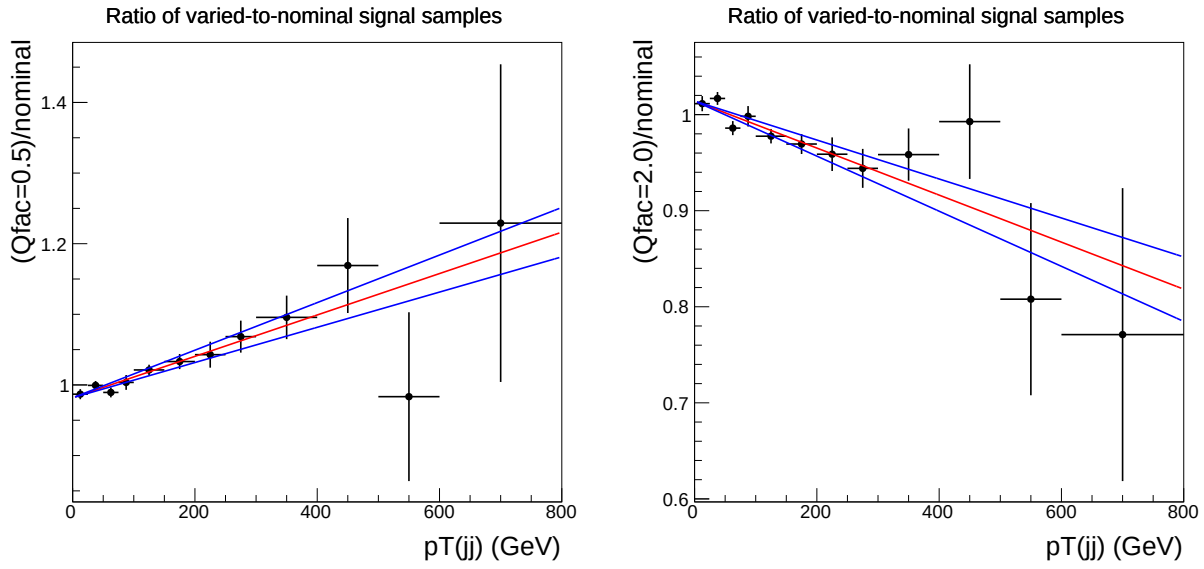

Figure 10.4: The distributions show the ratio (black points) of the varied renormalization/factorization scale samples compared to the nominal distribution, 05_05 (Qfac=0.5, nominal scales divided by 2) left and 20_20 (Qfac=2.0, nominal scales multiplied by 2) on the right. The red line in each plot signifies the best linear fit to the ratio and the two blue lines represent the $\pm 1\sigma$ lines of the best fit line. The line with the largest deviation from nominal is taken as the scale systematic for the signal and symmetrized around the nominal distribution.

10.2.2 W/Z+jets Modeling Uncertainties

Analogous to the cross section measurement, the modeling uncertainty in W/Z+jets was evaluated by considering the variations in the shape due to changes in the renormalization/factorization multiplicative scale factor (*qfac* in ALPGEN) and the ΔR parton-jet matching parameter. These systematics have a high potential of changing the shape in the high $p_{\mathrm{T}}(jj)$ tails so special consideration to their shape uncertainty is taken here. The normalization uncertainty is already taken into account in the global 20% uncertainty for the W/Z+jets process.

The ΔR systematic is evaluated the same way as in the cross section measurement. Samples produced with the ΔR(jet,parton) parameter set to either 0.4 or 1.0 (nominal is equal to 0.7) are compared with the nominal samples by constructing the ratio of their distributions after applying the aTGC event selection. The only difference other than the m_{jj} window is that in the case of the aTGC analysis, the shape differences in the $p_{\mathrm{T}}(jj)$ distribution are considered instead of m_{jj} . Figure 10.5 shows these ratios as a function of $p_{\mathrm{T}}(jj)$. The ratio corresponding to ΔR(jet,parton) = 0.4 has a dramatic step at approximately 250 GeV and this is due to the $\Delta R(Jet_1, Jet_2) > 0.7$ cut being dropped for $p_{\mathrm{T}}(jj) > 250$ GeV in the event selection. The ΔR(jet,parton) parameter dictates the matching between the parton shower jets and the partons from the matrix element (ME). Shifting the ΔR parameter from 0.7 to 0.4 only affects events in which partons from the ME were within the 0.4 to 0.7 ΔR range, resulting previously in the event being vetoed. Since the ΔR(jet,parton) parameter

is very closely related to the event selection cut of $\Delta R(Jet_1, Jet_2)$, the larger cut value of 0.7 imposed by the event selection causes the effect of the ΔR(jet,parton) = 0.4 sample to be negligible until $p_{\mathrm{T}}(jj) > 250$ GeV where the $\Delta R(Jet_1, Jet_2) > 0.7$ is removed. From the two ratios shown, the ratio with the largest deviation from the nominal (ΔR(jet,parton) = 0.4) is used as a shape uncertainty for the W/Z+jets process. The systematic is symmetrized with respect to the nominal distribution and used as "up" and "down" template inputs for the limit setting.

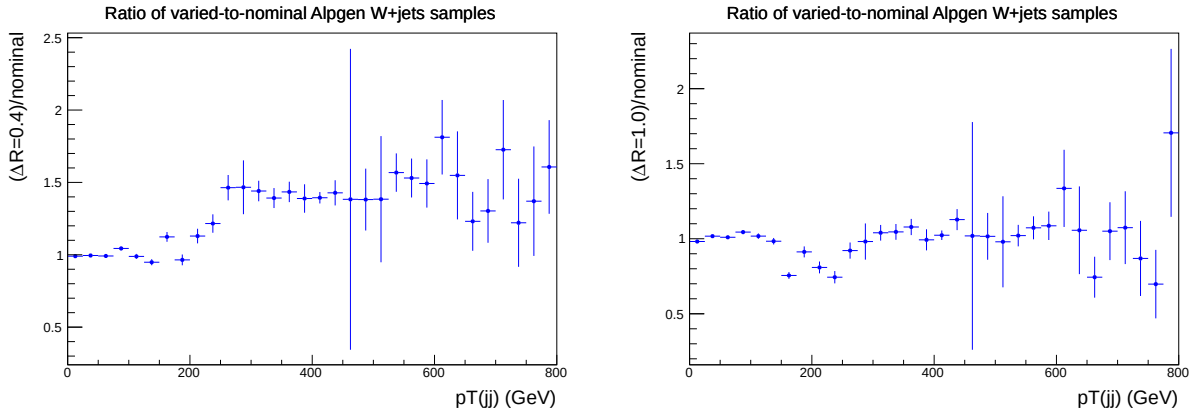

Figure 10.5: Distributions show the ratio between the varied ΔR(jet,parton) ALPGEN parameter samples, 0.4 (left) and 1.0 (right), and the nominal samples produced with ΔR(jet,parton) = 0.7 as a function of $p_{\mathrm{T}}(jj)$

.

Likewise, the renormalization/factorization multiplicative scale systematic ($qfac$) is evaluated with varied ALPGEN parameter W/Z+jets samples. Unlike the varied samples produced for ΔR(jet,parton) = 0.4, there were no varied scale high statistics AFII samples produced in slices of the $p_T(W)$ which restricted the evaluation of the systematic in the high $p_{\mathrm{T}}(jj)$ tails. As a result, new event-generation (truth) varied qfac samples were produced to improve the statistics. The truth level calculated systematic ratios were first validated with the original AFII qfac samples to ensure that they were comparable within their systematics. The selection at truth-level follows the same selection done for the fiducial volume (section 6.1) in the cross section measurement, with the addition of the m_{jj} window. Plots from this validation study can be seen in figure 10.6 and agree within their large uncertainties. The resulting systematic ratios using the additionally produced samples can be seen in figure 10.7 using coarse binning to reduce statistical fluctuations. Following the same approach as the scale shape uncertainty for the signal, each ratio is fitted by a linear polynomial and then the fit is varied by $\pm 1\sigma$. The fit with the largest deviation from 1 (the nominal value) is considered the final systematic. These ratio is symmetrized and applied to the reconstructed nominal $p_{\mathrm{T}}(jj)$ distributions to create the "up" and "down" template inputs for the limit setting.

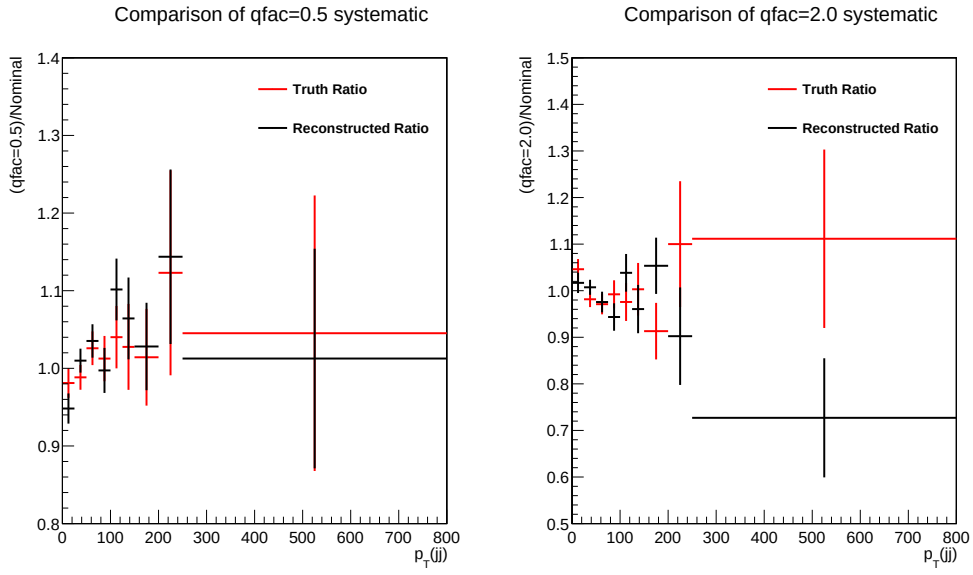

Figure 10.6: Distributions show the ratio comparison of qfac varied samples to nominal W/Z+jets ALPGEN samples as a function of $p_{\mathrm{T}}(jj)$. The ratio corresponding to qfac=0.5 is shown on the left and qfac=2.0 is on the right. In red is the ratio calculated using the truth information of the event and in black is the ratio using events simulated with AFII.

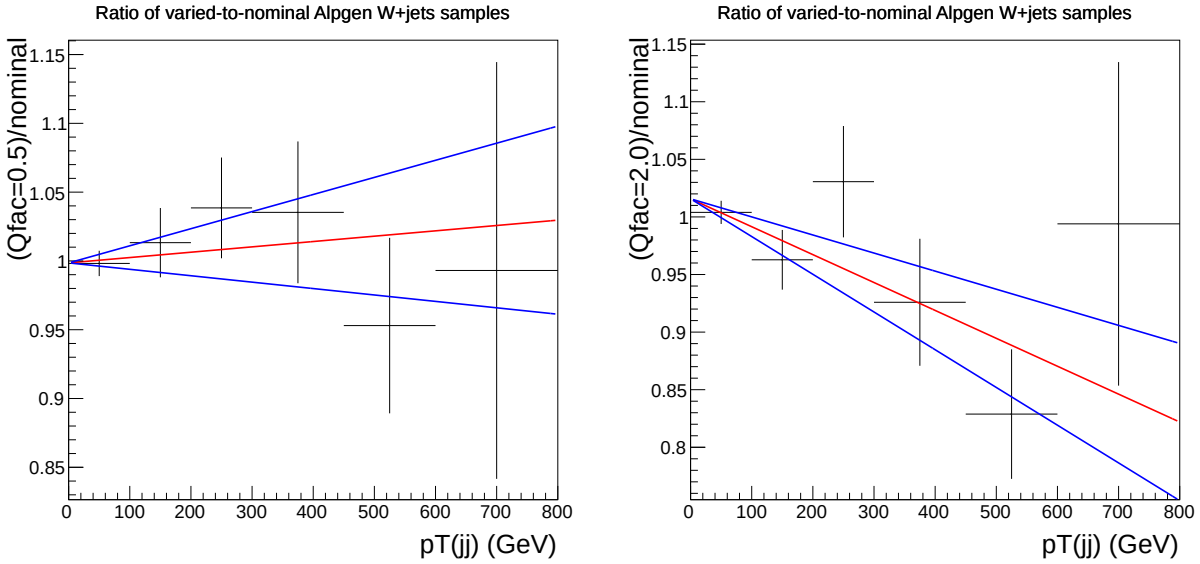

Figure 10.7: The distributions show the ratio (black points) of the varied qfac scale samples compared to the nominal distribution, qfac=0.5 (left) and qfac=2.0 (right). The red line in each plot signifies the best linear fit to the ratio and the two blue lines represent the $\pm 1\sigma$ lines of the best fit line. The line with the largest deviation from nominal is taken as the corresponding shape systematic for the W/Z+jets process and symmetrized around the nominal distribution.

10.3 MC@NLO Reweighting

The MC@NLO generator allows for reweighting of events to arbitrary aTGC values [38], the reweighting scheme is described in this section. The MC@NLO generator generalizes the WW amplitude for the case where the amplitude contains all six aTGC couplings as:

$$\begin{aligned} A =& A_0 + \Delta g_1^Z A_{\Delta g_1^Z} + \Delta\kappa^Z A_{\Delta\kappa^Z} + \lambda^Z A_{\lambda^Z} + \\ & \Delta g_1^\gamma A_{\Delta g_1^\gamma} + \Delta\kappa^\gamma A_{\Delta\kappa^\gamma} + \lambda^\gamma A_{\lambda^\gamma} \end{aligned} \tag{10.1}$$

where A_0 is the SM amplitude and A_i are kinematically dependent. The amplitude squared is proportional to the cross section which is proportional to the number of events produced. Therefore by squaring A it is possible to calculate an event weight (ω_{tot}) that reweights the event to any aTGC value. The equation of the weights is written as:

$$\begin{aligned} \omega_{tot} = \omega_0 &+ (\Delta g_1^Z)^2\omega_1 + (\Delta\kappa^Z)^2\omega_2 + (\lambda^Z)^2\omega_3 \\ &+ (\Delta g_1^\gamma)^2\omega_4 + (\Delta\kappa^\gamma)^2\omega_5 + (\lambda^\gamma)^2\omega_6 \\ &+ 2\Delta g_1^Z\omega_7 + ... + 2\lambda^\gamma\omega_{12} \\ &+ 2\Delta g_1^Z\Delta\kappa^Z\omega_{13} + ... + 2\Delta\kappa^\gamma\lambda^\gamma\omega_{27} \end{aligned} \tag{10.2}$$

MC@NLO stores these 28 weights as a vector ($\vec{\alpha_j} = \omega_j/\omega_{tot}$) during event generation for each event, so a simple calculation of plugging in particular values for the aTGC couplings will derive a new ω_{tot} that can be used to scale each event to that respective aTGC point. In regards to the WZ samples, the reweighting scheme is the same except there is no WZγ vertex so all terms that include Δg_1^γ, $\Delta\kappa^\gamma$, or λ^γ are removed leaving only 9 aTGC weights for WZ events.

Using this scheme, the number of total reweighted[5] signal events can be parametrized in terms of the weight distributions summed over all reweighted signal events in each bin i (W_j^i). The total number of expected signal events in each bin i therefore has a quadratic dependence on the anomalous coupling parameters such that

$$\begin{aligned} N_{sig}^i(\vec{\rho}) = W_0^i &+ (\Delta g_1^Z)^2 W_1^i + (\Delta\kappa^Z)^2 W_2^i + (\lambda^Z)^2 W_3^i \\ &+ (\Delta g_1^\gamma)^2 W_4^i + (\Delta\kappa^\gamma)^2 W_5^i + (\lambda^\gamma)^2 W_6^i \\ &+ 2\Delta g_1^Z W_7^i + ... + 2\lambda^\gamma W_{12}^i \\ &+ 2\Delta g_1^Z\Delta\kappa^Z W_{13}^i + ... + 2\Delta\kappa^\gamma\lambda^\gamma W_{27}^i \end{aligned} \tag{10.3}$$

in the case for WW events, where $\vec{\rho}$ is a vector containing the six anomalous couplings (Δg_1^γ, $\Delta\kappa^\gamma$, etc). This can be generalized for both WW and WZ as

$$N_{sig}^i(\vec{\rho}) = W_0^i + \sum_{i,k,j} W_j^i \rho_k \rho_j, \qquad k, j = 1, ..., n \tag{10.4}$$

where $\vec{\rho}$'s length is dependent on the sample (WW or WZ). The coefficients W_j^i become the signal inputs for the aTGC limit fit discussed in the following section.

[5]Events are reweighted with MC correction weights (pile-up, z-vertex, Reconstruction scale factors, etc) and scaled to the integrated luminosity of the data.

The validation of the reweighting procedure has been done by reweighting the MC@NLO generated SM samples to the aTGC value used to generate the aTGC signal samples and vice versa. Figure 10.8 shows these validation plots for the WW and WZ samples as a function of $p_{\mathrm{T}}(jj)$.

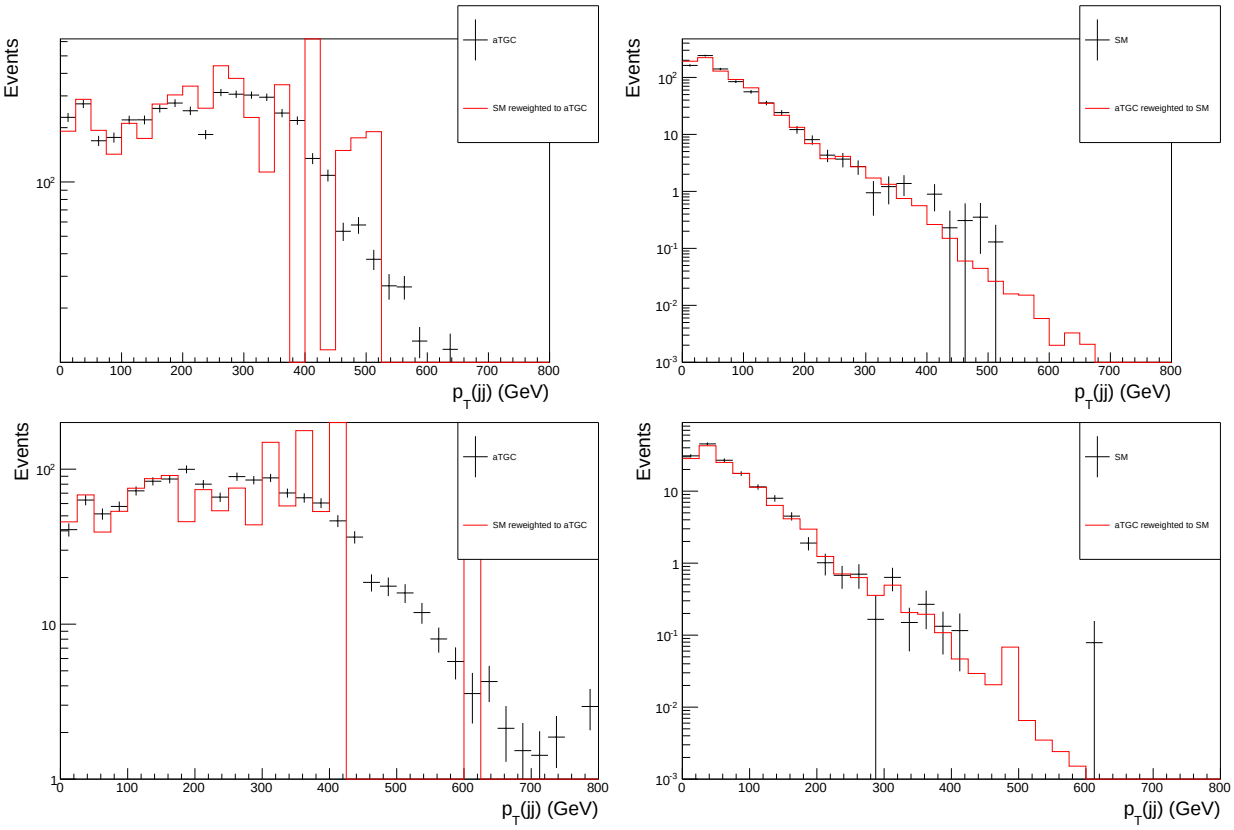

Figure 10.8: Validation plots for the MC@NLO reweighting scheme for WW (top) and WZ (bottom). The plots are of the $p_{\mathrm{T}}(jj)$ distribution for the muon channel after the aTGC event selection was applied. The plots on the left show the SM (red) samples reweighted to the aTGC (black) value used to generate the aTGC signal samples, while the plots on the right show the aTGC (red) sample being reweighted to the SM (black). The aTGC sample was generated with the following aTGC values: $\Delta g^Z = -0.3$, $\Delta\kappa^Z = 1.0$, $\lambda^Z = 0.3$, $\Delta g_1^\gamma = 0$, $\Delta\kappa^\gamma = 0$, $\lambda^\gamma = 0$. The distributions produced with the SM samples has significant statistical uncertainties in the tails of the $p_{\mathrm{T}}(jj)$ distribution as expect for the number of events generated.

10.4 Method to Calculate Anomalous Coupling Limits

The limit setting is performed using the TGClim package[6]. The package calculates the aTGC limits using a binned maximum likelihood fit to the $p_{\mathrm{T}}(jj)$ distribution. An example

[6]Package originally developed by the ATLAS WZ analysis group, code linked in this reference [138].

of the $p_{\mathrm{T}}(jj)$ distribution after the aTGC modified event selection can be seen in figure 10.9. An aTGC signal corresponding to $\lambda = 0.05$ is shown for comparison.

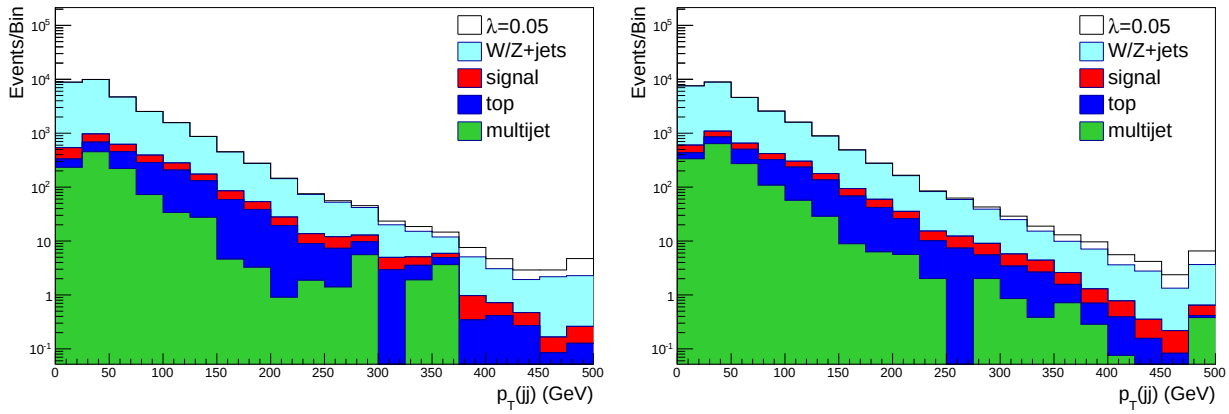

Figure 10.9: Expected $p_{\mathrm{T}}(jj)$ distribution for the muon (left) and electron (right) channels. The white-filled histogram is the expected signal in the presence of an aTGC of $\lambda = 0.05$.

The likelihood fit used for the limit setting is different from the fit used in the cross section measurement due to it's technical implementation. The TGClim package implements systematics on a bin by bin basis using nuisance parameters. Therefore, unlike the m_{jj} fit where each nuisance parameter represents a particular systematic, for the aTGC fit each nuisance parameter represents the systematic uncertainty for one particular $p_{\mathrm{T}}(jj)$ bin. The likelihood function can be written out as

$$\mathcal{L}(\vec{\rho},\vec{\alpha}) = \prod_{i=1}^{m} \mathrm{Pois}(N^i_{data}, N^i_{tot}(\vec{\rho},\vec{\alpha})) \times \frac{1}{(2\pi)^m} e^{-\frac{1}{2}(\vec{\alpha}\cdot C^{-1}\cdot\vec{\alpha})}, \tag{10.5}$$

where the Poisson probability of observing N_{data} events is given by

$$\mathrm{Pois}(N^i_{data}, N^i_{tot}(\vec{\rho},\vec{\alpha})) = \frac{(N^i_{tot}(\vec{\rho},\vec{\alpha}))^{N_{data}} e^{-(N^i_{tot}(\vec{\rho},\vec{\alpha}))}}{N_{data}!}. \tag{10.6}$$

$\vec{\rho}$ is a vector of the anomalous coupling parameters (i.e. $\rho_1 = \lambda$,$\rho_2 = \Delta\kappa^{\gamma}$, etc...) and $\vec{\alpha}$ is a vector of the nuisance parameters related to the systematic uncertainties. The product is over the total number of bins, m, in the $p_{\mathrm{T}}(jj)$ distribution and the total number of expected events in each bin i is given by

$$N^i_{tot}(\vec{\rho},\vec{\alpha}) = N^i_{sig}(\vec{\rho})(1+\alpha_i) + N^i_{bkg}(1+\alpha_{i+m}). \tag{10.7}$$

where $N^i_{sig}(\vec{\rho})$ (described in equation 10.4) and N^i_{bkg} are the total number of expected signal and background events in bin i, respectively. The vector of nuisance parameters, $\vec{\alpha}$, has a length of $2m$. The nuisance parameter $\vec{\alpha_i}$ terms for each bin i from 0 to m are related to the uncertainty in the signal for bin i, while the terms between m and $2m$ are related to the background uncertainty for bin i.

The α nuisance parameters are allowed to vary within their Gaussian constraints defined by their covariance matrix, C, given by

$$C_{ij} = \sum_k \sigma_{ik}\sigma jk. \tag{10.8}$$

where σ_{ik} are the fractional uncertainties on N^i_{sig} and N^i_{bkg} in bin i due to systematic source k (e.g. JES, MC statistics, etc). Systematics due to normalization uncertainties are inputted using a flat uncertainty for all σ_{ik}, while shape uncertainties are calculated on a bin-by-bin basis as a variation between the nominal and the systematic variation. The covariance matrix describes all the systematic uncertainties for signal and background, their correlations and the correlations between bins. Appendix D.3 contains tables detailing the size of the systematics for the diagonal of the covariance matrix per each lepton channel and bin.

The expected and observed 95% confidence intervals are determined following a frequentist method first utilized by the ATLAS $W(\ell\nu)Z(\ell^+\ell^-)$ aTGC analysis [51]. The method to calculate the observed limits is described below:

- A test statistic,$\lambda(\rho)$, is constructed from the profile-maximum likelihood ratio defined as

  $$\lambda(\rho) = \frac{\mathcal{L}(N_{data}|\rho, \hat{\hat{\alpha}})}{\mathcal{L}(N_{data}|\hat{\rho}, \hat{\alpha})} \tag{10.9}$$

  where $\hat{\hat{\alpha}}$ is the estimated values for the nuisance parameter vector α that maximizes the likelihood for a given fixed value of ρ, and $\hat{\rho}$ and $\hat{\alpha}$ represent the ρ and α values that maximize the likelihood when both are allowed to vary.

- The observed value of the test statistic, λ_{obs}, is then determined for many different values of ρ.

- The probability of determining an outcome at least as unlikely then the observed test statistic at a given ρ is estimated by using a large amount (10,000) of "toy" datasets for each value of ρ. For each toy dataset, the profile maximum likelihood ratio is calculated and compared to $\lambda_{obs}(\rho)$. Each toy is generated by varying the nuisance parameters α by their Gaussian constraints around the mean value of $\hat{\hat{\alpha}}$ and then the number of "observed" events N^i_{toy} is randomly drawn from a Poisson distribution using a mean calculated from the values of ρ and α using equation 10.4.

- A p-value for each ρ value is estimated as

  $$\text{p-value}(\rho) = \frac{\text{Number of toys with less likely results than } \lambda_{obs}}{\text{Total number of generated toys}}. \tag{10.10}$$

  If the p-value is less (greater) than 5% then the ρ value is rejected (accepted) and outside (inside) the 95% confidence interval.

The precision for the 95% confidence interval boundary is determined by varying ρ such that the distance between an accepted and rejected ρ value is less than the value of the precision. At which point the scan over values of ρ is terminated and the half way value between the last rejected and accepted ρ is taken as the 95% confidence interval boundary. The precision of the interval is set dynamically by taking the best fit point defined by $\hat{\rho}$ and $\hat{\alpha}$, and then determining the point which corresponds to a 0.1% shift in the asymptotic probability. This is defined by the equations below where the level of precision is given by ϵ.

$$t_{\hat{\rho}} = -2 \ln \frac{\mathcal{L}(\hat{\rho}, \hat{\hat{\alpha}})}{\mathcal{L}(\hat{\rho}, \hat{\alpha})} \tag{10.11}$$

$$t_{\hat{\rho}+\epsilon} = -2 \ln \frac{\mathcal{L}(\hat{\rho}+\epsilon, \hat{\hat{\alpha}})}{\mathcal{L}(\hat{\rho}, \hat{\alpha})} \tag{10.12}$$

$$0.001 = \chi^2(t_{\hat{\rho}}, NDF = 1) - \chi^2(t_{\hat{\rho}+\epsilon}, NDF = 1) \tag{10.13}$$

Additionally, because the number of signal events N^i_{sig} are quadratically dependent on ρ and the prediction for N^i_{sig} continually grows from a minimum value near $\rho = 0$, it is possible that there may be one or two values of ρ which best describes the observed data. This results in the 95% confidence interval for ρ to be either one continuous interval or two disjoint intervals.

The expected anomalous coupling limits are done by generating a large number of pseudo-datasets for the SM prediction ($\rho = 0$) similar to how the pseudo-datasets were generated in section 8.2, but for the aTGC modified event selection. For each pseudo-dataset, the 95% confidence interval on ρ is determined using the same procedure used for the observed limits. The mean of the 95% confidence interval for all pseudo-datasets is taken as the expected limits.

Due to limit-setting method being very computationally intensive, this method has only been utilized for calculating the final results for the observed and expected limits in section 10.6. For all other studies, the Asimov [139] dataset has been used and the confidence interval estimated using $\Delta(\ln \mathcal{L}) = 1.92$ which is approximately the 95% confidence limit. The Asimov dataset is taken to be the expect SM prediction directly.

10.4.1 Binning Optimization

The binning used for the $p_{\mathrm{T}}(jj)$ distribution was studied in order to optimize the expected limit sensitivity and reduce the amount of computational time necessary to calculate the aTGC limits. The starting point used was the binning utilized by the CMS lvjj analysis [53], which consists of 25 GeV bins out to 500 GeV with a final bin containing any additional overflow events. As shown in table 10.2, additional bins were added above 500 GeV but only a 2% improvement was seen due to possible binning extensions. It was decided to include a 500–550 GeV bin with a final bin consisting of the overflow events.

Reduction on the number of bins below 500 GeV was also considered. The computing time for the aTGC limits is directly related to the number of nuisance parameters and the total number of bins used, therefore any reduction in the total bin count is very beneficial. A study was performed and showed that reducing the bins between 0–250 GeV to two 125

Expected 95% limits on aTGC's		
Binning	λ	$\Delta\kappa^{\gamma}$
Basic (25 GeV bins from 0–500)	[−0.0508, 0.0506]	[−0.251, 0.274]
Basic+(500+)	[−0.0453, 0.0451]	[−0.228, 0.246]
Basic+(500–550, 550+)	[−0.0445, 0.0443]	[−0.224, 0.241]
Basic+(500–550, 550–600, 600+)	[−0.0445, 0.0443]	[−0.223, 0.241]

Table 10.2: Results from the study done to determine if additional bins in the high $p_{\mathrm{T}}(jj)$ improved the expected aTGC limit sensitivity. The limits included all systematics except for the scale-dependence of the signal. The expect limits were approximated using the $\Delta\ln\mathcal{L} = 1.92$ approximation.

GeV bins reduced the computational time by a factor of three, while only reducing the limit sensitivity by less than one percent. A later study with the full suite of systematics determined that the limits were degradation was closer to 4–5%. The final binning used for the aTGC study is shown in figure 10.10.

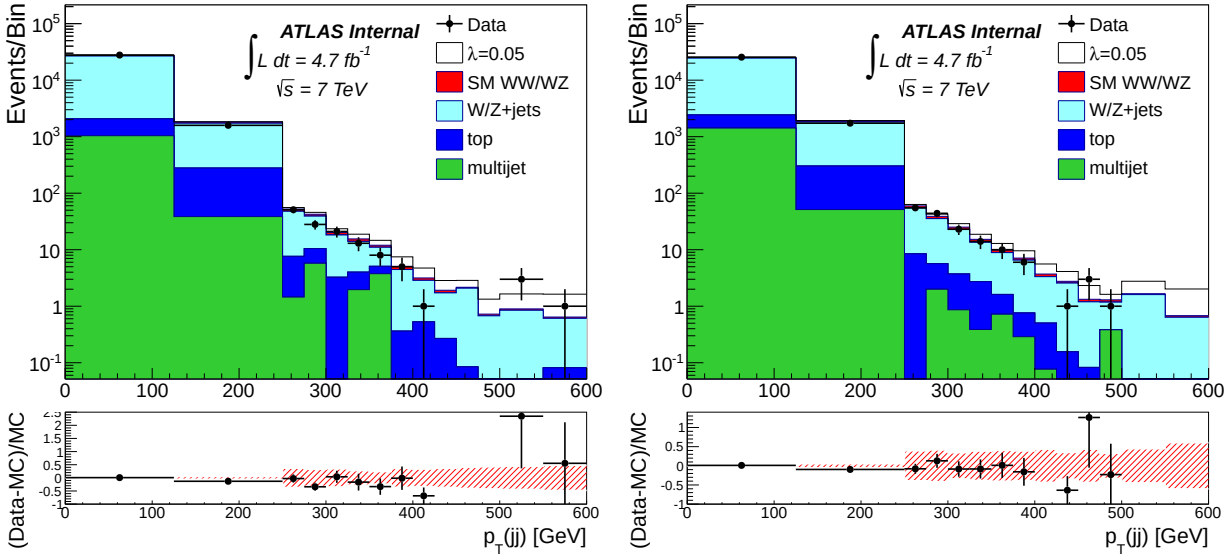

Figure 10.10: The $p_{\mathrm{T}}(jj)$ distribution for the muon (left) and electron (right) channels is shown for both the data and the expected SM prediction using the final binning for the limit setting. The effect of an aTGC point with $\lambda = 0.05$ is shown for comparison. The right most bin contains any overflow events. The lower panel shows the percent difference between the MC and data with respect to the MC and the red band shows the total systematic uncertainty band.

10.5 Effect of Systematic Uncertainties on the Limit Calculations

As shown in section 10.4, the number of signal events for each bin are calculated as a quadratic function of the aTGC coupling parameters. This results in the uncertainties for the anomalous coupling limits to be fundamentally non-Gaussian and therefore adding the uncertainties in quadrature would be incorrect. In order to get an idea of how the various systematics effect the limits, the expected aTGC limits have been calculated by adding and/or removing different sets of nuisance parameters related to the different systematic sources. Due to limited computational resources the approximate expected limits were calculated using the Asimov dataset and the formula $\Delta ln\mathcal{L} = 1.92$, which is approximately equivalent to the 95% confidence interval. The results can be seen in table 10.3. From the table, the significant systematic sources are the ΔR variation in the W/Z+jets background process, JES, background normalization, and the MC statistics.

Expected 95% limits on aTGC's		
	λ	$\Delta\kappa^{\gamma}$
95% CL with no systematics	[−0.035, 0.035]	[−0.17, 0.20]
95% CL with MC stat	[−0.036, 0.037]	[−0.18, 0.20]
95% CL with MC stat, norm.	[−0.038, 0.038]	[−0.19, 0.21]
95% CL with MC stat, norm., qfac	[−0.038, 0.038]	[−0.19, 0.21]
95% CL with MC stat, norm., JER	[−0.038, 0.038]	[−0.19, 0.21]
95% CL with MC stat, norm., JES	[−0.042, 0.042]	[−0.21, 0.23]
95% CL with MC stat, norm., ΔR	[−0.044, 0.044]	[−0.22, 0.24]
95% CL with all systematics (*)	[−0.047, 0.046]	[−0.24, 0.25]

Table 10.3: Effect of systematics on expected aTGC limits. The expected limits are approximated using the Asimov dataset and the $\Delta\ln\mathcal{L} = 1.92$ approximation. (*) All systematics except for the scale systematic on the signal are included in the estimation.

10.6 Expected and Observed aTGC Limits

The expected and observed limits on anomalous couplings are calculated for aTGC approach for the three aTGC parameters (Δg_1^Z, $\Delta\kappa^{\gamma}$, and λ) defined in the LEP constraint and for the five parameters (Δg_1^Z, $\Delta\kappa^Z$, $\Delta\kappa^{\gamma}$, λ_Z, and λ_{γ}) any constraint applied. Additionally, limits using the Effective Field Theory (EFT) approach are also calculated for the coupling coefficients: c_{WWW}/Λ^2, c_W/Λ^2, and c_B/Λ^2. A description of the aTGC and EFT approach can be found in section 1.5.

The limits shown in the previous sections of this chapter have all been calculated using the Asimov dataset. The following 95% CL expected limits are calculated using the procedure described in section 10.4. The expected limits are computed using approximately 500 pseudo-datasets and the mean of the limit distributions is taken to be the expected limit. A distribution of the limits using the pseudo datasets and data can be seen in figure 10.11 for

Parameter	Observed Limit	Expected Limit	Prob. (observation)
λ	[−0.039, 0.040]	[−0.048, 0.047]	34%
$\Delta\kappa^{\gamma}$	[−0.21, 0.22]	[−0.23, 0.25]	40%
Δg_1^Z	[−0.055, 0.071]	[−0.072, 0.085]	29%

Table 10.4: The observed and expected 95% confidence level limits on the aTGC parameters λ, $\Delta\kappa^{\gamma}$, and Δg_1^Z in the LEP scenario. The limits on each parameter are calculated while fixing the other two parameters to zero. Also listed is the probability (from pseudo-experiments) of observing a limit interval narrower or of the same width as the actual observed limit interval.

Parameter	Observed Limit	Expected Limit	Prob. (observation)
λ^Z	[−0.043 , 0.044]	[−0.056, 0.056]	26%
$\Delta\kappa^Z$	[−0.090 , 0.105]	[−0.11, 0.12]	40%
Δg_1^Z	[−0.073, 0.095]	[−0.11, 0.12]	20%
λ^{γ}	[−0.15, 0.15]	[−0.17, 0.16]	41%
$\Delta\kappa^{\gamma}$	[−0.19, 0.23]	[−0.22, 0.25]	34%

Table 10.5: The observed and expected 95% confidence level limits on the aTGC parameters λ^Z, $\Delta\kappa^Z$, Δg_1^Z, λ^{γ}, and $\Delta\kappa^{\gamma}$ are shown, not subject to any additional constraints between them. The limits on each parameter are calculated while fixing the other four parameters to zero. Also listed is the probability (from pseudo-experiments) of observing a limit interval narrower or of the same width as the actual observed limit interval.

the LEP constraint. Table 10.4 summarizes the expected and observed limits from using the LEP constraint. The limits for each aTGC parameter are calculated while fixing the other aTGC parameters to zero, therefore these limits are all one dimensional (1D).

Figures 10.12 and 10.13, along with table 10.5 show the expected and observed 1D limits for all five aTGC parameters using the unconstrained aTGC approach. Likewise, table 10.6 shows a summary of the 1D limits using the EFT approach and figure 10.14 shows the expected and observed limits for c_{WWW}.

Lastly, 2D contours for the observed 95% CL limits using the LEP scenario are shown in figure 10.15 for each of the aTGC parameter pairs: Δg_1^Z-$\Delta\kappa^{\gamma}$, Δg_1^Z-λ, λ-$\Delta\kappa^{\gamma}$. Each contour is formed in a radial fashion, by calculating the 95% CL limits at different azimuthal angles in the 2D plane. The 95% limit is calculated by traveling along the radial component of each angle (like traveling along the spokes of a wagon wheel) and the resulting points are connected together by lines to create a rough elliptical contour. The 95% CL limits are calculated using the method described in section 10.4. Additionally, 2D limits for the EFT approach are shown in figure 10.16.

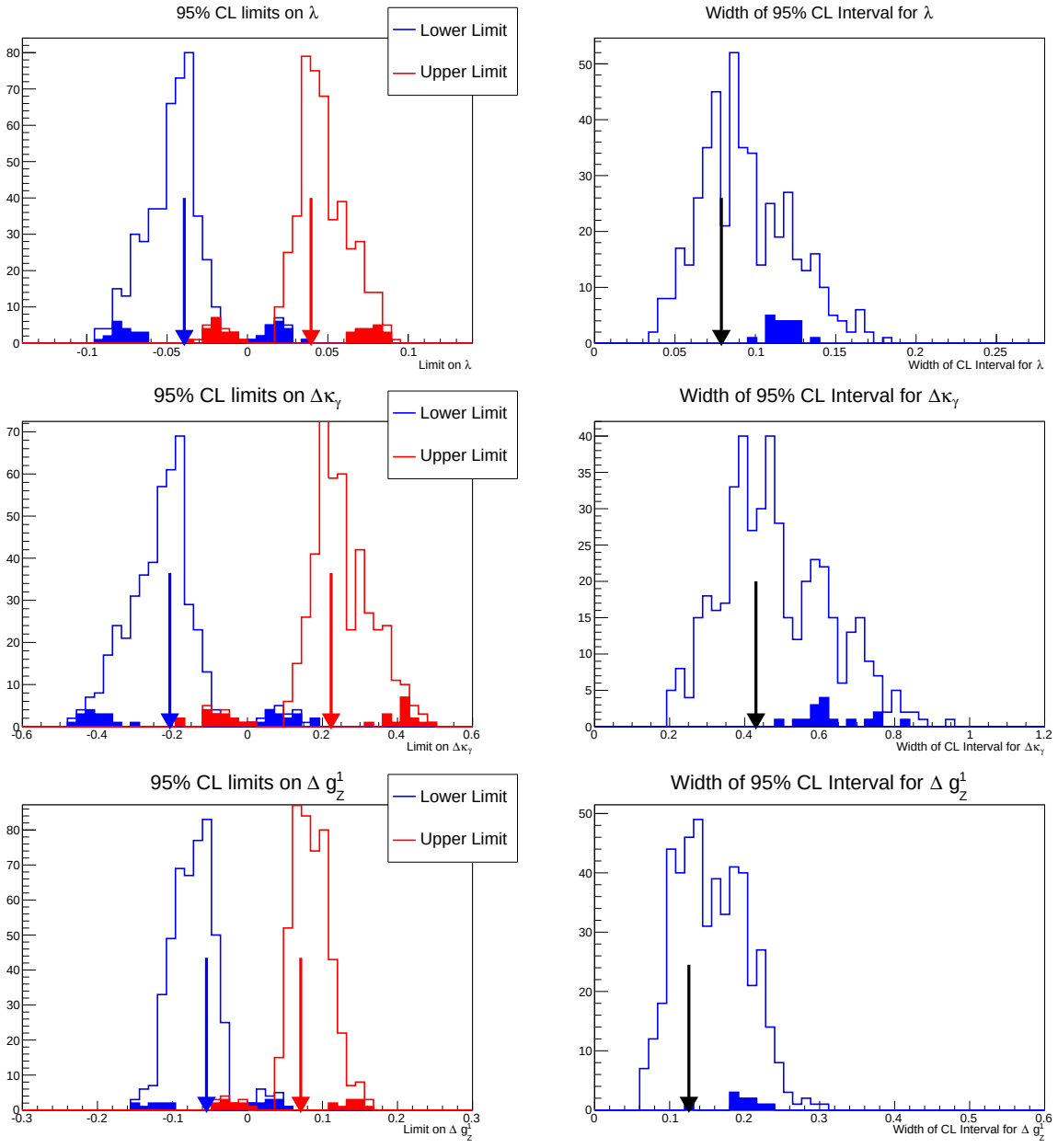

Figure 10.11: Summary of pseudo-experiments used to calculate the expected 1D aTGC limits, in the LEP scenario. Limits for λ, $\Delta\kappa^{\gamma}$, and Δg_1^Z are shown in the top, middle, and bottom plots, respectively. The left plots give the upper (red) and lower (blue) 95% limits calculated for each pseudo-dataset. The right plots show the total width of the 95% confidence interval for each pseudo-dataset. The solid histograms indicate pseudo-datasets for which the 95% confidence region consists of two separate intervals rather than a single interval. The arrows in both the left and right plots indicate the observed limits from the data.

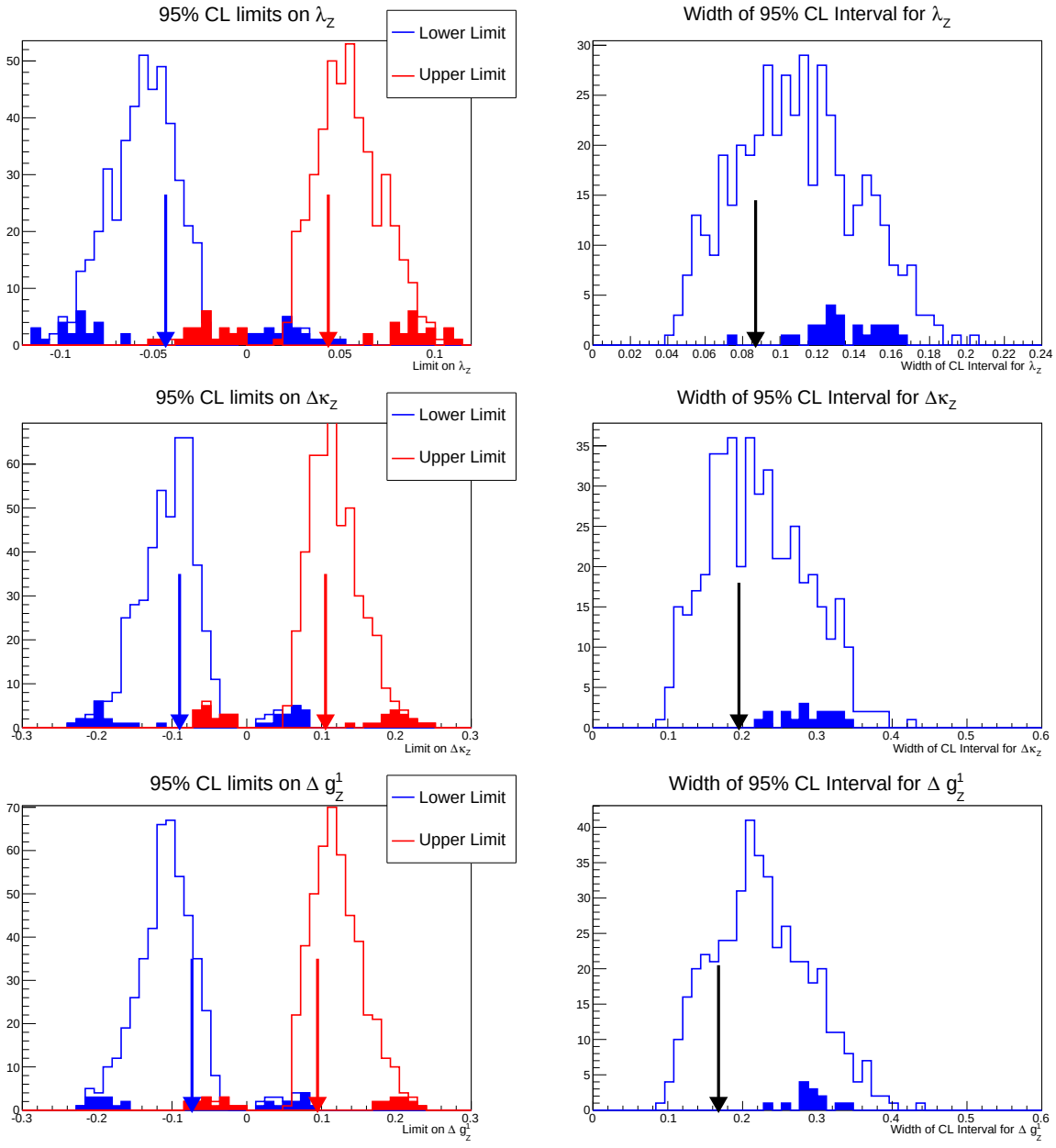

Figure 10.12: Summary of pseudo-experiments used to calculate the expected 1D aTGC limits in the no-constraint scenario. Limits for for λ^Z, $\Delta\kappa^Z$, and Δg_1^Z are shown in the top, middle, and bottom plots, respectively. The left plots give the upper (red) and lower (blue) 95% limits calculated for each pseudo-dataset. The right plots show the total width of the 95% confidence interval for each pseudo-dataset. The solid histograms indicate pseudo-datasets for which the 95% confidence region consists of two separate intervals rather than a single interval. The arrows in both the left and right plots indicate the observed limits from the data.

Parameter	Observed Limit	Expected Limit	Prob. (observation)
c_{WWW}/Λ^2	$[-9.5, 9.6]$ TeV^{-2}	$[-11.6, 11.5]$ TeV^{-2}	34%
c_B/Λ^2	$[-64, 69]$ TeV^{-2}	$[-73, 79]$ TeV^{-2}	40%
c_W/Λ^2	$[-13, 18]$ TeV^{-2}	$[-17, 21]$ TeV^{-2}	28%

Table 10.6: The observed and expected 95% C.L. limits on the EFT parameters c_{WWW}/Λ^2, c_B/Λ^2, and c_W/Λ^2. The limits on each parameter are calculated while fixing the other two parameters to zero. Also listed is the probability (from pseudo-experiments) of observing a limit interval narrower or of the same width as the actual observed limit interval.

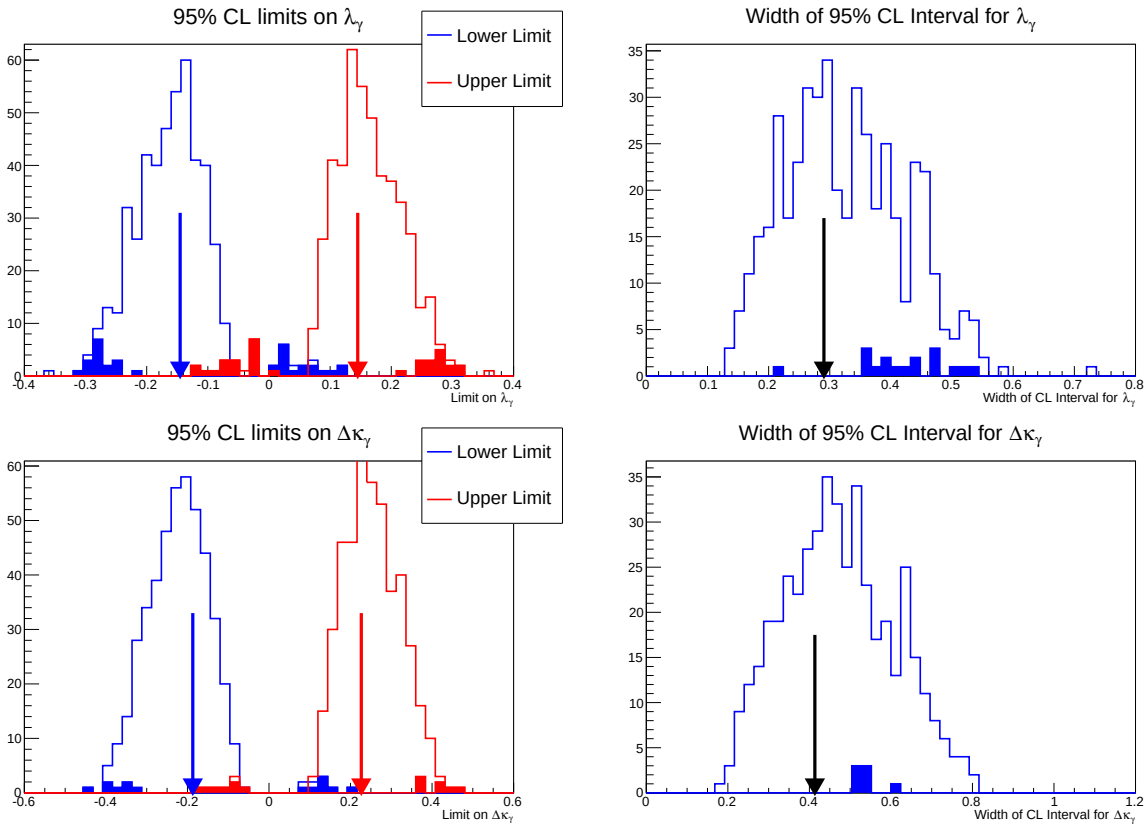

Figure 10.13: Summary of pseudo-experiments used to calculate the expected 1D aTGC limits in the no-constraint scenario. Limits for λ^γ and $\Delta\kappa^\gamma$ are shown in the top and bottom plots, respectively. The left plots give the upper (red) and lower (blue) 95% limits calculated for each pseudo-dataset. The right plots show the total width of the 95% confidence interval for each pseudo-dataset. The solid histograms indicate pseudo-datasets for which the 95% confidence region consists of two separate intervals rather than a single interval. The arrows in both the left and right plots indicate the observed limits from the data.

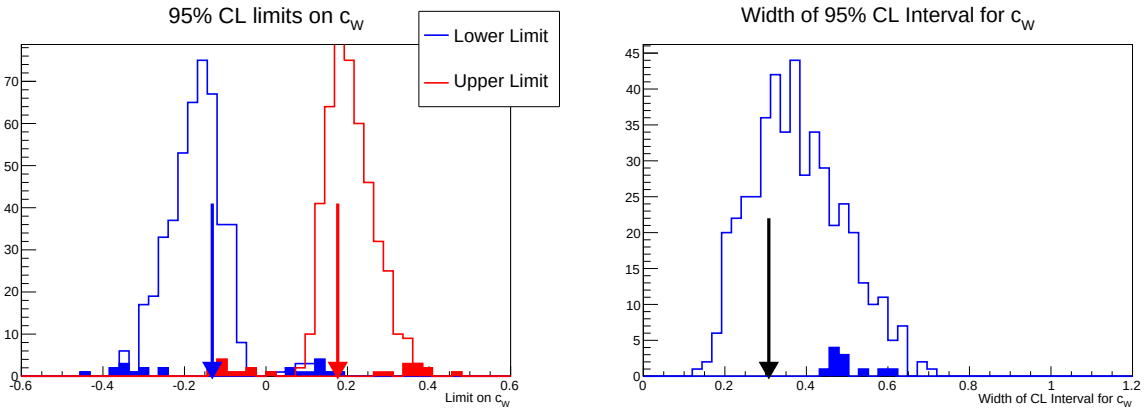

Figure 10.14: Summary of pseudo-experiments used to calculate the expected limits on the EFT paramter c_{WWW}/Λ^2. The left plots give the upper (red) and lower (blue) 95% limits calculated for each pseudo-dataset. The right plots show the total width of the 95% confidence interval for each pseudo-dataset. The solid histograms indicate pseudo-datasets for which the 95% confidence region consists of two separate intervals rather than a single interval. The arrows in both the left and right plots indicate the observed limits from the data.

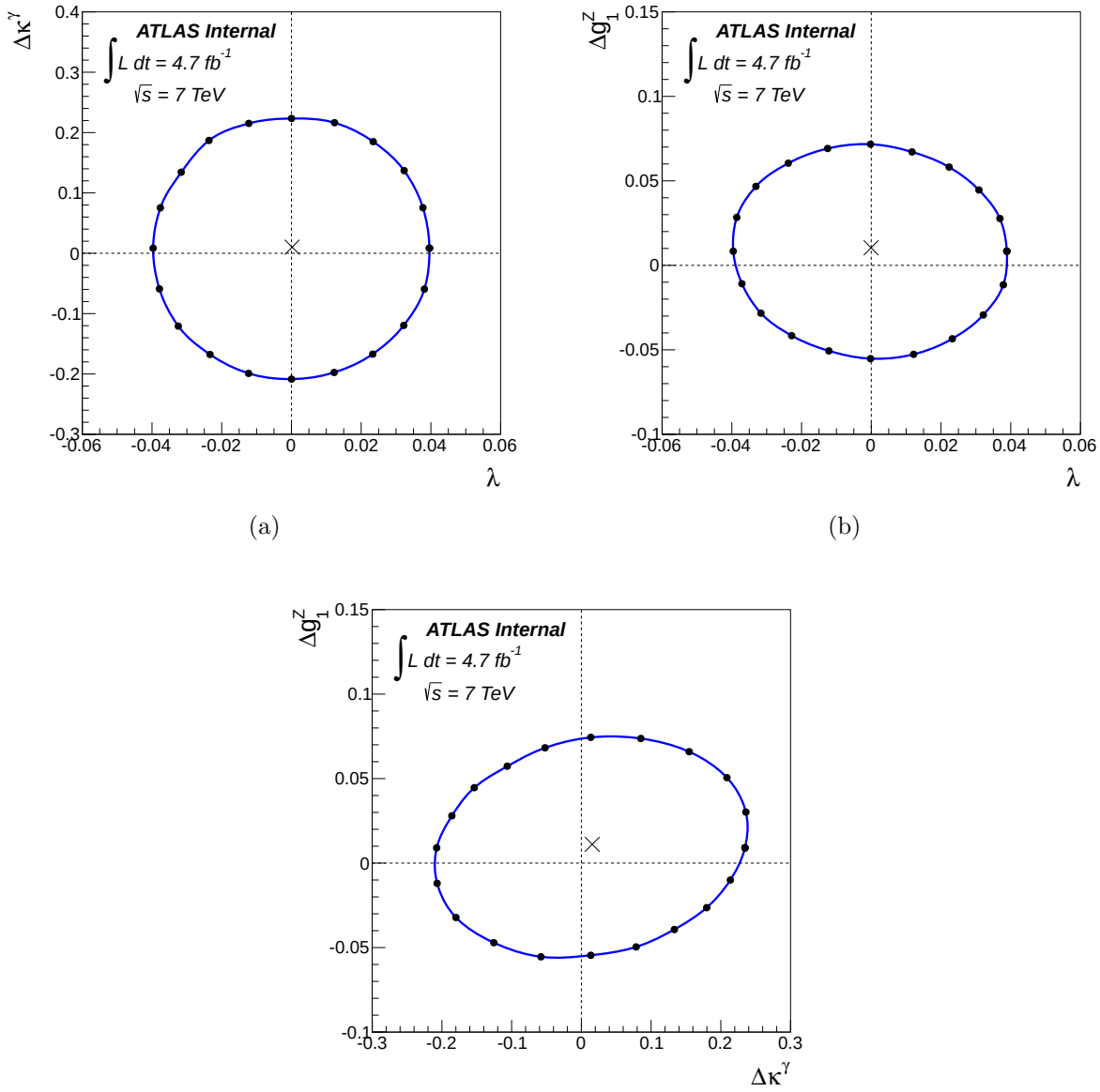

Figure 10.15: The observed two-dimensional 95% C.L. contours for the anomalous triple gauge couplings a) λ versus $\Delta\kappa^{\gamma}$, b) λ versus $\Delta\kappa^{Z}$, and c) $\Delta\kappa^{\gamma}$ versus $\Delta\kappa^{Z}$. The limits are for the LEP scenario without any form factor applied. The cross marker indicates the best-fit values for the anomalous couplings.

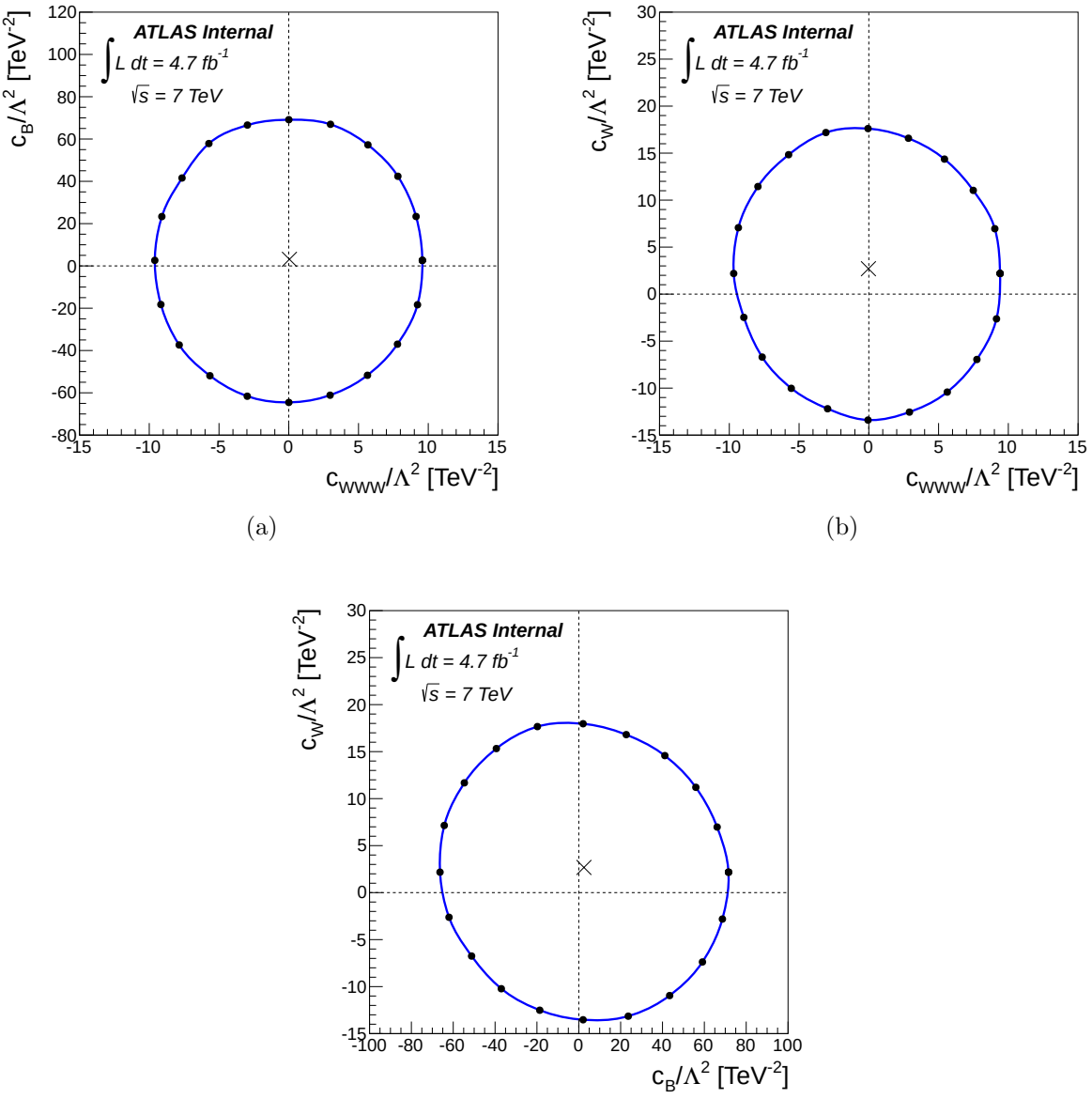

(a) (b)

(c)

Figure 10.16: The observed two-dimensional 95% C.L. contours for the EFT parameters a) c_{WWW}/Λ^2 versus c_B/Λ^2, b) c_{WWW}/Λ^2 versus c_W/Λ^2, and c) c_B/Λ^2 versus c_W/Λ^2. The cross marker indicates the best-fit values for the EFT parameters.

Chapter 11

Conclusions

This thesis has presented a detailed overview of the analysis and results for the WW+WZ production cross section measurement done at a center-of-mass energy of 7 TeV with 4.7 ± 0.2 fb^{-1} of data collected by the ATLAS detector in 2011. The measurement was performed by selecting events consistent with the $WW/WZ \to \ell\nu jj$ final state, where ℓ is an electron or muon, and performing a binned maximum likelihood fit to the dijet invariant mass. The total WW+WZ cross section was measured to be $\sigma_{tot}(WW+WZ) = 68 \pm 7$ (stat.) ± 18 (syst.) pb and is consistent with the NLO SM prediction of 61.1 ± 2.5 pb. The observed significance of the signal is calculated to be 3.4 σ, with 3.2 σ expected. Furthermore, the fiducial cross section for the WW+WZ process was measured in a phase space closely corresponding to the event selection used in this analysis and was found to be $\sigma_{fid}(WW + WZ) = 1.35 \pm 0.14$ (stat.) $\pm$ 0.36 (syst.) pb, consistent with the SM expectation of 1.22 ± 0.05 pb.

Using close to the same selection criteria as was used for the cross section measurement, limit studies on anomalous triple gauge couplings were also done. 95% confidence level limits were set for anomalous couplings using an effective Lagrangian approach with the LEP constraint and an effective field theory approach. The measured 1D 95% CL limits using the LEP constraints are determined to be $\lambda = [-0.039, 0.040]$, $\Delta\kappa^{\gamma}[-0.21, 0.22]$, and $\Delta g_1^Z = [-0.055, 0.071]$. These measured limits are comparable with previously-published results, as shown in figure 11.1, by ATLAS [49, 51, 55], DZero [57], LEP [58], and CMS [50, 53, 56]. The measured 1D 95% CL limits on the parameters for the effective field theory approach are also reported as $c_{WWW}/\Lambda^2 = [-9.5, 9.6]$ TeV^{-2}, $c_B/\Lambda^2 = [-64, 69]$ TeV^{-2}, and $c_W/\Lambda^2 = [-13, 18]$ TeV^{-2}.

Future studies of the WW+WZ cross section using the semi-leptonic decay channel will benefit from increased statistics and a better uncertainty calculation for the jet energy scale. Due to the measurement being systematically limited by the uncertainty in the W/Z+jets normalization and jet uncertainties, it is assumed that only fractional improvements can be made on the measurement in the near future. With enough data statistics available, it may be more feasible to choose a region of phase space with large demands on the transverse momentum of the objects. This type of boosted event selection would have a larger signal-to-background ratio due to a smaller W/Z+jets contribution, but would trade this improvement for a larger top background and potentially larger jet uncertainty.

The anomalous coupling limit studies have been shown to be competitive with previous results. An increased in the dataset size and center-of-mass energy would only show marginal

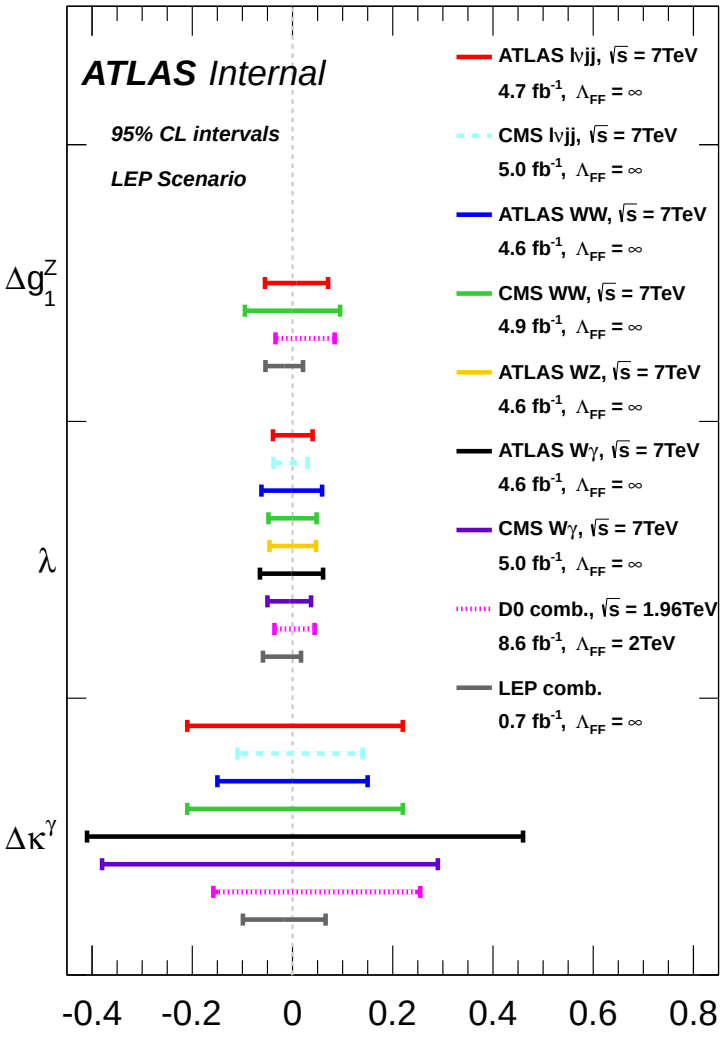

Figure 11.1: Comparison of aTGC limits obtained in this analysis with limits obtained by other experiments and/or in different channels. All limits are given at 95% CL, and calculated within the LEP scenario. The form factor Λ used in each analysis is listed; $\Lambda = \infty$ is equivalent to no form factor. The limits for each parameter are obtained by fixing the other two parameters to zero. In the CMS $\ell\nu jj$ analysis and the ATLAS and CMS $W\gamma$ analyses, no limits on Δg_1^Z were given. The ATLAS WW and WZ analyses gave limits on Δg_1^Z, but with $\Delta\kappa^Z = 0$ rather than $\Delta g_1^Z = 0$, so they are not comparable with these results and are thus excluded. For the ATLAS WW result, the published limits on $\Delta\kappa^Z$ are converted to limits on $\Delta\kappa^\gamma$ using the formula $\Delta\kappa^Z = -\Delta\kappa^\gamma \tan^2\theta_w$. The ATLAS WZ analysis published $\Delta\kappa^Z$ limits which can also be converted to $\Delta\kappa^\gamma$, but the limits are much worse than the other limits in this figure, and so are not shown.

improvements on the limits, as the anomalous couplings are quadratically dependent on the cross section, resulting in the statistical uncertainty only being reduced by approximately a factor of $\mathcal{L}^{1/4}$. Larger improvements could be made in the near future by constraining

the W/Z+jets modeling systematics using higher statistic samples and possibly using the sidebands of the m_{jj} distribution to restrict the modeling uncertainty in the high $p_{\mathrm{T}}(jj)$ tails. It is also possible in the semi-leptonic channel to compute limits on the diboson system itself by reconstructing the leptonically decaying W using a W mass constraint to calculate the z component of the neutrino coming from the $W \to \ell n\nu$ decay. The kinematics of the diboson system would be a more direct probe to possible anomalous couplings.

Bibliography

[1] Siegfried Bethke. The 2009 World Average of alpha(s). *Eur.Phys.J.*, C64:689–703, 2009. doi: 10.1140/epjc/s10052-009-1173-1.

[2] A.D. Martin, W.J. Stirling, R.S. Thorne, and G. Watt. Parton distributions for the LHC. *Eur.Phys.J.*, C63:189–285, 2009. doi: 10.1140/epjc/s10052-009-1072-5.

[3] Anwar Bhatti and Don Lincoln. Jet Physics at the Tevatron. *Ann.Rev.Nucl.Part.Sci.*, 60:267–297, 2010. doi: 10.1146/annurev.nucl.012809.104430.

[4] J.J. Goodson. *Search for Supersymmetry in States with Large Missing Transverse Momentum and Three Leptons including a Z-Boson*. PhD thesis, Stony Brook University, May 2012. Presented 17 Apr 2012.

[5] C Hill. The CERN Hadron Ion Sources, 1999. URL `http://linac2.home.cern.ch/linac2/sources/source.htm`.

[6] Joao Pequenao. Computer generated image of the whole ATLAS detector. Mar 2008.

[7] Regina Caputo and John D Hobbs. *A Search for First Generation Leptoquarks at the ATLAS detector*. PhD thesis, Stony Brook U., 2011. Presented 12 Aug 2011.

[8] Joao Pequenao. Computer generated image of the ATLAS inner detector. Mar 2008.

[9] Joao Pequenao. Computer generated images of the Pixel, part of the ATLAS inner detector. Mar 2008.

[10] F Djama. Commissioning and Operation of the ATLAS Pixel Detector at the CERN LHC Collider. Technical Report ATL-INDET-PROC-2010-042, CERN, Geneva, Nov 2010.

[11] ATLAS Collaboration. SCT Documentation and Tutorials, . URL `https://twiki.cern.ch/twiki/bin/viewauth/Atlas/SctCommissioningDocumentation`.

[12] John Alison and I. J. Kroll. *The Road to Discovery: Detector Alignment, Electron Identification, Particle Misidentification, WW Physics, and the Discovery of the Higgs Boson*. PhD thesis, Pennsylvania U., Pennsylvania U., Dec 2012. Presented 08 Nov 2012.

[13] Joao Pequenao. Computer Generated image of the ATLAS calorimeter. Mar 2008.

[14] ATLAS Collaboration. *ATLAS liquid-argon calorimeter: Technical Design Report*. Technical Design Report ATLAS. CERN, Geneva, 1996.

[15] Joao Pequenao. Computer generated image of the ATLAS Muons subsystem. Mar 2008.

[16] ATLAS Collaboration. *ATLAS muon spectrometer: Technical Design Report*. Technical Design Report ATLAS. CERN, Geneva, 1997.

[17] M Aleksa, F Bergsma, P A Giudici, A Kehrli, M Losasso, X Pons, H Sandaker, P S Miyagawa, S W Snow, J C Hart, and L Chevalier. Measurement of the atlas solenoid magnetic field. *Journal of Instrumentation*, 3(04):P04003, 2008. URL `http://stacks.iop.org/1748-0221/3/i=04/a=P04003`.

[18] ATLAS Collaboration. *ATLAS detector and physics performance: Technical Design Report, 1*. Technical Design Report ATLAS. CERN, Geneva, 1999.

[19] ATLAS Collaboration. Luminosity Public Results, 2011. URL `https://twiki.cern.ch/twiki/bin/view/AtlasPublic/LuminosityPublicResults`.

[20] MJ Tibbetts. Tracking, vertexing and b-tagging performance in ATLAS. Technical Report ATL-PHYS-PROC-2012-307, CERN, Geneva, Dec 2012.

[21] Matteo Cacciari, Gavin P. Salam, and Gregory Soyez. The Anti-k(t) jet clustering algorithm. *JHEP*, 0804:063, 2008. doi: 10.1088/1126-6708/2008/04/063.

[22] ATLAS Collaboration. Jet energy scale and its systematic uncertainty in proton-proton collisions at sqrt(s)=7 TeV with ATLAS 2011 data. Technical Report ATLAS-CONF-2013-004, CERN, Geneva, Jan 2013.

[23] Steve Marsden. Spin Correlations. URL `https://indico.cern.ch/event/240251/contribution/2/material/slides/0.pdf`.

[24] J. Beringer et al. Review of Particle Physics (RPP). *Phys.Rev.*, D86:010001, 2012. doi: 10.1103/PhysRevD.86.010001.

[25] John M. Campbell and R. Keith Ellis. An Update on vector boson pair production at hadron colliders. *Phys.Rev.*, D60:113006, 1999. doi: 10.1103/PhysRevD.60.113006.

[26] J. Campbell, K. Ellis, and C. Williams. Vector Boson Pair Production at the LHC. *FERMILAB-PUB-11-182-T*, 000:035, 2011.

[27] ATLAS Collaboration. Measurement of the W^+W^- production cross section in proton-proton collisions at $\sqrt{s} = 8$ TeV with the ATLAS detector. Technical Report ATLAS-CONF-2014-033, CERN, Geneva, Jul 2014.

[28] ATLAS Collaboration. A Measurement of WZ Production in Proton-Proton Collisions at sqrt(s)=8TeV with the ATLAS Detector. Technical Report ATLAS-CONF-2013-021, CERN, Geneva, Mar 2013.

[29] ATLAS Collaboration. *ATLAS calorimeter performance: Technical Design Report*. Technical Design Report ATLAS. CERN, Geneva, 1996.

[30] ATLAS Collaboration. Jet Uncertainities 2011 Twiki, . URL `https://twiki.cern.ch/twiki/bin/viewauth/AtlasProtected/JetUncertainties2011`.

[31] Michael Edward Peskin and Daniel V. Schroeder. *An Introduction to Quantum Field Theory*. Advanced book program. Westview Press Reading (Mass.), Boulder (Colo.), 1995. ISBN 0-201-50934-2. Autre tirage : 1997.

[32] C.P. Burgess and G.D. Moore. The standard model: A primer. 2007.

[33] N Venturi. Higgs couplings and properties with the ATLAS detector at the LHC. Technical Report ATL-PHYS-PROC-2014-070, CERN, Geneva, Jul 2014.

[34] G.J. Feldman, J. Hartnell, and T. Kobayashi. Long-baseline neutrino oscillation experiments. *Adv.High Energy Phys.*, 2013:475749, 2013. doi: 10.1155/2013/475749.

[35] D. Griffiths. *Introduction to Elementary Particles*. John Wiley & Sons, New York, USA, 1987.

[36] ATLAS Collaboration. Measurement of the Higgs boson mass from the $H \to \gamma\gamma$ and $H \to ZZ^* \to 4\ell$ channels with the ATLAS detector using 25 fb^{-1} of pp collision data. 2014.

[37] John C. Collins, Davison E. Soper, and George F. Sterman. Factorization of Hard Processes in QCD. *Adv.Ser.Direct.High Energy Phys.*, 5:1–91, 1988.

[38] Stefano Frixione and Bryan R. Webber. Matching NLO QCD computations and parton shower simulations. *JHEP*, 06:029, 2002.

[39] Hung-Liang Lai, Marco Guzzi, Joey Huston, Zhao Li, Pavel M. Nadolsky, et al. New parton distributions for collider physics. *Phys.Rev.*, D82:074024, 2010. doi: 10.1103/PhysRevD.82.074024.

[40] Lance J. Dixon, Z. Kunszt, and A. Signer. Vector boson pair production in hadronic collisions at order α_s : Lepton correlations and anomalous couplings. *Phys.Rev.*, D60: 114037, 1999. doi: 10.1103/PhysRevD.60.114037.

[41] K. Hagiwara, R.D. Peccei, D. Zeppenfeld, and K. Hikasa. Probing the weak boson sector in e+ew+w. *Nuclear Physics B*, 282(0):253 – 307, 1987. ISSN 0550-3213. doi: http://dx.doi.org/10.1016/0550-3213(87)90685-7. URL `http://www.sciencedirect.com/science/article/pii/0550321387906857`.

[42] Celine Degrande, Nicolas Greiner, Wolfgang Kilian, Olivier Mattelaer, Harrison Mebane, et al. Effective Field Theory: A Modern Approach to Anomalous Couplings. *Annals Phys.*, 335:21–32, 2013. doi: 10.1016/j.aop.2013.04.016.

[43] CDF Collaboration. Measurement of the WW Production Cross Section with Jets at CDF Using 9.7 fb^{-1} of Data, . URL http://www-cdf.fnal.gov/physics/ewk/2014/WWjets/.

[44] Victor Mukhamedovich Abazov et al. Measurement of the ww production cross section with dilepton final states in $p\overline{p}$ collisions at $\sqrt{s} = 1.96$ TeV and limits on anomalous trilinear gauge couplings. *Phys. Rev. Lett.*, 103:191801, Nov 2009. doi: 10.1103/PhysRevLett.103.191801. URL http://link.aps.org/doi/10.1103/PhysRevLett.103.191801.

[45] Victor Mukhamedovich Abazov et al. Measurement of the wz and zz production cross sections using leptonic final states in 8.6 fb^{-1} of $p\overline{p}$ collisions. *Phys. Rev. D*, 85:112005, Jun 2012. doi: 10.1103/PhysRevD.85.112005. URL http://link.aps.org/doi/10.1103/PhysRevD.85.112005.

[46] CDF Collaboration. Measurement of the WZ Cross Section and Triple Gauge Couplings in $p\bar{p}$ Collisions at $\sqrt{s} = 1.96$ TeV. *Phys.Rev.*, D86:031104, 2012. doi: 10.1103/PhysRevD.86.031104.

[47] Victor Mukhamedovich Abazov et al. Measurements of ww and wz production in $w+$ jets final states in $p\overline{p}$ collisions. *Phys. Rev. Lett.*, 108:181803, May 2012. doi: 10.1103/PhysRevLett.108.181803. URL http://link.aps.org/doi/10.1103/PhysRevLett.108.181803.

[48] CDF Collaboration. Measurement of WW/WZ cross section in ljj decay using 4.3 fb^{-1}, . URL http://www-cdf.fnal.gov/physics/ewk/2010/WW_WZ/index.html.

[49] ATLAS Collaboration. Measurement of W^+W^- production in pp collisions at $\sqrt{s}$=7 TeV with the ATLAS detector and limits on anomalous WWZ and WWγ couplings. *Phys.Rev.*, D87(11):112001, 2013. doi: 10.1103/PhysRevD.87.112001,10.1103/PhysRevD.88.079906.

[50] Measurement of the W^+W^- Cross section in pp Collisions at $\sqrt{s} = 7$ TeV and Limits on Anomalous $WW\gamma$ and WWZ couplings. *Eur.Phys.J.*, C73:2610, 2013. doi: 10.1140/epjc/s10052-013-2610-8.

[51] ATLAS Collaboration. Measurement of WZ production in proton-proton collisions at $\sqrt{s} = 7$ TeV with the ATLAS detector. *Eur.Phys.J.*, C72:2173, 2012. doi: 10.1140/epjc/s10052-012-2173-0.

[52] CMS Collaboration. Measurement of WZ production rate. Technical Report CMS-PAS-SMP-12-006, CERN, Geneva, 2013.

[53] CMS Collaboration. Measurement of the sum of ww and wz production with w+dijet events in pp collisions at $\sqrt{s} = 7$ TeV. *Eur. Phys. J.*, C73(2):1–18, 2013. ISSN 1434-6044. doi: 10.1140/epjc/s10052-013-2283-3.

[54] CMS Collaboration. Measurement of W+W- and ZZ production cross sections in pp collisions at sqrt(s) = 8 TeV. *Phys.Lett.*, B721:190–211, 2013. doi: 10.1016/j.physletb.2013.03.027.

[55] ATLAS Collaboration. Measurements of Wγ and Zγ production in pp collisions at $\sqrt{s}$=7 TeV with the ATLAS detector at the LHC. *Phys.Rev.*, D87(11):112003, 2013. doi: 10.1103/PhysRevD.87.112003.

[56] CMS Collaboration. Measurement of the W gamma and Z gamma inclusive cross sections in pp collisions at $\sqrt{s} = 7$ TeV and limits on anomalous triple gauge boson couplings. *Phys.Rev.*, D89:092005, 2014. doi: 10.1103/PhysRevD.89.092005.

[57] Victor Mukhamedovich Abazov et al. Limits on anomalous trilinear gauge boson couplings from WW, WZ and $W\gamma$ production in $p\bar{p}$ collisions at $\sqrt{s} = 1.96$ TeV. *Phys.Lett.*, B718:451–459, 2012. doi: 10.1016/j.physletb.2012.10.062.

[58] S. Schael et al. Electroweak Measurements in Electron-Positron Collisions at W-Boson-Pair Energies at LEP. *Phys.Rept.*, 532:119–244, 2013. doi: 10.1016/j.physrep.2013.07.004.

[59] ATLAS Collaboration. Jet energy resolution in proton-proton collisions at $\sqrt{s} = 7$ TeV recorded in 2010 with the ATLAS detector. *Eur. Phys. J. C*, 73(arXiv:1210.6210. CERN-PH-EP-2012-191):2306. 26 p, Oct 2012. Comments: 13 pages plus author list (26 pages total), 15 figures, 1 table, submitted to European Physical Journal C.

[60] S Myers. Large Hadron Collider commissioning and first operation. LHC Commissioning and First Operation. *Phil. Trans. R. Soc. A*, 370(CERN-ATS-2011-013):859–875. 12 p, Jun 2011.

[61] ATLAS Collaboration. The ATLAS Experiment at the CERN Large Hadron Collider. *J. Instrum.*, 3:S08003. 437 p, 2008. Also published by CERN Geneva in 2010.

[62] Ed Daw. Lecture 7 Rapidity and Pseudorapidity. URL `http://www.hep.shef.ac.uk/edaw/PHY206/Site/2012_course_files/phy206rlec7.pdf`.

[63] ATLAS Collaboration. Improved luminosity determination in *pp* collisions at $\sqrt{s} = 7$ TeV using the ATLAS detector at the LHC. *Eur.Phys.J.*, C73:2518, 2013. doi: 10.1140/epjc/s10052-013-2518-3.

[64] V Cindro, D Dobos, I Dolenc, H Frais-Klbl, A Goriek, E Griesmayer, H Kagan, G Kramberger, B Macek, I Mandi, M Miku, M Niegl, H Pernegger, D Tardif, W Trischuk, P Weilhammer, and M Zavrtanik. The atlas beam conditions monitor. *Journal of Instrumentation*, 3(02):P02004, 2008. URL `http://stacks.iop.org/1748-0221/3/i=02/a=P02004`.

[65] D. Caforio. *Luminosity measurement using Cherenkov Integrating Detector (LUCID) in ATLAS*, chapter 72, pages 413–417. doi: 10.1142/9789812819093_0072. URL `http://www.worldscientific.com/doi/abs/10.1142/9789812819093_0072`.

[66] Ivan Peri, Laurent Blanquart, Giacomo Comes, Peter Denes, Kevin Einsweiler, Peter Fischer, Emanuele Mandelli, and Gerrit Meddeler. The {FEI3} readout chip for the {ATLAS} pixel detector. *Nuclear Instruments and Methods in Physics Research Section A: Accelerators, Spectrometers, Detectors and Associated Equipment*, 565(1):178 – 187, 2006. ISSN 0168-9002. doi: http://dx.doi.org/10.1016/j.nima.2006.05.032. URL `http://www.sciencedirect.com/science/article/pii/S0168900206007649`. Proceedings of the International Workshop on Semiconductor Pixel Detectors for Particles and Imaging {PIXEL} 2005 International Workshop on Semiconductor Pixel Detectors for Particles and Imaging.

[67] ATLAS Collaboration. *ATLAS inner detector: Technical Design Report, 1*. Technical Design Report ATLAS. CERN, Geneva, 1997.

[68] N Barlow. Operation of the ATLAS Semiconductor Tracker. Technical Report ATL-INDET-PROC-2010-003, CERN, Geneva, Feb 2010.

[69] J Degenhardt. Performance of the ATLAS Transition Radiation Tracker with Cosmic Rays and First High Energy Collisions at the LHC. Technical Report ATL-INDET-PROC-2010-040, CERN, Geneva, Nov 2010.

[70] ATLAS Collaboration. *ATLAS central solenoid: Technical Design Report*. Technical Design Report ATLAS. CERN, Geneva, 1997.

[71] ATLAS Collaboration. *ATLAS magnet system: Technical Design Report, 1*. Technical Design Report ATLAS. CERN, Geneva, 1997.

[72] T Cornelissen, M Elsing, S Fleischmann, W Liebig, E Moyse, and A Salzburger. Concepts, Design and Implementation of the ATLAS New Tracking (NEWT). Technical Report ATL-SOFT-PUB-2007-007. ATL-COM-SOFT-2007-002, CERN, Geneva, Mar 2007.

[73] R. Fruhwirth. Application of Kalman filtering to track and vertex fitting. *Nucl.Instrum.Meth.*, A262:444–450, 1987. doi: 10.1016/0168-9002(87)90887-4.

[74] Daniel Wicke. A New algorithm for solving tracking ambiguities. 1999.

[75] Richard O. Duda and Peter E. Hart. Use of the hough transformation to detect lines and curves in pictures. *Commun. ACM*, 15(1):11–15, January 1972. ISSN 0001-0782. doi: 10.1145/361237.361242. URL `http://doi.acm.org/10.1145/361237.361242`.

[76] E Bouhova-Thacker, P Lichard, V Kostyukhin, W Liebig, M Limper, G Piacquadio, P Lichard, C Weiser, and A Wildauer. Vertex Reconstruction in the ATLAS Experiment at the LHC. Technical Report ATL-INDET-PUB-2009-001. ATL-COM-INDET-2009-011, CERN, Geneva, May 2009. Note was a proceeding for IEEE/NSS Dresden 2008 and is now intended for possible publication in TNS.

[77] W Lampl, S Laplace, D Lelas, P Loch, H Ma, S Menke, S Rajagopalan, D Rousseau, S Snyder, and G Unal. Calorimeter Clustering Algorithms: Description and Performance. Technical Report ATL-LARG-PUB-2008-002. ATL-COM-LARG-2008-003, CERN, Geneva, Apr 2008.

[78] ATLAS Collaboration. Expected electron performance in the ATLAS experiment. Technical Report ATL-PHYS-PUB-2011-006, CERN, Geneva, Apr 2011.

[79] SX Oda. Commissioning of the Muon Track Reconstruction in the ATLAS Experiment. Technical Report ATL-MUON-PROC-2009-006, CERN, Geneva, Oct 2009.

[80] ATLAS Collaboration. Muon Staco documentation, 2010. URL `https://twiki.cern.ch/twiki/bin/view/AtlasProtected/STACODocumentation`.

[81] ATLAS Collaboration. Properties of Jets and Inputs to Jet Reconstruction and Calibration with the ATLAS Detector Using Proton-Proton Collisions at $\sqrt{s} = 7$ TeV. Technical Report ATLAS-CONF-2010-053, CERN, Geneva, Jul 2010.

[82] ATLAS Collaboration. Jet energy measurement with the ATLAS detector in proton-proton collisions at $\sqrt{s} = 7$ TeV. *Eur.Phys.J.*, C73:2304, 2013. doi: 10.1140/epjc/s10052-013-2304-2.

[83] ATLAS Collaboration. MET Utility tool documentation, 2013. URL `https://twiki.cern.ch/twiki/bin/viewauth/AtlasProtected/MissingETUtility`.

[84] Torbjorn Sjostrand et al. High-energy physics event generation with PYTHIA 6.1. *Comput. Phys. Commun.*, 135:238–259, 2001. doi: 10.1016/S0010-4655(00)00236-8.

[85] Bo Andersson, G. Gustafson, G. Ingelman, and T. Sjostrand. Parton Fragmentation and String Dynamics. *Phys.Rept.*, 97:31–145, 1983. doi: 10.1016/0370-1573(83)90080-7.

[86] Torbjorn Sjostrand. The Lund Monte Carlo for Jet Fragmentation and e+ e- Physics: Jetset Version 6.2. *Comput.Phys.Commun.*, 39:347–407, 1986. doi: 10.1016/0010-4655(86)90096-2.

[87] G Corcella, I Knowles, G Marchesini, S Moretti, K Odagiri, P Richardson, M Seymour, and B Webber. Herwig 6.5. *JHEP*, 0101:010, 2001.

[88] J.M. Butterworth, J.R Forsaw, and M.H. Seymour. Multiparton interactions in photoproduction at hera. *Z. Phys. C*, 72:637–646, 1996.

[89] M L Mangano, M Moretti, F Piccinini, R Pittau, and A Polosa. Alpgen, a generator for hard multiparton processes in hadronic collisions. *JHEP*, 0307, 2003.

[90] Borut Paul Kersevan and Elzbieta Richter-Was. The Monte Carlo event generator AcerMC versions 2.0 to 3.8 with interfaces to PYTHIA 6.4, HERWIG 6.5 and ARIADNE 4.1. *Comput.Phys.Commun.*, 184:919–985, 2013. doi: 10.1016/j.cpc.2012.10.032.

[91] S. Agostinelli et al. Geant 4, a simulation toolkit. *Nucl. Instrum. Meth.*, A506:250, 2003.

[92] ATLAS Collaboration. The ATLAS Simulation Infrastructure. *Eur.Phys.J.*, C70:823–874, 2010. doi: 10.1140/epjc/s10052-010-1429-9.

[93] Wolfgang Lukas. Fast Simulation for ATLAS: Atlfast-II and ISF. *Journal of Physics: Conference Series*, 396:1–10, 2012. doi: doi:10.1088/1742-6596/396/2/022031.

[94] Michael Leyton. Minimum Bias and Underlying Event Measurements with ATLAS. pages 11–19, 2012.

[95] Zachary Marshall and the Atlas Collaboration. Simulation of pile-up in the atlas experiment. *Journal of Physics: Conference Series*, 513(2):022024, 2014. URL `http://stacks.iop.org/1742-6596/513/i=2/a=022024`.

[96] J Butterworth, E Dobson, U Klein, B Mellado Garcia, T Nunnemann, J Qian, D Rebuzzi, and R Tanaka. Single boson and diboson production cross sections in pp collisions at sqrts=7 tev.

[97] Johan Alwall et al. MadGraph/MadEvent v4: The New Web Generation. *JHEP*, 09: 028, 2007.

[98] A.D. Martin, W.J. Stirling, R.S. Thorne, and G. Watt. Parton distributions for the LHC. *Eur. Phys. J.*, C 63:189, 2009.

[99] A.D Martin, W.J. Stirling, R.S. Thorne, and G. Watt. Uncertainties on α_s global pdf analyses and implications for predicted hadronic cross sections. *Eur. Phys. J.*, C 64: 653, 2009.

[100] J. Pumplin, D.R. Stump, J. Huston, H.L. Lai, Pavel M. Nadolsky, et al. New generation of parton distributions with uncertainties from global QCD analysis. *JHEP*, 0207:012, 2002. doi: 10.1088/1126-6708/2002/07/012.

[101] Charalampos Anastasiou, Lance J. Dixon, Kirill Melnikov, and Frank Petriello. High precision QCD at hadron colliders: Electroweak gauge boson rapidity distributions at NNLO. *Phys.Rev.*, D69:094008, 2004. doi: 10.1103/PhysRevD.69.094008.

[102] Kirill Melnikov and Frank Petriello. Electroweak gauge boson production at hadron colliders through O(alpha(s)**2). *Phys.Rev.*, D74:114017, 2006. doi: 10.1103/PhysRevD.74.114017.

[103] ATLAS Collaboration. Measurement of the production cross section for W-bosons in association with jets in pp collisions at $\sqrt{s} = 7$ TeV with the ATLAS detector. *Phys.Lett.*, B698:325–345, 2011. doi: 10.1016/j.physletb.2011.03.012.

[104] M Mangeno. Merging multijet matrix elements and shower evolution in hadronic collisions. URL `http://cern.ch/%7Emlm/talks/lund-alpgen.pdf`.

[105] Alpgen Presentation. URL http://www-d0.fnal.gov/computing/MonteCarlo/generators/matching_prescriptions/mlm/alpgen.pdf.

[106] H. L. Lai, M. Guzzi, J. Huston, Z. Li, P. M. Nadolsy, et al. New parton distributions for collider physics. D82:074024, 2010. doi: 10.1103/PhysRevD.82.074024.

[107] M. Aliev, H. Lacker, U. Langenfeld, S. Moch, P. Uwer, et al. HATHOR: HAdronic Top and Heavy quarks crOss section calculatoR. *Comput.Phys.Commun.*, 182:1034–1046, 2011. doi: 10.1016/j.cpc.2010.12.040.

[108] Matteo Cacciari, Michal Czakon, Michelangelo Mangano, Alexander Mitov, and Paolo Nason. Top-pair production at hadron colliders with next-to-next-to-leading logarithmic soft-gluon resummation. *Phys.Lett.*, B710:612–622, 2012. doi: 10.1016/j.physletb.2012.03.013.

[109] Peter Bärnreuther, Michal Czakon, and Alexander Mitov. Percent Level Precision Physics at the Tevatron: First Genuine NNLO QCD Corrections to $q\bar{q} \to t\bar{t} + X$. *Phys.Rev.Lett.*, 109:132001, 2012. doi: 10.1103/PhysRevLett.109.132001.

[110] Michal Czakon and Alexander Mitov. NNLO corrections to top-pair production at hadron colliders: the all-fermionic scattering channels. *JHEP*, 1212:054, 2012. doi: 10.1007/JHEP12(2012)054.

[111] Michal Czakon and Alexander Mitov. NNLO corrections to top pair production at hadron colliders: the quark-gluon reaction. *JHEP*, 1301:080, 2013. doi: 10.1007/JHEP01(2013)080.

[112] Michal Czakon, Paul Fiedler, and Alexander Mitov. Total Top-Quark Pair-Production Cross Section at Hadron Colliders Through $O(\alpha_S^4)$. *Phys.Rev.Lett.*, 110(25):252004, 2013. doi: 10.1103/PhysRevLett.110.252004.

[113] Michal Czakon and Alexander Mitov. Top++: A Program for the Calculation of the Top-Pair Cross-Section at Hadron Colliders. 2011.

[114] Michiel Botje, Jon Butterworth, Amanda Cooper-Sarkar, Albert de Roeck, Joel Feltesse, et al. The PDF4LHC Working Group Interim Recommendations. 2011.

[115] Jun Gao, Marco Guzzi, Joey Huston, Hung-Liang Lai, Zhao Li, et al. The CT10 NNLO Global Analysis of QCD. *Phys.Rev.*, D89:033009, 2014. doi: 10.1103/PhysRevD.89.033009.

[116] Richard D. Ball, Valerio Bertone, Stefano Carrazza, Christopher S. Deans, Luigi Del Debbio, et al. Parton distributions with LHC data. *Nucl.Phys.*, B867:244–289, 2013. doi: 10.1016/j.nuclphysb.2012.10.003.

[117] N. Kidonakis. Next-to-next-to-leading-order collinear and soft gluon corrections for t-channel single top quark production. D83:091503, 2011. doi: 10.1103/PhysRevD.83.091503.

[118] N. Kidonakis. NNLL resummation for s-channel single top quark production. D81: 054028, 2010. doi: 10.1103/PhysRevD.81.054028.

[119] Nikolaos Kidonakis. Two-loop soft anomalous dimensions for single top quark associated production with a W- or H-. *Phys.Rev.*, D82:054018, 2010. doi: 10.1103/PhysRevD.82.054018.

[120] ATLAS Collaboration. Z Vertex Reweighting README, 2012. URL `https://svnweb.cern.ch/trac/atlasoff/browser/Reconstruction/egamma/egammaAnalysis/egammaAnalysisUtils/tags/egammaAnalysisUtils-00-03-35/egammaAnalysisUtils/VertexPositionReweightingTool.h`.

[121] ATLAS Collaboration. Electron performance measurements with the ATLAS detector using the 2010 LHC proton-proton collision data. *Eur. Phys. J. C*, 72(arXiv:1110.3174. CERN-PH-EP-2011-117):1909. 45 p, Oct 2011. Comments: 33 pages plus author list (45 pages total), 24 figures, 12 tables, submitted to Eur. Phys. J. C.

[122] ATLAS Collaboration. Electron reconstruction and identification efficiency measurements with the ATLAS detector using the 2011 LHC proton-proton collision data. 2014.

[123] ATLAS Collaboration. Performance of the ATLAS Electron and Photon Trigger in p-p Collisions at sqrts = 7 TeV in 2011. Technical Report ATLAS-CONF-2012-048, CERN, Geneva, May 2012.

[124] ATLAS Collaboration. EGamma Calibration Twiki, 2014. URL `https://twiki.cern.ch/twiki/bin/view/AtlasProtected/EGammaCalibrationGEO20History`.

[125] ATLAS Collaboration. Electron and photon energy calibration with the ATLAS detector using LHC Run 1 data. Technical Report ATL-COM-PHYS-2013-1652, CERN, Geneva, Dec 2013.

[126] ATLAS Collaboration. Calorimeter Isolation Corrections, 2014. URL `https://twiki.cern.ch/twiki/bin/view/AtlasProtected/CaloIsolationCorrections`.

[127] ATLAS Collaboration. Muon reconstruction efficiency in reprocessed 2010 LHC proton-proton collision data recorded with the ATLAS detector. Technical Report ATLAS-CONF-2011-063, CERN, Geneva, Apr 2011.

[128] ATLAS Collaboration. Muon Momentum Resolution in First Pass Reconstruction of pp Collision Data Recorded by ATLAS in 2010. Technical Report ATLAS-CONF-2011-046, CERN, Geneva, Mar 2011.

[129] N Makovec. LAr hole treatment, 2011. URL `https://indico.cern.ch/event/161237/contribution/1/material/0/10.pdf`.

[130] ATLAS Collaboration. Performance of the ATLAS muon trigger in 2011. Technical Report ATLAS-CONF-2012-099, CERN, Geneva, Jul 2012.

[131] ATLAS Collaboration. Recommendation for jet cleaning for data 2011, 2014. URL https://twiki.cern.ch/twiki/bin/viewauth/AtlasProtected/HowToCleanJets2011.

[132] ATLAS Collaboration. Jet Energy Resolution Provider 2012 Twiki, . URL https://twiki.cern.ch/twiki/bin/viewauth/AtlasProtected/JetEnergyResolutionProvider2012.

[133] ATLAS Collaboration. Measurement of the combined ww and wz production cross section in the semileptonic final state in proton-proton collisions at sqrt(s) = 7 tev with atlas detector. .

[134] F James and M Roos. MINUIT: a system for function minimization and analysis of the parameter errors and corrections. *Comput. Phys. Commun.*, 10(CERN-DD-75-20): 343–367. 38 p, Jul 1975.

[135] Lorenzo Moneta, Kevin Belasco, Kyle S. Cranmer, S. Kreiss, Alfio Lazzaro, et al. The RooStats Project. *PoS*, ACAT2010:057, 2010.

[136] M. Bahr, S. Gieseke, M.A. Gigg, D. Grellscheid, K. Hamilton, et al. Herwig++ Physics and Manual. *Eur.Phys.J.*, C58:639–707, 2008. doi: 10.1140/epjc/s10052-008-0798-9.

[137] ATLAS Collaboration. Guide to profile likelihood analyses, . URL https://twiki.cern.ch/twiki/bin/viewauth/AtlasProtected/ProfilingChecksDraft.

[138] TGClim Code. URL https://svnweb.cern.ch/trac/atlasphys/browser/Physics/StandardModel/ElectroWeak/Common/Software/TGC/TGClim.

[139] Glen Cowan, Kyle Cranmer, Eilam Gross, and Ofer Vitells. Asymptotic formulae for likelihood-based tests of new physics. *The European Physical Journal C*, 71(2):1554, 2011. ISSN 1434-6044. doi: 10.1140/epjc/s10052-011-1554-0. URL http://dx.doi.org/10.1140/epjc/s10052-011-1554-0.

Appendix A

Monte Carlo Data Samples

This appendix contains tables listing the Monte Carlo samples used for this analysis. For each sample, the ATLAS-specific naming scheme is used which contains the process ID and the corresponding production tags.

Sample Name
Di-boson
mc11_7TeV.105985.WW_Herwig.merge.NTUP_SMWZ.e825_s1310_s1300_r3043_r2993_p1035/
mc11_7TeV.105987.WZ_Herwig.merge.NTUP_SMWZ.e825_s1310_s1300_r3043_r2993_p1035/
mc11_7TeV.105986.ZZ_Herwig.merge.NTUP_SMWZ.e825_s1310_s1300_r3043_r2993_p1035/
mc11_7TeV.147358.McAtNloJimmy_AU2CT10_WW_V_V.merge.NTUP_SMWZ.e1797_a186_s1571_a145_r2993_p1035/
mc11_7TeV.147361.McAtNloJimmy_AU2CT10_WW_V_V.merge.NTUP_SMWZ.e1797_a186_s1571_a145_r2993_p1035/
mc11_7TeV.147360.McAtNloJimmy_AU2CT10_WmZ_V_V.merge.NTUP_SMWZ.e1797_a186_s1571_a145_r2993_p1035/
mc11_7TeV.147363.McAtNloJimmy_AU2CT10_WmZ_V_V.merge.NTUP_SMWZ.e1797_a186_s1571_a145_r2993_p1035/
mc11_7TeV.147359.McAtNloJimmy_AU2CT10_WpZ_V_V.merge.NTUP_SMWZ.e1797_a186_s1571_a145_r2993_p1035/
mc11_7TeV.147362.McAtNloJimmy_AU2CT10_WpZ_V_V.merge.NTUP_SMWZ.e1797_a186_s1571_a145_r2993_p1035/
Single-top
mc11_7TeV.108343.st_schan_enu_McAtNlo_Jimmy.merge.NTUP_SMWZ.e825_s1310_s1300_r3043_r2993_p1035/
mc11_7TeV.108344.st_schan_munu_McAtNlo_Jimmy.merge.NTUP_SMWZ.e825_s1310_s1300_r3043_r2993_p1035/
mc11_7TeV.108345.st_schan_taunu_McAtNlo_Jimmy.merge.NTUP_SMWZ.e835_s1310_s1300_r3043_r2993_p1035/
mc11_7TeV.117360.st_tchan_enu_AcerMC.merge.NTUP_SMWZ.e835_s1310_s1300_r3043_r2993_p1035/
mc11_7TeV.117361.st_tchan_munu_AcerMC.merge.NTUP_SMWZ.e835_s1310_s1300_r3043_r2993_p1035/
mc11_7TeV.117362.st_tchan_taunu_AcerMC.merge.NTUP_SMWZ.e825_s1310_s1300_r3043_r2993_p1035/
mc11_7TeV.108346.st_Wt_McAtNlo_Jimmy.merge.NTUP_SMWZ.e835_s1310_s1300_r3043_r2993_p1035/
mc11_7TeV.117214.st_schan_enu_AcerMC_LessPS.merge.NTUP_SMWZ.e1029_a131_s1353_a145_r2993_p1035/
mc11_7TeV.117213.st_schan_enu_AcerMC_MorePS.merge.NTUP_SMWZ.e1029_a131_s1353_a145_r2993_p1035/
mc11_7TeV.117216.st_schan_munu_AcerMC_LessPS.merge.NTUP_SMWZ.e1029_a131_s1353_a145_r2993_p1035/
mc11_7TeV.117215.st_schan_munu_AcerMC_MorePS.merge.NTUP_SMWZ.e1029_a131_s1353_a145_r2993_p1035/
mc11_7TeV.117218.st_schan_taunu_AcerMC_LessPS.merge.NTUP_SMWZ.e1029_a131_s1353_a145_r2993_p1035/
mc11_7TeV.117217.st_schan_taunu_AcerMC_MorePS.merge.NTUP_SMWZ.e1029_a131_s1353_a145_r2993_p1035/
mc11_7TeV.117220.st_tchan_enu_AcerMC_LessPS.merge.NTUP_SMWZ.e1029_a131_s1353_a145_r2993_p1035/
mc11_7TeV.117219.st_tchan_enu_AcerMC_MorePS.merge.NTUP_SMWZ.e1029_a131_s1353_a145_r2993_p1035/
mc11_7TeV.117222.st_tchan_munu_AcerMC_LessPS.merge.NTUP_SMWZ.e1029_a131_s1353_a145_r2993_p1035/
mc11_7TeV.117221.st_tchan_munu_AcerMC_MorePS.merge.NTUP_SMWZ.e1029_a131_s1353_a145_r2993_p1035/
mc11_7TeV.117224.st_tchan_taunu_AcerMC_LessPS.merge.NTUP_SMWZ.e1029_a131_s1353_a145_r2993_p1035/
mc11_7TeV.117223.st_tchan_taunu_AcerMC_MorePS.merge.NTUP_SMWZ.e1029_a131_s1353_a145_r2993_p1035/
mc11_7TeV.117246.AcerMC_Wt_LessPS.merge.NTUP_SMWZ.e1029_a131_s1353_a145_r2993_p1035/
mc11_7TeV.117245.AcerMC_Wt_MorePS.merge.NTUP_SMWZ.e1029_a131_s1353_a145_r2993_p1035/
ttbar
mc11_7TeV.105200.T1_McAtNlo_Jimmy.merge.NTUP_SMWZ.e835_s1272_s1274_r3043_r2993_p1035/
mc11_7TeV.117209.AcerMCttbar_MorePS.merge.NTUP_SMWZ.e1029_a131_s1353_a145_r2993_p1035/
mc11_7TeV.117210.AcerMCttbar_LessPS.merge.NTUP_SMWZ.e1029_a131_s1353_a145_r2993_p1035/

Table A.1: List of Monte Carlo samples used in the analysis.

Sample Name
W+heavy flavor
mc11_7TeV.107280.AlpgenJimmyWbbFullNp0_pt20.merge.NTUP_SMWZ.e887_s1310_s1300_r2920_r2900_p1035/
mc11_7TeV.107281.AlpgenJimmyWbbFullNp1_pt20.merge.NTUP_SMWZ.e887_s1310_s1300_r2920_r2900_p1035/
mc11_7TeV.107281.AlpgenJimmyWbbFullNp1_pt20.merge.NTUP_SMWZ.e887_a131_s1353_a145_r2993_p1035/
mc11_7TeV.107282.AlpgenJimmyWbbFullNp2_pt20.merge.NTUP_SMWZ.e887_s1310_s1300_r2920_r2900_p1035/
mc11_7TeV.107283.AlpgenJimmyWbbFullNp3_pt20.merge.NTUP_SMWZ.e887_s1310_s1300_r2920_r2900_p1035/
mc11_7TeV.117293.AlpgenWcNp0_pt20.merge.NTUP_SMWZ.e887_s1310_s1300_r3043_r2993_p1035/
mc11_7TeV.117294.AlpgenWcNp1_pt20.merge.NTUP_SMWZ.e887_s1310_s1300_r3043_r2993_p1035/
mc11_7TeV.117294.AlpgenWcNp1_pt20.merge.NTUP_SMWZ.e887_a131_s1353_a145_r2993_p1035/
mc11_7TeV.117295.AlpgenWcNp2_pt20.merge.NTUP_SMWZ.e887_s1310_s1300_r3043_r2993_p1035/
mc11_7TeV.117295.AlpgenWcNp2_pt20.merge.NTUP_SMWZ.e887_a131_s1353_a145_r2993_p1035/
mc11_7TeV.117296.AlpgenWcNp3_pt20.merge.NTUP_SMWZ.e887_s1310_s1300_r3043_r2993_p1035/
mc11_7TeV.117297.AlpgenWcNp4_pt20.merge.NTUP_SMWZ.e887_s1310_s1300_r3043_r2993_p1035/
mc11_7TeV.117284.AlpgenWccFullNp0_pt20.merge.NTUP_SMWZ.e887_s1310_s1300_r3043_r2993_p1035/
mc11_7TeV.117285.AlpgenWccFullNp1_pt20.merge.NTUP_SMWZ.e887_s1310_s1300_r3043_r2993_p1035/
mc11_7TeV.117285.AlpgenWccFullNp1_pt20.merge.NTUP_SMWZ.e1792_a131_s1353_a145_r2993_p1035/
mc11_7TeV.117286.AlpgenWccFullNp2_pt20.merge.NTUP_SMWZ.e887_s1310_s1300_r3043_r2993_p1035/
mc11_7TeV.117286.AlpgenWccFullNp2_pt20.merge.NTUP_SMWZ.e887_a131_s1353_a145_r2993_p1035/
mc11_7TeV.117287.AlpgenWccFullNp3_pt20.merge.NTUP_SMWZ.e887_s1310_s1300_r3043_r2993_p1035/
W(enu)+jets
mc11_7TeV.107680.AlpgenJimmyWenuNp0_pt20.merge.NTUP_SMWZ.e825_s1299_s1300_r3043_r2993_p1035/
mc11_7TeV.107680.AlpgenJimmyWenuNp0_pt20.merge.NTUP_SMWZ.e825_a131_s1353_a145_r2993_p1035/
mc11_7TeV.107681.AlpgenJimmyWenuNp1_pt20.merge.NTUP_SMWZ.e825_s1299_s1300_r3043_r2993_p1035/
mc11_7TeV.107681.AlpgenJimmyWenuNp1_pt20.merge.NTUP_SMWZ.e825_a131_s1353_a145_r2993_p1035/
mc11_7TeV.107682.AlpgenJimmyWenuNp2_pt20.merge.NTUP_SMWZ.e825_s1299_s1300_r3043_r2993_p1035/
mc11_7TeV.107682.AlpgenJimmyWenuNp2_pt20.merge.NTUP_SMWZ.e1815_a131_s1353_a145_r2993_p1035/
mc11_7TeV.107683.AlpgenJimmyWenuNp3_pt20.merge.NTUP_SMWZ.e825_s1299_s1300_r3043_r2993_p1035/
mc11_7TeV.107683.AlpgenJimmyWenuNp3_pt20.merge.NTUP_SMWZ.e825_a131_s1353_a145_r2993_p1035/
mc11_7TeV.107684.AlpgenJimmyWenuNp4_pt20.merge.NTUP_SMWZ.e825_s1299_s1300_r3043_r2993_p1035/
mc11_7TeV.107684.AlpgenJimmyWenuNp4_pt20.merge.NTUP_SMWZ.e825_a131_s1353_a145_r2993_p1035/
mc11_7TeV.107685.AlpgenJimmyWenuNp5_pt20.merge.NTUP_SMWZ.e825_s1299_s1300_r3043_r2993_p1035/
mc11_7TeV.107685.AlpgenJimmyWenuNp5_pt20.merge.NTUP_SMWZ.e825_a131_s1353_a145_r2993_p1035/

Table A.2: List of Monte Carlo samples used in the analysis.

Sample Name
W(munu)+jets
mc11_7TeV.107690.AlpgenJimmyWmunuNp0_pt20.merge.NTUP_SMWZ.e825_s1299_s1300_r3043_r2993_p1035/
mc11_7TeV.107690.AlpgenJimmyWmunuNp0_pt20.merge.NTUP_SMWZ.e825_a131_s1353_a145_r2993_p1035/
mc11_7TeV.107691.AlpgenJimmyWmunuNp1_pt20.merge.NTUP_SMWZ.e825_s1299_s1300_r3043_r2993_p1035/
mc11_7TeV.107691.AlpgenJimmyWmunuNp1_pt20.merge.NTUP_SMWZ.e825_a131_s1353_a145_r2993_p1035/
mc11_7TeV.107692.AlpgenJimmyWmunuNp2_pt20.merge.NTUP_SMWZ.e825_s1299_s1300_r3043_r2993_p1035/
mc11_7TeV.107692.AlpgenJimmyWmunuNp2_pt20.merge.NTUP_SMWZ.e1815_a131_s1353_a145_r2993_p1035/
mc11_7TeV.107693.AlpgenJimmyWmunuNp3_pt20.merge.NTUP_SMWZ.e825_s1299_s1300_r3043_r2993_p1035/
mc11_7TeV.107693.AlpgenJimmyWmunuNp3_pt20.merge.NTUP_SMWZ.e825_a131_s1353_a145_r2993_p1035/
mc11_7TeV.107694.AlpgenJimmyWmunuNp4_pt20.merge.NTUP_SMWZ.e825_s1299_s1300_r3043_r2993_p1035/
mc11_7TeV.107694.AlpgenJimmyWmunuNp4_pt20.merge.NTUP_SMWZ.e825_a131_s1353_a145_r2993_p1035/
mc11_7TeV.107695.AlpgenJimmyWmunuNp5_pt20.merge.NTUP_SMWZ.e825_s1299_s1300_r3043_r2993_p1035/
mc11_7TeV.107695.AlpgenJimmyWmunuNp5_pt20.merge.NTUP_SMWZ.e825_a131_s1353_a145_r2993_p1035/
W(taunu)+jets
mc11_7TeV.107700.AlpgenJimmyWtaunuNp0_pt20.merge.NTUP_SMWZ.e835_s1299_s1300_r3043_r2993_p1035/
mc11_7TeV.107701.AlpgenJimmyWtaunuNp1_pt20.merge.NTUP_SMWZ.e835_s1299_s1300_r3043_r2993_p1035/
mc11_7TeV.107702.AlpgenJimmyWtaunuNp2_pt20.merge.NTUP_SMWZ.e835_s1299_s1300_r3043_r2993_p1035/
mc11_7TeV.107703.AlpgenJimmyWtaunuNp3_pt20.merge.NTUP_SMWZ.e835_s1299_s1300_r3043_r2993_p1035/
mc11_7TeV.107704.AlpgenJimmyWtaunuNp4_pt20.merge.NTUP_SMWZ.e835_s1299_s1300_r3043_r2993_p1035/
mc11_7TeV.107705.AlpgenJimmyWtaunuNp5_pt20.merge.NTUP_SMWZ.e835_s1299_s1300_r3043_r2993_p1035/
Z(ee)+jets
mc11_7TeV.107650.AlpgenJimmyZeeNp0_pt20.merge.NTUP_SMWZ.e835_s1299_s1300_r3043_r2993_p1035/
mc11_7TeV.116250.AlpgenJimmyZeeNp0_Mll10to40_pt20.merge.NTUP_SMWZ.e959_s1310_s1300_r3043_r2993_p1035/
mc11_7TeV.107651.AlpgenJimmyZeeNp1_pt20.merge.NTUP_SMWZ.e835_s1299_s1300_r3043_r2993_p1035/
mc11_7TeV.116251.AlpgenJimmyZeeNp1_Mll10to40_pt20.merge.NTUP_SMWZ.e959_s1310_s1300_r3043_r2993_p1035/
mc11_7TeV.107652.AlpgenJimmyZeeNp2_pt20.merge.NTUP_SMWZ.e835_s1299_s1300_r3043_r2993_p1035/
mc11_7TeV.116252.AlpgenJimmyZeeNp2_Mll10to40_pt20.merge.NTUP_SMWZ.e944_s1310_s1300_r3043_r2993_p1035/
mc11_7TeV.107653.AlpgenJimmyZeeNp3_pt20.merge.NTUP_SMWZ.e835_s1299_s1300_r3043_r2993_p1035/
mc11_7TeV.116253.AlpgenJimmyZeeNp3_Mll10to40_pt20.merge.NTUP_SMWZ.e944_s1310_s1300_r3043_r2993_p1035/
mc11_7TeV.107654.AlpgenJimmyZeeNp4_pt20.merge.NTUP_SMWZ.e835_s1299_s1300_r3043_r2993_p1035/
mc11_7TeV.116254.AlpgenJimmyZeeNp4_Mll10to40_pt20.merge.NTUP_SMWZ.e944_s1310_s1300_r3043_r2993_p1035/
mc11_7TeV.107655.AlpgenJimmyZeeNp5_pt20.merge.NTUP_SMWZ.e835_s1299_s1300_r3043_r2993_p1035/
mc11_7TeV.116255.AlpgenJimmyZeeNp5_Mll10to40_pt20.merge.NTUP_SMWZ.e944_s1310_s1300_r3043_r2993_p1035/
mc11_7TeV.109300.AlpgenJimmyZeebbNp0_nofilter.merge.NTUP_SMWZ.e835_s1310_s1300_r3043_r2993_p1033/
mc11_7TeV.109301.AlpgenJimmyZeebbNp1_nofilter.merge.NTUP_SMWZ.e835_s1310_s1300_r3043_r2993_p1035/
mc11_7TeV.109302.AlpgenJimmyZeebbNp2_nofilter.merge.NTUP_SMWZ.e835_s1310_s1300_r3043_r2993_p1035/
mc11_7TeV.109303.AlpgenJimmyZeebbNp3_nofilter.merge.NTUP_SMWZ.e835_s1310_s1300_r3043_r2993_p1035/

Table A.3: List of Monte Carlo samples used in the analysis.

Sample Name
Z(mumu)+jets
mc11_7TeV.107660.AlpgenJimmyZmumuNp0_pt20.merge.NTUP_SMWZ.e835_s1299_s1300_r3043_r2993_p1035/
mc11_7TeV.116260.AlpgenJimmyZmumuNp0_Mll10to40_pt20.merge.NTUP_SMWZ.e959_s1310_s1300_r3043_r2993_p1035/
mc11_7TeV.107661.AlpgenJimmyZmumuNp1_pt20.merge.NTUP_SMWZ.e835_s1299_s1300_r3043_r2993_p1035/
mc11_7TeV.116261.AlpgenJimmyZmumuNp1_Mll10to40_pt20.merge.NTUP_SMWZ.e959_s1310_s1300_r3043_r2993_p1035/
mc11_7TeV.107662.AlpgenJimmyZmumuNp2_pt20.merge.NTUP_SMWZ.e835_s1299_s1300_r3043_r2993_p1035/
mc11_7TeV.116262.AlpgenJimmyZmumuNp2_Mll10to40_pt20.merge.NTUP_SMWZ.e944_s1310_s1300_r3043_r2993_p1035/
mc11_7TeV.107663.AlpgenJimmyZmumuNp3_pt20.merge.NTUP_SMWZ.e835_s1299_s1300_r3043_r2993_p1035/
mc11_7TeV.116263.AlpgenJimmyZmumuNp3_Mll10to40_pt20.merge.NTUP_SMWZ.e944_s1310_s1300_r3043_r2993_p1035/
mc11_7TeV.107664.AlpgenJimmyZmumuNp4_pt20.merge.NTUP_SMWZ.e835_s1299_s1300_r3043_r2993_p1035/
mc11_7TeV.116264.AlpgenJimmyZmumuNp4_Mll10to40_pt20.merge.NTUP_SMWZ.e944_s1310_s1300_r3043_r2993_p1035/
mc11_7TeV.107665.AlpgenJimmyZmumuNp5_pt20.merge.NTUP_SMWZ.e835_s1299_s1300_r3043_r2993_p1035/
mc11_7TeV.116265.AlpgenJimmyZmumuNp5_Mll10to40_pt20.merge.NTUP_SMWZ.e944_s1310_s1300_r3043_r2993_p1035/
mc11_7TeV.109305.AlpgenJimmyZmumubbNp0_nofilter.merge.NTUP_SMWZ.e835_s1310_s1300_r3043_r2993_p1035/
mc11_7TeV.109306.AlpgenJimmyZmumubbNp1_nofilter.merge.NTUP_SMWZ.e835_s1310_s1300_r3043_r2993_p1035/
mc11_7TeV.109307.AlpgenJimmyZmumubbNp2_nofilter.merge.NTUP_SMWZ.e835_s1310_s1300_r3043_r2993_p1035/
mc11_7TeV.109308.AlpgenJimmyZmumubbNp3_nofilter.merge.NTUP_SMWZ.e835_s1310_s1300_r3043_r2993_p1035/
Z(tautau)+jets
mc11_7TeV.107670.AlpgenJimmyZtautauNp0_pt20.merge.NTUP_SMWZ.e835_s1299_s1300_r3043_r2993_p1035/
mc11_7TeV.116270.AlpgenJimmyZtautauNp0_Mll10to40_pt20.merge.NTUP_SMWZ.e959_s1310_s1300_r3043_r2993_p1035/
mc11_7TeV.107671.AlpgenJimmyZtautauNp1_pt20.merge.NTUP_SMWZ.e835_s1299_s1300_r3043_r2993_p1035/
mc11_7TeV.116271.AlpgenJimmyZtautauNp1_Mll10to40_pt20.merge.NTUP_SMWZ.e959_s1310_s1300_r3043_r2993_p1035/
mc11_7TeV.107672.AlpgenJimmyZtautauNp2_pt20.merge.NTUP_SMWZ.e835_s1299_s1300_r3043_r2993_p1035/
mc11_7TeV.116272.AlpgenJimmyZtautauNp2_Mll10to40_pt20.merge.NTUP_SMWZ.e959_s1310_s1300_r3043_r2993_p1035/
mc11_7TeV.107673.AlpgenJimmyZtautauNp3_pt20.merge.NTUP_SMWZ.e835_s1299_s1300_r3043_r2993_p1035/
mc11_7TeV.116273.AlpgenJimmyZtautauNp3_Mll10to40_pt20.merge.NTUP_SMWZ.e959_s1310_s1300_r3043_r2993_p1035/
mc11_7TeV.107674.AlpgenJimmyZtautauNp4_pt20.merge.NTUP_SMWZ.e835_s1299_s1300_r3043_r2993_p1035/
mc11_7TeV.116274.AlpgenJimmyZtautauNp4_Mll10to40_pt20.merge.NTUP_SMWZ.e959_s1310_s1300_r3043_r2993_p1035/
mc11_7TeV.107675.AlpgenJimmyZtautauNp5_pt20.merge.NTUP_SMWZ.e835_s1299_s1300_r3043_r2993_p1035/
mc11_7TeV.116275.AlpgenJimmyZtautauNp5_Mll10to40_pt20.merge.NTUP_SMWZ.e959_s1310_s1300_r3043_r2993_p1035/

Table A.4: List of Monte Carlo samples used in the analysis.

Appendix B

Additional Distributions

B.1 JES/JER Shape Systematic Pre-fit Distributions and Tables

This section contains additional tables and figures in regards to the jet energy scale and jet energy resolution uncertainty. The following subsection contains the JES and JER tables for the aTGC selection.

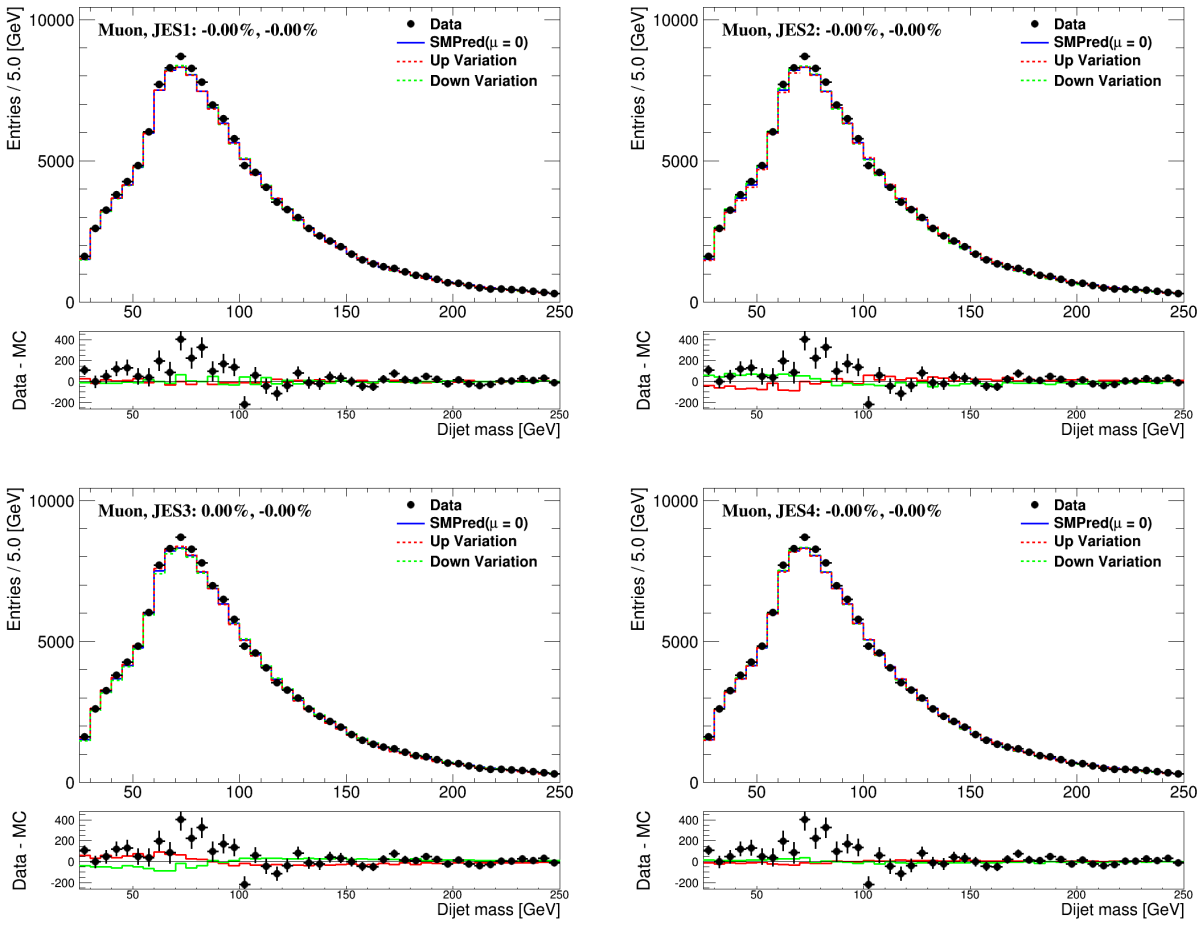

Figure B.1: Muon Channel: Comparison of the m_{jj} templates for data (black dots) with templates produced using the SM prediction assuming zero signal ($\beta = 0$) and templates produced by varying up/down the uncertainties of the JES1 (top left), JES2 (top right), JES3 (bottom left) and JES4 (bottom right) components. The bottom panels contain the difference between the data and the nominal prediction($\beta = 0$) in black and the difference between the systematic variations and the nominal prediction in green/red.

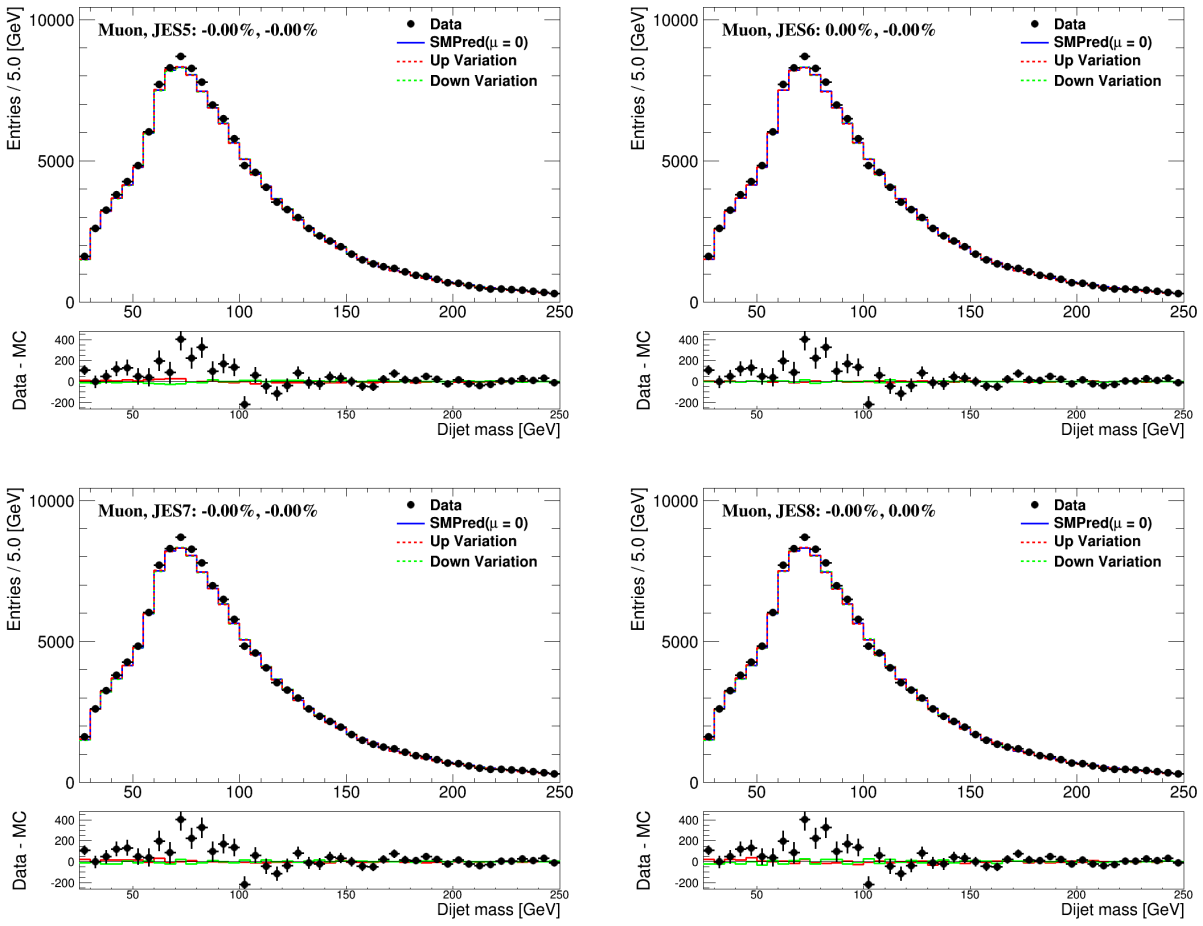

Figure B.2: Muon Channel: Comparison of the m_{jj} templates for data (black dots) with templates produced using the SM prediction assuming zero signal ($\beta = 0$) and templates produced by varying up/down the uncertainties of the JES5 (top left), JES6 (top right), JES7 (bottom left) and JES8 (bottom right) components. The bottom panels contain the difference between the data and the nominal prediction($\beta = 0$) in black and the difference between the systematic variations and the nominal prediction in green/red.

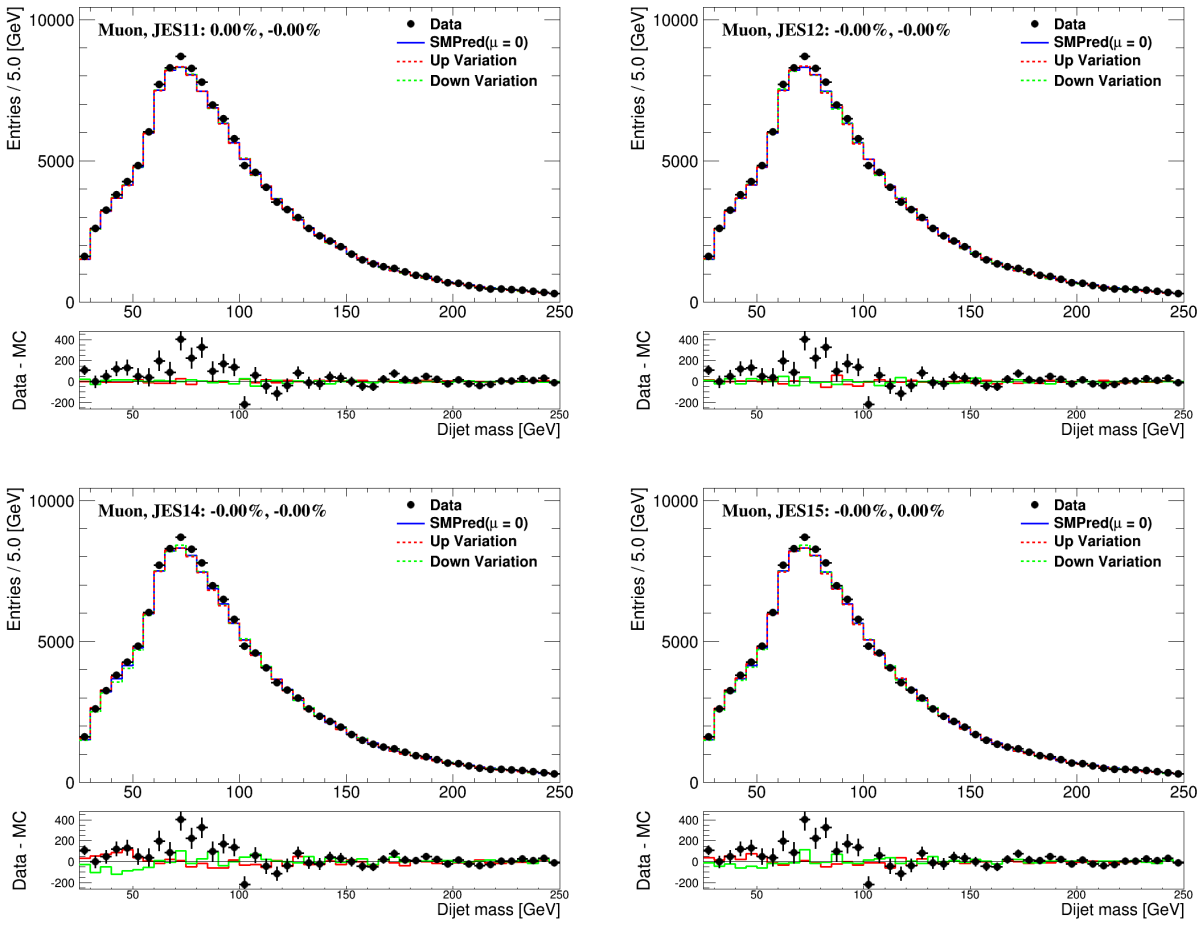

Figure B.3: Muon Channel: Comparison of the m_{jj} templates for data (black dots) with templates produced using the SM prediction assuming zero signal ($\beta = 0$) and templates produced by varying up/down the uncertainties of the JES11 (top left), JES12 (top right), JES14 (bottom left) and JES15 (bottom right) components. The bottom panels contain the difference between the data and the nominal prediction($\beta = 0$) in black and the difference between the systematic variations and the nominal prediction in green/red.

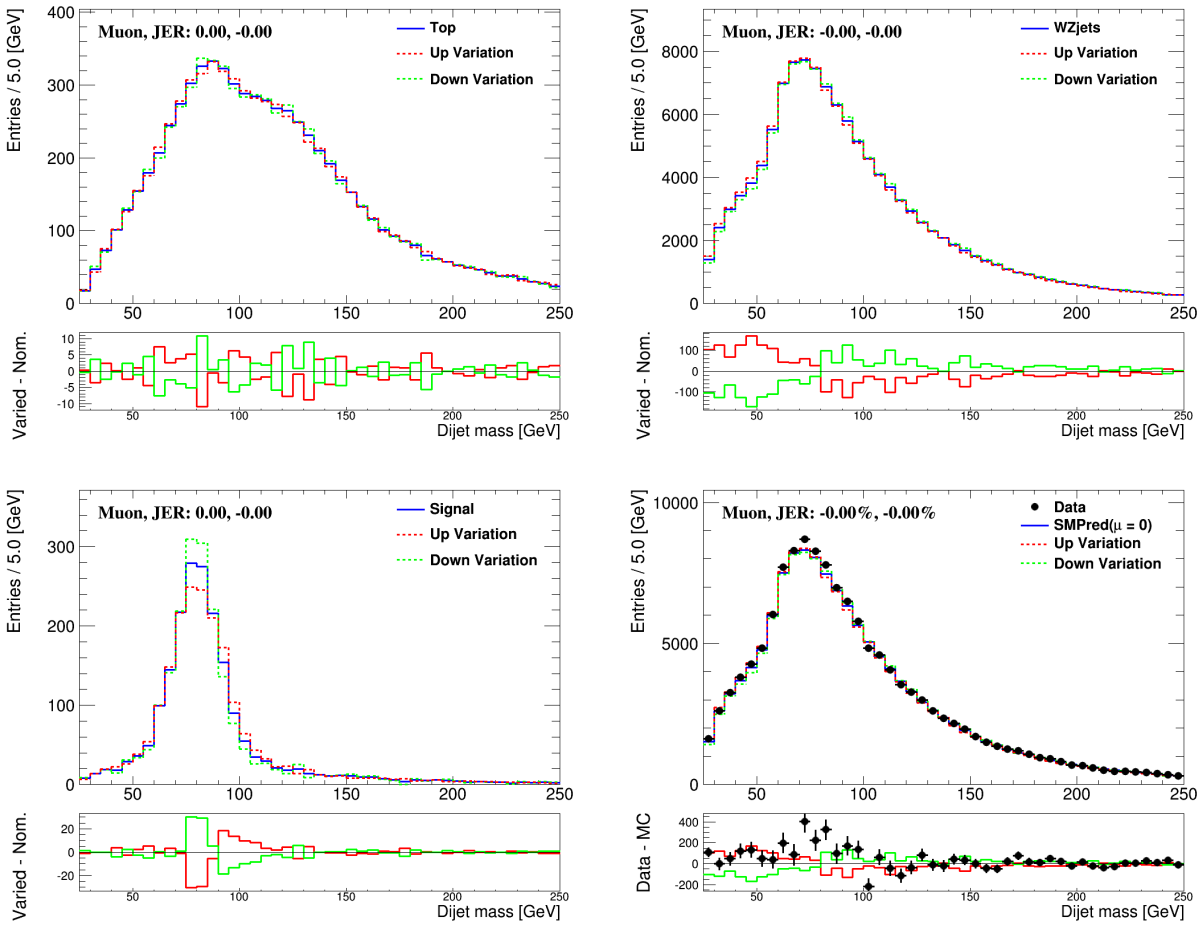

Figure B.4: Muon Channel: m_{jj} templates for the top (top left), W/Z+jets (top right), and Signal (bottom left) processes are shown. For the top panels, the nominal (blue) templates are compared with the up and down systematically varied templates corresponding to the JER component. The bottom panels show the difference between each varied template and the nominal template. The bottom right plot contains all the data overlayed by the nominal and varied templates assuming a signal yield of 0 ($\beta = 0$). The bottom panel of the bottom right plot contains the difference between the data and the nominal prediction($\beta = 0$) in black and the difference between the systematic variation and the nominal prediction in green/red.

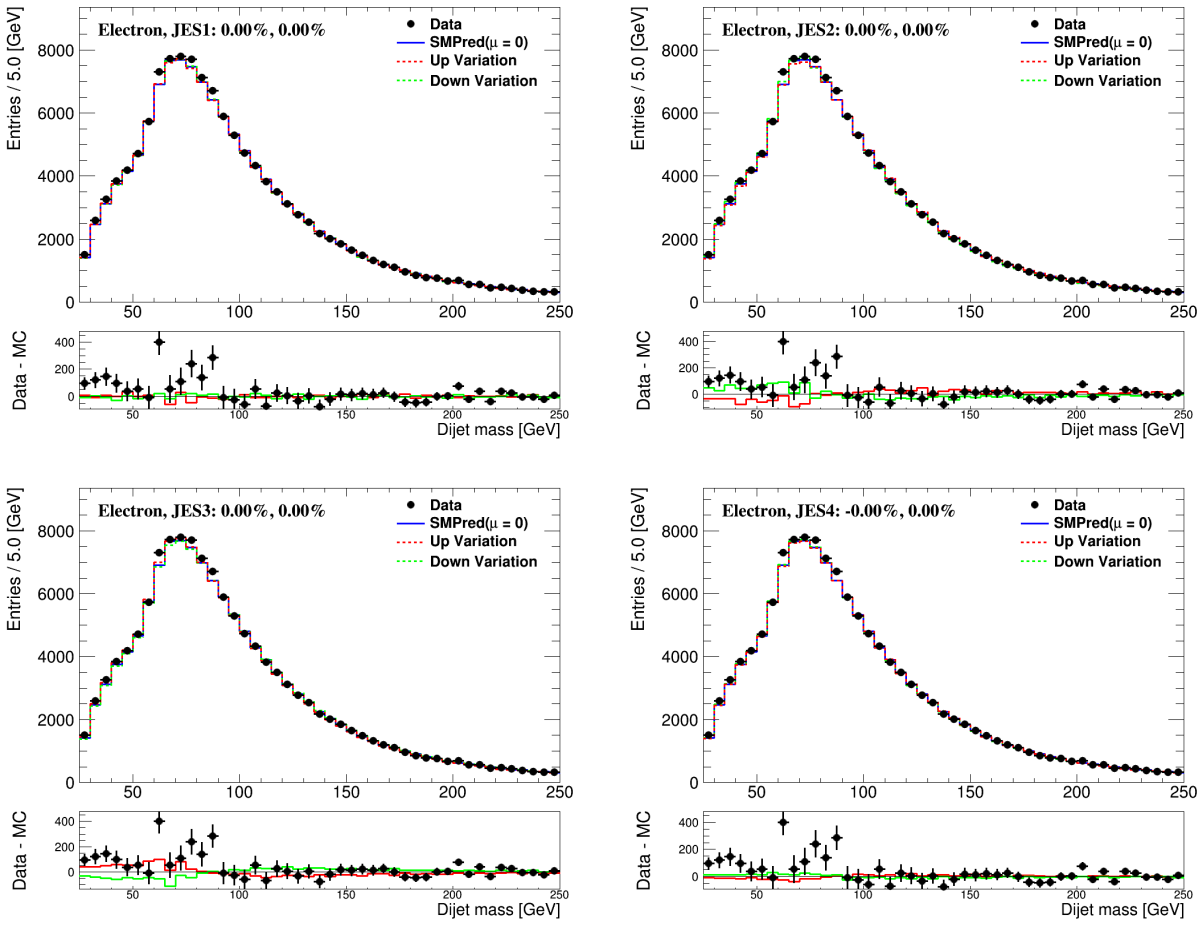

Figure B.5: Electron Channel: Comparison of the m_{jj} templates for data (black dots) with templates produced using the SM prediction assuming zero signal ($\beta = 0$) and templates produced by varying up/down the uncertainties of the JES1 (top left), JES2 (top right), JES3 (bottom left) and JES4 (bottom right) components. The bottom panels contain the difference between the data and the nominal prediction($\beta = 0$) in black and the difference between the systematic variations and the nominal prediction in green/red.

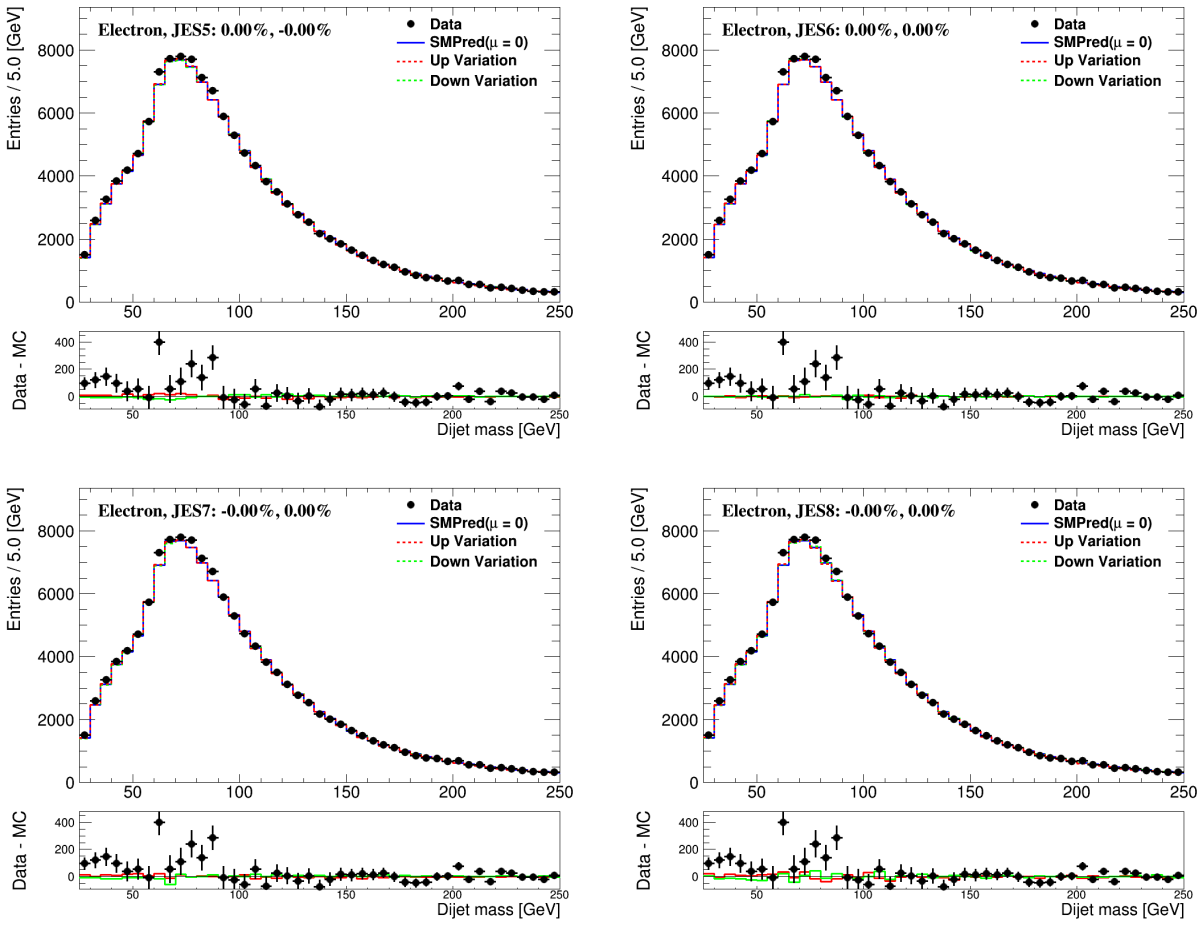

Figure B.6: Electron Channel: Comparison of the m_{jj} templates for data (black dots) with templates produced using the SM prediction assuming zero signal ($\beta = 0$) and templates produced by varying up/down the uncertainties of the JES5 (top left), JES6 (top right), JES7 (bottom left) and JES8 (bottom right) components. The bottom panels contain the difference between the data and the nominal prediction($\beta = 0$) in black and the difference between the systematic variations and the nominal prediction in green/red.

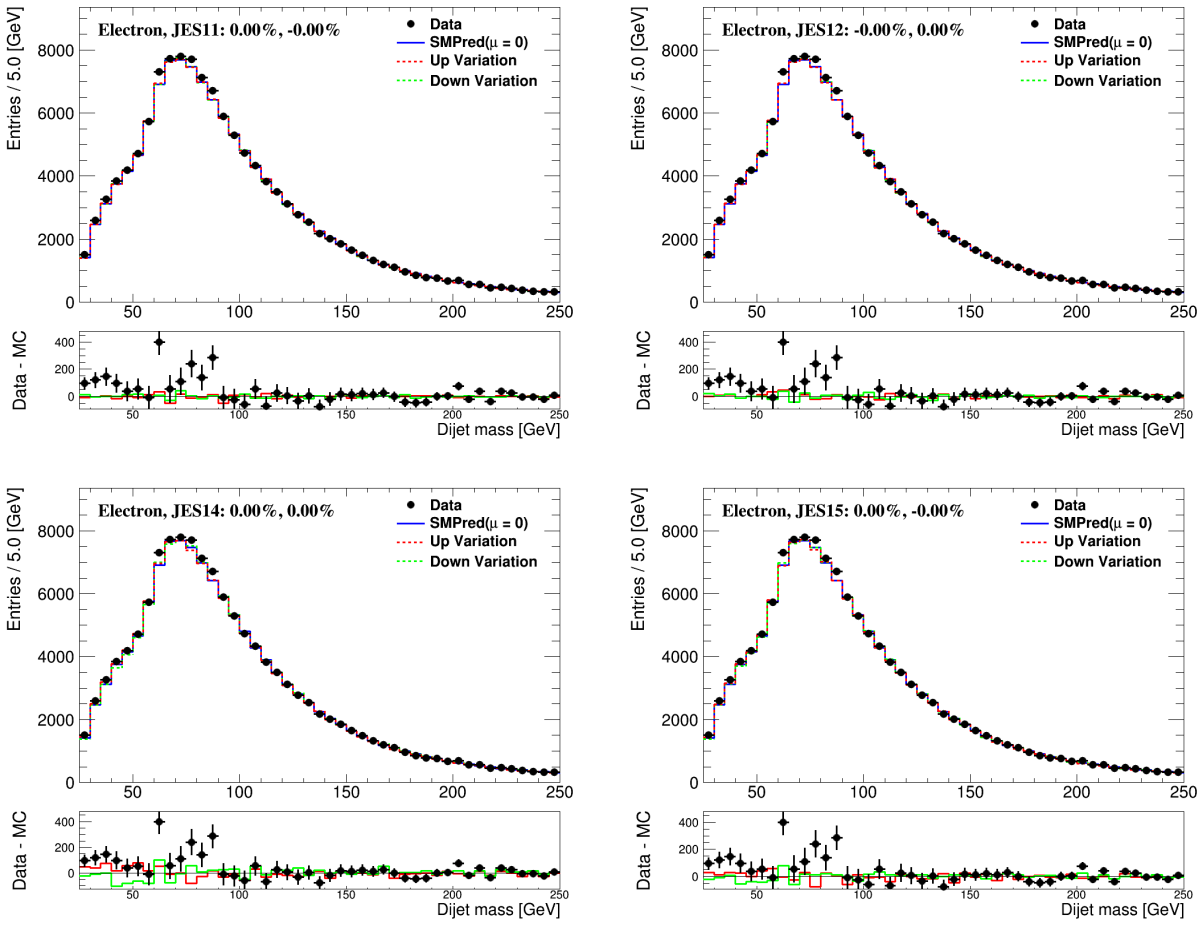

Figure B.7: Electron Channel: Comparison of the m_{jj} templates for data (black dots) with templates produced using the SM prediction assuming zero signal ($\beta = 0$) and templates produced by varying up/down the uncertainties of the JES11 (top left), JES12 (top right), JES14 (bottom left) and JES15 (bottom right) components. The bottom panels contain the difference between the data and the nominal prediction($\beta = 0$) in black and the difference between the systematic variations and the nominal prediction in green/red.

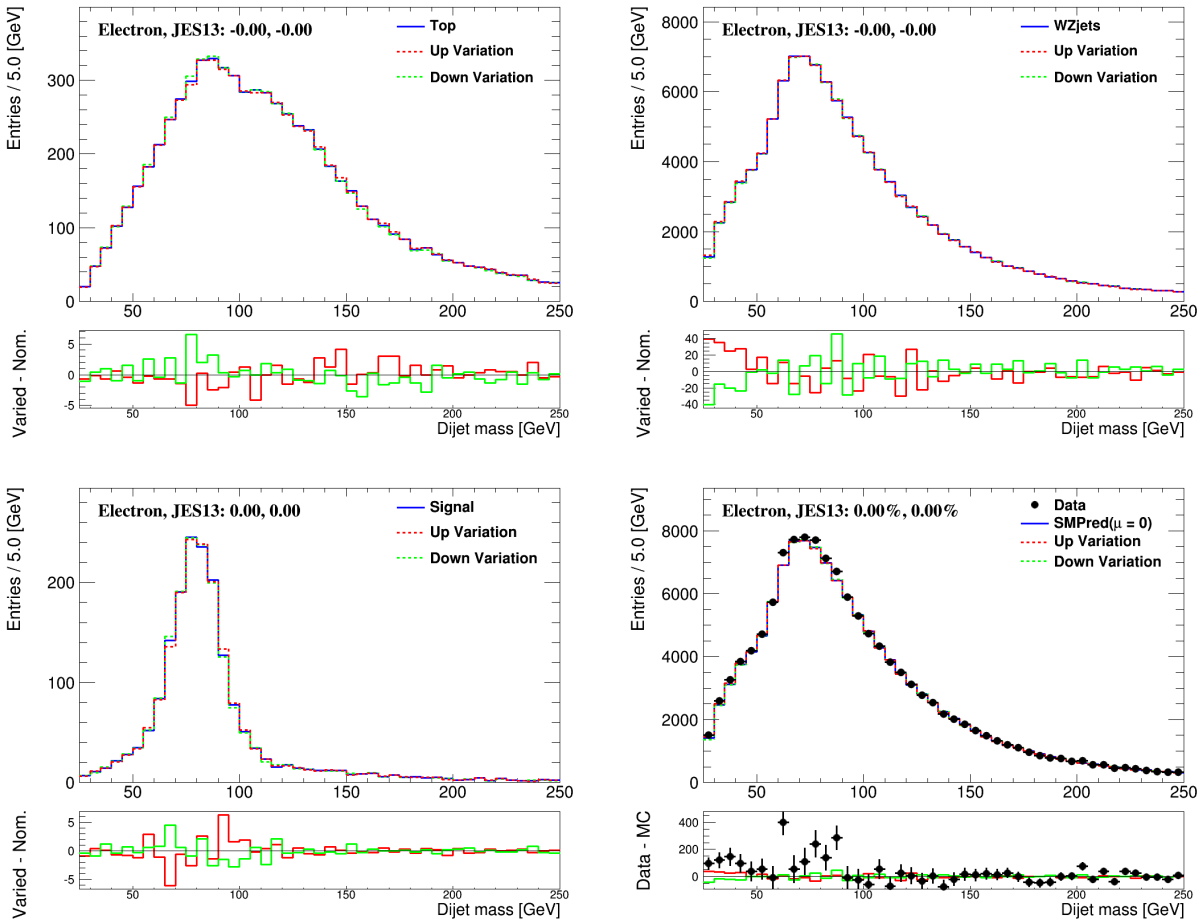

Figure B.8: Electron Channel: m_{jj} templates for the top (top left), W/Z+jets (top right), and Signal (bottom left) processes are shown. For the top panels, the nominal (blue) templates are compared with the up and down systematically varied templates corresponding to the JES13 component. The bottom panels show the difference between each varied template and the nominal template. The bottom right plot contains all the data overlayed by the nominal and varied templates assuming a signal yield of 0 ($\beta = 0$). The bottom panel of the bottom right plot contains the difference between the data and the nominal prediction($\beta = 0$) in black and the difference between the systematic variation and the nominal prediction in green/red.

Muon Channel	**W/Z+jets samples only**			
JES/JER Systematic on Event Yield	$+\sigma$	**% Diff.**	**-σ**	**% Diff.**
Nominal Values	**121016**	**N/A**	**121016**	**N/A**
Effective JES Unc.Component 1	122339	1.1	119627	-1.1
Effective JES Unc.Component 2	118190	-2.3	123890	2.4
Effective JES Unc.Component 3	122472	1.2	119571	-1.2
Effective JES Unc.Component 4	120843	-0.1	121213	0.2
Effective JES Unc.Component 5	121056	0.0	120973	0.0
Effective JES Unc.Component 6	121180	0.1	120835	-0.1
Eta Intercalibration: Stat Unc.	121594	0.5	120450	-0.5
Eta Intercalibration: MC Gen. Modelling Unc.	122008	0.8	120087	-0.8
High Pt jet Uncertainty	121016	0.0	121016	0.0
Closure of the Calib. Uncertainty	121016	0.0	121016	0.0
NPV Pile-up Uncertainty	120901	-0.1	121159	0.1
Mu Pile-up Uncertainty	121091	0.1	120981	0.0
Close-by Jet Uncertainty	121534	0.4	120406	-0.5
Flavor Comp. Uncertainty	128311	6.0	113772	-6.0
Flavor Response Uncertainty	124995	3.3	116971	-3.3
b-jet Uncertainty	121046	0.0	120973	0.0
JER	123509	**2.1**	123509	**2.1**
JES components added in quadrature		**7.5**		**7.5**
JES and JER		**7.8**		**7.8**

Table B.1: Calculated values for the event yield in the muon channel for the W/Z+jets samples after varying the JES components and JER by $\pm\sigma$. % Diff. shows the relative percent difference with respect to the nominal value.

Electron Channel	**W/Z+jets samples only**			
JES/JER Systematic on Event Yield	$+\sigma$	**% Diff.**	$-\sigma$	**% Diff.**
Nominal Values	**112535**	**N/A**	**112535**	**N/A**
Effective JES Unc.Component 1	113683	1.0	111195	-1.2
Effective JES Unc.Component 2	109985	-2.3	115137	2.3
Effective JES Unc.Component 3	113695	1.0	111291	-1.1
Effective JES Unc.Component 4	112333	-0.2	112638	0.1
Effective JES Unc.Component 5	112534	0.0	112504	0.0
Effective JES Unc.Component 6	112655	0.1	112360	-0.2
Eta Intercalibration: Stat Unc.	113040	0.4	111921	-0.5
Eta Intercalibration: MC Gen. Modelling Unc.	113350	0.7	111609	-0.8
High Pt jet Uncertainty	112535	0.0	112535	0.0
Closure of the Calib. Uncertainty	112535	0.0	112535	0.0
NPV Pile-up Uncertainty	112427	-0.1	112513	0.0
Mu Pile-up Uncertainty	112611	0.1	112499	0.0
Close-by Jet Uncertainty	113280	0.7	111727	-0.7
Flavor Comp. Uncertainty	119133	5.9	105877	-5.9
Flavor Response Uncertainty	116085	3.2	108825	-3.3
b-jet Uncertainty	112586	0.0	112495	0.0
JER	113907	**1.2**	113907	**1.2**
JES components added in quadrature		**7.3**		**7.4**
JES and JER		**7.4**		**7.5**

Table B.2: Calculated values for event yields in the electron channel for the W/Z+jets samples after varying the JES components and JER by $\pm\sigma$. % Diff. shows the relative percent difference with respect to the nominal value.

Muon Channel	$t\bar{t}$ + **single top samples only**			
Systematics on Event Yield	$+\sigma$	**% Diff.**	$-\sigma$	**% Diff.**
Nominal Values	**6778**	**N/A**	**6778**	**N/A**
Effective JES Unc.Component 1	6726	-0.8	6833	0.8
Effective JES Unc.Component 2	6911	2.0	6629	-2.2
Effective JES Unc.Component 3	6694	-1.2	6857	1.2
Effective JES Unc.Component 4	6794	0.2	6764	-0.2
Effective JES Unc.Component 5	6773	-0.1	6785	0.1
Effective JES Unc.Component 6	6771	-0.1	6785	0.1
Eta Intercalibration: Stat Unc.	6745	-0.5	6812	0.5
Eta Intercalibration: MC Gen. Modelling Unc.	6629	-2.2	6919	2.1
High Pt jet Uncertainty	6778	0.0	6778	0.0
Closure of the Calib. Uncertainty	6778	0.0	6778	0.0
NPV Pile-up Uncertainty	6787	0.1	6770	-0.1
Mu Pile-up Uncertainty	6768	-0.1	6781	0.1
Close-by Jet Uncertainty	6691	-1.3	6865	1.3
Flavor Comp. Uncertainty	6546	-3.4	7017	3.5
Flavor Response Uncertainty	6655	-1.8	6900	1.8
b-jet Uncertainty	6730	-0.7	6820	0.6
JER	6734	**-0.6**	6734	**-0.6**
JES components added in quadrature		**5.3**		**5.4**
ISR/FSR	7128	**5.2**	7172	**5.8**
JES, JER, and ISR/FSR		**7.4**		**8.0**

Table B.3: Calculated values for event yields in the muon channel for the $t\bar{t}$ + single top samples after varying the JES components and JER by $\pm\sigma$, as well as the rate change due to using samples with varied ISR/FSR parameters. % Diff. shows the relative percent difference with respect to the nominal value.

Electron Channel	$t\bar{t}$ + **single top samples only**			
Systematics on Event Yield	$+\sigma$	**% Diff.**	$-\sigma$	**% Diff.**
Nominal Values	**6736**	**N/A**	**6736**	**N/A**
Effective JES Unc.Component 1	6677	-0.9	6786	0.7
Effective JES Unc.Component 2	6867	1.9	6590	-2.2
Effective JES Unc.Component 3	6647	-1.3	6808	1.1
Effective JES Unc.Component 4	6750	0.2	6719	-0.3
Effective JES Unc.Component 5	6728	-0.1	6743	0.1
Effective JES Unc.Component 6	6729	-0.1	6742	0.1
Eta Intercalibration: Stat Unc.	6699	-0.5	6769	0.5
Eta Intercalibration: MC Gen. Modelling Unc.	6581	-2.3	6871	2.0
High Pt jet Uncertainty	6736	0.0	6736	0.0
Closure of the Calib. Uncertainty	6736	0.0	6736	0.0
NPV Pile-up Uncertainty	6741	0.1	6726	-0.2
Mu Pile-up Uncertainty	6721	-0.2	6741	0.1
Close-by Jet Uncertainty	6643	-1.4	6832	1.4
Flavor Comp. Uncertainty	6503	-3.5	6950	3.2
Flavor Response Uncertainty	6615	-1.8	6845	1.6
b-jet Uncertainty	6690	-0.7	6790	0.8
JER	6614	**-1.8**	6614	**-1.8**
JES components added in quadrature		**5.4**		**5.1**
ISR/FSR	7105	**5.5**	7241	**7.5**
JES, JER, and ISR/FSR		**7.9**		**9.3**

Table B.4: Calculated values for event yields in the electron channel for the $t\bar{t}$ + single top samples after varying the JES components and JER by $\pm\sigma$, as well as the rate change due to using samples with varied ISR/FSR parameters. % Diff. shows the relative percent difference with respect to the nominal value.

B.1.1 Tables for aTGC Selection

Muon Channel	**Signal samples only**			
JES/JER Systematic on Event Yield	$+\sigma$	**% Diff.**	$-\sigma$	**% Diff.**
Nominal Values	**923**	**N/A**	**923**	**N/A**
Effective JES Unc.Component 1	938	1.5	904	-2.1
Effective JES Unc.Component 2	890	-3.7	948	2.6
Effective JES Unc.Component 3	933	1.0	912	-1.3
Effective JES Unc.Component 4	924	0.0	923	0.0
Effective JES Unc.Component 5	921	-0.3	925	0.2
Effective JES Unc.Component 6	926	0.3	920	-0.3
Eta Intercalibration: Stat Unc.	929	0.6	917	-0.6
Eta Intercalibration: MC Gen. Modelling Unc.	936	1.3	905	-2.0
High Pt jet Uncertainty	923	0.0	923	0.0
Closure of the Calib. Uncertainty	923	0.0	923	0.0
NPV Pile-up Uncertainty	918	-0.6	923	-0.1
Mu Pile-up Uncertainty	918	-0.5	922	-0.2
Close-by Jet Uncertainty	930	0.7	914	-1.0
Flavor Comp. Uncertainty	975	5.6	822	-11.0
Flavor Response Uncertainty	962	4.1	871	-5.6
b-jet Uncertainty	923	0.0	923	-0.1
JER	860	**-6.9**	860	**-6.9**
JES components added in quadrature		**8.3**		**13.1**
JES and JER		**10.8**		**14.8**

Table B.5: Calculated values for the aTGC event selection in the muon channel for the signal samples after varying the JES components and JER by $\pm\sigma$. % Diff. shows the relative percent difference with respect to the nominal value.

Electron Channel	**Signal samples only**			
JES/JER Systematic on Event Yield	$+\sigma$	**% Diff.**	**-σ**	**% Diff.**
Nominal Values	**811**	**N/A**	**811**	**N/A**
Effective JES Unc.Component 1	824	1.6	796	-1.8
Effective JES Unc.Component 2	782	-3.6	834	2.8
Effective JES Unc.Component 3	820	1.2	798	-1.5
Effective JES Unc.Component 4	810	-0.1	809	-0.2
Effective JES Unc.Component 5	807	-0.4	812	0.2
Effective JES Unc.Component 6	813	0.3	806	-0.5
Eta Intercalibration: Stat Unc.	817	0.8	805	-0.7
Eta Intercalibration: MC Gen. Modelling Unc.	821	1.3	792	-2.2
High Pt jet Uncertainty	811	0.0	811	0.0
Closure of the Calib. Uncertainty	811	0.0	811	0.0
NPV Pile-up Uncertainty	808	-0.3	810	-0.1
Mu Pile-up Uncertainty	805	-0.6	804	-0.8
Close-by Jet Uncertainty	819	1.0	805	-0.7
Flavor Comp. Uncertainty	860	6.1	711	-12.3
Flavor Response Uncertainty	846	4.3	759	-6.3
b-jet Uncertainty	811	0.1	811	0.0
JER	757	**-6.6**	757	**-6.6**
JES components added in quadrature		**8.7**		**14.6**
JES and JER		**11.0**		**16.0**

Table B.6: Calculated values for aTGC event selection in the electron channel for the Signal samples after varying the JES components and JER by $\pm\sigma$. % Diff. shows the relative percent difference with respect to the nominal value.

Muon Channel	**W/Z+jets samples only**			
JES/JER Systematic on Event Yield	$+\sigma$	**% Diff.**	$-\sigma$	**% Diff.**
Nominal Values	**26250**	**N/A**	**26250**	**N/A**
Effective JES Unc.Component 1	26531	1.1	25930	-1.2
Effective JES Unc.Component 2	25556	-2.6	26869	2.4
Effective JES Unc.Component 3	26642	1.5	25837	-1.6
Effective JES Unc.Component 4	26211	-0.1	26298	0.2
Effective JES Unc.Component 5	26241	0.0	26240	0.0
Effective JES Unc.Component 6	26303	0.2	26196	-0.2
Eta Intercalibration: Stat Unc.	26393	0.5	26054	-0.7
Eta Intercalibration: MC Gen. Modelling Unc.	26480	0.9	25994	-1.0
High Pt jet Uncertainty	26250	0.0	26250	0.0
Closure of the Calib. Uncertainty	26250	0.0	26250	0.0
NPV Pile-up Uncertainty	26179	-0.3	26256	0.0
Mu Pile-up Uncertainty	26248	0.0	26209	-0.2
Close-by Jet Uncertainty	26334	0.3	26130	-0.5
Flavor Comp. Uncertainty	27728	5.6	24691	-5.9
Flavor Response Uncertainty	27070	3.1	25349	-3.4
b-jet Uncertainty	26265	0.1	26234	-0.1
JER	26433	**0.7**	26433	**0.7**
JES components added in quadrature		**7.3**		**7.6**
JES and JER		**7.3**		**7.7**

Table B.7: Calculated values for the aTGC event selection in the muon channel for the W/Z+jets samples after varying the JES components and JER by $\pm\sigma$. % Diff. shows the relative percent difference with respect to the nominal value.

Electron Channel	**W/Z+jets samples only**			
JES/JER Systematic on Event Yield	$+\sigma$	**% Diff.**	$-\sigma$	**% Diff.**
Nominal Values	**23776**	**N/A**	**23776**	**N/A**
Effective JES Unc.Component 1	23895	0.5	23537	-1.0
Effective JES Unc.Component 2	23198	-2.4	24173	1.7
Effective JES Unc.Component 3	24009	1.0	23501	-1.2
Effective JES Unc.Component 4	23726	-0.2	23818	0.2
Effective JES Unc.Component 5	23803	0.1	23767	0.0
Effective JES Unc.Component 6	23792	0.1	23759	-0.1
Eta Intercalibration: Stat Unc.	23863	0.4	23689	-0.4
Eta Intercalibration: MC Gen. Modelling Unc.	23863	0.4	23584	-0.8
High Pt jet Uncertainty	23776	0.0	23776	0.0
Closure of the Calib. Uncertainty	23776	0.0	23776	0.0
NPV Pile-up Uncertainty	23742	-0.1	23764	-0.1
Mu Pile-up Uncertainty	23728	-0.2	23648	-0.5
Close-by Jet Uncertainty	23893	0.5	23616	-0.7
Flavor Comp. Uncertainty	24842	4.5	22325	-6.1
Flavor Response Uncertainty	24271	2.1	22971	-3.4
b-jet Uncertainty	23778	0.0	23766	0.0
JER	23740	**-0.2**	23740	**-0.2**
JES components added in quadrature		**5.7**		**7.4**
JES and JER		**5.7**		**7.4**

Table B.8: Calculated values for aTGC event selection in the electron channel for the W/Z+jets samples after varying the JES components and JER by $\pm\sigma$. % Diff. shows the relative percent difference with respect to the nominal value.

Muon Channel	$t\bar{t}$ + **single top samples only**			
Systematics on Event Yield	$+\sigma$	**% Diff.**	$-\sigma$	**% Diff.**
Nominal Values	**1284**	**N/A**	**1284**	**N/A**
Effective JES Unc.Component 1	1266.46	-1.4	1306.1	1.7
Effective JES Unc.Component 2	1320.91	2.9	1250.21	-2.6
Effective JES Unc.Component 3	1271.26	-1.0	1299.92	1.2
Effective JES Unc.Component 4	1284.58	0.0	1283.41	-0.1
Effective JES Unc.Component 5	1286.1	0.1	1282.51	-0.1
Effective JES Unc.Component 6	1281.31	-0.2	1287.2	0.2
Eta Intercalibration: Stat Unc.	1276.76	-0.6	1293.45	0.7
Eta Intercalibration: MC Gen. Modelling Unc.	1248.05	-2.8	1321.71	2.9
High Pt jet Uncertainty	1284.2	0.0	1284.2	0.0
Closure of the Calib. Uncertainty	1284.2	0.0	1284.2	0.0
NPV Pile-up Uncertainty	1284.56	0.0	1284.25	0.0
Mu Pile-up Uncertainty	1284.61	0.0	1290.08	0.5
Close-by Jet Uncertainty	1260.37	-1.9	1309.65	2.0
Flavor Comp. Uncertainty	1233.45	-4.0	1330.1	3.6
Flavor Response Uncertainty	1257.56	-2.1	1312.22	2.2
b-jet Uncertainty	1261.3	-1.8	1307.97	1.9
JER	1266.27	**-1.4**	1266.27	**-1.4**
JES components added in quadrature		**6.8**		**6.8**
ISR/FSR	1346.52	**4.9**	1333.51	**3.8**
JES, JER, and ISR/FSR		**8.5**		**7.9**

Table B.9: Calculated values for aTGC event selection in the muon channel for the $t\bar{t}$ + single top samples after varying the JES components and JER by $\pm\sigma$, as well as the rate change due to using samples with varied ISR/FSR parameters. % Diff. shows the relative percent difference with respect to the nominal value.

Electron Channel	$t\bar{t}$ + **single top samples only**			
Systematics on Event Yield	$+\sigma$	**% Diff.**	**-σ**	**% Diff.**
Nominal Values	**1272**	**N/A**	**1272**	**N/A**
Effective JES Unc.Component 1	1251	-1.7	1294	1.7
Effective JES Unc.Component 2	1308	2.8	1240	-2.6
Effective JES Unc.Component 3	1258	-1.2	1284	0.9
Effective JES Unc.Component 4	1272	0.0	1272	0.0
Effective JES Unc.Component 5	1272	0.0	1272	-0.1
Effective JES Unc.Component 6	1270	-0.2	1275	0.2
Eta Intercalibration: Stat Unc.	1264	-0.7	1280	0.6
Eta Intercalibration: MC Gen. Modelling Unc.	1239	-2.6	1308	2.8
High Pt jet Uncertainty	1272	0.0	1272	0.0
Closure of the Calib. Uncertainty	1272	0.0	1272	0.0
NPV Pile-up Uncertainty	1271	-0.1	1275	0.2
Mu Pile-up Uncertainty	1268	-0.3	1281	0.7
Close-by Jet Uncertainty	1246	-2.1	1303	2.4
Flavor Comp. Uncertainty	1227	-3.6	1312	3.1
Flavor Response Uncertainty	1249	-1.8	1298	2.0
b-jet Uncertainty	1251	-1.7	1299	2.1
JER	1241	**-2.4**	1241	**-2.4**
JES components added in quadrature		**6.5**		**6.5**
ISR/FSR	1349	**6.1**	1354	**6.4**
JES, JER, and ISR/FSR		**9.2**		**9.4**

Table B.10: Calculated values for aTGC event selection in the electron channel for the $t\bar{t}$ + single top samples after varying the JES components and JER by $\pm\sigma$, as well as the rate change due to using samples with varied ISR/FSR parameters. % Diff. shows the relative percent difference with respect to the nominal value.

B.2 Additional Systematic Distributions

This section contains additional distributions and comparisons related to non−JES/JER systematics that were discussed in chapter 7.

- Figures B.9 and B.10 shows the E_T^{miss} and m_{jj} distributions compared with data in the QCD systematic CR discussed in section 7.4.

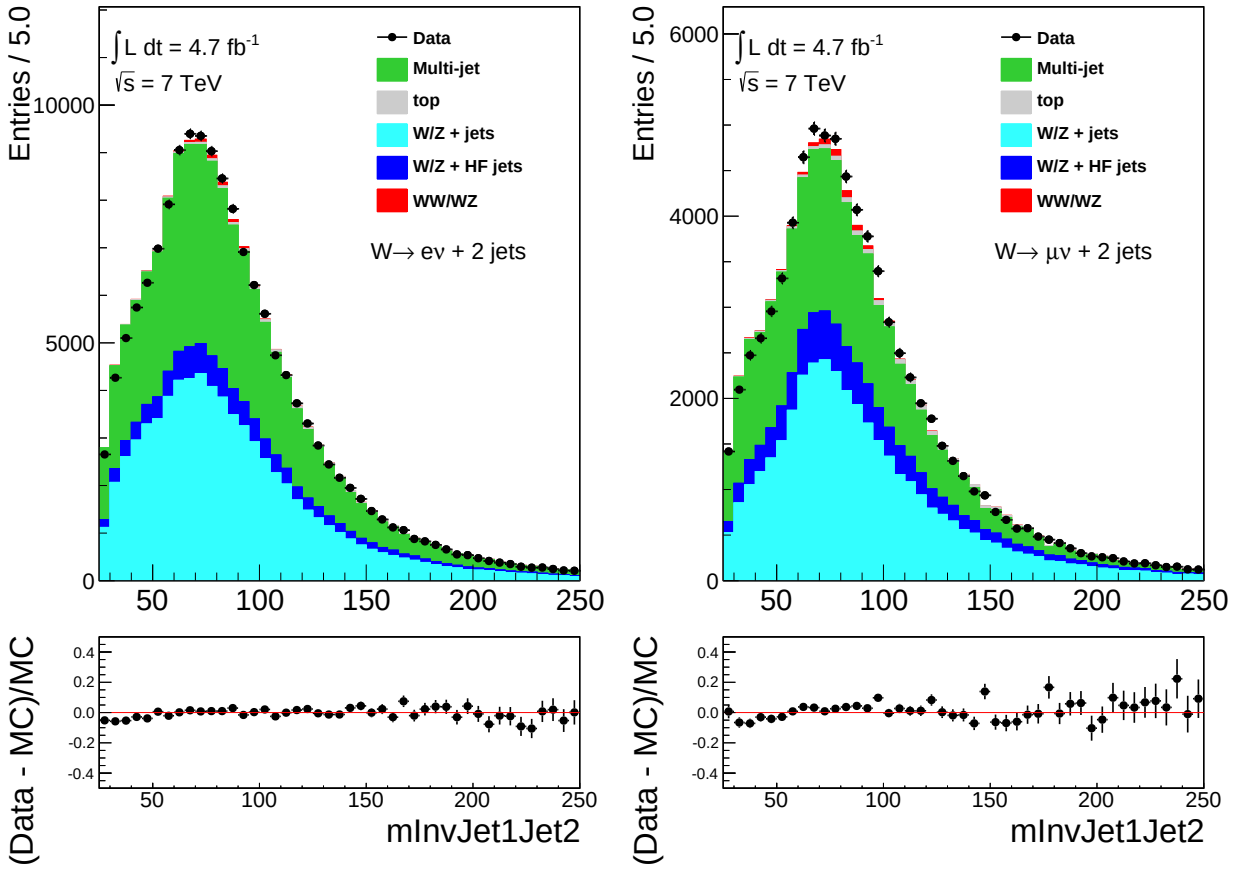

Figure B.9: Comparison of the m_{jj} distributions for data (solid circles) and MC (histograms) for the electron (left) and muon (right) channel after applying the QCD systematic CR selection discussed in section 7.4. The lower panel shows the percent difference between data and the MC prediction with respect to th MC (solid circles).

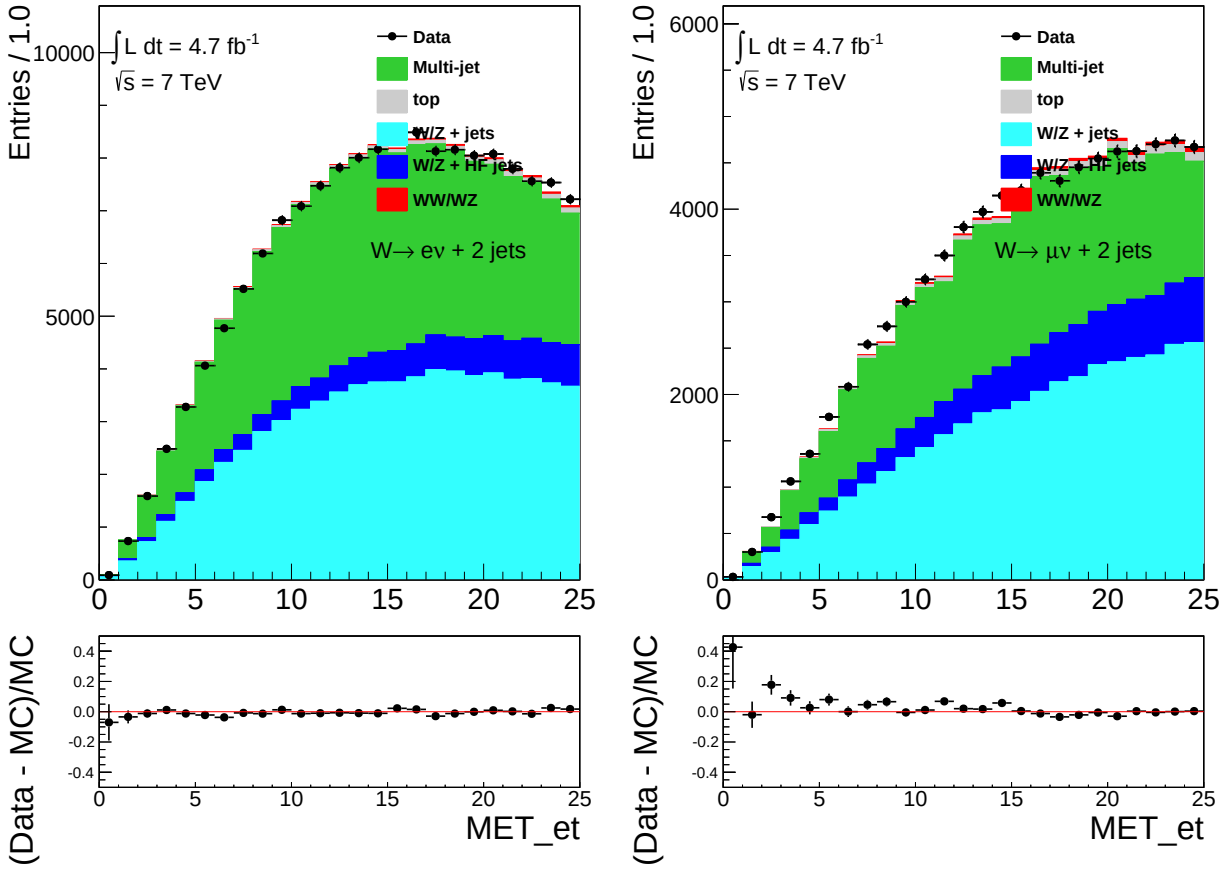

Figure B.10: Comparison of the E_T^{miss} distributions for data (solid circles) and MC (histograms) for the electron (left) and muon (right) channel after applying the QCD systematic CR selection discussed in section 7.4. The lower panel shows the percent difference between data and the MC prediction with respect to th MC (solid circles).

Appendix C

Tables for the Fiducial Cross Section Calculation and Corresponding Signal Systematics

This appendix contains many tables showing the values used to calculate the A and C fiducial efficiencies and the corresponding JES, JER and fragmentation/ISR-FSR systematics. A short description for the varying tables is shown below for easy navigation.

- Table C.1 and table C.2 show the raw values used to calculate the fiducial acceptance and reconstruction correction factor for the muon and electron channel respectively. These values go into the equation to calculate D_{fid} and D_{tot} , and then eventually into the fiducial cross section calculation.
- Table C.3 shows the calculated D_{fid} and D_{tot} values for both lepton channels.
- Table C.4 shows the fiducial truth selection cutflow for both lepton channels.
- Table C.5 shows the calculated D_{fid} and D_{tot} values used to determine the jet veto scale dependence systematic for the signal as described in section 7.5.4.
- Table C.6 shows the raw values used to calculate the fiducial acceptance and reconstruction correction factor for the muon and electron channel using HERWIG AND PYTHIA signal samples. This is used to estimate the normalization uncertainty from fragmentation in the signal(see section 7.5.2).

Muon Channel						
Sample(MC@NLO)	N_{Gen}	$N_{Gen}^{WW\to\mu\nu jj}$	N_{fid}^{truth}	N_{fid}^{reco}	A	C
SM WW	1053481.6	153796.2 ± 488.9	12462.6 ± 137.7	8381.2 ± 112.7	0.081 ± 0.001	0.673 ± 0.009
SM WmZ	735937.5	55590.8 ± 286.9	4867.6 ± 85.5	3590.6 ± 72.8	0.088 ± 0.001	0.738 ± 0.015
SM WpZ	739953.0	55664.0 ± 286.6	4710.7 ± 82.2	3263.3 ± 69.1	0.085 ± 0.001	0.693 ± 0.014
aTGC WW	418464.5	60828.1 ± 279.4	4889.6 ± 74.8	3343.0 ± 60.5	0.080 ± 0.001	0.684 ± 0.012
aTGC WmZ	221932.5	16657.7 ± 135.4	1507.6 ± 38.2	1120.9 ± 32.5	0.091 ± 0.002	0.743 ± 0.021
aTGC WpZ	194921.2	14671.0 ± 121.9	1213.5 ± 34.4	905.9 ± 30.4	0.083 ± 0.002	0.747 ± 0.024
SM+aTGC WW	1471946.1	214624.2 ± 563.1	17352.2 ± 156.7	11724.23 ± 128.0	0.081 ± 0.001	0.676 ± 0.007
SM+aTGC WmZ	957870.0	72248.5 ± 317.2	6375.3 ± 93.7	4711.464 ± 79.8	0.088 ± 0.001	0.739 ± 0.012
SM+aTGC WpZ	934874.2	70335.1 ± 311.5	5924.3 ± 89.1	4169.206 ± 75.5	0.084 ± 0.001	0.704 ± 0.012

Table C.1: The table shows the values used to calculate the A and C efficiencies for the nominal MC@NLO signal sample in the muon channel. Where N_{Gen} is the total number of generated events in the sample, $N_{Gen}^{WW\to\mu\nu jj}$ is the total number of generated events that also have a true WW$\to \mu\nu$jj decay, and N_{fid} is the total number of events that pass the fiducial event selection at the truth and reconstruction level. For the variables N_{Gen},$N_{Gen}^{WW\to\mu\nu jj}$, and N_{fid}^{truth} the events are weighted by the MC event weight and Z vertex position weight. In the case of the aTGC samples, they are additionally reweighted to SM values using the MC@NLO reweighting scheme. The variable N_{fid}^{reco} contains all additional event weights used for all final event selection at reconstruction level. The uncertainities on the values just contain the statistical uncertainty.

Electron Channel						
Sample(MC@NLO)	N_{Gen}	$N_{Gen}^{WW\to e\nu jj}$	N_{fid}^{truth}	N_{fid}^{reco}	A	C
SM WW	1053481.6	153172.2 ± 487.6	12200.7 ± 137.1	7453.0 ± 107.8	0.080 ± 0.001	0.611 ± 0.008
SM WmZ	735937.5	55283.7 ± 286.8	4828.1 ± 84.7	3190.6 ± 69.0	0.087 ± 0.001	0.661 ± 0.014
SM WpZ	739953.0	56052.7 ± 287.2	4604.0 ± 81.1	3056.8 ± 67.1	0.082 ± 0.001	0.664 ± 0.014
aTGC WW	418464.5	61032.5 ± 278.4	4867.6 ± 75.6	3023.1 ± 59.3	0.080 ± 0.001	0.621 ± 0.012
aTGC WmZ	221932.5	16721.8 ± 129.7	1518.4 ± 36.5	1002.0 ± 29.8	0.091 ± 0.002	0.660 ± 0.019
aTGC WpZ	194921.2	14661.6 ± 121.7	1200.9 ± 33.3	778.1 ± 25.9	0.082 ± 0.002	0.648 ± 0.022
SM+aTGC WW	1471946.1	214204.7 ± 561.5	17068.2 ± 156.6	10476.1 ± 123.0	0.080 ± 0.001	0.614 ± 0.007
SM+aTGC WmZ	957870.0	72005.6 ± 314.7	6346.5 ± 92.2	4192.6 ± 75.2	0.088 ± 0.001	0.661 ± 0.012
SM+aTGC WpZ	934874.2	70714.3 ± 311.9	5804.9 ± 87.7	3834.9 ± 71.9	0.082 ± 0.001	0.661 ± 0.012

Table C.2: The table shows the values used to calculate the A and C efficiencies for the nominal MC@NLO signal sample in the electron channel. Where N_{Gen} is the total number of generated events in the sample, $N_{Gen}^{WW\to e\nu jj}$ is the total number of generated events that also have a true WW$\to e\nu$jj decay, and N_{fid} is the total number of events that pass the fiducial event selection at the truth and reconstruction level. For the variables N_{Gen},$N_{Gen}^{WW\to\mu\nu jj}$, and N_{fid}^{truth} the events are weighted by the MC event weight and Z vertex position weight. In the case of the aTGC samples, they are additionally reweighted to SM values using the MC@NLO reweighting scheme. The variable N_{fid}^{reco} contains all additional event weights used for all final event selection at reconstruction level. The uncertainities on the values just contain the statistical uncertainty.

	MC@NLO SM Only	MC@NLO aTGC Only	MC@NLO SM+aTGC
Muon			
D_{fid}	0.679	0.695	0.683
D_{tot}	6.99E-03	7.08E-03	7.01E-03
Electron			
D_{fid}	0.620	0.627	0.622
D_{tot}	6.26E-03	6.36E-03	6.29E-03

Table C.3: Table shows the calculated values for D_{fid} and D_{tot} in both channels. Values are calculated for SM and aTGC samples separately and then combined.

	Muon Channel Cutflow			**Electron Channel Cutflow**		
	SM WW	SM WmZ	SM WpZ	SM WW	SM WmZ	SM WpZ
True lvjj Event	100	100	100	100	100	100
Dressed Lepton, $p_T > 25$ GeV, $\|\eta\| < 2.47$	66.6	69.4	63.8	66.2	68.9	63.8
True $E_T^{miss} > 30$ GeV	42.3	44.2	40.9	42.2	44.0	40.8
≥ 2 Jets, $p_T > 25$ GeV, $\|\eta\| < 2.8$, no overlap	22.1	27.2	25.9	21.8	27.1	25.5
$M_T > 40$ GeV	19.8	24.0	22.8	19.5	24.1	22.5
Leading Jet, $p_T > 30$ GeV, $\|\eta\| < 2.0$	16.7	20.2	19.5	16.4	20.4	19.1
Sub-leading Jet, $p_T > 25$ GeV, $\|\eta\| < 2.0$	14.4	17.7	16.9	14.3	17.8	16.7
$\|\Delta\phi(E_T^{miss}, Jet_1)\| > 0.8$	13.2	16.2	15.6	13.1	16.4	15.3
$\|\Delta\eta(Jet_1, Jet_2)\| < 1.5$	11.3	13.7	13.3	11.2	13.9	13.0
$\Delta R(Jet_1, Jet_2) > 0.7$ || $p_T(jj) > 250$ GeV	10.9	13.3	12.9	10.9	13.5	12.7
Jet Multiplicity == 2	8.2	8.9	8.6	8.1	9.0	8.4

Table C.4: Table shows the event cutflow(in relative percentage to the total lvjj events) for the truth selection on the SM samples for both channels. Events are only weighted by the MC event weight, this differs from table C.1 and table C.2 which are weighted by the MC event weight and Z vertex event weight.

	MC@NLO, Nominal	MC@NLO, No Veto	HERWIG, Nominal	HERWIG, No Veto
Muon Channel				
D_{tot}	6.99E-03	9.75E-03	8.27E-03	1.10E-03
Electron Channel				
D_{tot}	6.26E-03	8.93E-03	7.63E-03	1.02E-03

Table C.5: Table shows the calculated values for D_{tot} for the nominal selection and the nominal selection without applying the 3rd jet veto in both channels. HERWIG values are computed using the same branching ratios as the MC@NLO samples in order to remove differences in how the samples were originally generated since the HERWIG samples were generated with an event filter and the MC@NLO samples were not.

Muon Channel						
Sample	N_{Gen}	$N_{Gen}^{WW\to\mu\nu jj}$	N_{fid}^{truth}	N_{fid}^{reco}	A	C
WW Herwig	2471197.8	813710.1 ± 945.2	73973.9 ± 285.0	52241.1 ± 239.1	0.091 ± 0.000	0.706 ± 0.003
WZ Herwig	990826.9	212243.6 ± 482.6	20922.7 ± 151.6	15476.8 ± 130.5	0.099 ± 0.001	0.740 ± 0.006
WW Pythia	397598.6	130528.3 ± 378.7	11932.5 ± 114.5	8777.8 ± 98.1	0.091 ± 0.001	0.736 ± 0.008
WZ Pythia	397602.2	87117.2 ± 309.3	8575.3 ± 97.0	6589.7 ± 85.1	0.098 ± 0.001	0.768 ± 0.010
Electron Channel						
Sample	N_{Gen}	$N_{Gen}^{WW\to e\nu jj}$	N_{fid}^{truth}	N_{fid}^{reco}	A	C
WW Herwig	2471197.8	810639.6 ± 943.5	73610.8 ± 284.4	48104.9 ± 231.8	0.091 ± 0.000	0.654 ± 0.003
WZ Herwig	990826.9	209851.8 ± 479.7	21048.7 ± 151.9	14187.7 ± 125.8	0.100 ± 0.001	0.674 ± 0.006
WW Pythia	397598.6	129176.4 ± 376.8	11785.7 ± 113.7	8072.2 ± 94.7	0.091 ± 0.001	0.685 ± 0.008
WZ Pythia	397602.2	86515.7 ± 308.3	8501.1 ± 96.7	5744.3 ± 79.9	0.098 ± 0.001	0.676 ± 0.009

Table C.6: The table shows the values used to calculate the A and C efficiencies for the HERWIG and PYTHIA systematic signal sample in the muon and electron channel. Where N_{Gen} is the total number of generated events in the sample, $N_{Gen}^{WW\to\mu\nu jj}$ is the total number of generated events that also have a true WW→ lνjj decay, and N_{fid} is the total number of events that pass the fiducial event selection at the truth and reconstruction level. For the variables N_{Gen},$N_{Gen}^{WW\to l\nu jj}$, and N_{fid}^{truth} the events are weighted by the MC event weight and Z vertex position weight. The variable N_{fid}^{reco} contains all additional event weights used for all final event selection at reconstruction level. The uncertainities on the values just contain the statistical uncertainty.

Appendix D

Additional Studies

D.1 Jet Vertex Fraction Study

The Jet Vertex Fraction(JVF) jet variable is an important variable in distinguishing jets coming from the primary vertex and those coming from pile-up interactions. The JVF is defined as the sum p_T of all jet-matched tracks from a given primary vertex divided by the sum of the total jet-matched track p_T. A JVF close to 1 means the majority of jet-matched tracks originate from the primary vertex, while a JVF value close to 0 signifies that the matched tracks do not. A JVF value equal to -1 is given to jets in which there are an insufficient number of tracks matched to it. The standard requirement used to reject jets coming from pile-up interactions is $|JVF| > 0.75$. This study calculates the efficiency of the JVF cut as a function of the jet η using a tag-and-probe method in the muon channel. The selection criteria for the tag jet is defined below:

- Require the event to pass the muon triggers, see section 5.2.
- Require at least 1 good primary vertex, see section 5.4.
- Require exactly 1 muon passing object selection with $p_T > 20GeV$.
- Require $E_T^{\text{miss}} > 25$ GeV
- Pass the LAr Hole simple veto, see section 5.4.
- Require there to be only 1 jet passing object selection with a $p_T > 15GeV$ and $|eta| < 4.5$.
- Jet $p_T > 30GeV$ and $|eta| < 2.8$.
- Jet JVF != 1, ignore jets which do not contain enough matched tracks in their reconstruction.
- $\Delta\phi(W(\mu,\nu), Jet) > 165^\circ$

This criteria selects well balanced back-to-back W+1 jet events which can be used to access the JVF efficiency. The JVF efficiency is calculated by the ratio of tag jets passing the JVF

cut over the number of total tag jets. The JVF efficiency as a function of η for data and MC is shown on figure D.1, as well as the ratio of between the data and MC efficiencies. In conclusion, the JVF cut is shown to be 95% efficient out to an $|\eta| < 2.5$ and the JVF efficiency in data is modeled very well in MC and no correction scale factor is required.

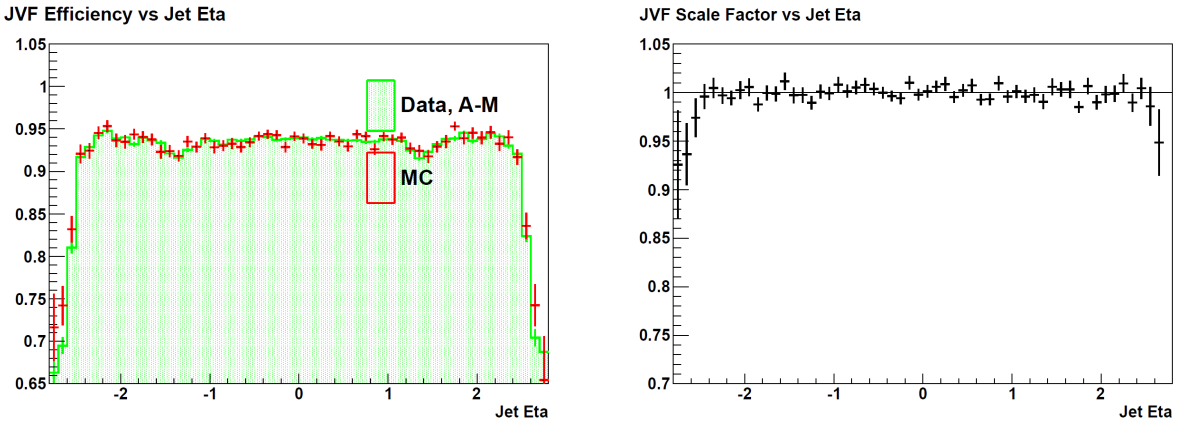

Figure D.1: Left:Efficiency of the JVF cut as a function of the jet η for data and MC. Right: Ratio between the data and MC JVF efficiencies.

D.2 Further Studies on the QCD Contribution

Electroweak Contribution to the QCD Shape for the Dijet Mass

This section looks at the electroweak contribution to the QCD shape for the dijet mass distribution after applying the event selection for the cross section measurement. The electroweak contribution that passes the QCD event selection criteria described in section 5.5.1 is subtracted from the data in order to get the shape for the QCD background. Figure D.2 shows the events passing the QCD selection prior to this substraction. The percentage of electroweak events in the data is shown in table D.1 (approximity 40%) and a breakdown of the electroweak contribution is shown in table D.2. The final QCD normalization is derived from a likelihood fit to the E_T^{miss} , described in section 5.5.1.

Figure D.3 shows the events passing the QCD systematic CR selection(sec 7.4) prior to the EWK substraction. The percentage of electroweak events in the data passing the QCD systematic CR is shown in table D.3 (approximately 5%).

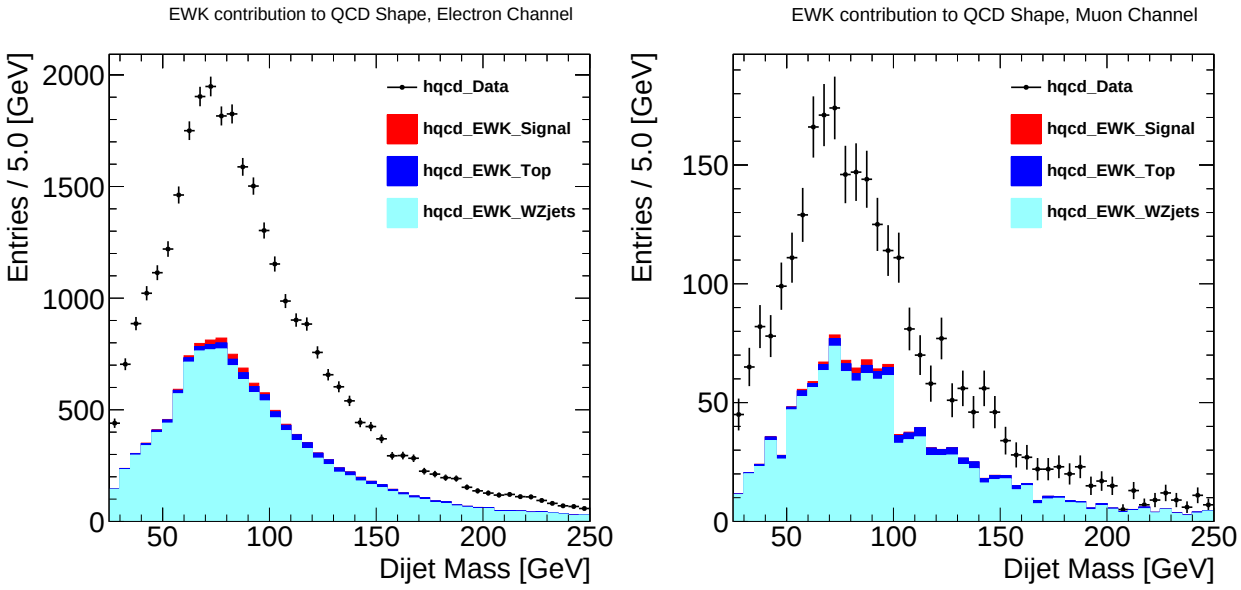

Figure D.2: Distributions of the dijet invariant mass m_{jj} for events passing the QCD selection criteria for electron (left) and muon (right) channels. The points are data and the stacked histograms are SM predictions.

Stability of E_T^{miss} fit as a function of the Dijet Mass

The likelihood fit to E_T^{miss} distribution(no E_T^{miss} cut applied) that is used to calculate the multijet contribution in the signal region is compared with doing the fit in three separate regions of the dijet mass distribution in order to see if the fit returns consistent normalizations

Electroweak Contribution to QCD Shape			
Lepton Channel	Data	Electroweak	Electroweak Percentage
Muon	2773	1209	44%
Electron	31148	12867	41%

Table D.1: This table shows the total number of events passing the QCD selection in Data and all electroweak processes for the cross section selection. The percentage of the electroweak contribution with respect to data is also shown.

Electroweak Contribution Breakdown to QCD Shape			
Lepton Channel	Signal(%)	Top (%)	$W/Z + jets$ (%)
Muon	1.4	6.2	92.4%
Electron	1.5	4.7	93.9%

Table D.2: This table shows the breakdown of the electroweak events that pass the QCD selection for the cross section selection. All values shown are in percentages of the total electroweak contribution.

as a function of m_{jj} . Figure D.4 shows this comparison for regions: $m_{\mathrm{jj}} < 60$ GeV, 60 GeV $< m_{\mathrm{jj}} < 110$ GeV, and $m_{\mathrm{jj}} > 110$ GeV. The error bars represent the uncertainty given by the likelihood fit and show good agreement between regions.

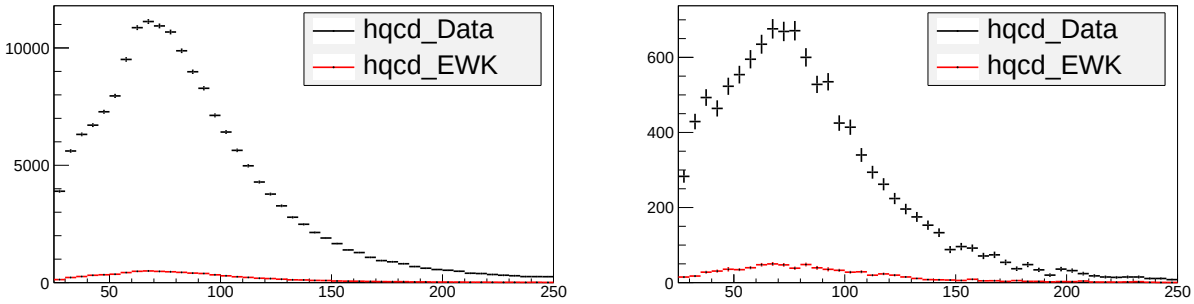

Figure D.3: Distributions of the dijet invariant mass m_{jj} for events passing the QCD systematic CR selection(sec 7.4) criteria for electron (left) and muon (right) channels. The points are data and the stacked histograms are SM predictions.

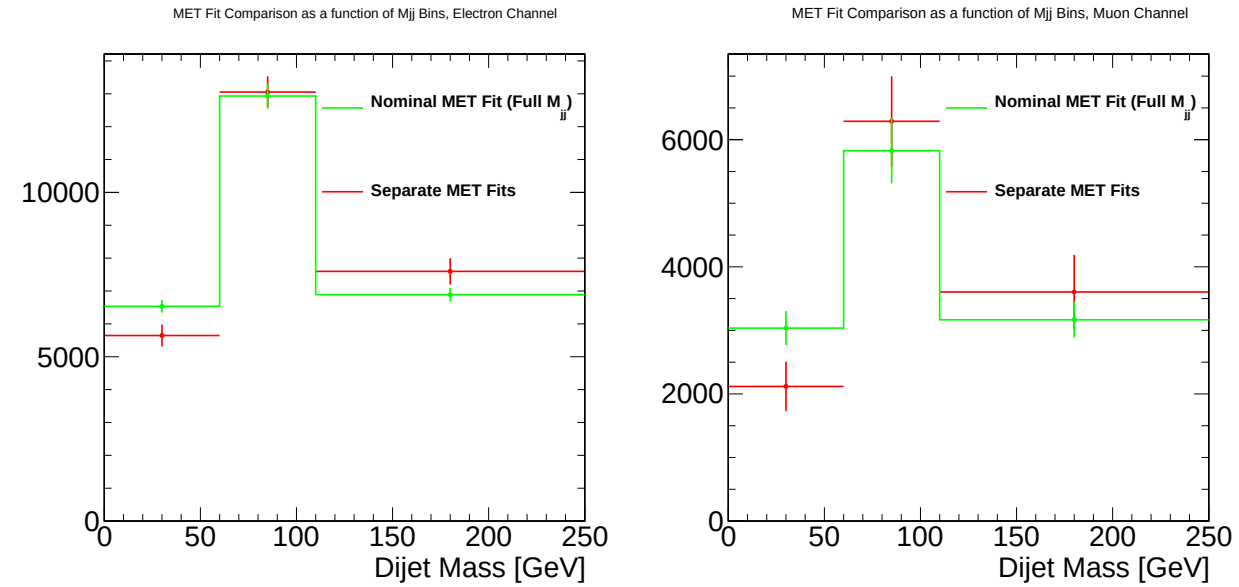

Figure D.4: Distributions of the multijet normalization returned by the likelihood fit to the full E_T^{miss} distribution for the electron (left) and muon (right) channels are compared between the normalization returned by the nominal fit(green) to the full dijet mass distribution and the normalization returned for separate regions(red) of the dijet mass distribution. The error bars represent only the uncertainties given by the likelihood fit.

Electroweak Contribution to QCD Systematic CR Shape			
Lepton Channel	Data	Electroweak	Electroweak Percentage
Muon	11084	771	7%
Electron	176243	7830	4%

Table D.3: This table shows the total number of events passing the QCD systematic CR selection(sec 7.4) in Data and all electroweak processes for the cross section selection. The percentage of the electroweak contribution with respect to data is also shown.

D.3 Tables of Systematics for the aTGC Analysis

Syst	Bin Number 1	2	3	4	5	6	7	8	9	10	11	12	13	14
Signal														
Total	15	16	21	24	21	23	29	28	48	36	38	34	28	35
MC Stat	1	3	8	11	7	7	13	8	8	18	17	13	11	11
Signal Norm.	15	15	15	15	15	15	15	15	15	15	15	15	15	15
Renorm/Fact Scales	1	3	7	7	8	9	10	11	12	13	13	14	15	18
JER	0	4	9	9	1	3	2	6	30	13	22	11	8	16
JES1	0	0	2	1	3	2	3	7	7	8	3	12	3	15
JES2	0	1	2	3	1	2	0	9	5	1	1	6	3	5
JES3	0	2	3	2	4	3	4	5	10	4	5	6	4	1
JES13	0	1	2	3	5	0	15	5	20	6	16	6	5	1
JES14	0	2	2	9	5	10	8	11	14	16	0	11	7	7
JES15	0	1	3	2	6	6	5	7	14	7	4	10	6	5
Background														
Total	18	18	45	41	42	45	44	45	41	45	69	51	52	54
MC Stat	0	2	9	15	4	29	33	6	8	8	51	11	14	10
Δ R	0	2	39	34	36	28	24	36	32	36	37	38	42	46
Qfac	0	3	6	6	7	7	6	10	10	11	13	14	15	16
W/Z+$jets$ Norm.	18	17	17	15	16	14	11	18	16	17	19	20	19	17
Top Norm.	1	2	2	2	3	2	2	1	3	2	1	0	1	2
Multijet Norm.	1	0	0	2	0	2	5	0	0	0	0	0	0	0
JER	0	1	1	2	5	3	3	3	11	10	2	1	7	7
JES1	0	1	1	0	1	2	3	7	3	7	6	10	3	6
JES2	0	0	1	1	0	0	3	1	0	3	2	0	1	1
JES3	0	1	0	0	4	2	1	5	4	0	6	4	2	2
JES13	0	1	3	1	4	6	5	13	7	2	8	12	3	2
JES14	0	3	6	5	6	5	5	1	5	4	6	4	8	10
JES15	0	2	2	1	2	4	3	7	1	7	6	10	3	4

Table D.4: Systematic uncertainties for each bin of $p_{\mathrm{T}}(jj)$ in the muon channel for the aTGC event selection. The systematic uncertainties are given in percentages and only the diagonal entries from the covariance matrix are shown.

Syst	Bin Number 1	2	3	4	5	6	7	8	9	10	11	12	13	14
Signal														
Total	15	16	21	21	21	33	34	55	33	30	27	96	50	26
MC stat	2	3	12	8	6	11	9	7	10	9	11	41	10	9
Signal Norm.	15	15	15	15	15	15	15	15	15	15	15	15	15	15
Renorm/Fact Scales	1	3	6	7	8	9	10	11	12	12	13	14	15	18
JER	0	2	0	7	4	16	0	50	9	14	7	50	5	3
JES1	0	1	0	1	7	12	18	7	3	8	2	38	7	3
JES2	0	0	2	3	1	2	2	4	5	3	5	39	4	3
JES3	0	2	1	3	3	4	3	1	23	7	1	4	1	2
JES13	0	0	4	1	5	5	16	7	1	9	7	7	2	3
JES14	0	1	1	5	0	13	1	0	4	5	7	2	43	0
JES15	0	1	4	2	1	9	11	1	3	7	6	40	1	3
Background														
Total	18	18	46	49	42	46	48	48	53	46	52	50	66	67
MC stat	0	1	4	6	7	6	8	15	16	20	5	33	42	4
Δ R	0	2	41	45	36	41	43	40	46	35	44	33	43	61
Qfac	0	3	6	7	7	8	8	10	10	12	13	10	15	18
W/Z+$jets$ Norm.	18	17	17	17	17	16	16	18	17	19	19	14	20	20
Top Norm.	1	2	2	2	2	3	2	1	2	1	1	0	0	0
Multijet Norm.	1	0	0	1	1	0	1	1	0	0	0	5	0	0
JER	0	1	6	4	0	2	5	4	1	2	5	6	5	4
JES1	0	1	1	1	0	3	1	0	2	1	6	2	2	1
JES2	0	0	1	0	3	2	3	4	1	3	1	1	4	0
JES3	0	1	1	2	1	2	3	2	4	3	3	2	2	2
JES13	0	0	2	2	4	7	7	7	7	3	11	3	3	1
JES14	0	3	5	1	2	7	3	1	6	4	2	1	2	3
JES15	0	2	0	1	0	2	0	1	1	1	3	2	7	3

Table D.5: Systematic uncertainties for each bin of $p_{\mathrm{T}}(jj)$ in the electron channel for the aTGC event selection. The systematic uncertainties are given in percentages and only the diagonal entries from the covariance matrix are shown.